Development of Novel Computational Fluid Dynamics (CFD) based Calibration Methods for Pipeline Fluid Flow Measurement

A thesis submitted in partial fulfilment of the requirements for the degree of doctor of philosophy at the University of Huddersfield

by

Chukwubiadam Okwuikpo

School of Computing and Engineering

University of Huddersfield

UK

June 2019

ABSTRACT

The measurement of fluid flows is encountered in most engineering applications, such as oil and gas, power etc. Lack of efficient and straightforward methods of flow measurement cause inaccuracies in process control. One of the instruments that are widely used for measurements is the five-hole pressure probe because of its effectiveness in measuring flow parameters such as the velocity of the flow stream, static and stagnation pressures.

The present study describes the design, manufacture and Computation fluid dynamics (CFD) based novel methods of calibration of conical and hemispherical five-hole pressure probes appropriate for three-dimensional flow field measurements, capable of improving calibration and flow measurement accuracies. The conical and hemispherical five-hole pressure probes have been designed and tested in a wind tunnel and hydraulic pipeline flows respectively. The correlation between each geometrical shape of the probes and their yaw and pitch angles flow interference have been investigated. More specifically, the effect of each probe shape on the calibration of the process in the wind tunnel have been investigated. Furthermore, the effect of the hydraulic pipeline flow regime and fluid properties on the calibration process has been investigated, and comparisons have been made for results obtained in air and water flows.

The novel method of calibration is based on the use of Computational Fluid Dynamics (CFD) techniques to develop calibration methods for five-hole probes and incorporating these calibration methods into fluid flow measurements. Even though the concept of using CFD to analyse the flow around a five-hole probe numerically has been in practice for more than a decade now, there are severe limitations to it. These limitations range from the accuracy of the numerical and experimental data. In the present study, these two factors have been thoroughly investigated, leading to the accurate integration of numerical datasets into the conventional experimental calibration datasets for both wind tunnel and in hydraulic pipeline flows to cover a wide range of applications.

The first aspect of this study has been to carry out the calibration of a five-hole pressure probe using standard experimental methods, in a wind tunnel and hydraulic pipeline flows respectively. A pressure normalisation and data analysis technique introduced by Paul Akshoy coupled with sixth order regression method have been used for calibrations dataset analysis to improve the accuracy of calibration. The calibration maps, calibration coefficients and coefficients of determination have been calculated using sectoring scheme. However, due to several sources of error in several

calibration procedures, the calibration coefficients of determination are not usually up to the expected accuracy level needed for accurate flow measurements. Therefore, by first carrying out the conventional calibration of the five-hole pressure probe using sectoring scheme, the coefficients of determination, also known as calibration constants (a_0 to $a_{27)}$ are calculated. The calibration determinants, which performed less than 90%, are assumed inaccurate and are marked for improvements.

The second method of calibration developed in this study (CFD based numerical calibration method) has been to repeat the calibration of the five-hole probe using numerical datasets generated through the use of CFD simulations under the same flow and system conditions. The numerical calibration coefficients, calibration maps and coefficients of determination are calculated and tabulated. The third aspect of this study is to identify the sector of the experimental calibrations that has its coefficients of determination less than 90% assumed to be contributing a factor of measurements inaccuracies, this coefficient of calibration is replaced by the highly accurate CFD based numerical coefficients of calibration with above 90% accuracy. Hence integrating the two methodologies to develop a novel calibration method.

The process of integrating CFD based numerical datasets into experimental datasets is the second novel method of calibrations developed in this study, known as CFD based integration calibration. The same calibration technique used for the previous two methods is applied to the CFD based integrated datasets to generate calibration coefficients, calibration maps and calibration coefficients of determination and tabulated. The performances of the calibration method are tested by comparing their results for accuracy. For each wind tunnel and hydraulic pipeline flow respectively, and for the conical and hemispherical five-hole probe, the calibration procedures for all the novel based CFD calibration methods are the same.

The fourth and last aspect of the of this study has been to extend the calibration angles (pitch and yaw) of the CFD based integrated calibration method of the probes, through the use of CFD based numerical simulation. It involves using the CFD technique to simulate each probe for $\pm 35^0$ to $\pm 45^0$ under their respective flow conditions, acquire the pressure datasets, and reapply the calibration formula, pressure normalisation, and data reduction technique to obtain calibration data that can be used in systems with larger flow angles to cover a wide range of space for measurements.

DECLARATION

- The author of this thesis (including any appendices and schedules to this thesis) owns any copyright in it (the “Copyright”), and he has given The University of Huddersfield the right to use such Copyright for administrative, promotional, educational and teaching purposes of any kind.

- Copies of this thesis, either in full or in extracts, may be made only by the regulations of the University library. Details of these regulations may be obtained from the librarian. This page must form part of any such copies made.

- The ownership of any patents, designs, trademarks and any another intellectual property right except for the Copyright (the "Intellectual Property Rights"), which may be described in this thesis may not be owned by the author and may be held by third parties. Such Intellectual Property Right and Reproductions cannot and must not be made available for use without the prior written permission of the owner(s) of the relevant Intellectual Property Rights and Reproductions.

ACKNOWLEDGEMENTS

First and foremost, I would like to thank God Almighty in Heaven for giving me the grace, strength, knowledge, ability and the opportunity to undertake and complete this research study satisfactorily. This lifetime achievement was possible because of His love, grace, and blessings towards me.

I want to express my deepest gratitude to my supervisor Professor Rakesh Mishra for his continuous support, guidance, his innovative ideas, and encouragement throughout the research. His knowledge of fluid mechanics, fluid dynamics, instrumentation and process control as well as his unique research and supervision techniques were the driving force throughout the research study. His critical appraisal and constructive feedbacks made it possible for this thesis. He gave me the latitude to express myself at every meeting we had and have been quick to suggest new ways that made sure this research was successful in all areas.

I want to acknowledge the support of Dr Taimoor Asim for his considerable help in modelling and design of the five-hole probes in the flow domain, his guidance, and supervision throughout this research study. I want to acknowledge my friends and colleagues at the Energy, Emissions and Environment Research group at the University of Huddersfield, Antonio Oliveira and Yusuf Airede for their support and cooperation at the fluid laboratory. Furthermore, I would like to acknowledge the support of the administrative staff at the School of Computing and Engineering and the technicians at the technology building such Dr R. Cattley, Denis Town, Richard Bailey, Steve, and Bob Powis. Thank you all for your help.

I am hugely grateful and indebted to my parents, Senior Pastor G. N Okwuikpo and Mrs Elizabeth Okwuikpo, My Grandmother (Nnakwu) Deaconess Sarah Adaozuruoke Victor, my siblings, nieces, nephews and most importantly, my Elder Brother Ndenso Gabriel Okwuikpo. Their sacrifice, support, encouragement, and motivation were vital in making my journey possible.

CONTENTS

LIST OF FIGURES

LIST OF TABLES

NOMENCLATURE

a_0, $a_1 \ldots a_{27}$	Polynomial constants calculated by least square method (-)
AI	Analogue input (Volts)
AO	Analogue output (Volts)
B_P	Base pressure (Pa)
Cp_{itch}	Pitch coefficient (-)
C_{Static}	Static pressure coefficient (-)
C_{Ptotal}	Total pressure coefficient (-)
C_{Pyaw}	Yaw coefficient (-)
D_o	Outer diameter of the probe (m)
D_{HP}	Outer diameter of the hydraulic pipeline (m)
d_{HP}	Inner diameter of the hydraulic pipeline (m)
d	Probe hole diameter (m)
k	Flow coefficient (-)
L_{WT}	Length of wind tunnel (m)
L_{HP}	Length of hydraulic pipeline (m)
Ma	Mach number (-)
N	Number of calibration points used by local least-squares in interpolation (-)
P	Pressure (Pa)
P_1	Pressure sensed at hole 1 (Pa)
P_2	Pressure sensed at hole 2 (Pa)
P_3	Pressure sensed at hole 3 (Pa)
P_4	Pressure sensed at hole 4 (Pa)

P_5	Pressure sensed at hole 5 (Pa)
P_I	Pressure input (Pa)
P_i	Any hole pressure (Pa)
P_O	Pressure output (Pa)
P_{ref}	Reference pressure (Pa)
P_d	Dynamic pressure (Pa)
P_{Top}	Pressure sensed by the top hole (Pa)
P_{Bottom}	Pressure sensed by the bottom hole (Pa)
P_{Center}	Pressure sensed by the centre hole (Pa)
P_{Right}	Pressure sensed by the right hole (Pa)
P_{Left}	Pressure sensed by the left hole (Pa)
$\bar{p}$	Average pressure (Pa)
P_m	Arithmetic mean of pressures P_1, P_2, P_3, P_4, P_5 (Pa)
P_{Static}	The true local static pressure of flow (Pa)
P_{Total}	Th true local total pressure of flow (Pa)
R	A results of a measurement (-)
Re	Reynolds number (-)
Ref	Reference value (-)
Q	Flow rate (m^3/sec)
U	Flow velocity magnitude (m/sec)
Ux	x component velocity (m/sec)
Uy	y component velocity (m/sec)
Uz	z component velocity (m/sec)

U_∞	Flow free stream reference velocity (m/sec)
W_{WT}	Width of the wind tunnel (m)
W_F	Wedged Face (m)

SYMBOLS

c	A/D counts
e	A measurement-system dependent quantity
α	Pitch angle (^{o})
β	Yaw angle (^{o})
ρ	Density of fluid (kg/m^3)
Δ	Difference (-)
θ	Angular position (^{o})
h	Manometer height (-)
m	Manometer (-)
n	Sector number (-)
∞	Free stream condition (-)
γ	Roll angle (^{o})
μ	Viscosity (kg/ms)
Ψ	conical probe chamfer angle (^{o})
z	zero applied pressure (Pa)

ABBREVIATIONS

5HP	5-Hole Probe
ANFIS	Adaptive Network and Fuzzy Interference System
CAD	Computer Aided Design
CFD	Computational Fluid Dynamics
DAQ	Data Acquisition
FADS	Flush Air Data System
LDV	Laser Doppler Velocimetry
LES	Large Eddy Simulations
MEMS	Micro-Electro-Mechanical System
MWP	Multihole Wedged Probe
PIV	Particle Image Velocimetry
PVC	Polyvinyl Chloride
RMS	Root Mean Square
USB	Universal Serial Bus

Chapter 1 Introduction

This chapter provides an introductory discussion about fluid flow measurements using multi-hole pressure probes. These include studies on the operating principles of multi-hole pressure probes, their calibration and data reduction processes, and error analysis. Furthermore, this chapter provides with the details of the selection of the multi-hole pressure probes for flow measurements. The research motivations and aims are the highlights of this chapter.

1.1 Background

In this era of sophisticated electronics and optical fluid flow measurement systems, in many scenarios and applications, process parameters measurement using multi-hole pressure probes is often more suitable. In cases where there is a need to measure the three components of velocity vectors accurately, a well-designed multi-hole probe excels in measurement accuracy of the measurements compared to much modern equipment, at a fractional cost and effort. If flow intrusion is not a primary problem, the simplicity of a multi-hole probe is often preferred over other types of flow measuring instruments.

Multi-hole pressure probes are the extension of the Pitot tube concept. The known relative position of each pressure hole allows the measurement of flow magnitude and direction, in addition to the static and total pressures. Multi-hole probes come in different designs depending on the application. Three-hole probes are capable of measuring flow angle in the yaw direction, for example, measurement of a two-dimensional flow. Five-hole probes are capable of resolving two flow angles, i.e. pitch and yaw directions. These allow the measurements of a three-dimensional velocity field. Additional two holes allow a seven-hole probe to measure higher pitch and yaw angles than the five-hole probes. However, it will require redesigning, fabrication, recalibrations, which are time-consuming and not very cost-effective Bryer, D.W., & Pankhurst, R.C. (1971).

Multi-hole pressure probes have been in use to obtain velocities, pressure data and flow angles in fluid flows. Numerous multi-hole probe geometries have been developed over time. These include certain probes that are application-based, for example in turbomachines etc. The principle of operation, which most multi-hole pressure probes have in common, is the calibration procedures and the ability to determine flow velocity from measured differential pressure and the. The specific design of the probe depends on interference effects, access, volume, response time and sensitivity Everett, K., Gerner, A., & Durtson, D. (1983).

1.1.1 Theoretical Analysis of Multi-Hole Pressure Probes

It would be advantageous if analytical procedures could determine the calibration characteristics and response of a five-hole pressure probe. In actuality, other methods can assist in the theoretical analysis point of view. One of these methods is the aerodynamic projection method. For probes head with complex head geometric features such as prism probes, any analytical procedure is

complicated. Huffman, G.D., Rabe, D.C., & Poti, N.D. (1980) suggest that these complex geometries, which are characterised by sudden changes in the contour, are subject to flow separation and viscous effects that cannot be modelled by computational methods only.

However, the method of aerodynamic projection is used in addition to experimental studies as well as computational studies. This method will appear to easily predict multi-hole pressure probe calibration coefficients, at least qualitatively Leland, B.J, Hall, J.L., Joensen, A.W., & Carrol, J.M. (1977).

1.1.2 Multi-Hole Probe Design and Shapes

Multi-hole pressure probes with simple geometry of contours such as conical probes, the aerodynamic projection method is valid. However, the analytical relationship is worthwhile for the characterisation of the probe behaviour and as a guide to the functional form of calibration equations. Nevertheless, this will probably not be able to replace an individual probes calibration because of both performance constraints and production irregularities of probes. Regardless of the accuracy of the theoretical analysis, production irregularities always necessitate individual calibration of any multi-hole pressure probe, especially miniaturised probes Delhaye, D., Penagua, G., & Fernandez J.M. (2011).

Pawel R., Kamila, G., Przenyslaw, M., Lucas, S., and Daniel, B. (2018) suggest that the primary goal of a miniaturised sized multi-hole probe is for it to cause the least interference in the flow field as well as to measure the changes in differential pressure with reasonable accuracy. Multi-hole probes are designed in a way that minimises the adverse effects of flow blockage and spatial resolution in flow measurements. The pressure holes of the probe are located along the probe head at such places that they can register changes in local pressure of the flow. Figure 1.1 depicts a five-hole pressure probe.

Figure 1.1. Five-hole pressure probe

The most commonly used multi-hole probes are five-hole and seven-hole probes because they are capable of resolving three-dimensional flows. These probes are designed in such a way that the holes are located along the head of the probe. Multi-hole pressure probes come in different shapes and sizes; in addition to a prism and conical probes, there is a hemispherical pressure probe etc. Figure 1.2 depicts these three different probe heads Zilliac, G.G. (1989).

Figure 1.2. Faceted, conical and hemispherical probe heads Zilliac, G.G. (1989)

When using the faceted shaped pressure probe, the highest pressure measured is at the stagnation point, and the pressure on the surface of the probe decreases away from this point. Conically shaped pressure probe is the most preferred choice due to its superiority in spatial resolution, and it is easier to calibrate. Furthermore, the conically shaped pressure probes minimise near-wall flow blockage effects, which are particularly strong for prismatic type probes Rediniotis, O., Hoang, N., & Telionis, D. (1993).

In the case of a hemispherically shaped multi-hole pressure probe, pressure on the tip of the probe is necessarily the same as the pressure above the hemisphere because of the smooth surface of the probe head. This inherent characteristic of the hemispherical probe is a useful approximation for the flow solution as the pressure depends only on the angle θ and the stagnation point will cause the pressure coefficient to change. When hemispherical pressure probes are used to carry out flow measurements, the pressure on the surface is dependent only on the angle θ between the probe axis and the point of interest Kinser, R. E, & Rediniotis, O. K. (1998).

In theory, any head or shape should work for a multi-hole pressure probe. The principal criterion to determine the appropriate shape (for a particular application) is that the pressure recorded by the pressure hole should vary smoothly with flow angle. However, due to some sharp changes in the

calibration curve, $\Delta p/\Delta \alpha$ or at any other angle, there may be inaccuracies in the angles that the probe read. The different types of multi-hole pressure probes used to carry out flow analysis have provided acceptable results. The most common of them are the conical and hemispherical heads. However, faceted heads with flattened surfaces also show reasonable performance Koppel, P., Roduner, C., Kupferschmied, P., & Gyarmathy, G. (2000). The difference between the performance of smooth and faceted heads is the flow separation characteristics. Flow separation over a flat surface is gradual and displaces smoothly over the probe surface, which is an attractive characteristic for hemispherical multi-hole pressure probe. However, a faceted probe is more sensitive to unsteady stall effects that introduce errors in detecting dynamic phenomena Matsunaga, S., Ishibashi, H., & Nishi, M. (1980).

The pressure hole located at the head of the multi-hole pressure probe must communicate with pressure transducers. Metal tubes are connected at the output terminal of each pressure probe and the input terminal of the other end to the pressure transducer. The length of these tubes may vary and can be as long as several meters according to the requirement for applications. Measurement of data and development of an interpolation procedure for the data analysis in the responsibility of the probe user and must be developed to capture calibration data Naughton, J.W., Cattafesta III, L.N., & Settles, G.S. (1992).

1.1.3 Operating Principles of Multi-Hole Pressure Probes

Any object introduced in a flowing fluid will experience pressure being exerted on its surface. In the case of incompressible flow over bluff bodies, the maximum pressure is equal to the total pressure (Pt), which is the sum of the static pressure (P_S) and dynamic pressure (P_d) Rediniotis, O.K., & Pathhak, M.M., (1999).

$$p_{total} = p_{static} + \frac{\rho U^2}{2} \tag{1.1}$$

ρ and U are the density and velocity magnitude of fluid flow respectively. The lowest pressure on the body is typically expected to be at the regions where the body inclination is almost parallel to the free flow, however, is not always the case. Often, the flow over bluff bodies separates. Separation of flow changes the local pressure distribution and leads to unfavourable pressure gradients in areas where the slope of the body surface decreases. For example, in the case of a

laminar flow over a circular cylinder, separation occurs at about 80^{o} from stagnation point, rather than at 90^{o} , where the tangent to the surface is parallel to free stream velocity Kupferschmied, P., Koppel, P., Roduner, C., & Gyarmathy, G. (2000).

The principle of measurement using multi-hole pressure probes is based on the law of a bluff body immersed in a flow field, i.e. the pressure acting on their surfaces is related to the flow velocity can be mathematically expressed using Bernoulli's principle in equation (1.2).

$$p_{static,1} + \frac{\rho}{2} U_1{}^2 = p_{static,2} + \frac{\rho}{2} U_2{}^2 \tag{1.2}$$

The potential flow solution for a circular cylinder gives the velocity on the cylinder by using equation (1.3).

$$U(\theta) = 2U \sin\theta \tag{1.3}$$

θ is the angular distance from the stagnation point to the point of interest.

To demonstrate the operating principle, consider a multi-hole probe consisting of a circular cylinder exposing pressure holes 1, 2 and in pitch position along the meridional angles θ=0, $\pm 45^{o}$ as depicted in figure 1.1. If the free stream is coming in the horizontal direction assumed to be normal to the axial of the cylinder, the pressure reading at θ=0 will be stagnation pressure and the readings along the other pressure holes will be equal to each other. On the other hand, if the probe is inserted in a two-dimensional flow field inclined with respect to the axis of the probe by a pitch angle (α), then the pressure measurements at points θ=0, $\pm 45^{o}$ can return the free stream velocity magnitude U, the pitch angle, and the static and dynamic pressures Rediniotis, O. K., Johansen, E.S., Tsao, T., Seifert, A. & Pack, L.G. (1999).

1.1.4 Basic Concept of Calibration and Measurement Relationship

Multi-hole pressure probes are handy tools for studying the fluid flow fields of any flow facility. However, due to design imperfections as well as fabrications and manufacturing defects, all multi-hole pressure probes need calibration before they can be used to carry out flow measurements. Calibration of a five-hole pressure probe requires the probe to be subjected to a known flow field at various combinations of pitch and yaw angles planes and the pressure data on the holes are recorded for further analysis. The physical quantities of the fluid flow that are expected to be obtained by the

user of the probe are the local fluid flow velocities, the static and total pressure at the point of measurement. These quantities are functions of the pressure measured by the pressure holes located at the tip of the pressure probe. Figure 1.3 depicts a typical numbering of five-hole pressure probe holes related to the calibration method Johansen E.S., Rediniotis, O.K., & Jones, G.S. (2001).

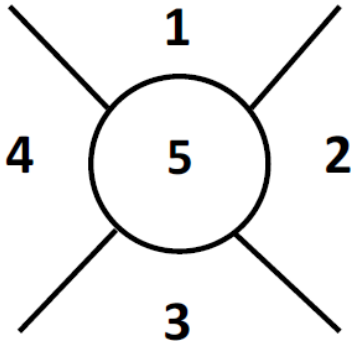

Figure 1.3. The numbering of a five-hole pressure probe holes Johansen E.S., Rediniotis, O.K., & Jones, G.S. (2001)

Before pressure measurement on the flow field is made, the orientation of the probe is adjusted to two angles positions. These could be a cone (θ) and roll (φ) or pitch (α) and yaw (β), as depicted in figure 1.4. The measuring systems (θ, φ) and (α, β) are interchangeable, and the conversion between them is shown in the goniometric relations in equations (1.4) and (1.5). In the present study, the two angles used are pitch (α) and yaw (β) angles.

$$\alpha = \tan^{-1}(\tan\theta \sin\varphi) \tag{1.4}$$

$$\beta = \tan^{-1}(\sin\theta \cos\varphi) \tag{1.5}$$

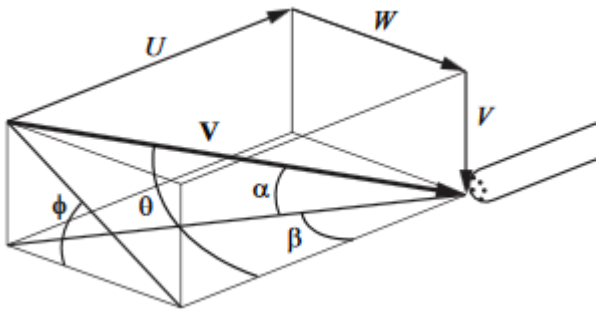

Figure 1.4. Graphical representation of flow velocities Johansen E.S., Rediniotis, O.K., & Jones, G.S. (2001)

When the probe is subjected to an unknown velocity field, the hole registering the maximum pressure is identified. Appropriate coefficients are then evaluated using the corresponding sector's

equation. The flow angle is determined using the corresponding calibration function that described calibration coefficients corresponding to the values of Cp_{total} and $Cp_{static.}$ The velocities of the flow, true local total, and static pressures can then be computed using equation (1.6) through (1.10).

$$U_x = |U| \cos(\alpha) \tag{1.6}$$

$$U_y = |U| \sin(\alpha) \sin(\beta) \tag{1.7}$$

$$U_z = |U| \sin(\alpha) \cos(\beta) \tag{1.8}$$

$$Cp_{total} = \frac{p_{sector} - p_{total}}{D} \tag{1.9}$$

$$Cp_{static} = \frac{\bar{p} - p_{static}}{D} \tag{1.10}$$

$$|U| = \sqrt{\frac{2(p_{total} - p_{static})}{\rho}} \tag{1.11}$$

Where Δp is the difference between the approximations of stagnation and total pressures and P_{Bar} is the average pressure of all the holes. The calibration data of the multi-hole pressure probe are discrete data; therefore, when a five-hole pressure probe is to measure flow velocity, the measured quantities fall between the discrete calibration data. Special software is required to interpolate the discrete data so that it can return measurements regarding the calibration coefficients Kerrebrock, J.L, Thompkins, W.T., & Epstein, A.H. (1980).

The basic calibration parameters are the flow angles that determine the probe orientation, Reynolds Number (Re) and Mach number (Ma). The calibration coefficients are unique to each pressure probe. However, even when two multi-hole probes are designed and manufactured in the same computer-controlled machine with the same specifications, their calibration coefficients will differ from each other because the smallest mechanical difference on the surface of the probe can cause significant differences in the calibration coefficients Achenbach, E. (1971). Therefore, each multi-hole probe must be calibrated before it can be used for measurements.

In the present study, the conical and hemispherical five-hole pressure probes have been used for fluid flow diagnostics in wind tunnels and hydraulic pipelines. The non-nulling sector method of calibration has been used. Furthermore, pressure normalisation and data reduction techniques have been employed where the pressure measured by the centre hole of the five-hole pressure probe is

taken into account while defining the non-dimensional pressure coefficients. A sixth order curve-fitting polynomial regression technique has been used for data analysis and interpolation to further improve calibration and measurement accuracies.

1.2 Applications of Multi-Hole Pressure Probes

In many complex flow fields like the ones found in turbomachines, the experimental measurement of the steady-state velocities of the flow is often required. However, the free jet and flow field in the systems exhibit strong velocity gradients induced by the blade wakes as well as by the hub and casing boundary layers. Hash measurement environments make the multi-hole pressure probes particularly attractive for measurement of flow velocities and pressures. These types of probes are becoming more popular and useful with the development of cost-effective computer controlled traversing systems, fast response transducers, and computer-based data acquisition. The choice of a multi-hole pressure probe depends on the fluid flow to be measured. Fluid flow can occur in two main types of systems for which measurements are likely to be necessary. These are:

1. The attached boundary layer flow systems where large changes in the flow direction are limited to the planes parallel to the surface.
2. The rotational flows systems such as the wake or part–span vortices in which arbitrary flow changes can occur on any plane.

For both (1) and (2) conditions, flow parameters are obtained by separate local measurements using different measuring instruments in each setting. Due to errors in the positioning of successive devices, these methods, including the time needed to make measurements, have proved not to be the right methods. It evident that the first step forward is to use an improved technique to find a single measuring instrument that can be used to measure all relevant flow parameters at once with reasonable accuracies. To this effect, the five-hole multi-hole pressure probe is the best choice.

The five-hole pressure probes are simple to design, robust, time saving and cost-effective for all local measurements. Because of the small nature of the probes, they do not affect the flow significantly. Furthermore, five-hole pressure probes are typically used in areas where pressure measurement is necessary. Most importantly, five-hole pressure probes can operate in harsh flow environments, and in transparent and opaque flows. In the present study, the conical head and hemispherical head five-hole pressure probes are the two types of multi-hole pressure probes used

for wind tunnel and hydraulic pipeline flows. Five-hole pressure probes remain one of the most straightforward and most robust means to measure fluid velocities, pressures and flow angles.

Five-hole probes provide robustly, cost-effective alternative to non-intrusive optical, and laser flow interrogation techniques. A five-hole pressure probe can be used to perform superior to high-flow analysis, which can provide simultaneous and multi-point measurements for statistical analysis, in a wind tunnel environment. Shevchenko, A.M., & Shmakov, A.S. (2017) suggest the use of five-hole pressure probes provide significant measurement capacity within a compact design and with a minimally intrusive package for wind tunnel experiments and numerical studies. Figure 1.5 depicts a wind tunnel laboratory where the services of a five-hole can be used for optimal operations of the systems.

Figure 1.5. A typical wind tunnel Shevchenko, A.M., & Shmakov, A.S. (2017)

Bonham, C., Thorpe, S., Erlund, M., and Stevenson, J.(2017), suggests the use of the stagnation pressure probe in gas turbine exhaust ducts and engines. In many gas turbine laboratories experiments, due to the robustness and cost-effective nature of five-hole probes, it is used to examine the auxiliary gas turbine exhaust components and other performance measurements that provide flow velocities, static pressure, and Mach numbers. Figure 1.6 depicts a gas turbine jet engine and its internal components descriptions.

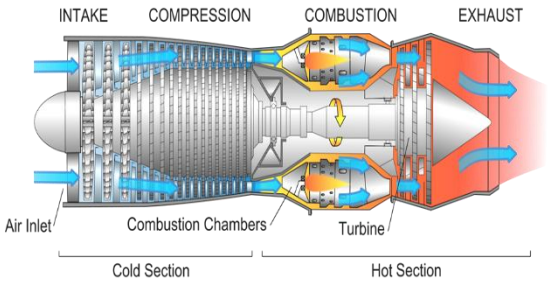

Figure 1.6. Gas Turbine Jet Engine Bonham, C., Thorpe, S., Erlund, M., and Stevenson, J. (2017)

This engine can produce flows in the engine components of about 2.5kg/s of hot air at a temperature of about 600°C. These flows are typically highly three dimensional with high velocity and pressure gradients. There is a need to take measurements of pressure, velocity, and temperature of these flows both inside the engine components and at the exit planes.

Local velocity measurement is usually carried out in one of the three main methods of using an optical probe, hotwire, and Pitot tubes. Optical techniques include laser Doppler anemometry (LDA) and particle velocimetry (PIV). These methods use lasers to illuminate the flow locally, and the behaviour of seeding particles that pass through the area of interest is recorded using a high-speed camera or Doppler phase shift. However, it is challenging to implement laser methods of measurements for Gas engine flows because of high initial mass flow rates require vast amounts of seedlings materials, and seeding of secondary eject flows is difficult. Hotwire methods measure the current flow through the heating wire and correlate heat loss from the wire to flow velocities over the wire. High-temperature hot wire and hot-film type probes are available. However, they are expensive, and the tips of the probe itself can be fragile and thus not suitable for such measurements. Given the scale of devices tested in these hash measurement environment and the manufacturing tolerances in some convex and welded sheet metal ducts, there is a high risk that these type of measurement techniques and probes would collide with walls and edges of these ducts Sieverding, C.H, Art, T. Denos, R., & Broukarert J.F. (2000).

Five-hole pressure probes are the most attractive option for measuring flow information in harsh environments mainly due to its mechanical strength and relatively low cost. Hotwire and laser systems can cost more than £25,000, whereas a multi-hole pressure probe can be produced for less than £15000. Five-hole pressure probes can be made from stainless steel that is corrosion-resistant. They can provide full three-dimensional velocity and pressure measurement in a single measurement, something that is not possible with optical or hot-wire probes.

Aschenbruck, J., Hauptmann, T., & Seume, J.R. (2015) established the influence of multi-hole probes in axial turbines. Drilled elbow pressure probes can be used to measure the performance of a diffuser designed for a gas turbine. One probe is used to measure the inlet flow conditions to the diffuser to demonstrate how flow would exit the turbine in real-world applications. The conditions that are measured are the radial distribution of flow angles, pressures, and Mach number to ensure the system is outputting the desired in-flow to the diffuser. On the outlet of the diffuser, another

vast drilled pressure probe can be installed to measure the outlet flow from the diffuser. Figure 1.7 depicts the schematic arrangement of a gas turbine for power generation.

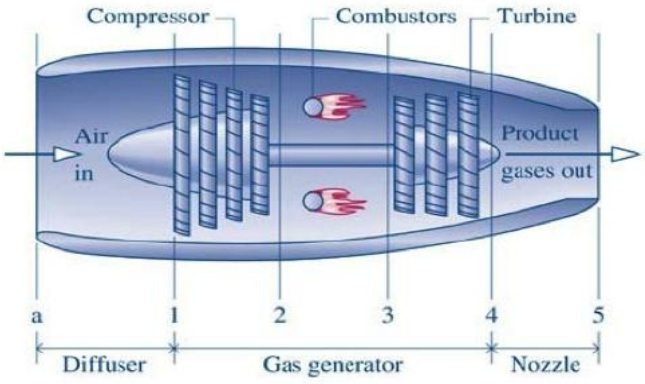

Figure 1.7. Gas Turbine Diffuser for Power Generation Aschenbruck, J., Hauptmann, T., & Seume, J.R. (2015)

By comparing the measured inlet and outlet flows as depicted in figure 1.7, the static pressure rise and the total pressure drop across the diffuser can be determined.

Furthermore, the probe is also used to gather detailed flow maps used to validate computational predictions that will enhance the performance of the diffuser. The measurements can be recorded in numerous simulated operating conditions to collect data for multiple operational scenarios of the diffuser. Also, Techsburg uses L-shaped five-hole pressure probe in the linear cascade wind tunnel to measure the total pressure drop across turbine vane rows. These measurements are then used to calculate and study the vane's efficiency.

In addition to the above applications, the use of five-hole pressure probe can be extended to other fluid mechanic measurements studies such as cooling systems, the design of hydraulic systems, other areas of wind tunnel studies related vibrations, noise radiations, and lift and drag. It can equally be extended to compressors research involving both reciprocating and rotating types of machinery. It is, however, essential to understanding fluid mechanics and dynamics of a five-hole pressure probe for useful experimentation, interpolation, and interpretation of results and for estimating deterministic errors because of flow modification by the probe when it is immersed in a flow field. The purpose of measurements and the problem should be understood.

Nearly all types of measurement methods depend on the nature of the flow under test and this in turns guide the selection of measurement instruments. Almost all fluid measurements are direct. Moffat, R.J. (1988) suggests that for that reason, the methods of measurements rely heavily on the physical interpretation of the physical quantity measured from the flow. Therefore, it is necessary to have a clear understanding of the problem, the principle of fluid mechanics, the law of operation of the flow instrumentation, and the elements of statistical analysis Groth, J. & Johansson, A.V. (1988). Without data taken with five-hole probes, these applicable systems are just fancy noisemakers. It is imperative to calibrate a five-hole pressure probe successfully and accurately map the flows around and through the systems. In all, applying the use of five-hole pressure probes in any application helps to measure flow velocity and direction. Also, it helps to provide a better understanding of design efficiency and recommend design changes in other to improved system performance Laws, E.M., Livesey, J.L. (1978).

The flowchart shown in figure 1.8 clearly summaries this chapter and provides insight on the approach followed in this study. Furthermore, it depicts the flow link between the research motivation, background, aims and objectives and the entire thesis structure.

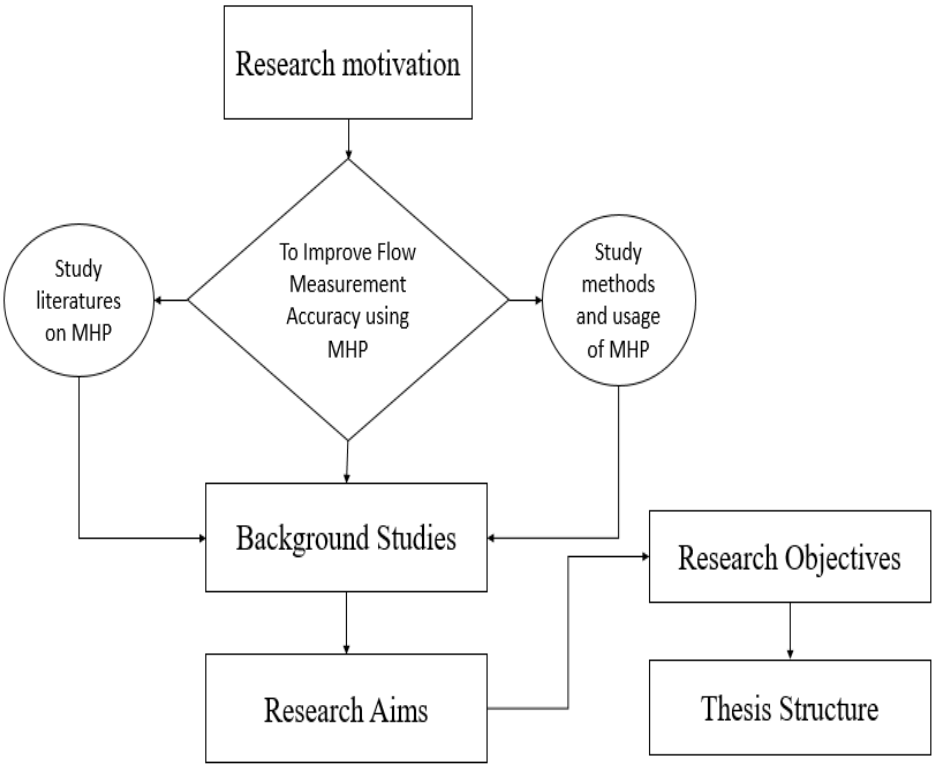

Figure 1.8. Chapter flowchart

1.3 Research Motivation

The ability to accurately measure the properties of a complex three-dimensional flow field is essential in modern fluid dynamics and aerodynamics. Such measurements contribute to the fundamental understanding of fluid dynamics, and they can be used to understand and improve the performance of fluid systems. Accurate three-dimensional flow field measurements are critical to validating and enhancing modern CFD tools. Within the fluid industries, it has been recognised that accurate flow measurements can lead to higher profits in the areas of production monitoring, flow assurance and production cost-effectiveness. The accurate knowledge of flow properties, including velocities, pressure etc. is of utmost importance for the optimum design and operation of compressors, blowers, fans and turbines. Many experimental techniques can be used to study three-dimensional flow fields with the most common being hotwires, optical techniques such as LDV or PIV and multi-hole pressure probes. Hotwires and LDV can be used to measure the mean and fluctuating velocity at a point, and PIV can mean the mean and varying velocity over a two-dimensional plane. Of the many possible techniques, multi-hole pressure probe, in particular, five-hole probes are unique because of their ability to measure all three components of the velocity vectors as well as the exact local total and static pressures.

Although various instruments and measurement methods are available to measure flow properties, accuracy in flow measurement is often questionable with conventional measurement methods. Many intrusive devices have failed to account for errors introduced by the unsteadiness in flow fields and on pressure dependent flow velocity measurements. Moreover, present multi-hole pressure probes can only measure flow properties at a severely restricted range of flow angles and velocities. Hence, in the present study, a novel calibration methodology has been developed for conical and hemispherical five-hole pressure probes. The developed calibration methodology integrates the numerical data with the experimental data to enhance the accuracy of the probe. The calibration methodology has been extensively tested and verified against standard experimental tests. Further investigations have been carried out in the present study to use numerical methods for the extension of the measurement range of the five-hole probes. These experiments were carried out in both wind tunnel, and hydraulic pipeline flows, using a hemispherical and a conical head five-hole pressure probes.

Based on the global demand for accurate measurement of velocities and pressures especially in the power, chemical, and oil and gas industries, it is imperative to review the current calibration and measurement methods of flow using five-hole pressure probes and develop a new calibration and measurement methods. A systematic study of the effectiveness and limitations of the existing methods has been carried out to identify new methods of improving calibration and measurement results in internal and external flow systems. Computational fluid dynamics (CFD) has been considered as an effective tool to integrate with experimental results and investigate flow velocities and pressures in pipelines and wind tunnels to capture flow fields. CFD would provide a platform to simulate and analyse conical and hemispherical five-hole pressure probes. Furthermore, numerical results would also allow direct comparison with experimental results and both results have been integrated where necessary to increase accuracies.

1.8 Research Aims

The aims of the current research are centred on the development of a novel calibration methodology, and measurement technique, for intrusive flow measurement using five-hole pressure probes in a variety of flow conditions. The specific aims of the research work are:

1 Development of a numerical and experimental based calibration method for conical five-hole probes for wind tunnel flows.
2 Development of an integrated calibration method for hemispherical five-hole probes for wind tunnel flows.
3 Extension of the calibration range of conical five-hole probes for hydraulic pipeline flows.
4 Extension of the calibration range of hemispherical five-hole probes in hydraulic pipeline flows.

The study can overcome the knowledge gaps between the use of experimental and CFD based numerical calibration datasets and measurement of flow information using five-hole probes having defined the research aim. It also has enormous potential to significantly improve the accuracy in the monitoring of internal and external flow systems. Furthermore, the research has tremendous possibilities for process and instrumentation applications. The need for a calibration method of five-hole probes that is capable of measuring flow velocity with high precision is highly desirable to obtain real-time flow information for internal and external flows. Also, the study can be applied in

the physical monitoring of a harsh environment that is crucial for intellectual control of modern energy production systems such as improved gas turbines. Also, the research offers an alternative method for using a sophisticated but easy and cost-effective approach to read data from a remote miniature five-hole probe specially designed to operate in a particular flow and condition. Based on the challenges and the need for the research identified above, the objectives for this study that can assist in bridging the knowledge gaps identified earlier are as follows:

1.9 Research Objectives

Based on the thorough literature review carried out, the objectives for the current study to bridge the knowledge gaps are identified as follows:

- To develop Computational Fluid Dynamics (CFD) integrated calibration process for the conical five-hole probe and increase the accuracy for wind tunnel flows measurements.
- To extend the calibration range of conical five-hole probe using CFD in wind tunnel flows.
- To estimate the accuracy of velocity measured by a conical five-hole probe in wind tunnel flows calibrated with integrated calibration method.
- To develop CFD integrated calibration process for the hemispherical five-hole pressure probe and increase the accuracy of measurement as well as establish a probe head effect in wind tunnel flows.
- To extend the calibration range of the hemispherical five-hole probe using CFD in wind tunnel flow and establish a probe head effect.
- To estimate the accuracy of velocity measured by a hemispherical probe in wind tunnel flows after calibrating it with CFD integrated process and establish probe head effects.
- To develop CFD integrated calibration process of the conical five-hole probe and increase the accuracy of measurement in pipeline flows and establish performance characteristics when used for analysis with different fluids.
- To extend the calibration range of conical five-hole probe using CFD in pipeline flows and establish performance characteristics when used for measurement with different fluids.
- To estimate the accuracy of velocity measured by a conical pressure probe in pipeline flows and establish performance characteristics when used for measurement with different fluids.

- To develop CFD integrated calibration process of the hemispherical five-hole pressure probe and increase accuracy in pipeline flows and establish performance characteristics of probes with different shapes when used for measurement with various fluids.
- To extend the calibration range of hemispherical five-hole pressure probe using CFD in pipeline flows and establish performance characteristics of probes with different shapes when used for measurement with various fluids.
- To estimate the accuracy of velocity measured by hemispherical pressure probe in pipeline flows computed by CFD integrated and CFD extension of range calibration data and establish performance characteristics of probes with different shapes when used for measurement with various fluids.

1.10 Thesis Structure

Chapter 2 This chapter discusses the results of the previous works carried out in the area of multi-hole pressure probes, with a focus on the different calibration methods. The chapter includes a critical analysis of the published literature on the effects of multi-hole pressure probes shapes, design patterns and fabrication principles. Furthermore, various research works that detail pressures and velocities measurement using multiple types of multi-hole pressure probes are presented in this chapter. Also, it discusses the state-of-the-art researches carried out in the area of multi-hole pressure probes.

Chapter 3 This chapter discusses the experimental methodologies adopted in this study, which includes the mechanical design and construction of the probes to achieve the aims and objectives of the research study. It further discusses the novel calibration methods and techniques involved in the use of conical and hemispherical five-hole pressure probes used in wind tunnel and hydraulic pipelines flow in a systematic approach, and the process of error analysis carried out for the study. Also, it describes the pressure normalisation and sectoring techniques in the study in details. Lastly, it discusses the method of sixth order polynomial regression analysis and the process of coefficients and three-dimensional velocity calculations.

Chapter 4 This chapter discusses the CFD simulation methodologies used in this study. It describes the numerical setups of the CFD based novel calibration methods and techniques involved in the use of conical and hemispherical five-hole pressure probes in wind tunnel and hydraulic pipeline flow domains. It includes the mechanical design of the probes and simulation procedures involved to achieve the aims and objectives of the study. Also, it describes the numerical modelling and simulation techniques such as solver settings, meshing techniques and the appropriate boundary conditions specified for the simulations.

Chapter 5 A novel calibration method for conical five-hole pressure probes for wind tunnel flows has been developed in this chapter. It has been achieved through the use of both the experimental and CFD numerical techniques. Furthermore, this chapter discusses the integration of the numerical data with that of the experimental data to enhance the accuracy of measurements from the conical five-hole pressure probes. Also, the calibration range of the conical five-hole pressure probe has been extended using CFD based numerical methods to cover a wide range of flow measurements in wind tunnels. The validation of the calibration method developed has been carried out at different angular positions of the probe concerning the flow.

Chapter 6 This chapter presents a novel calibration method for hemispherical five-hole pressure probes for wind tunnel flows. For this purpose, both the experimental and numerical techniques have been used. The numerical pressure data has been integrated with the experimental pressure data to enhance the accuracy of measurements from the hemispherical five-hole pressure probes. The calibration range of the hemispherical five-hole pressure probe has been extended, using numerical simulations, to cover a wide range of flow measurements in wind tunnel flows. The validity of the extended calibration method has been checked against a known flow field. Furthermore, this chapter discusses the effect of the probe head shape on accurate measurement.

Chapter 7 This chapter quantifies the effects of the flow regime on the calibration of both conical and hemispherical five-hole probes. Therefore, both the experimental and numerical works have been carried out in hydraulic pipelines, where the flow is internal, complex and three-dimensional. An integrated calibration method has been

developed for both the probes. The range of calibration for both the probes has also been extended. The suitability of the wind tunnel calibration equations, for both probes, has been checked in hydraulic pipeline flows. Furthermore, this chapter discusses the effect of conical and hemispherical head probes on the flow regime and properties measurement accuracy on both probes in wind tunnel and hydraulic pipeline flows.

Chapter 8 This chapter presents the comparisons of performances of the CFD based calibration methods of the conical and hemispherical five-hole pressure probes in air and water flow fields. The calibration sector maps of the probes have been generated and compared using calibration datasets for air and water flow field respectively. Furthermore, the conical and hemispherical probe has been used to measure air and water flow and using their respective datasets to compute flow information such as three-dimensional velocities. Comparisons of the flow information have been carried out to establish the performance accuracy of each probe in air and water flow fields respectively.

Chapter 9 This chapter presents the significant achievements of the research work in details. Furthermore, detailed significant conclusions of the study based on the results reported in this thesis are highlighted in this chapter. Also, the major contributions to the knowledge gaps in the area of the work as well as recommendations for future work have been provided in this chapter.

Chapter 2 Literature Review

Measuring technique for fluid flow can be categorised in two main methods. These are invasive and non-invasive methods. An invasive procedure is when the measurement is acquired from inside the environment where the phenomenon takes place, while a non-invasive measurement is taken from outside the environment where the phenomenon of interest takes place. Furthermore, each of these methods is classified into two categories depending on measurement resolution and accuracy. These two subcategories are local and global measurements. The local measurements involve the process in which a specific parameter in the flow is measured in a predetermined position in the wind tunnel or hydraulic pipeline.

In order words, the measurement of the parameter is made at a single point in the test section. Global measurement is made when an average-valued flow is of interest. However, it is possible to have measurements that are invasive and either global or local. Any decision is taken regarding the technique and the type of measurement to be used on the requirements and specifications of the study. For example, one of the differences between local and global measurements is that the local measurement has a better spatial resolution of the flow characteristic than the global.

In general, the global can provide average fluidity information at a shorter time than local measurements. Regarding the technique, one of the differences between invasive and non-invasive methods are their applicability in a particular environment. A non-invasive method that uses laser light, as an observation tool may be inappropriate a working environment in which the pipes are metallic or not transparent to the laser wavelength; but the Pitot tube or a multi-hole pressure probe may be more suitable. In this study of multi-hole pressure probes, the calibration and measurement are invasive and local.

A detailed review of the published literature has been presented in this chapter, which will highlight the knowledge gaps in the existing knowledge regarding multi-hole pressure probes. This chapter includes published works regarding the design and calibration of multi-hole pressure probes and using these probes for flow measurements. Based on the knowledge gaps found in the literature, the scope of research has been defined, and the research objectives of this study have been formulated. The detailed ascriptions for various multi-hole probe calibration and measurement methods that give better ideas and understanding are presented in the next sections.

2.1 Calibration Methods for Multi-Hole Pressure Probes

Five-hole pressure probes have been widely used to measure three-dimensional velocity vectors, the static and total pressures at the point of flow measurement. There are other types of pressure probes as well, such as Pitot-static probes and yaw probes, which are conventionally used to measure the flow velocity magnitude only. Over the years, numerous calibration methods for five-hole pressure probes, for flow measurements, have been introduced. One of such approaches relates the velocity magnitude and angle of the flow to the theoretical flow model. Lee, S.W., & Jun, S.B. (2005) provided some useful theoretical model to provide the relationship between the pressure ports of the probe, velocity magnitude, and incidence angles.

The earliest pressure probes calibration was carried out using the nulling calibration method. A Pitot tube was mounted in the flow, and the pressure on the diametrically opposite static pressure holes was measured at each separately. The probe was rotated until the difference between the opposite holes becomes zero. The angle at which the opposite hole of the probe registered zero is noted as the reference point. The inclination angle of the probe then become the flow direction, and the Pitot tube equally measured the magnitude of the flow.

Pressure probes give an accurate resolution of velocity vectors for flow angle as high as 60° for the five-hole probe or 70° for the seven-hole probe. These probes are usable in air and water environments at a flow speeds from 5m/sec to 325m/sec and Mach 0.02 to Mach 0.95. However, due to their intrusive nature, they may interfere with flows, cause flow separation, thereby increasing error in pressure reading. At high flows, shocks could be created near the tip of the probe or any part of the steam leading to the error. Bryer, D.W., & Pankhurst, R.C. (1971) explain the two calibration procedural techniques used for multi-hole pressure probe are null calibration and non-null calibration techniques.

2.1.1 Multi-hole Pressure Calibration Definitions and Conventions

The null calibration technique is extremely time-consuming and relies on the assumption that the flow is locally symmetric about the pressure probe, which put constraints on probe manufacturing tolerances. Furthermore, a null calibration technique requires a great deal of apparatus and equipment for the instrumentation setup. Therefore, it creates a demand for another technique of calibration known as non-nulling calibration method. This technique is cost-effective and

straightforward to implement, however, it leads to complicated computational calculations and use of surface response curve to derive the calibration coefficients using a data reduction method. Furthermore, it is unable to capture turbulence properties, not suitable for highly unsteady flows with high Reynolds number, and not suitable for flows having significant total pressure gradient for if Mach number is significantly high. Garlington, R.W. (1980) introduced the non- null calibration concept and the procedure that is largely accepted and used today. The four basic elements required for flow measurement using a multi-hole pressure probe are:

1 Construction and selection of probe
2 Accurate probe calibration
3 The means to measure probe hole pressures
4 Data reduction and analysis to convert the measured pressures into velocities based on the calibration map or coefficients

The numbering convention of the probe holes must first be established before any other thing, and the holes are numbering that must be relative to the orientation. Figure 2.1shows the sign convention of three angles defined as pitch, yaw, and a roll of a five-hole probe. The flow angles relative to the probe tip can are defined using two coordinates systems, the pitch and yaw also referred to as the probe X and Y-axis. The cone and roll coordinate systems is a polar coordinate system. The cone is the total angle of attack to the probe axis while the roll angle is the rotational angle of the probe that is referenced to a fixed probe axis.

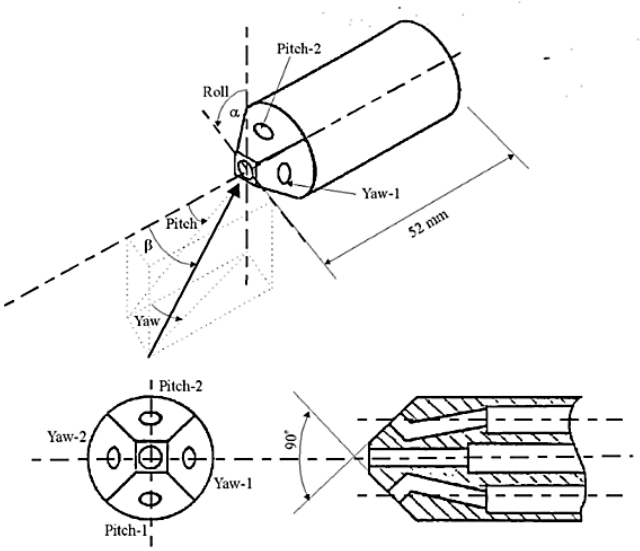

Figure 2.1. Flow Angle and Coordinate Systems Garlington, R.W (1980)

Table 2.1. Flow Angle Definitions Garlington, R.W. (1980)

Angle	Term	Regime	Definition
α	Pitch	Low Angle	Angle between w and Y-Z projection of velocity
β	Yaw	Low Angle	Angle between velocity vector and Y-Z projection of velocity
θ	Cone	High Angle	Angle between w and the velocity vector
γ	Roll	High Angle	Angle between –v and X-Y projection of velocity

The angles defined in table 2.1 are used to introduce the concept of flow regime. The response equations of the probe will be different for different angles of attack. At low angles of attack, the flow remains attached over the entire flow tip. However, as the angle of attack begins to increase in the flow on the downwind side of the probe will begin to separate. The pressure data in the separated region is reported to be unsteady and do not represent the flow under measurement. Therefore, at high angles of attack, data from the holes are measuring at the separated region of the flow are ignored, and the flow was calculated using only the data measured by the holes attached in the flow. The low angle regime is therefore defined as the regime in which flow is attached over all holes, and the high angle flow regime is the regime in which flow is attached over only on some holes. The pitch and yaw coordinates systems are used to analyse low angle flow regime, while cone and roll coordinate systems are used to analyse high angle flow regime Garlington, R.W. (1980). A detailed explanation, formulation of the governing equations and choice of different coordinate systems and found in section 2.2.

2.2 Calibration Governing Parameters

The concept of direct pressure coefficients remains one of the preferred methods for formulating calibration-governing equations for a seven-hole pressure probe Garlington, R.W. (1980). The first step in this method is to determine whether measured flow falls into low and high angle regime by identifying the hole of the probe reading the highest pressure, which is indicative of the general direction of the flow. If the centre hole read the highest-pressure value, the flow is assumed low angle flow, and the data from all the holes are used in the calculations. If the peripheral holes read the highest pressure, the flow is assumed high angle flow, and there is a significant probability of flow separation over the holes on the downwind side of the probe. In high angle flow, the flow is calculated based on the hole that read the highest pressure only and the other adjacent holes where

the flow is known to be attached. The structure and form of the governing calibration parameters are the same for high and low flow regimes. Whichever way, two directional pressure coefficients are defined. This allows the flow direction to be determined through correlation techniques described in section 2.4. The magnitude and pressure of the flow are also determined through the of the dimensionless pressure coefficients.

The total pressure of the flow under test is the sum of the static and dynamic pressure of the flow. The highest pressure read by any single hole (sometimes the centre hole) of the probe is the available approximation of the total flow pressure. The average of the remainder of the peripheral pressure holes that are in the attached flow is the best possible approximation for the static pressure of the flow. The difference between the two pressures gives an approximate dynamic pressure of the flow. Gerner A.A., Maurer, C.L., & Gallington, R.W. (1984) proposed the dimensionless coefficients that are used to formulate the total and dynamic pressure of the flow, as the essential correction factor to the approximations of total and dynamic pressure that are calculated from pressure datasets measured by the holes of the probe.

2.2.1 Low Angle Coefficients

In a low angle flow, the highest pressure is sensed at the top pressure tap of the probe, which is then approximated as the total pressure of the flow. Furthermore, the flow in the low angle regime is assumed to be attached over all the peripheral pressure holes. Therefore, the approximate static pressure is calculated as shown in equation (2.1) Garlington, R.W. (1980).

$$\overline{P} = \frac{1}{6}\sum_{i=2}^{7} P_i \tag{2.1}$$

The directional pressure coefficients for the low angle regime are shown in equation (2.2) Gallington Garlington, R.W. (1980). The Pressure differences were normalised using the approximated dynamic pressure of the flow.

$$C_a = \frac{P_3 - P_2}{P_1 - \overline{P}}, C_b = \frac{P_4 - P_7}{P_1 - \overline{P}}, C_c = \frac{P_6 - P_5}{P_1 - \overline{P}} \tag{2.2}$$

The coefficients are weighted according to the relative positions of the probe and used to generate a further pair of coefficients that are used to represent the pitch and yaw angles planes of the flow.

The formulated equations for pitch and yaw coefficients demonstrated in equation (2.3) and (2.4) are based on the geometry of the probe head.

$$C_\alpha = \frac{2C_a + C_b + C_c}{3} \tag{2.3}$$

$$C_\beta = \frac{C_b + C_c}{\sqrt{3}} \tag{2.4}$$

The definition of the total and dynamic pressure coefficients are shown in equation (2.5) and (2.6) respectively.

$$C_t = \frac{P_1 - P_t}{P_1 - \overline{P}} \tag{2.5}$$

$$C_q = \frac{P_1 - \overline{P}}{P_q} \tag{2.6}$$

P_t and P_q are the true total and dynamic pressure of the flow.

2.2.2 High Angle Coefficients

In a high angle flow regime, the highest pressure is recorded in one of the peripheral holes, and this port is referred to as hole Pn. Therefore, this hole is taken to be approximately the true local total pressure of the flow. There is a high possibility that in this flow regime, the downside of the probe could be measuring in the separate flow. Therefore, only pressures from the port Pn, the two immediately adjacent peripheral ports and the centre port are considered. The pressure in the two adjacent peripheral holes is defined as P+ and P-. The approximate flow of static pressure is calculated by equation (2.7).

$$\overline{P}_n = \frac{P_+ + P_-}{2} \tag{2.7}$$

Directional coefficients in the high angle flow regime are defined based on the polar coordinate system as illustrated in figure 2.1 is easy because it only allows a single pair of coefficients to be determined and a couple of factors applies to all outer holes. Determining yaw and pitch coefficient for the outer holes would have required using particular scalar weightings for the pressure difference terms at each hole. The cone and roll coefficients normalised by the relative flow dynamic are shown in equation (2.8) and (2.9) respectively.

$$C_\theta = \frac{P_n - P_1}{P_n - \overline{P}_n} \tag{2.8}$$

$$C_\gamma = \frac{P_- - P_+}{P_n - \overline{P}_n} \tag{2.9}$$

The total and dynamic pressure coefficients are defined in a similar to those in low angle flow regime can be seen in equation (2.10) and (2.11) respectively.

$$C_{tn} = \frac{P_n - P_t}{P_n - \overline{P_n}} \tag{2.10}$$

$$C_{in} = \frac{P_n - \overline{P_n}}{P_q} \tag{2.11}$$

The disadvantage of this method is that the high angle flow regime equation is only valid if at least four holes of the probe are reading in the attached flow. Section 2.3 describes the assumption that the two adjacent peripheral holes attached flow is reasonable and it is highly unlikely that the presumption could be violated. However, it is possible that the flow at the centre hole could become separated, leading to the possibility of producing double-valued directional pressure coefficients which could introduce an enormous amount of error to measurement or render the measurement invalid. The chance of these double-valued coefficients is shown in figure 2.2, which demonstrates pressure coefficients on the surface of a cylinder in cross-flow as a function angle of attack. The pressure distribution around a cylinder is often approximated using equations of flow around a 2-D circular cylinder Zilliac, G.G. (1993).

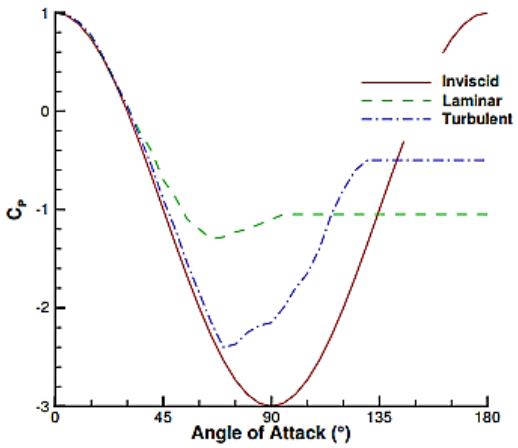

Figure 2.2. Pressure Coefficients on the Surface of a Circular Cylinder in Crossflow Zilliac, G.G. (1993)

The figure demonstrates the pressure coefficients characteristics for a cylinder in an inviscid, laminar and turbulent flow. The flow on the downwind cylindrical shape separates in both laminar and turbulent flows. The most important thing about this figure is not about the separation point but that in both low and high angle regimes, the flow recovers some pressure before separation occurs. This pressure recovery is what leads to the possibility of double-valued pressure coefficients.

2.3 Inviscid Flow Solutions and Calibration Limitations

The pressure distribution around the head of a multi-hole pressure can be calculated analytically using inviscid flow equations. Huffman, G.D., Rabe, D.C, & Poti, N.D. (1980) Introduced the use of slender body theory to define a set of response equations that would analytically predict the pressure distribution around the head of the probe at an arbitrary angle of attack. Given the fixed location of the pressure holes, a set of response equations, different from those shown in section 2.2 are introduced. The assumptions behind this alternative approach are because of the theory that the governing equations are mainly physically significant on inviscid flow. The curve fitting and interpolation process techniques that relate flow properties to directional coefficients are merely used because it produces acceptable results but not grounded in an expected physical response Zilliac, G.G (1993). However, Huffman, G.D., Rabe, D.C, & Poti, N.D. (1980) acknowledged that the inability of inviscid flow theory to predict flow separation and the sensitivity of probe response to manufacturing tolerance. This disadvantage means that of the multi-hole pressure probe calibration is very important.

The response of pressure can be demonstrated with simple geometry modelled using potential flow theory. Pisdale, A.J., & Ahmed, N.A. (2004) elaborated on the possible flow solution approach for a five-hole pressure probe by generating a set of probe head response equations that can be numerically or graphically interpolated. The justification for this method is that it is grounded in a potential flow approach that is physically significant. The disadvantage of this method is that if a polynomial curve fit or direct interpolation technique with directional pressure coefficients is used in the calibration, it must be demonstrated that the physical response of the probe head is modelled accurately. Furthermore, it must confirm that the calibration curve fits the data well over the entire probe head, which is the response region and that all the real trend of the probe response, are captured accurately.

2.4 Multi-hole Pressure Probe Calibration Techniques

Testing of flows, be it swirling or not, be it water, gas or wind, requires the measurement of three components of velocity, flow angles, and static pressure and total pressure. These parameters can be extracted from pressure probes with at least five distinct holes. The probe has to be calibrated in a flow with known velocity magnitude while pitch and yaw angles of the probe are adjusted to known angle values to give the pressure response of each hole versus pitch and yaw angles. A calibration theory generates a calculation of four pressure coefficients that are independent of flow velocities below 20% the velocity of sound which allows the probe to be calibrated at a constant velocity magnitude but then is used to measure unknown flow at any velocity Paul C. (2013).

The definitions of four pressure coefficients distinguish the methods of calibration of multi-hole probes. Error propagates from measurement calibration pressures to the pressure coefficients and then to continues from the four measured hole pressures to the calculated components of velocity and pressures. Therefore, the error propagation is different for each method, and it is possible to compare the different methods according to the resulting errors for the measurement flow. The best approach is one that has the lowest velocity and pressure errors Louis (2012).

The ultimate goal of calibrating a multi-hole pressure probe is to establish a correlation between the directional pressure coefficients, flow angles, total and dynamic pressure coefficients. The calibration is carried out by placing the probe in a known axial flow and moving the probe to some known angles. The directional pressure coefficients known as independent variables are then related to the dependent variables, which are the flow angles, total and static pressure coefficients Silva M.C.G, Perira, C.A.C, & Cruz, J.M.S. (2003). The methods that are used to relate the independent and the dependent variable are have been extensively studied in this chapter. A detailed description of these calibration methods is demonstrated in the following sections. The process of calibration technique used in this research study is the multi-variable polynomial curve fit method. Therefore, the mathematical approach is presented extensively in section 2.4.1. For brevity, the mathematics of this approach of deriving them are omitted. All the methods described in this chapter used the same governing parameters to define the probe response. The methods described below only deals with how the independent variables and dependent variables are related to one another.

2.4.1 Multivariable Polynomial Curve Fits

Garlington, R.W (1980) introduced the concept of a polynomial power series fit. This concept used a bivariate surface polynomial to relate directional pressure coefficients to the flour flow desired flow properties. The output of the calibration is a set of coefficients that allow a flow of property to be determined using simple matrix multiplication. Gerner, A.A., Maurer, C.L., & Gallington, R.W. (1984) introduced a similar concept but added a degree of freedom by defining a compressibility coefficient that is also included in the calibration. Gerner, A.A., Maurer, C.L., & Gallington, R.W. (1984) however, used the multivariate surface polynomial method to relate the directional coefficients, and compressibility coefficients to the four desired flow properties.

The main advantage of the polynomial surface method is the number of calibration coefficients that is required is very small. The sectors of the probe are determined according to the number of holes in the probe and are calibrated independently; every four dependent variables requires its correlation to the directional coefficients. A fourth order, bivariate polynomial, with 15 terms, therefore, requires 420 calibration coefficients. A third order requires 280 calibrations points.

The optimal choice of power series is not part of this literature. Gallington, R.W. (1984) proposed a fourth order method of the bivariate polynomial method. Sumner, D. (2002) suggested a third order method of the bivariate polynomial method. Gerner, A.A., Maurer, C.L., & Gallington, R.W. (1984) used a third order method of the bivariate polynomial method. Furthermore, Everett, K.N., Gerner, A.A, & Durston, D.A. (1983) used the bivariate polynomial method. The order of the power series must be high enough so that physical phenomena occurring within the solution domain are capture. However, a power series of a rule that is too high is very likely to introduce noise to the calibration data and may well generate curves with peaks and valley that unphysical especially in the area within the boundaries.

The number of points that are used to calibrate a sector is an essential factor in determining the correct order of curve fit to be used in a particular calibration. Everett, K.N., Gerner, A.A, & Durston, D.A. (1983) show that in a given grid density, for a conical pressure probe, as the maximum cone angle considered during the calibration is decreased, the standard error in the calibration is also reduced. The standard errors are measured by feeding the calibration data back through its calibration curve to measure the quality of the curve fit to a given set of calibration data. Decreasing the maximum cone angle would reduce the number of points in a given sector.

However, Everett, A.A. (1983) did not decrease the number of degrees of freedom in the curve fit. Therefore, the reduced standard error observed could be considered an expected result. When calculating the standard errors, it is important to find the ratio of the size of the calibration set to the number of degree of freedom in the curve fit. Therefore, this ensures that reductions in errors are not because of the effective increase in the order of the polynomial curve fit.

2.4.2 Pressure Normalisation Techniques for Five-hole Pressure Probes

For the calibration of five-hole pressure probes, it is revealed that there are four ways to define the four significant non-dimensional pressure coefficients, which are used for calibration calculation. Krause., & Dudzindki. (1969) first described the pressure coefficients normalisation technique, for five-hole pressure probe with the centre hole labelled as P_5 and the off-axis holes, are labelled P_1, P_2, P_3, and P_4. The four pressure coefficients are demonstrated in equation (2.12) through to equation (2.15).

$$P_{p\alpha} = \frac{P_1 - P_3}{P_5 - \overline{P}} \tag{2.12}$$

$$P_{p\beta} = \frac{P_2 - P_4}{P_5 - \overline{P}} \tag{2.13}$$

$$P_{total} = \frac{P_5 - P_{total}}{P_5 - \overline{P}} \tag{2.14}$$

$$C_{static} = \frac{\overline{P} - P_{static}}{P_5 - \overline{P}} \tag{2.15}$$

$$\overline{P} = \frac{P_1 + P_2 + P_3 + P_4}{4}$$

A Normalisation of by $P_5 - \overline{P}$ has been incorporated in the majority of multi-hole pressure probe calibration procedures developed in subsequent years by Treaster, A.L, &Yocum, M. (1979), Sitram, N., & Treaster, A.L. (1985). The advantage of this method is its simplicity and provides an excellent foundation to understand the operation of multi-hole pressure probes. However, the disadvantage is that at large flow angles measurement it becomes increasingly inaccurate due to singularity issues.

A different method of pressure normalisation that extend Pisasale, A.J., & Ahmed suggested the range of calibration, N.A. (2004), which indicate the removal of singularity issues by about $\pm 70^{o}$. This work, the denominator proposed by Krause, L.N & Dudzinski, T.J. (1995) and later $P_5 - \overline{P} + Aq$ were replaced which successfully allows the calibration to much higher angles of pitch and yaw while maintaining the simplicity of the original procedure. However, the results obtained did not exhibit much improvement for the calibration data taken in the range of $\pm 30^{o}$ pitch and $\pm 45^{o}$ yaw angles. The correct assessment of value influences a lot in determining the calibration coefficients.

By considering 4th order regression analysis, the goodness of fit (r^2) parameters as per the coefficients in defined by Pisasale and Ahmed are 0.9772 and 0.9476 for pitch and yaw angles respectively, which are much lower, considering that fact that the same parameters reported by Gallington, R.W. (1980) are 0.9957 and 0.9910. Zilliac, G.G. (1993) observed that the flow on the lee side of most probes begins to separate the flow at approximately 30^{o} . Gallington, R.W. (1980) in a bit to avoid this used the method of sectoring scheme was adopted, which selects combinations of holes for which the flow is attached. According to the sectoring technique, the entire calibration sector is divided into five parts, one central zone (sector 5) and four side zones (zone 1 to 4). For a particular sector, the pressure coefficients are formed by using the hole that records the highest pressure and the holes adjacent to the maximum pressure hole. This process is known as zonal discrimination, and for a five-hole pressure probe, the pressure coefficients in various zone/sectors as defined by Gallington, R.W. (1980) are shown in equation (2.16).

Zone 1	Zone 2	Zone 3	Zone 4	Zone 5
$D = P_1 - \frac{P_2 - P_4}{2}$	$D = P_2 - \frac{P_1 - P_3}{2}$	$D = P_3 - \frac{P_2 - P_4}{2}$	$D = P_4 - \frac{P_1 - P_3}{2}$	$D = P_1 - \frac{P_2 - P_4}{2}$
$C_{p\alpha} = \frac{P_1 - P_5}{D}$	$C_{p\alpha} = \frac{P_1 - P_3}{D}$	$C_{p\alpha} = \frac{P_5 - P_3}{D}$	$C_{p\alpha} = \frac{P_1 - P_3}{D}$	$C_{p\alpha} = \frac{P_5 - P_3}{D}$
$C_{p\beta} = \frac{P_2 - P_4}{D}$	$C_{p\beta} = \frac{P_2 - P_5}{D}$	$C_{p\beta} = \frac{P_2 - P_4}{D}$	$C_{p\beta} = \frac{P_5 - P_4}{D}$	$C_{p\beta} = \frac{P_2 - P_4}{D}$
$C_{ptotal} = \frac{P_1 - P_{total}}{D}$	$C_{ptotal} = \frac{P_2 - P_{total}}{D}$	$C_{ptotal} = \frac{P_3 - P_{total}}{D}$	$C_{ptotal} = \frac{P_4 - P_{total}}{D}$	$C_{ptotal} = \frac{P_3 - P_{total}}{D}$
$C_{pstatic} = \frac{\frac{P_2 + P_4}{2} - P_{static}}{D}$	$C_{pstatic} = \frac{\frac{P_1 + P_3}{2} - P_{static}}{D}$	$C_{pstatic} = \frac{\frac{P_2 + P_4}{2} - P_{static}}{D}$	$C_{pstatic} = \frac{\frac{P_2 + P_4}{2} - P_{static}}{D}$	$C_{pstatic} = \frac{\frac{P_2 + P_4}{2} - P_{static}}{D}$

(2.16)

Applying the sectoring scheme technique with a 4th order regression analysis, the goodness of fit (r^2) parameters for all sectors are 0.9975 and 0.9907 for pitch and yaw angles respectively, which

exhibit the usefulness of the sector scheme. However, it has been felt that for any combination of pitch and yaw angles, the influence of pressure sensed by the central hole of the probe cannot be neglected as did in the above equation (2.13). With these limitations as recorded in the coefficients, a new set of pressure coefficients were proposed for a five-hole pressure probe by Akshoy, R.P, Ravi, R.U., & Anu, J. (2011). This method overcomes the limitations in Gallington, R.W. (1980) and gives a less computational error in calculating the flow parameters. In this recent work, the influence of pressure recorded by the central hole of the probe (P_5) is considered in defining these coefficients. The pressure normalisation sectoring formulae as proposed by Akshoy, R.P, Ravi, R.U., & Anu, J. (2011) is shown in equation (2.17).

Zone 1:	Zone 2	Zone 3	Zone 4	Zone 5
$\overline{P} = \frac{P_4+P_5+P_2}{3}$	$\overline{P} = \frac{P_1+P_5+P_3}{3}$	$\overline{P} = \frac{P_4+P_5+P_2}{3}$	$\overline{P} = \frac{P_1+P_5+P_3}{3}$	$\overline{P} = \frac{P_1+P_2+P_3+P_4}{3}$
$D = P_1 - \overline{P}$	$D = P_2 - \overline{P}$	$D = P_3 - \overline{P}$	$D = P_4 - \overline{P}$	$D = P_5 - \overline{P}$
$C_{p\alpha} = \frac{P_1-P_5}{D}$	$C_{p\alpha} = \frac{P_1-P_3}{D}$	$C_{p\alpha} = \frac{P_5-P_3}{D}$	$C_{p\alpha} = \frac{P_1-P_3}{D}$	$C_{p\alpha} = \frac{P_1-P_3}{D}$
$C_{p\beta} = \frac{P_2-P_4}{D}$	$C_{p\beta} = \frac{P_2-P_5}{D}$	$C_{p\beta} = \frac{P_2-P_4}{D}$	$C_{p\beta} = \frac{P_5-P_4}{D}$	$C_{p\beta} = \frac{P_2-P_4}{D}$
$C_{ptotal} = \frac{P_1-P_{total}}{D}$	$C_{ptotal} = \frac{P_2-P_{total}}{D}$	$C_{ptotal} = \frac{P_3-P_{total}}{D}$	$C_{ptotal} = \frac{P_4-P_{total}}{D}$	$C_{ptotal} = \frac{P_5-P_{total}}{D}$
$C_{pstatic} = \frac{\overline{P}-P_{static}}{D}$	$C_{pstatic} = \frac{\overline{P}-P_{static}}{D}$	$C_{pstatic} = \frac{\overline{P}-P_{static}}{D}$	$C_{pstatic} = \frac{\overline{P}-P_{static}}{D}$	$C_{pstatic} = \frac{\overline{P}-P_{static}}{D}$

(2.17)

By applying a sectoring technique to the polynomial curve fit to all four new pressure normalisation coefficients to a 4th order regression analysis, the goodness of fit (r^2) parameters for all sectors were reported to be 0.9979 for pitch angle, 0.9979 for yaw angle, 0.9761 for total pressure and 0.9938 for static pressure.

Error analysis is helpful in these regards, where the following parameters are useful in deciding the perfect combination. The error analyses were carried out using equation (2.18) and (2.19).

$$\sigma_\theta = \sqrt{\frac{1}{n}\sum_{i=1}^{n}\left(\theta_{e,i} - \theta_{a,i}\right)^2} \tag{2.18}$$

$$SE = \frac{\sigma_\theta}{\sqrt{n}} \tag{2.19}$$

The goodness of fit of the calibration coefficient of determination, which is commonly known as r^2 and is, expected to be close to 1.0000. It compares the estimated (θ_e) and actual (θ_a) values and ranges from 0.0000 to 1.0000. If it is 1.0000, it shows there is a perfect correlation in the sample, and there is no difference between the estimated and the actual value. On the other hand, if the coefficient of determination is 0.0000, the regression equation is not helpful in predicting a y-value of the regression.

Another thing that this study attempt to investigate is the response of the probe head. Figure 2.3 depicts the calibration map obtained for the calibration of five-hole using the sectoring scheme to the calibration pressure probe.

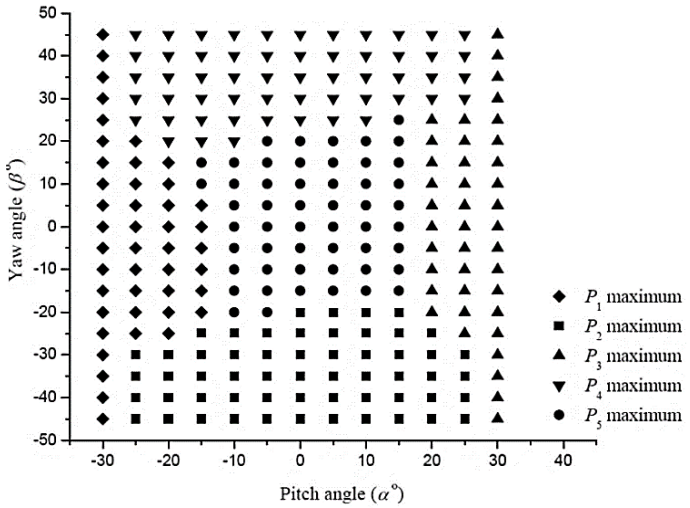

Figure 2.3. Sector Map of the five-hole probe Akshoy, R.P, Ravi, R.U., & Anu, J. (2011)

The sector map shows the map for the five-hole probe indicating the hole, which records the highest pressure for a particular pitch and yaw angles. It reveals that the central hole (P_5) covers the broadest range of the pitch and yaw angles among all the five holes. However, at lager pitch and yaw angles, the peripheral holes (hole 1 to 4) are likely to measure the total pressure, therefore, the pressure measured at the outer hole at their corresponding location in maximum. Asymmetry in the sector map shows the non-asymmetric of the five-hole pressure probe because of fabrication and manufacturing disadvantaged. Although the study shows good calibration results, however, it was just for wind tunnel flows. Furthermore, the calibration flow angles are only limited to $\pm 45^{\circ}$, and nothing suggests that examining the same results numerically or extending the probe angle or integrating experimental result with numerical results have been carried out.

This research study investigates three pressure normalisation techniques in combination with three data reduction techniques reported in this section. A particular set of calibration data for each five-hole pressure probe was generated experimentally and numerically and used the analysis of possible combinations of pressure normalisations and data reduction techniques. Furthermore, using the integrated calibration method of experimental and numerical data introduced in the study, new sets of calibration data have been generated and analysed using the pressure normalisation and data reduction techniques proposed by Akshoy, R.P, Ravi, R.U., & Anu, J. (2011) where the effect of the centre pressure hole is included in defining all pressure normalisation parameters.

2.4.3 Direct Interpolation

Zilliac, G.G. (1993) first introduced the direct interpolation method to improve the accuracy of flow property at high angles. This method has been compared to the polynomial curve fit method and has shown some form of improvements in high flow measurements. The increased error in the polynomial curve method is described in two ways when using direct interpolation. First, at a high angle of attack, there are errors in the directional coefficients, and this causes large changes in the calculated flow angles. Secondly, the noise in the polynomial curve appears to be high; this also exacerbates the problem of using direct interpolation to analyse multi-hole probe calibration data.

Direct interpolation method has two significant disadvantages. The computational cost is higher because a single expression cannot represent the response of the probe head. Furthermore, the amount of storage required for the calibration data is more substantial, and the complete calibration dataset must be stored for future use. The non-uniform calibration grid complicates the actual interpolation procedure. The spacing of the pitch and yaw coefficients in non-uniform which means that the definition of it nearest to the neighbours can be somewhat challenging doing. Akima, H. (1970) proposed a solution scheme for these problems, which is capable of interpolating non-uniform calibration grids of multiple independent variables. This solution scheme fits a local polynomial to at least five points in each direction and uses geometric conditions to ensure regional continuity of the function and its derivatives.

Sumner, D. (2002) conducted direct comparisons of the direct and interpolation method and the polynomial surface method. These two multi-hole pressure probe calibration methods were applied to the same data set using a different larger data set was processed using each technique. In the low angle flow regime, the difference in standard error was shown to be negligible. In high angle flow

regime, there was a recorded improvement of about 0.5° in error found in the flow angle. However, this improvement was found when the calibration grid is quite a course. Furthermore, Silva, M.C.G., Pereira, C.A.C., & Cruz, J.M.S. (2003) compared the polynomial curve method with simple linear interpolation. However, this demonstrates that the interpolation method proposed by Akima and the linear method by Silva may not have been responsible for the improvement of response but maybe because of the nature of the direct interpolation method.

2.4.4 Hybrid Model of Multi-Hole Probe Calibration

Hybrid models have been introduced in an attempted to reduce the fundamental error related to curve fitting. Wenger, C.W. (1999) proposed a combination of a global polynomial curve fit method with local direct interpolation of an error table that is equally calibration output. The reason behind this method is that the high order global curve fit would damp out any noise in the high order derivatives and the low order interpolated error term would allow for local variations of the low order derivatives. The results obtained by Wenger, C.W. (1999) were reasonably good as it reduced g interpolation error to about 1order magnitude below other sources of experimental error. However, the disadvantage of this method is that the accuracy and precision of the calibrator setup will become critical. If the transducers used to carry out pressure measurement are not accurate, the effect of noise in the calibration data can be significant.

Rediniotis, O.K., & Vijayagopal, R. (1999) proposed using a neural network approach to calibrate a multi-hole pressure probe. This approach creates a library of nodes at which a calibration data known as input and output are sorted. Some layers are then created with each node using a weighting factor on adjacent nodes to determine its influence on the calibration data. This approach used some optimisation cycles are completed, where the network calculates values that are compared with known measured values improving its weighting factors each time through until errors are minimised.

The disadvantage of this approach is that the neural architecture of the work, which comprise the number, and arrangement of the nodes of the network as well as the definition of layers, has a significant effect on the accuracy of calibration result. Additionally, the network architecture user is required to work through a significant number of combinations and network designs before reaching the optimal design. However, the advantage of this approach is that additional calibration data could be added easily to the network in an attempt to improve calibration results.

2.5 Reynolds Number Effect on Multi-Hole Pressure Probe Calibration

When the probe encounters flow at a high angle, the flow separates from the downwind side of the probe head. Flow separation is highly dependent on Reynolds number, therefore, understanding the mechanism of flow separation and finding representative problems for comparison is necessary Chue, S.H. (1975) and Leland, B.J., Hall, J.L., Joensen, A.W., & Carrol, J.M. (1977). Figure 2.4 depicts the two typical types of flow separation that are expected to be encountered when the probe is inside a flow.

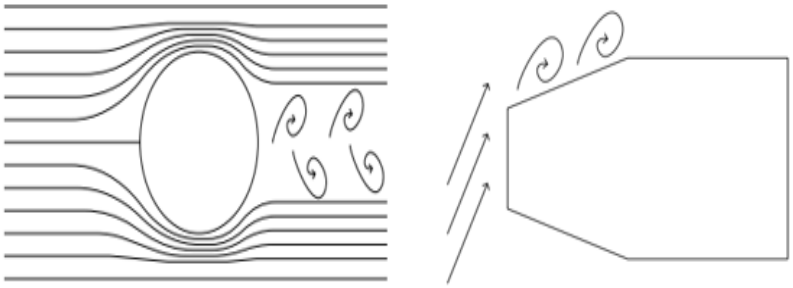

Figure 2.4. Flow Separation: (a) Downwind Separation at High Angles of Attack, (b) Downwind Separation at Moderate Angles of Attack Chue, S.H. (1975)

The flow separation is figure 2.4a is similar to the separation found in downstream of a cylinder in cross flow, while the flow separation in 2.4b is similar to the separation found in a backward facing step. The Reynolds number dependence of separation these flows very much likely to give some insights into Reynolds number dependence of the multi-hole pressure probes. However, in this present study, the effect of Reynolds number on multi-hole probe calibration is not the focus.

2.5.1 Flow Separation over a Backward Facing Step

Flow separation over a backward facing step mostly studied in the two-dimensional test section of internal flow. This issue can still be considered analogous to flow separation over the head of a conical multi-hole pressure probe as long as the step is relatively small on the same order of magnitude as the height of the incoming channel. The definition of the length scale of the Reynolds number is equally necessary. The Reynolds numbers of a flow over a seven-hole pressure probe are mainly reported regarding the diameter of the probe head. Sumner, D. (2002) demonstrated this to make reasonable comparisons with data from a backwards-facing step, the upstream height of the flow channel chosen as the characteristic length as depicted in figure 2.5.

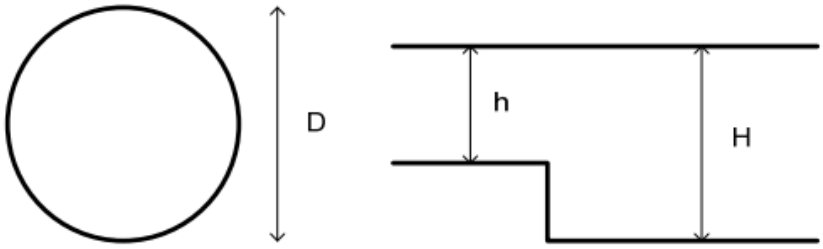

Figure 2.5. Characteristic Length of a Seven-hole Pressure Probe and a Backward-facing Step
Sumner, D. (2002)

Armaly, B.F., Durst, F., & Pereira, J.C.F. (1983) proposed an experimental method to study the separation downstream of a backwards-facing step in a channel with an expansion ratio of about 1.94. This experiment involves using LDA to collect data, and it was found that there were significant changes in the downstream reattachment lent at two critical Reynolds numbers. It was established that below a Reynolds number of 1200, the flow is laminar, and the reattachment length varies linearly with Reynolds number. Furthermore, at Reynolds number above 6600, the flow is fully turbulent, and the reattachment is constant. In the transition region where the Reynolds numbers are between 1200 and 6600, there was a non-linear variation of about 50% in the reattachment. The results of this study suggest that a seven-hole pressure probe response can be quite sensitive to Reynolds number between 1200 and 6600. The choice of transition criteria from the low to high angle flow regime will be critical to reducing this potential source of error as this occurrence takes place at angles of attack close to the transition region.

2.5.2 Crossflow over a Cylinder

When the probe encounters flow at a very high angle of attack, the flow separates on the downwind side of the pressure probe the same way as a cylinder in cross flow. The transition of flow from laminar too turbulent around a cylinder is described by a quick change in the region of separation. Laminar flows are described by a separation that occurs at about 82° from stagnation point, while turbulent flows are described by a separation that occurs at about 110° from the point. Figure 2.6 depicts these two occurrences schematically.

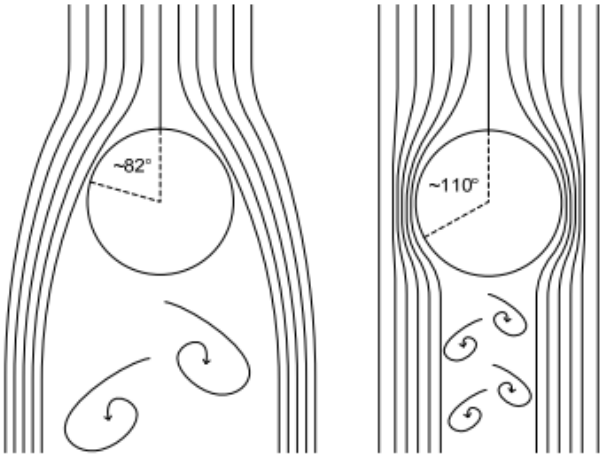

Figure 2.6. Flow Structures Downstream of a Cylinder in Laminar and Turbulent Crossflow Cantwell, B., & Coles, D. (1983)

Cantwell, B., & Coles, D. (1983) experimentally demonstrated that for a smooth cylinder, flow transition from laminar to turbulence is expected at approximately a Reynolds number of $2x10^5$, according to the cylinder diameter. However, it has equally been shown that surface roughness or dimples on the surface of the pressure probe triggers flow transition to turbulence. Flow transition is important to the present study because pressure holes alone act as vortex generators, thus trigger an earlier flow transition from laminar to turbulent flow than would a smooth surface. For a rough surface, flow transition occurs at a Reynolds number of $5x10^4$ Achenbach, E. (1971). Demonstrating a normal roughness height of the pressure holes is difficult. Therefore, it is possible that in this present study, probe response could be affected by Reynolds number effect anywhere between $2x10^5$ and $5x10^4$.

2.5.3 Effect of Mach number on Multi-Hole Pressure Probe Response

Mach number has always been acknowledged as having a significant effect on the performance of a multi-hole pressure probe. Gallington, R.W. (1980) has originally formulated this procedure to accommodate an extension to compressible flow. Gerner, A. A., Maurer, C.L., & Gallington, R.W. (1984) by proposing a compressibility coefficient, introduced this extension. This coefficient is defined for the low angle regime as shown in equations (2.20) and (2.21) for the high angle flow regime. These terms represent the ratio of the approximate dynamic pressure of the flow to the total pressure of the flow.

$$C_M = \frac{P_1 - \bar{P}}{P_1} \tag{2.20}$$

$$C_{M,n} = \frac{P_n - \bar{P}_n}{P_n} \tag{2.21}$$

This compressibility coefficient has been defined in such a way that it is substantially independent of flow direction; therefore, the probe response isolates compressibility effects. The compressibility coefficients became a third independent variable altogether with the two flow direction coefficients in data processing. The polynomial curve fit then became a function of three variables, which for a fourth order curve would result in 35° freedom instead of 15°. Therefore, the order of fit was typically decreased to third order, which includes only 20 terms Gerner, A. A., Maurer, C.L., & Gallington, R.W. (1984). It is possible to use a higher order curve; however, it would require a significantly large number of calibration points to ensure that standard errors in the curve fit are reasonable.

The main disadvantage of adding a third independent variable is to maintain a reasonable size of the calibration grid without losing resolution in any of the three variables. Gerner, A.A., Maurer, C.L., & Gallington, R.W. (1984) employed the method of the Least Squares to select calibration points and found that it was an economical way of choosing grid points in three variable.

This present study is subsonic with maximum Mach numbers 0.2, the limit of incompressible flow. Therefore, a compressibility coefficient is not incorporated into this study. The influence of Mach number is generally acknowledged but is ignored in incompressible flows.

2.6 Flow Turbulence Effect on Multi-Hole Pressure Probe

The accuracy of Pitot tube measurements is known to be affected by the turbulence effect. By Bernoulli's law, an increase or decrease of the same magnitude in flow velocity results in a different magnitude of increase or decrease in pressure because the pressure is proportional to the square of velocity. An error can be introduced through time averaging of Pitot tube data in a highly turbulent flow. Furthermore, any changes in the flow angle because of large-scale local turbulence results in a non-linear response of the probe, which then biases the time-averaged probe response.

Becker, H.A., & Brown, A.P.G. (1974) studied the effect of turbulence on Pitot tube response and found that the Pitot tube should be selected to match the flow that is measured. Four conditions to consider the typical multi-hole pressure probe response was given. Firstly, the turbulence must be large scale, with a mean scale approximately five times the diameter of the probe. Secondly, the Reynolds number must be significant. Thirdly, the Mach number must be small and fourthly, the velocity gradients should be low. Additionally, it was noted that many of the detrimental effects of turbulence could be reduced by installing a small flow obstruction inside the tube itself to effectively damps any oscillation within the pressure lines without affecting the mean pressure at the stagnant air inside the pressure probe head.

Christiansen, T., & Bradshaw, P. (1981) introduced a similar study but using a three-hole pressure probe, also known as yaw meter. The results were identical to Pitot tubes. Three-hole pressure probes were found to be sensitive to turbulence intensity. However, this sensitivity was less compared to that of a Pitot tube especially regarding the sensitivity of the averaging of pressure over multiple holes suppressed the effect of small-scale turbulence more than a Pitot tube.

The technology of developing pressure transducers has led to the development of pressure probes with transducers that are embedded in the probe head. Embedding transducers into the head eliminate the need for long pressure lines and significantly improves frequency response. It has been shown that with total pressure probes, frequency response in the kHz scale is possible using these embedded transducers Kang, J.S., & Yang, S.S. (2010). With this level of frequency resolution, viscous damping and resonance within a fluid carrying cavity in front of the pressure transducer will be significant. The probe must be designed in such a way that the resonant frequencies of the flow chamber are above data acquisition frequency. Furthermore, the transducers cannot be installed very close to the probe head or assume that flow stagnates within the chamber fails Fischer, A., Masden, H.A., & Bak, C. (2009).

The potential of such high-frequency probes for the measurement of transient flows, even those on a turbulent length and timescale has been shown. The main disadvantaged factor currently is the pressure transducers, both regarding the frequency response on a micro scale, regarding temperature and environment disadvantages. Pressure transducers capable of producing a frequency response of about 20 kHz at a temperature of approximately 600°C are presently available commercially and have been successfully implemented for seven-hole pressure probes Ned, A., VaDeWeert, J.,

Goodman, S & Carter, S. (2011). Furthermore, similar high-frequency response transducers have been used in three-hole pressure probes used to carry out measurements of unsteady flows in turbomachines.

2.7 Velocity Gradient Effects on Multi-Hole Probe Calibration

The governing equations multi-hole pressure probes especially seven-hole probes are predicated on the assumption that flow over the probe head is uniform. Boundary and shear layer flow have significant gradients, and thus, data collection at these regions will not be an accurate representation of the flow at that point. Silva, M.C.G., Pereira, C.A.C., & Cruz, J.M.S. (2003) studied the effect of velocity and pressure gradient on three-hole pressure probe, using a non-dimensional measure of a velocity gradient that was based on a streamline projection to create a correction factor for velocity measurements. The reduction in error was found to be in the order of 3° inflow angle in high shearing flows. The implementation of this correction factor is difficult with a five-hole or seven-hole pressure probes because the streamline must be defined in two dimensions and the resulting correction factor then becomes a function of two flow angles.

2.8 Research Work based on Multi-Hole Pressure Probes

In complex flow fields, the range of angle can be spatially or temporally higher than what a five-hole or a seven-hole pressure probe can resolve, for example, flow in the wake of a bluff body. For such flows, the omnidirectional probe is preferred. The Omni-pressure probe is an extension of the five-hole and seven-hole probes. It can resolve flow angles up to 160° from its outer axis. Like the five-hole pressure probe, the Omni-probe predicts flow angles, local total and static pressures, and velocities with reasonable accuracy. However, the head can distort the flow, thereby reducing accuracy in measurement. Figure 2.7 depicts the Omni-directional probe.

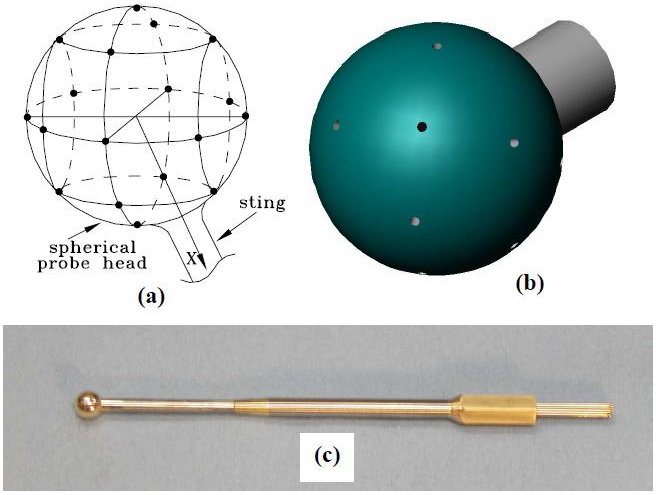

Figure 2.7. Schematics of omnidirectional 18hole pressure probe (a) port arrangement and grouping (b) isometric view depicting spherical tip and cylindrical sting (c) fully assembled 18hole pressure probe Shepherd, I. C. (1981)

Crilly, J., & Fryer, P. (1993) introduced the use of a hemispherical five-hole pressure probe together with elaboration algorithms for the reconstruction of the air data parameters. The determination of the air data parameters, such as velocity, static pressure, the angle of attack and angle of sideslip, is based on the local pressures and the local angle measurements. The results from the use of a hemispherical probe on the Flush Air Data System (FADS), constructed from a set of pressure slots, are directly obtained on the aircraft fuselage. The calibration of the pressure probe has been conducted from -5^0 to 15^0 angle of attack, $\pm 15^0$ angle of sideslip and at free stream velocities of 20m/sec and 70m/sec respectively. Figures 2.9 and 2.10 show pressure data compared to a reference value relative to the hemispherical five-hole pressure probe at an air velocity of 45m/sec. Figure 2.8 depicts the pressures as a function of the pitch angle (α) at a yaw angle of $\beta=0^0$.

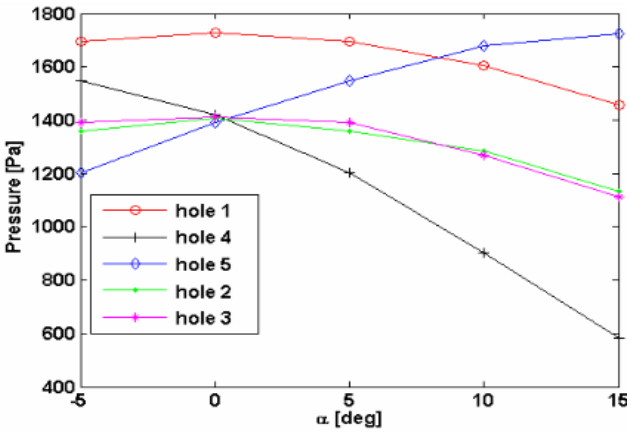

Figure 2.8. The pressure at the hemispherical probe's five holes (U = 45m/sec, $\beta=0^0$) Crilly, J., & Fryer, P. (1993)

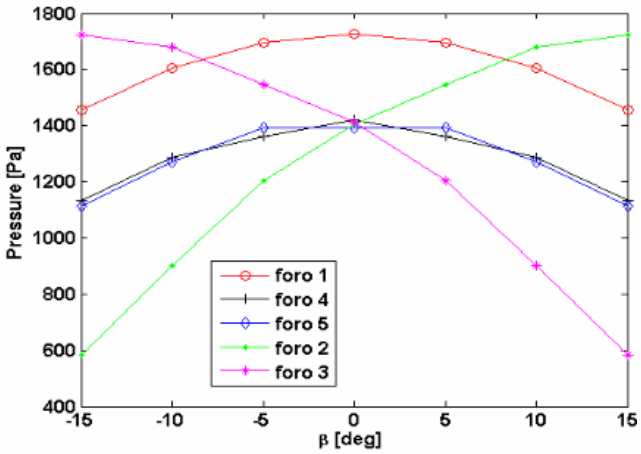

Figure 2.9. The pressure at the hemispherical probe's five holes (U = 45m/sec, $\alpha=0^0$) Crilly, J., & Fryer, P. (1993)

Figure 2.9 depicts the pressures as a function of the yaw angle (β) at pitch angle $\alpha = 0^0$. The pressures recorded by holes 2 and 3 are almost the same when the pitch angle is constant. These values became sensitive to the sideslip variations. The pressures recorded at holes 4 and 5 have an approximately linear dependence on α and are not influenced by β variations. The study is limited to airflow, where the accuracy of the new calibration data has not been tested.

Pfau, A., Schlienger, J., & Kalfas, A., and Abhari, S., (2003) established a method of measuring unsteady 3-D flow with four virtual sensors inserted into a single pressure transducer mounted on a small probe of 0.3mm inner diameter and a shaft of 1.8mm diameter. The probe consists of a semi-hemispherical probe head attached to a cylindrical rod. A pressure tap on the surface of the hemisphere connects the transducer to the instantaneous pressure sensor for measurements. The unsteady flow data is recorded at five consecutive pressure measurements, at five predefined angular positions relative to the probe axis, for a given geometric grid point in the flow field. Due to the three-dimensionality of the flow at the probe head, the measured pressure characteristics are dependent on the yaw and pitch angles.

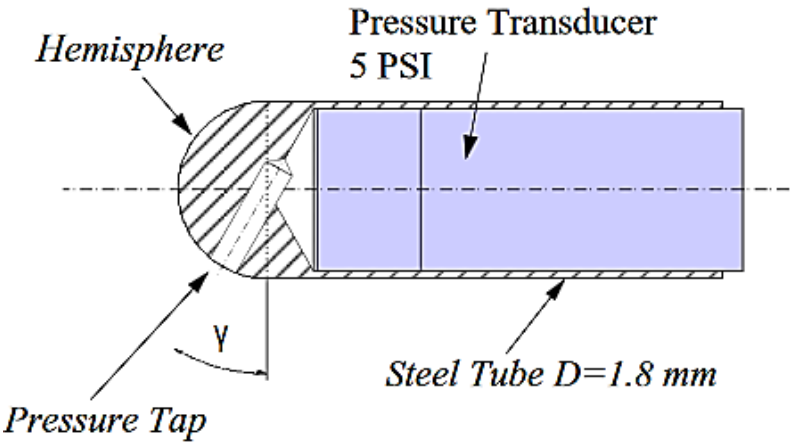

Figure 2.10. Miniature Fast Response Hemispherical Probe Pfau, A., Schlienger, J., & Kalfas, A., and Abhari, S., (2003)

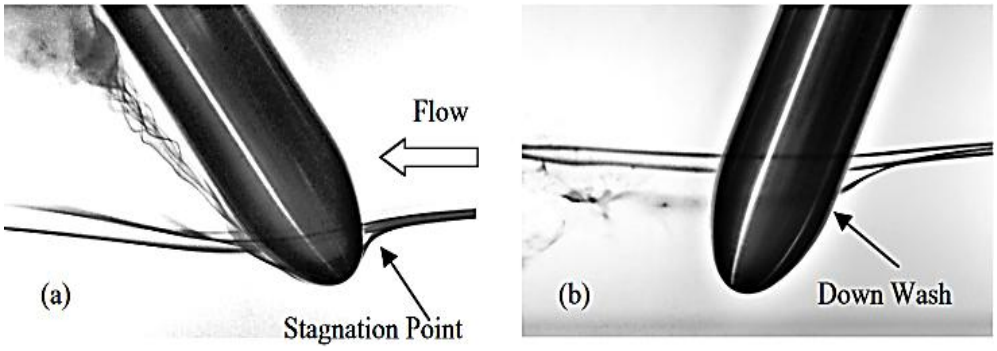

Figure 2.11. Streamlines around the probe head (a) negative pitch angle (b) positive pitch angle Pfau, A., Schlienger, J., & Kalfas, A., and Abhari, S., (2003)

Figure 2.11 shows the deflected streamlines as they interact with the probe. A variation of pitch angle changes the potential flow field, deflects the streamlines and affects the surface pressure on the probe body. For negative pitch angles (figure 2.11(a)), a distinct stagnation point is noticed at the head of the probe. The surface pressure at the front of the probe head reaches maximum total pressure. Pitching the probe to positive angles will remove the stagnation point at the probe head, resulting in a stagnation line along the stem axis. The pressure at the surface of the probe decreases due to the downwash of the flow, as seen in Figure 2.11 (b), leading to a pitch sensitive behaviour of the pressure field at the probe head.

Babinsky, U., Kuschel, H., Moore, D., & Welland, M. (1993) investigated the aerodynamic design and use of multi-sensor five-hole pressure probes for Micro-Electro-Mechanical System (MEMS) applications. The desired directional sensitivity required in the design of a multi-hole pressure probe is achieved by placing fences on the planar frontal surface of different cylindrical head probes. This has been carried out to determine the best design suitable for this particular application. The

investigation of flow over probes, with and without fences, has been carried out in a low-speed wind tunnel, with Reynolds Numbers between 1500 and 40000 based on the probe diameters. The potential of each design for being used as a five-hole probe was determined through pressure measurements and flow visualisations. The study suggested that the probe designed with fences has the potential to increase the directional sensitivity of the cylindrical probes significantly. Moreover, the study suggested that the probe with fences recorded least equivalent angular sensitivity compared to the probe without fences. However, the probe with fences displays no significant Reynolds Number effects in the range tested. Figure 2.12 depicts probe designs with fences tested.

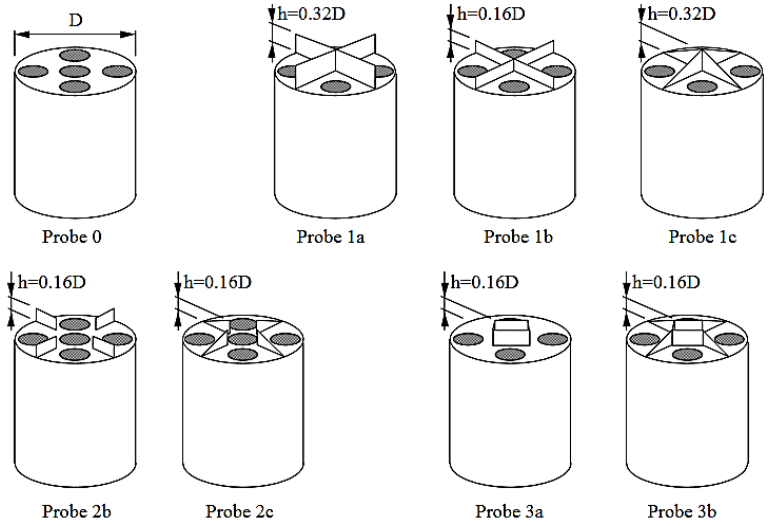

Figure 2.12. Probe designs tested Babinsky, U., Kuschel, H., Moore, D., & Welland, M. (1993)

These sensors have been directly exposed to the flow, and the desired sensitivity of the probe can be achieved by fitting flow-controlling fences protruding beyond the sensor plane. The purpose of the study was to examine the extent to which planar shapes, such as those shown in figure 2.12, are suitable for small five-hole probe designs, and how their sensitivity and range of application is compared to a standard multi-hole pressure probe design. First, the flow over a simple planar, cylindrical probe (probe 0 in figure 2.13) was investigated, and then, various fences were added to manipulate the flow to change surface pressure distribution. The effects of simple barriers were investigated. Figure 2.13 depicts the visualisation of the probe in oil-flow.

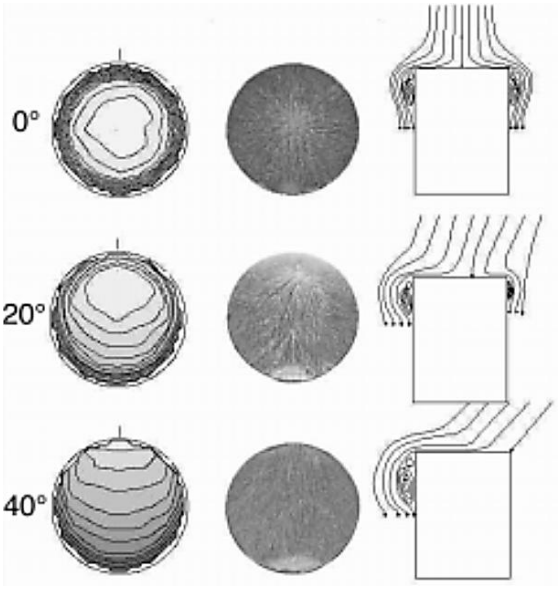

Figure 2.13. Surface pressure distribution and oil-flow visualisation for a cylindrical probe at pitch angles of 0^0, 20^0 and 40^0 Babinsky, U., Kuschel, H., Moore, D., & Welland, M. (1993)

Figure 2.13 shows the distribution of surface pressure of oil streams on the planar probe at three different pitch angles. It can be seen that the flow field is relatively uniform; with an increase in the pitch angle, the stagnation point moves towards the edge of the probe surface. It is interesting to observe that the pressure distribution along the frontal surface varies with pitch angle. The introduction of fences in the design of multi-hole pressure probes dramatically changes the flow over the probe head. Separation bubbles were found at the leeward side of each barrier at non-zero pitch angles. A family of geometries for five-hole pressure probes, based on a planar array of pressure sensors, was established. These shapes have the advantage over traditional designs, however; they can only be manufactured using MEMS technology. This technology is expensive and therefore, it is only available to a few organisations such as the defence and aviation industries etc.

Woong, K., Nguyen, D., Saeng, H., Jae, S. Hee, S., & Yong, M. (2015) conducted experimental and numerical studies aimed at measuring the flow rate of greenhouse gas emission using the S-type Pitot tube. The research focuses on investigating the factors that affect the accuracy of flow rate measurement. The effects of Reynolds number, non-uniform equipment and production quality on S-type Pitot tube coefficients were investigated concerning the flow measurement medium in industrial chimneys.

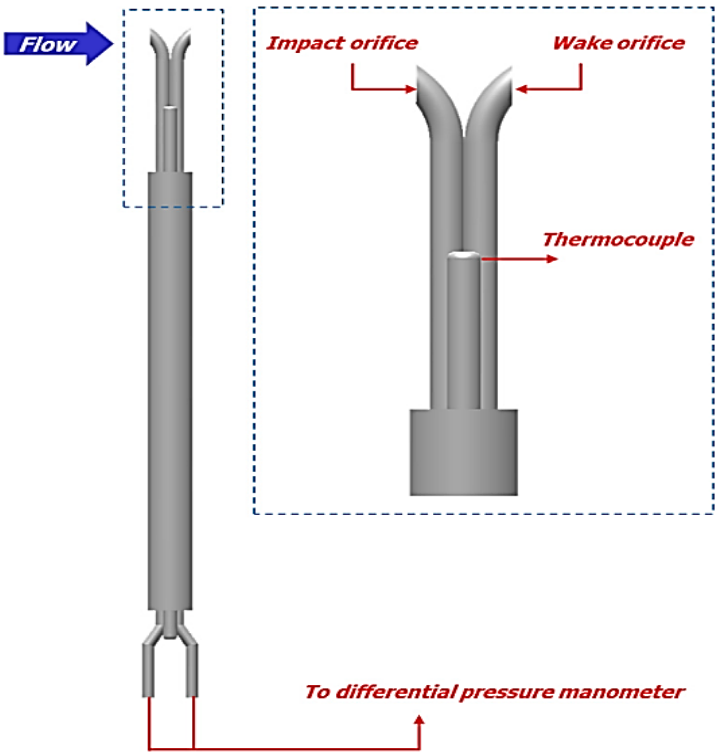

Figure 2.14. The configuration of the S-type Pitot tube Woong, K., Nguyen, D., Saeng, H., Jae, S., Hee, S., & Yong, M. (2015)

Figure 2.14 depicts the physical model and the geometry of the S-type Pitot tube. The probe on one end contains an impact orifice, wake orifice, and a thermocouple. The other end of the Pitot tube is used to measures the differential pressure. Various factors, such as Reynolds Number and misalignment of the angle, can be additional error sources for the S-type Pitot tube coefficients. Manufacturing quality of the S-type Pitot tube is also a factor affecting the measurement uncertainty of stack gas velocity. Figure 2.15 depicts the installation of the Pitot tube into the stack and the demonstration of velocity inside the chimney.

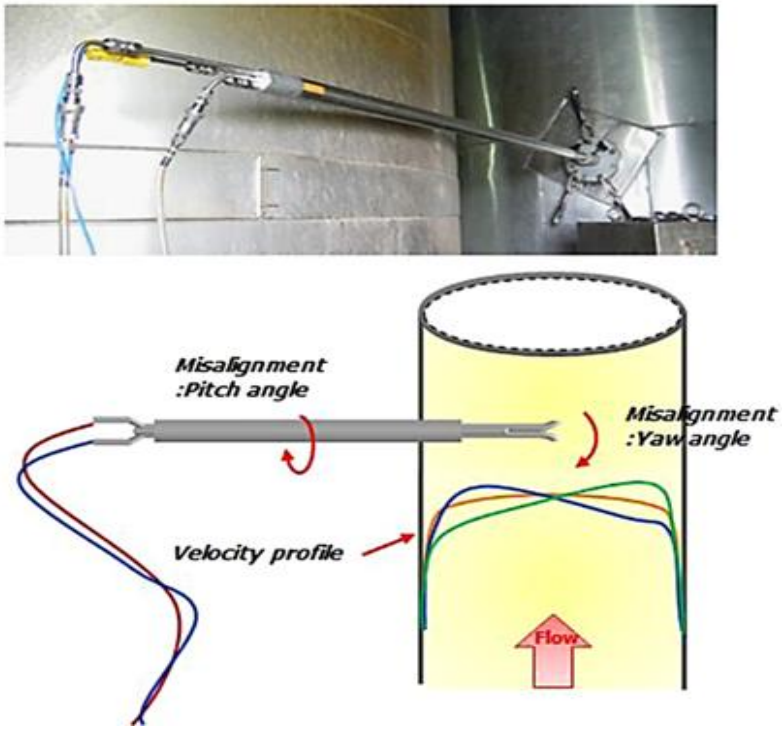

Figure 2.15. Installation effect of the S-type Pitot tube in the stack Woong, K., Nguyen, D., Saeng, H., Jae, S., Hee, S., & Yong, M. (2015)

The coefficients of the S-type Pitot tube are determined by comparing the coefficients of the L-type Pitot tube. The S-type Pitot tube and the L-type Pitot tube were installed in the opposite direction of the test section as depicted in figure 2.16.

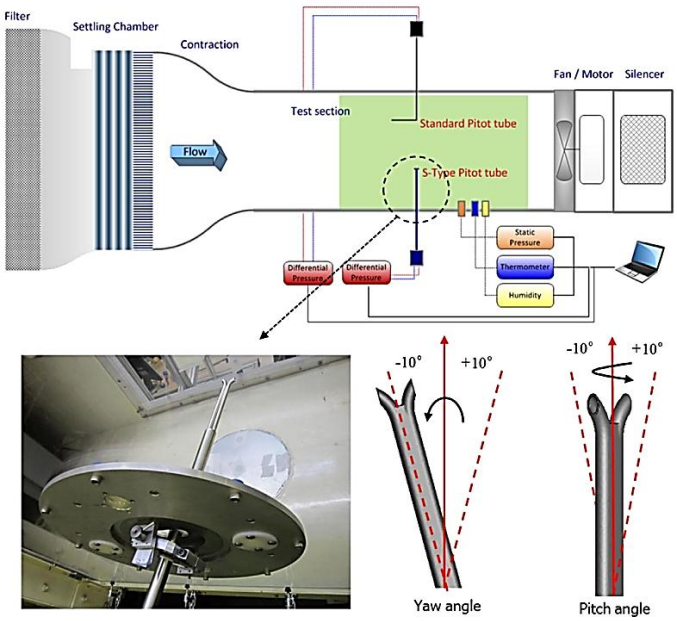

Figure 2.16. Experimental setup of the S-type and L-Type Pitot tubes in the wind tunnel Woong, K., Nguyen, D., Saeng, H., Jae, S., Hee, S., & Yong, M. (2015)

The coefficients of the S-type Pitot tube are determined to assume that the approaching velocity and density to each Pitot tube are the same. The coefficients are calculated by measuring and comparing the differential pressure of the two Pitot tubes at each inlet, using equation (2.22).

$$C_{p,S-type} = C_{p,Std.} = \sqrt{\frac{\Delta p_{Std}}{\Delta p_{S-type}}} \tag{2.22}$$

Where $C_{p,\,Std,}$ and $C_{p,\,S\text{-}type}$ are the L-type and S-type Pitot tubes' coefficients respectively. Δp_{Std} and $\Delta p_{S\text{-}type}$ are the differential pressures across the L-type and S-type Pitot tubes.

Experiments in the wind tunnel were conducted in the range of 3000<Re>22,000 to investigate the effects of Reynolds numbers on the S-type Pitot tubes' coefficients. The coefficients of the S-type Pitot tube, at each Reynolds Number, were determined, as depicted in figure 2.17.

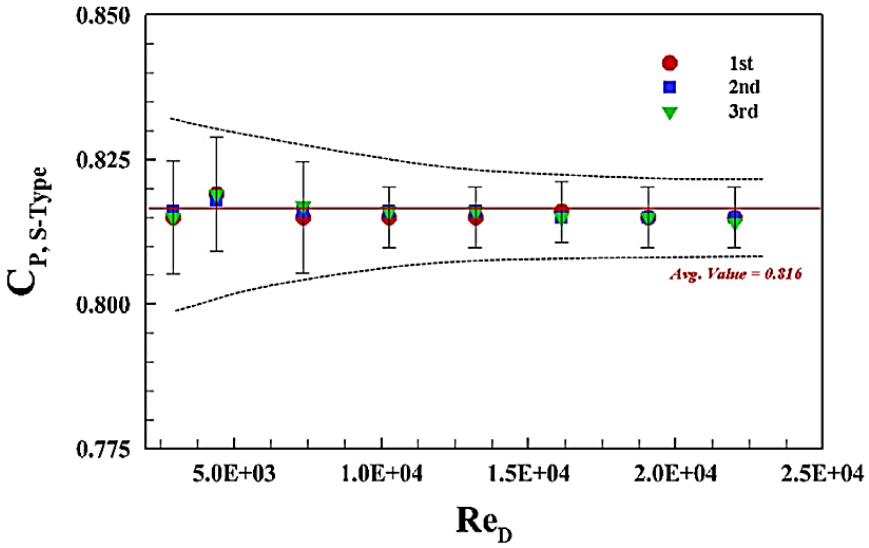

Figure 2.17. Reynolds number effect on the S-type Pitot tube Woong, K., Nguyen, D., Saeng, H., Jae, S., Hee, S., & Yong, M. (2015)

Figure 2.17 depicts the distribution of the average values and the standard deviations for the S-type Pitot tube coefficients across the Reynolds Number range. This study suggested that the expanded uncertainty of the S-type Pitot tubes was 1.2%, which was established to be slightly larger than that of the L-type Pitot-tube coefficients. Furthermore, the study proved that the deviation of each value from the average value of the S-type Pitot tube coefficients was less than 0.3% within the entire range of Reynolds numbers. In addition, it was noted that the effect of the Reynolds number on the S-type Pitot tube coefficients is negligible compared to the total uncertainty of the flow rate measurements.

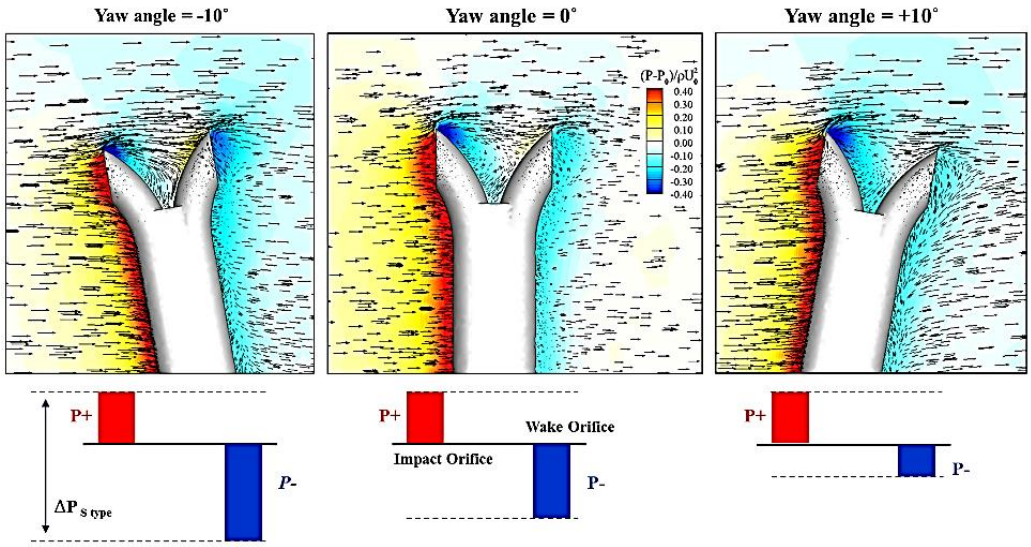

Figure 2.18. Pressure distributions and velocity vectors around the S-type Pitot tube at Re 10,000 Woong, K., Nguyen, D., Saeng, H., Jae, S. Hee, S., & Yong, M. (2015)

Figure 2.18 shows the effect of pitch and yaw angles misalignments of the S-type Pitot tube for misalignment in the range of $\pm 10^0$ with 2^0 increment. Figure 2.19 and figure 2.20 respectively show this effect.

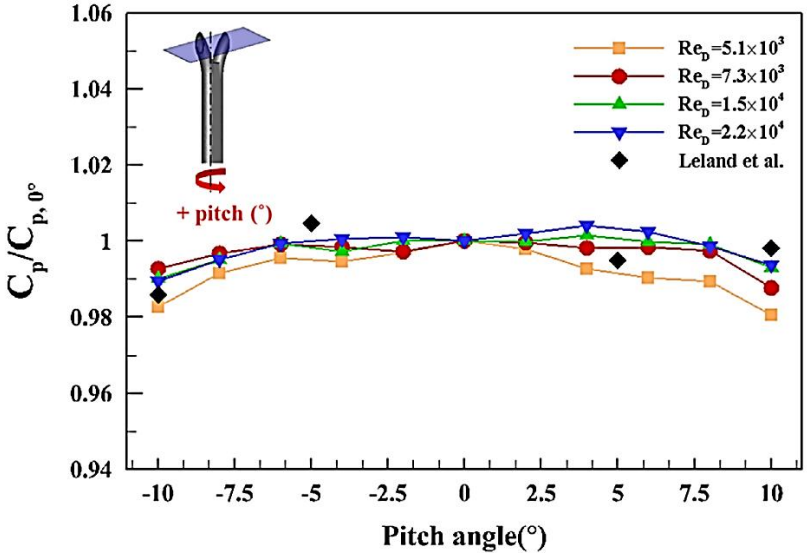

Figure 2.19. Effect of pitch angle misalignment on the S-type Pitot tube coefficient Woong, K., Nguyen, D., Saeng, H., Jae, S., Hee, S., & Yong, M. (2015)

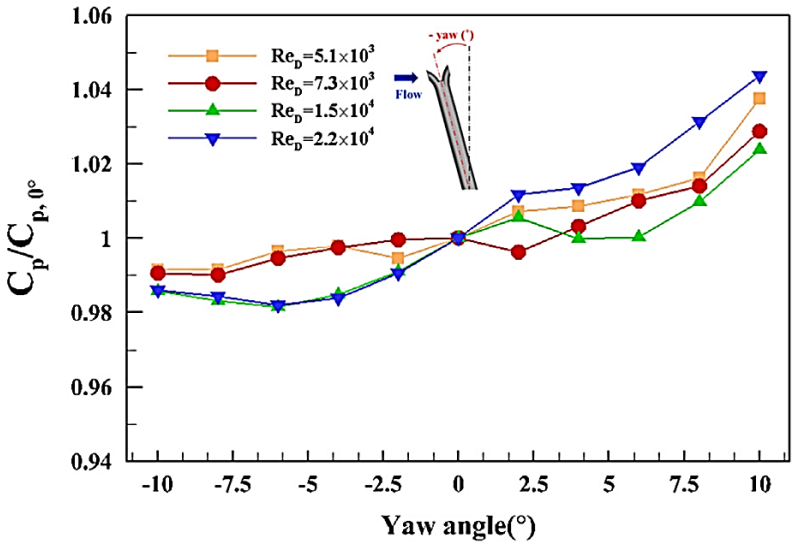

Figure 2.20. Effect of yaw angle misalignment on the S-type Pitot tube coefficient Woong, K. Nguyen, D., Saeng, H., Jae, S., Hee, S., & Yong, M. (2015)

Conclusively, it can be seen that the tube coefficient for the S-type Pitot is changing approximately by -2% for negative yaw and 4% for positive angle misalignment. It was further reported that at -10° yaw angle, the probe recorded low-pressure distributions near the wake of the orifice because a vertical structure grows behind the wake of the hole and causes the Pitot tube coefficients to decrease for negative yaw angles. Furthermore, when positive yaw angle misalignment occurs, flow separation develops at the upper edge of the impact orifice because of the tilted geometry in the wake. Therefore, causes the coefficients of the Pitot tube to increase the recovery of the pressure distribution near the wake orifice.

Although the studies include factors that affect the measurement, it was only limited to calculate flow information at flow fields corresponding to $\pm 10^0$ misalignment. There was nothing about extending the calibration or integrating experimental calibration with Computational Fluid Dynamic (CFD). Furthermore, the angle intervals for this study are too large to understand the misalignment effects of S-type Pitot tube in the real situation. Therefore, more refinements are needed to evaluate the uncertainty and accuracy of the flow rate measured by the Pitot tube.

Wecel, D., Chmielniak, T., & Kotowicz, J. (2008) introduced the use of experimental and numerical investigations for the characteristics of the averaging Pitot tube. The study further discusses the analysis and installation effects of the Pitot tube on the flow coefficient that was used to measure flow velocity in a 100m long pipeline with 200mm in diameter. One of the objectives of the study was to determine the flow coefficient k of the averaging Pitot tube and its relative change Δk, which

results from the installation effect. Furthermore, the focus was also to obtain correct calculations to obtain the location of flow separation and the differential pressure between ports of the Annubar. The numerical investigations were carried out on Annubar with a cross-section shaped as depicted in figure 2.21.

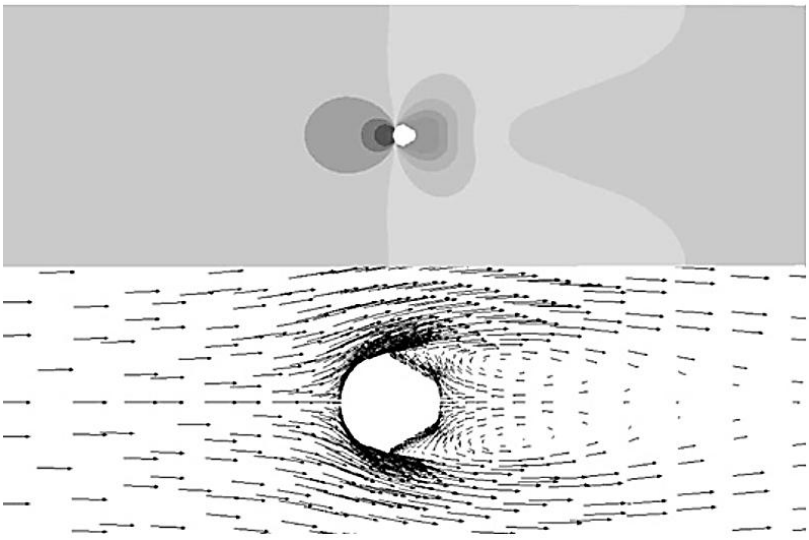

Figure 2.21. Distribution of static pressure and velocity vectors around a special cross-section Wecel, D., Chmielniak, T., & Kotowicz, J. (2008)

As depicted in figure 2.21, the emphasis was on the turbulence model and turbulence intensity at the inlet to obtain pressure distributions around the cylinder surface and the cross-section of various shapes is modelled to achieve a further significant value of differential pressure and lower amount of permanent pressure loss. The numerical studies show that the locations of flow separation are essential for stabilising pressure signal for various Reynolds Numbers. Figure 2.22 depicts the flow coefficient k as a function of Reynolds Number obtained experimentally.

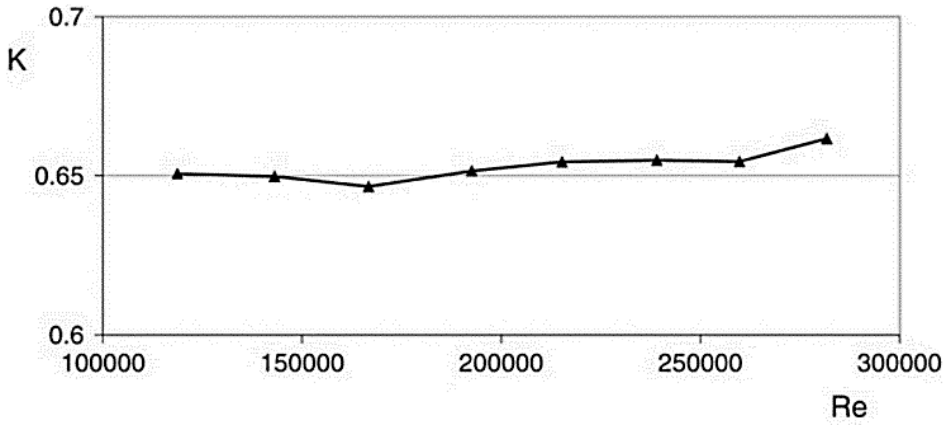

Figure 2.22. Flow coefficient k as a function of the Reynolds number Wecel, D., Chmielniak, T., & Kotowicz, J. (2008)

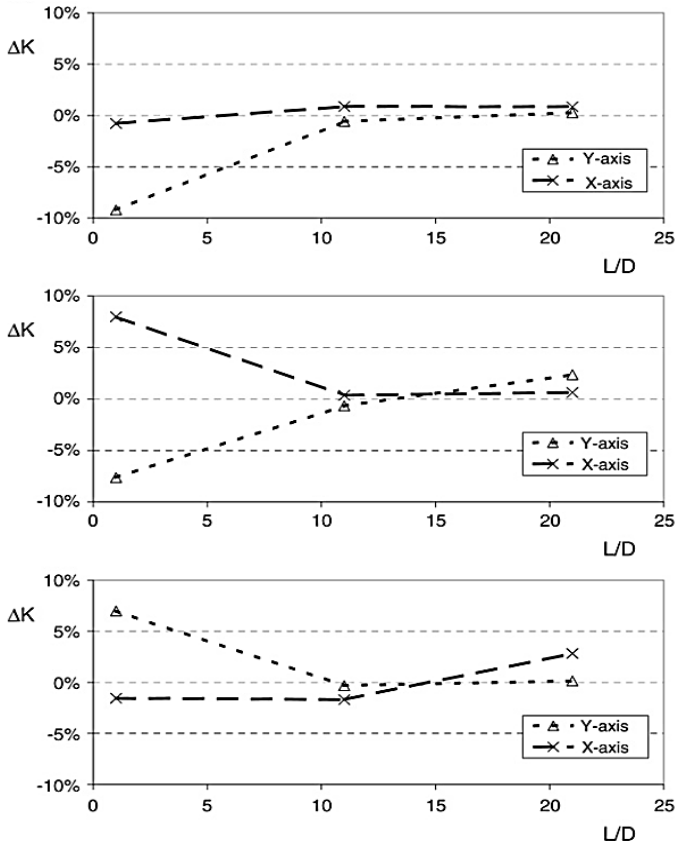

Figure 2.23. Relative change of the flow coefficient Δk as a function of the downstream distance behind (a) single elbow (b) two elbows in the same plane (c) two elbows out of plane Wecel, D., Chmielniak, T., & Kotowicz, J. (2008)

The averaging Pitot tube has upstream sensing ports, and flow coefficient k is expressed in equation (2.23) as:

$$k = \frac{q_{m_n}}{\pi . R^2 \sqrt{2\Delta p_n . \rho_n}} \tag{2.23}$$

At k value of 0.65, there were minimal deviations over the range of Reynolds Numbers from 1.2 x 10^5 to 2.8 x 10^5, with variations not lager than 1.5%. Even though the experiment focuses more on correcting the flow coefficient of the Pitot tube (k), it was only for airflow in a 10mm pipe with a specific diameter. However, limited information is available regarding the performance of averaging Pitot tube on wind tunnel flows. Figure 2.24 shows changes in the calibration value of the Pitot tube when used within elbows. It can be seen that K value changes as a function of L/D.

Gong, W., Zhang, H., & Liu C. (2013) developed an automatic calibration method for conical five-hole probe controlled by LabView platform. The study recorded a 0.5° maximum uncertainty for the flow angles and 1.7% maximum uncertainty for the velocity magnitude. The calibration was for

a $\pm 18^0$ angular position with an angle increment of 3^0 step at a free stream velocity of 60m/sec. The following equations define the non-dimensional pressure coefficients as shown in equations (2.24) through to equation (2.27).

$$C_{p,\alpha} = \frac{p_1 - p_3}{p_2 - \bar{p}} \tag{2.24}$$

$$C_{p,\beta} = \frac{p_4 - p_5}{p_2 - \bar{p}} \tag{2.25}$$

$$C_{p,total} = \frac{p_2 - p_{total}}{p_2 - \bar{p}} \tag{2.26}$$

$$C_{p,static} = \frac{\bar{p} - p_{static}}{p_2 - \bar{p}} \tag{2.27}$$

Where p_1, p_2, p_3, p_4, and p_5 are the pressures measured by each hole of the five-hole pressure probe. P_{TOTAL} is the total pressure of the oncoming flow and P_{static} is the static pressure of the flow at the probe location. Average pressure $\bar{p}$ is calculated using equation (2.28).

$$\bar{p} = \frac{p_1 + p_3 + p_4 + p_5}{4} \tag{2.28}$$

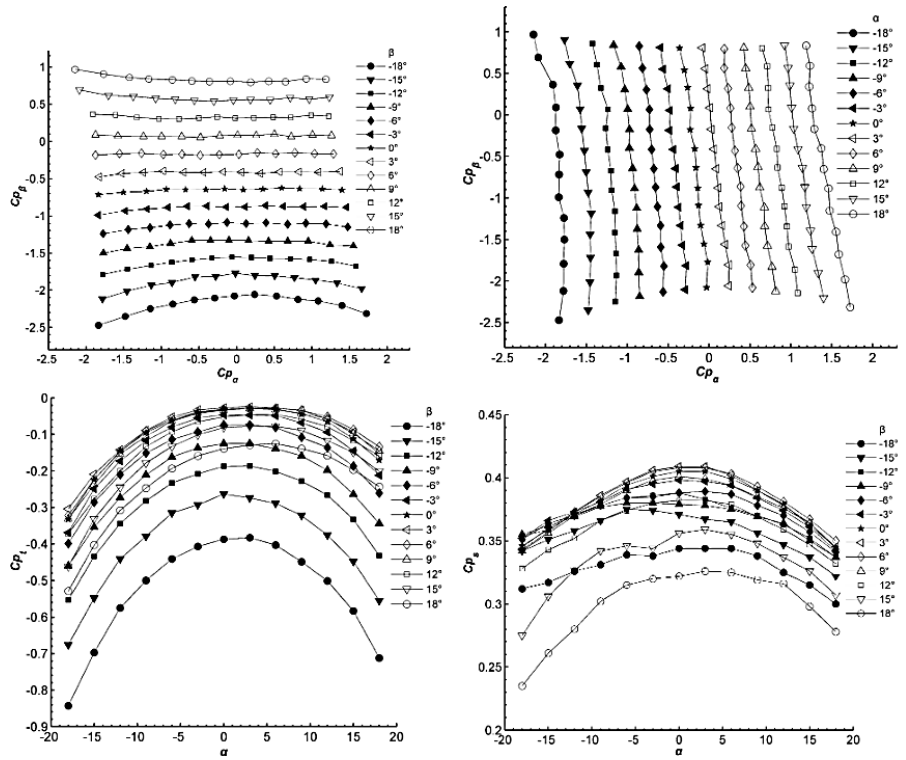

Figure 2.24. Calibration curves for 60m/sec Gong, W., Zhang H., & Liu C. (2013)

Figure 2.24 shows the calibration surface recorded. Although the probe showed a good response as demonstrated by the calibration curves, however, the calibration study was just for wind tunnel flow. In order words, the probe is limited to airflow with an angle, not more than $\pm 18^0$ as demonstrated in figure 2.24.

Hooper, J., & Musgrove, A. (1997) introduced an improved four-hole cobra probe with an extended frequency response of 1.5kHz. The probe measures the three components of the average velocity and turbulent intensity of fluid flow. The probe also resolves the average static pressure and local turbulent parts, allowing time between the parts of the fluctuating velocity and pressure to be determined. The pressure probe had improved frequency response at the time of measurement in a developed turbulent airflow in a round pipe. Figure 2.25 depicts the axial mean velocity distribution of the flow and figure 2.26 describes the axial turbulent intensity normalised by the frictional velocity obtained by the probe.

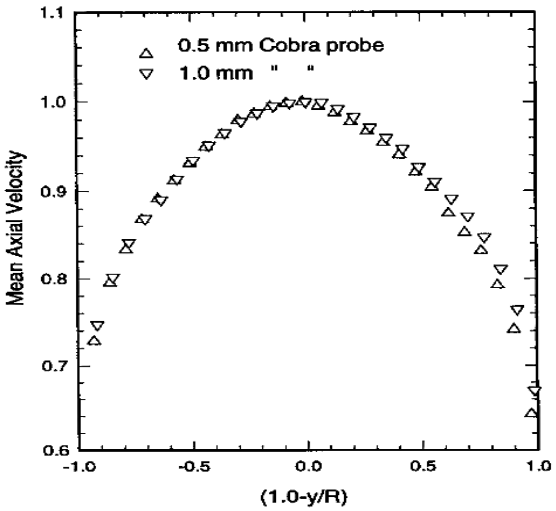

Figure 2.25. Axial mean velocity distribution Hooper, J., & Musgrove, A. (1997)

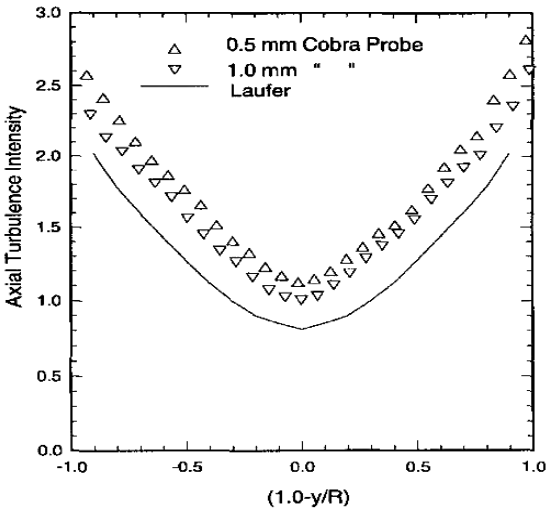

Figure 2.26. Axial turbulence intensity normalised by friction velocity Hooper, J., & Musgrove, A. (1997)

Although the four-hole pressure probes have successfully measured the velocities of airflow inside a round pipe, it is just on airflows study and not for water flow. Furthermore, the study was only based on the conventional probe calibration method, and no formation is available regarding the shape of probes or trying to increase the accuracy of the results.

Árpád, V., & Márton, B. (2013) established a calibration method of a conical head five-hole pressure probe of an outer diameter of 4mm, 0.4mm inner tube diameter, and 45^{o} angle to measure atmospheric boundary layer. The probe was used to study the characteristics of a wind tunnel boundary layer and far-field wakes of a building. Figure 2.27 shows the pitch, yaw orientations, and pressure sensor arrangements. The study was mainly for wind tunnel airflows, and nothing suggests that water or pipeline study has been carried out.

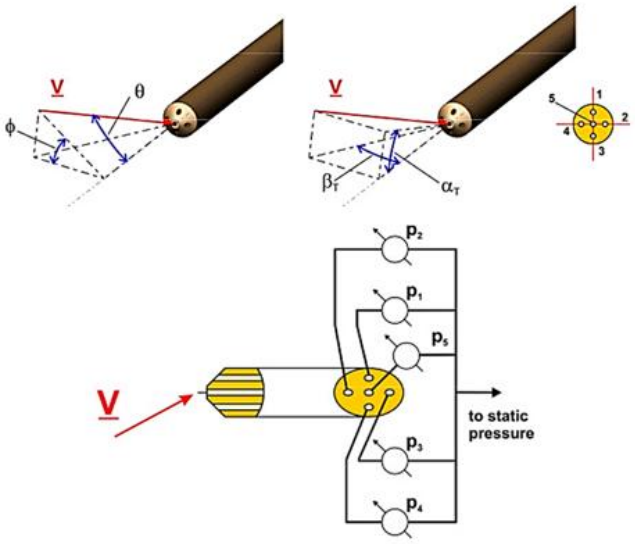

Figure 2.27. Five-hole probe angle and sensor definitions Árpád, V., & Márton B. (2013)

Susheela, V., & Michael, S. (2004) proposed the use of a four-hole cobra probe to determine the uncertainty in the measurements of the wake characteristics of a rotating object. The probe calibration was carried out in a wind tunnel facility to determine the calibration factors. The agreement between the manufacturer and the experimental calibration factors led to a practical assessment in a three-dimensional turbulent flow field. The study provided an overview of the assessment in the wake of the rotating and static objects and further explored the limitations and advantages of the cobra probe in subsonic flows. Figure 2.28 depicts the pressure distribution at the four holes of the pressure probe. It was established that the lesser number of holes in the pressure probe, the less the accurate the probe would be able to detect the direction of the flow at high angles of incidence. Hence, the study is limited to detecting flow angle of about $\pm 40^{o}$ or less. When the probe is used at high angles beyond $\pm 40^{o}$, it becomes prone to errors because of this limitation.

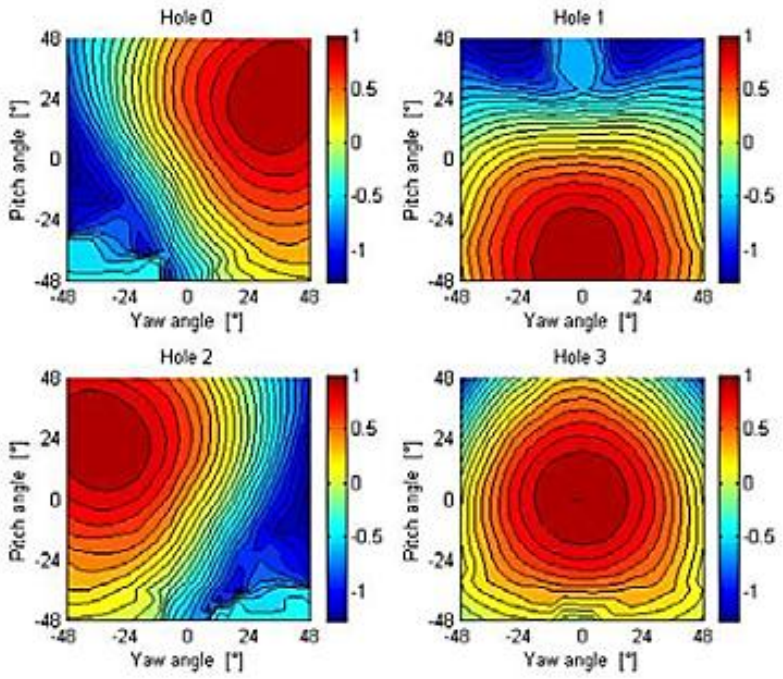

Figure 2.28. Four-hole probe pressure distribution Susheela, V., & Michael S. (2004)

Malviya, V., Mishra, R., & Palmer, E. (2010) established the use of Computational Fluid Dynamics (CFD) to investigate the three-dimensional interference caused by a conical head five-hole pressure probe in an automotive wheel arch. The study includes CFD simulation of flow around the probe when inserted at different locations inside the wheel arch. The study focuses on the pressure field, velocity along the y-axis and the extent of interference caused by the five-hole probe pressure along three orthogonal axes. Figure 2.29 shows the pressure variation on the wheel surface. This study was limited to the study of the probe inference on airflow and not on the water flow field. Furthermore, it was only limited to study the interference caused by the conical head probe and not the interference caused by the hemispherical probe on the wheel arch.

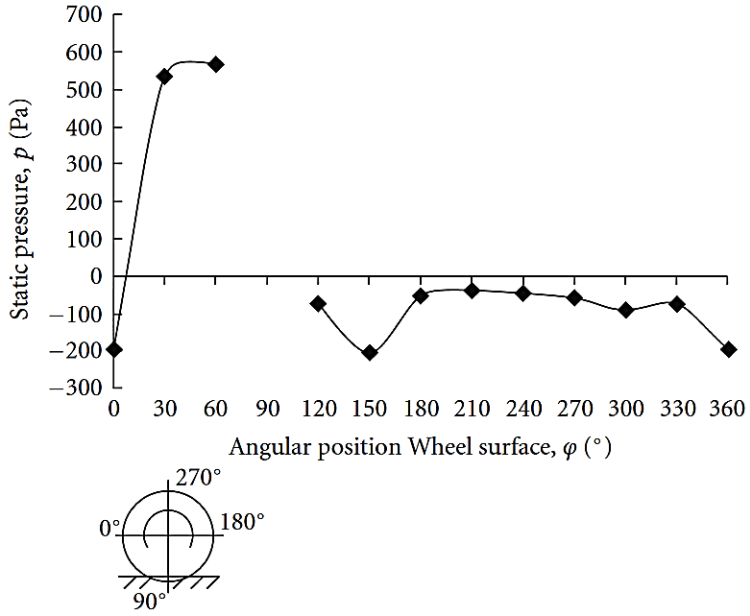

Figure 2.29. Pressure variation of on the wheel surface Malviya, V., Mishra, R., & Palmer, E. (2010)

Bryant, R., & Johnson, A. (2011) established a CFD numerical and experimental study to measure velocities, the static and total pressure of gas flow in a horizontal exhaust duct of a stationary source using conical head five-hole pressure probe. The study focused on experimental and numerical comparisons of two independent measurements of pressure and velocity profiles across two chords of the exhaust pipe. Figure 2.30 depicts the experimental and numerical maximum velocity profiles obtained using the probe in the traverse spacing of 1000mm along diametric chords of the duct spaced at 15^0. The study does not, however, present any insight on water flow. Furthermore, the probe did not compare two or more probes and limited flow field within $\pm 15^0$, anything other than this will introduce error in the results.

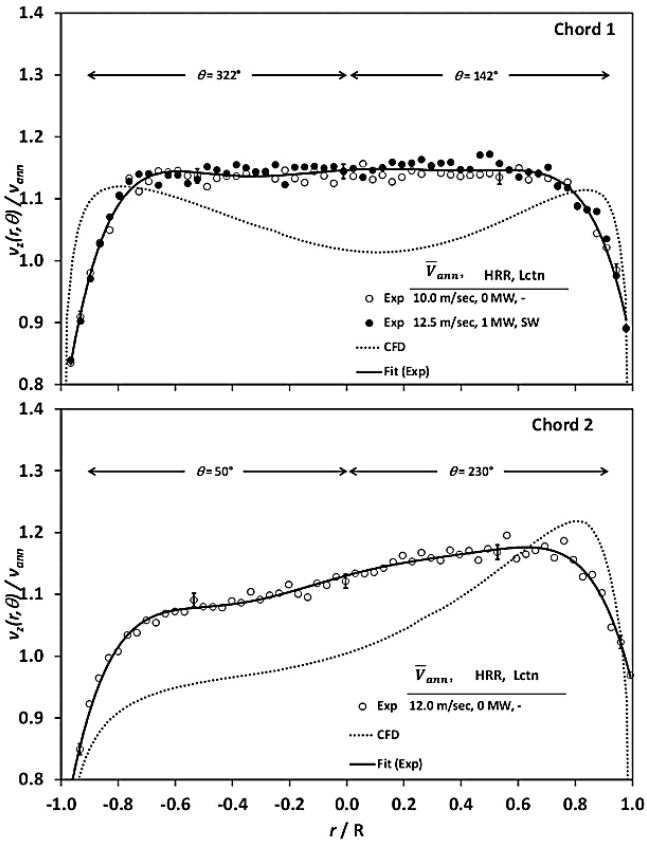

Figure 2.30. Velocity profiles along horizontal diametric chords Bryant, R., & Johnson, A. (2011)

Kim, S. H., & Kang, Y. J. (2009) introduced the study of helicopter air data using a hemispherical head five-hole pressure probe in a wind tunnel. The study focused on finding the angle of attack of the helicopter and flow directions, total and static pressures. The results of the calibration proved that the hemispherical head five-hole pressure probe gave an evenly distributed pressure as shown in figure 2.31. However, the study does not present any insight on the velocities at which the helicopter travels.

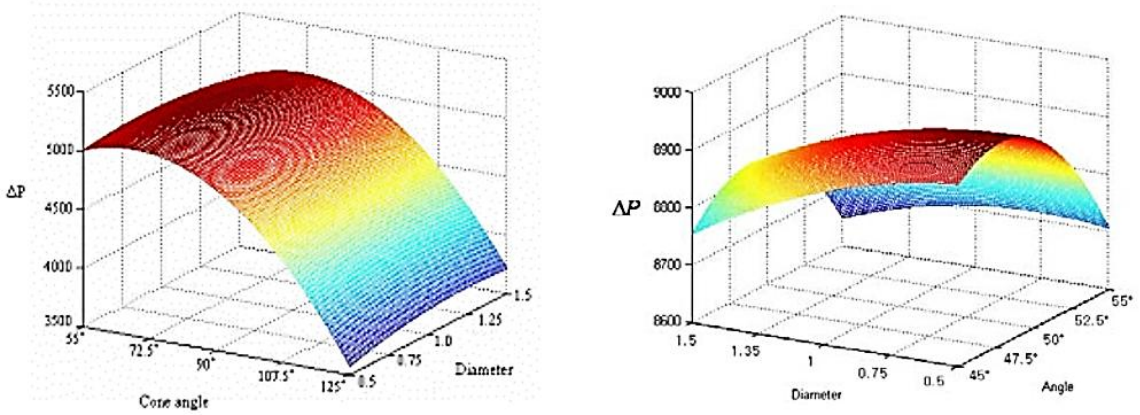

Figure 2.31. The response of surface reassures Kim, S H., & Kang, Y. J. (2009)

Malviya, V., Mishra, R., Palmer, E., & Majumdar, B. (2007) introduced using computational fluid dynamics (CFD) based analysis of the effect of conical and hemispherical heads pressure probes geometry on the flow field interference. The type of probes used in the study was the five-hole pressure probe. The influenced of probe geometry on flow disruption was analysed. The study further assessed the values and ranges of variations of the flow field parameters numerically. These are velocity and pressure fields in and outside the probe. The probes model for this study are conical and hemispherical shapes characteristics. The conclusions of the study took the need for complex flow metrology into consideration and found that the hemispherical head probe is advantageous over the conical head probe in complex flow mapping which may need multiple pneumatic probes. The numerical simulations of the conical and hemispherical probes in CFD wind tunnel flow domain are shown depicted in figure 2.32.

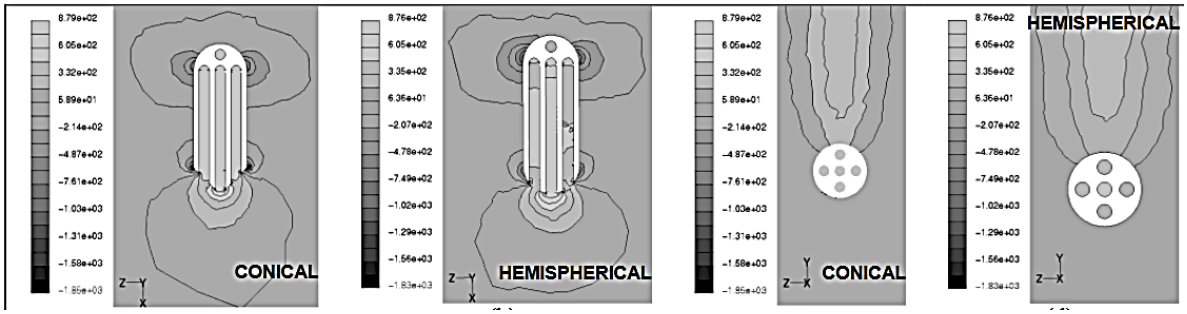

Figure 2.32. Pressure (Pa) distribution on conical and hemispherical probes Malviya, V., Mishra, R., Palmer, E., & Majumdar, B. (2007)

Figure 2.32 shows pressure distribution of static pressure on the horizontal symmetry plane for (a) conical probe and (b) hemispherical probe; and on a lateral plane through the head for (c) conical probe and (d) hemispherical probe. Figure 2.32 shows static pressure distribution profile on the horizontal symmetry for conical and hemispherical heads probes. Numerically, the study of these probes only considered for airflow in the wind tunnel and not in pipeline flows. Furthermore, there were no experimental studies to compare numerical studies. Also, it lacks the measurement validation of the airflow parameters such as velocities.

Duquesne, P., IIiescu, M., Fraser, R., Deschenes, C., & Ciocan, G. (2010) established the use of a pyramidal head five-hole pressure probe to monitor the velocity and pressure fields within an axial wind turbine. The uses five embedded piezo-resistive pressure sensors embedded inside the pressure holes. It has a dynamic response of over 50kHz. It was used in an unsteady flow to obtain the static pressure, total pressure, and the velocities within the flow of a propeller turbine. The inner

holes of the probe were 2mm in diameter; this allows for a compact design of a pyramidal shape at the head of the probe with an outer diameter of 8mm.

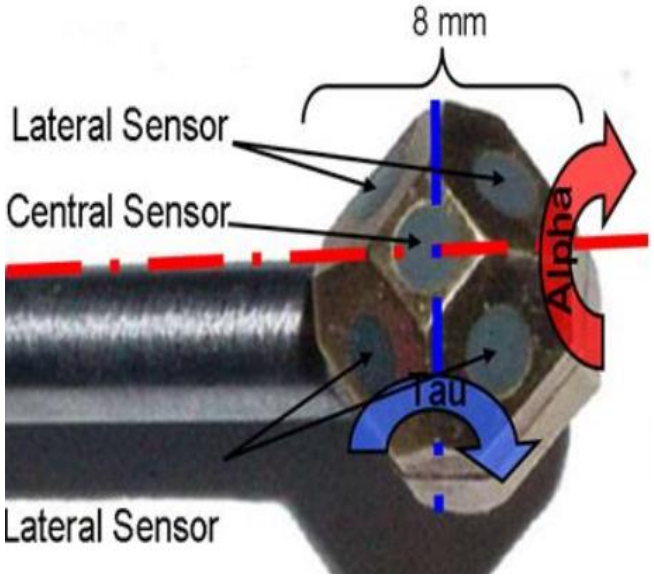

Figure 2.33. The geometry of the conical head five-hole pressure probe with embedded sensors Duquesne, P., IIiescu, M., Fraser, R., Deschenes, C., & Ciocan, G. (2010)

The first step of calibration was to define the four normalised non-dimensional pressure coefficients that characterise the unbalance of the pressure measured by the probe concerning the flow direction. The flow direction is mapped for a range of positions with pitch and yaw angles defined by α and τ of the probe in the flow field as expressed in equation (2.29) through to equation (2.33).

$$F(\alpha,\tau) = \frac{P_2 - P_3}{P_1 - P_M} \tag{2.29}$$

$$G(\alpha,\tau) = \frac{p_4 - p_5}{p_1 - P_M} \tag{2.30}$$

$$L(\alpha,\tau) = \frac{P_{TOTAL} - P_M}{-p_0} \tag{2.31}$$

$$H(\alpha,\tau) = \frac{P_1 - P_{TOTAL}}{P_T - P_0} \tag{2.32}$$

$$P_M = \frac{\sum_{i=2}^{5} P_i}{4} \tag{2.33}$$

From equation (2.29) to (2.30), the coefficients F and G are defined based on the pressure differences between opposite lateral sensors (p_i with i = 2, 3, 4 and 5) normalised by the difference between the pressure sensed by the central sensor p_1 and the mean pressure in the plane passing

through the four lateral sensors coefficients. L and H characterised the deviation of the pressure sensed by the central sensor, and the average pressure of the lateral sensors P_M and both L and H coefficients are normalised with the local dynamic pressure P_{TOTAL} obtained from a Pitot tube installed in the calibration wind tunnel. The calibration started after the flow had fully developed in the tunnel. The range of angle was $\pm 25^0$ for pitch and yaw angles with a resolution of $\pm 2.5^{\circ}$. Figure 2.34 depicts the coefficients' parametric surfaces obtained from the calibration.

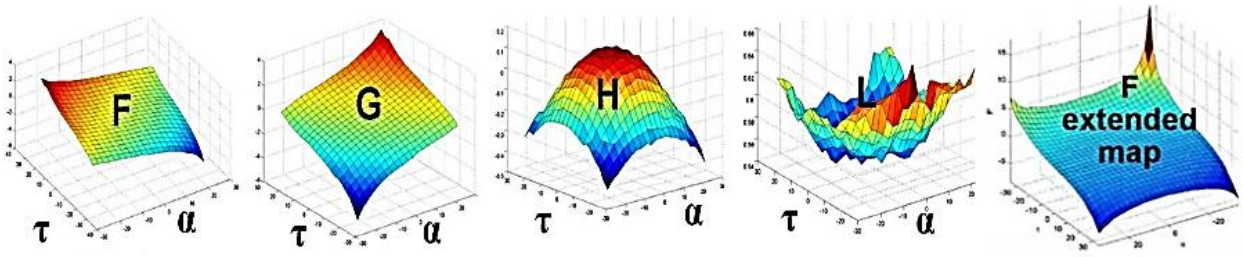

Figure 2.34. Normalised calibration coefficient charts and validation of the angular range
Duquesne, P., IIiescu, M., Fraser, R., Deschenes, C., & Ciocan, G. (2010)

Based on the calibration results, the accuracy of flow information measured by the probe regarding velocity is about ±2% for angles smaller than $\pm 25^0$ and ±3% for an angular range within $\pm 25^0$. Regarding pressure, the accuracy is ±3.4% and ±5.8% respectively. Probe tilted beyond 25^0 caused flow separation in this study. Even though the calibration was successful, the mathematical models used to define coefficients of the pressure values do not consider the pressure normalisation that takes in to account the fact that the centre hole measures the highest-pressure value. Furthermore, the probe cannot measure flow information at large angles beyond $\pm 25^0$, and it is only for airflow applications.

Brennan, M., Fry, M., Narasimha, M., & Holtham, P. (2007) introduced the use of conical head five-hole pressure probe to measure the radial velocity of water flow inside a hydro-cyclone system and used it for comparison with CFD predictions. In this study, the time average flow velocities estimated from the Large Eddy Simulation (LES) are found to be within 15% of the measured results. Figure 2.35 depicts the schematic description of a hydro-cyclone and the experimental setup.

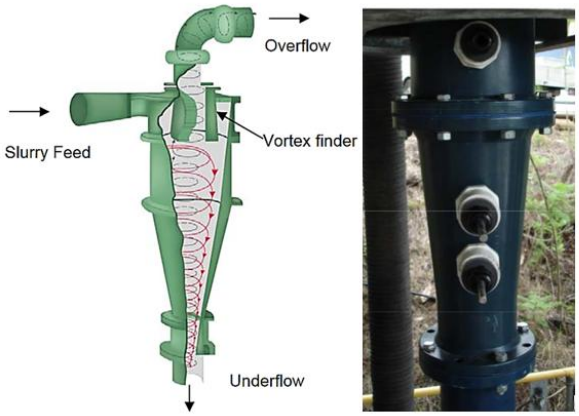

Figure 2.35. The arrangement of a hydro-cyclone and view of Krebs DF6 150mm hydro-cyclone used in the experiment with tapping ports Brennan, M., Fry, M., Narasimha, M., & Holtham, P. (2007)

Figure 2.35 depicts the physical formation of the hydro-cyclone and the conical head five-hole pressure measurement tapings as installed inside the hydro-cyclone. In this study, the probe measures the radial velocity at three different elevations of the hydro-cyclone at two constant flow rates in each measurement. Figure 2.36 and figure 2.37 depict the local radial velocity profiles measured by the probe at each point of local measurement using a particular set of calibration data.

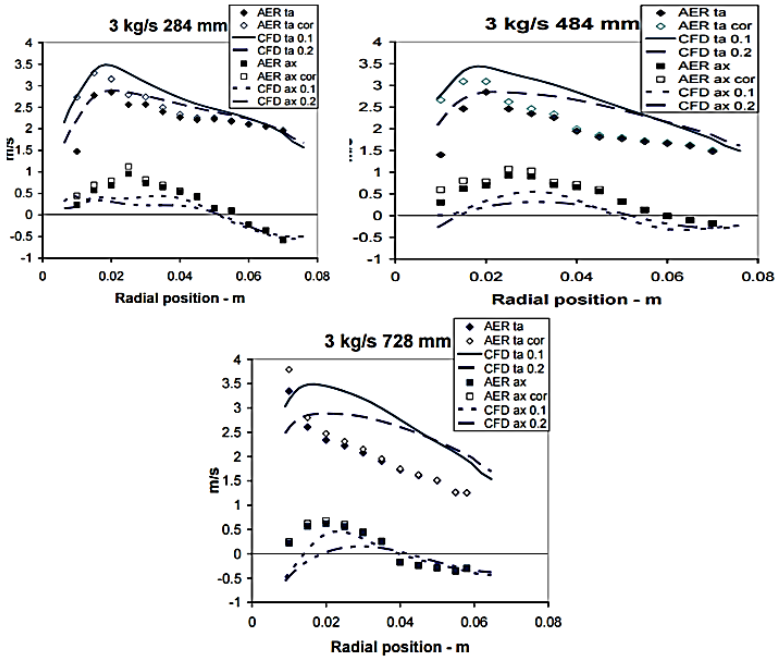

Figure 2.36. Velocities measure by aero-probe and that predicted by CFD at three different elevations with constant flow rate at 3kg/sec Brennan, M., Fry, M., Narasimha, M., & Holtham, P. (2007)

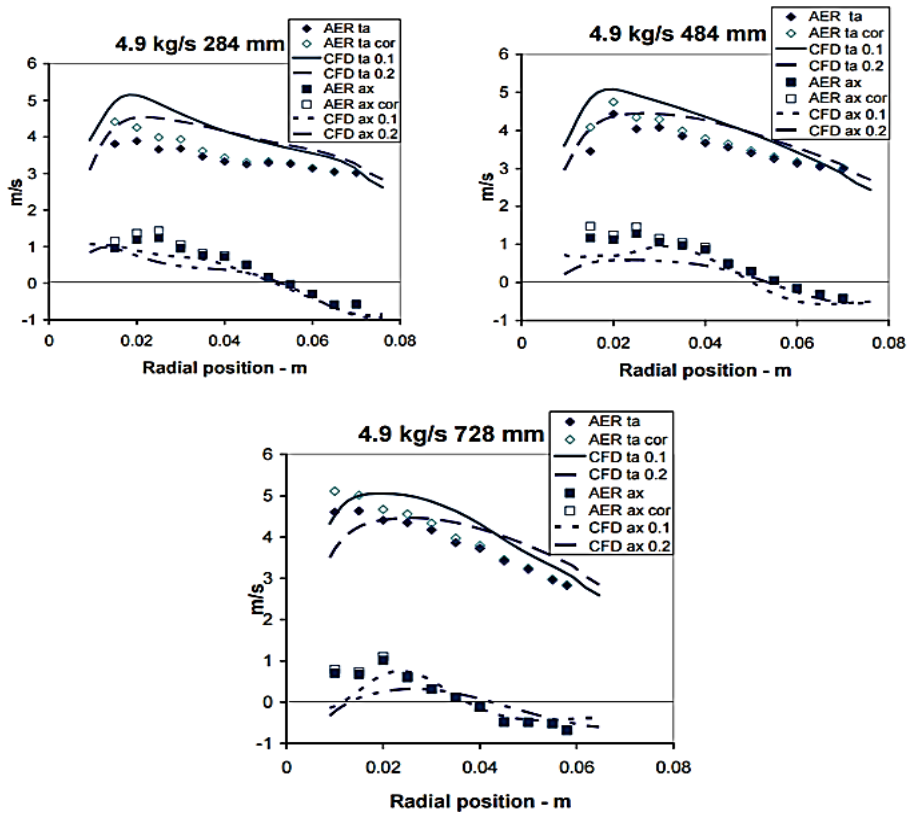

Figure 2.37. Velocities measure by aero-probe and that predicted by CFD at three different elevations with constant mass flow rate at 4kg/sec Brennan, M., Fry, M., Narasimha, M., & Holtham, P. (2007)

Figure 2.37 and 2.38 depicts the local radial velocity profiles measured by the conical head five-hole pressure probe. Figure 2.37 depicts radial velocity profile measured at three different elevations of 248mm, 484mm, and 728mm at a constant flow rate of 3kg/sec.

Furthermore, figure 2.37 depicts radial velocity profile measured at three different elevations of 248mm, 484mm, and 728mm at a constant flow rate of 4.9kg/sec. The results were compared with numerical results, and it all showed reasonable correlations. Furthermore, the probe is limited to measuring only flow fields within a smaller flow angle and does not suggest extending or integrating calibration processes for better measurement accuracies.

Vijay, B., Pravin S., Nilesh, P., & Pankaj, V. (2016) introduced a calibration method of conical head five-hole pressure probe that is suitable for velocity measurements at flow range of up to $\pm 30^{o}$ angles. The free stream average velocity magnitude is 25m/sec and the conventional calibration method of interpolating calibration curves was used. Table 2.2 demonstrates the non-dimensional coefficient values obtained for each pitch and yaw calibration.

Table 2.2. Pitch and yaw angle calibration constant Vijay B. Pravin S, Nilesh, P., & Pankaj V. (2016)

Pitch -30		Pitch -20		Pitch-10		Pitch 0		Pitch 10		Pitch 20		Pitch 30	
-4.1	-3.8	-3.8	-1.8	-3.4	-0.65	-3.2	0.4	-3.4	1.5	-3.6	3	-3.8	5.4
-2.3	-3	-2.1	-1.5	-2.4	-0.5	-2	0.3	-2	1.2	-2.15	2.3	-2.25	4
-1.1	-2.8	-1.1	-1.3	-1.1	-0.4	-1.1	0.2	-1.1	1	-1.15	2	-1.05	3.3
-0.4	-2.5	-0.2	-1.3	-0.1	-0.4	0	0.1	0.1	0.9	0	1.9	0	3
0.8	-2.6	0.9	-1.35	0.8	-0.45	0.7	0.1	0.8	0.9	0.9	1.9	0.9	3.1
1.9	-2.9	1.8	-1.4	1.6	-0.6	1.6	0.1	1.7	1	1.8	2.1	2	3.8
3	-3.4	2.8	-1.8	2.9	-0.8	2.9	0.1	3.1	1.1	3.4	2.4	3.6	4.7
Yaw -30		Yaw -20		Yaw -10		Yaw 0		Yaw 10		Yaw 20		Yaw 30	
-4.05	-3.75	-2.2	-3.1	-1.15	-2.8	-0.4	-2.5	0.85	-2.6	1.9	-2.81	3.12	-3.4
-3.85	-1.7	-2.15	-1.55	-1.1	-1.2	-0.2	-1.3	0.9	-1.3	1.89	-1.4	2.8	-1.86
-3.3	-0.6	-2.34	-0.55	-1.11	-0.4	-0.1	-0.4	0.83	-0.45	1.6	-0.69	2.75	-0.8
-3.26	0.47	-2.1	0.32	-1.05	0.25	0	0.1	0.7	0.17	1.51	0.1	2.9	0.19
-3.34	1.6	-2.08	1.28	-1.1	1.2	0.1	0.9	0.75	0.9	1.7	1.09	3.18	1.1
-3.51	3.2	-2.1	2.24	-1.25	2.05	0	1.9	0.9	1.86	1.88	2.1	3.4	2.31
-3.85	5.15	-2.21	4.1	-1.15	3.3	0	3	0.96	3.1	2	3.73	3.52	4.7

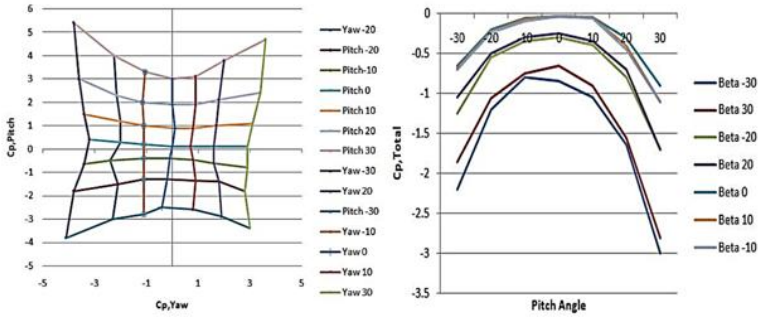

a b

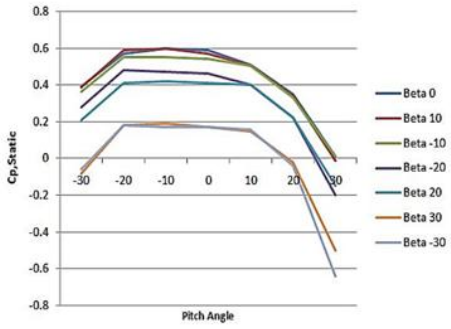

c

Figure 2.38. (a) Carpet map (calibration curve), (b) variation of total and (c) static pressure coefficient concerning pitch and yaw angles Vijay B., Pravin S., Nilesh, P., & Pankaj V. (2016)

Figure 2.38 shows that the probe is only capable of measurement for flow field within $\pm 30^0$ range of pitch and yaw angles. Furthermore, total pressure coefficient first increases with pitch angle and decreases after specific values of yaw angle. Also, the static calibration map shows that static pressure coefficients are a function of pitch and yaw angles. Even though the calibration results

show correlations regarding estimating non-dimensional constants, however, it is only limited to low-velocity flow airflow fields. Also, flow information measured is not validated.

Shah, R., & Banerjee, J. (2012) introduced the use of hemispherical head five-hole pressure probe in the isothermal analysis of CAN type combustor. The probe pressure taps and pressure ports are 0.55mm and 1mm in size. The probe is 10mm long and 4mm in overall size. Figure 2.39 depicts the probe schematics and the numbering information.

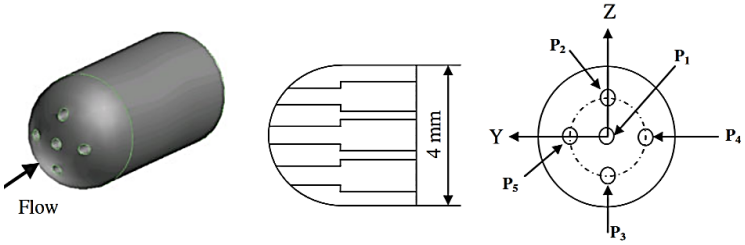

Figure 2.39. Schematics of the probe Shah, R., & Banerjee, J. (2012)

The probe calibration took place inside a wind tunnel with at a constant airflow velocity of 37.4m/sec at probe angles of $\pm 30^0$ with increment interval of $\pm 3^0$. The probe estimated the flow velocities inside the combustor system computed using calibration to make measurements. Correctly, the velocity magnitude was validated with a Pitot tube placed at zero pitch and yaw angles. Figure 2.40 depicts the locations of measurements at the pipe cross-section and the velocity profile.

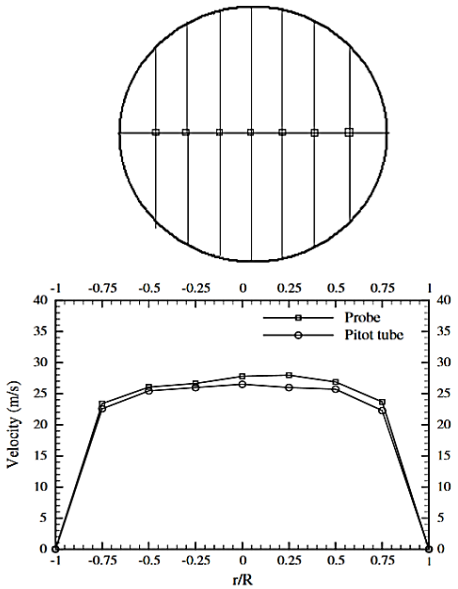

Figure 2.40. Measurement locations and velocity plots of the five-hole probe and Pitot tube Shah, R., & Banerjee, J. (2012)

In this study is the calibration of the probe is carried out only for low angle flow field, as it cannot measure flow with higher velocity where flow may exceed $\pm 30^0$. Furthermore, there were no studies on the comparison of two different probe shapes or integrating results to achieve an increase in accuracy.

Ligrani, P., Singer, B., & Baun, R. (2014) introduced the calibration method and used a 1.22mm conical head five-hole pressure probe to measure velocities. The calibration method used is based on the non-nulling procedure. A calibration curve is used that generated flow information during measurement. The probe measures velocity in airflow and the distribution of mean velocity and means vorticity over a cross-section of 12.7mm x 508mm of the curved channel was obtained. Although the probe can measure the flow field up to $\pm 45^0$, to an accuracy of 0.5^0, it cannot measure the turbulence. Also, the study is only on airflow and limited by Reynolds Number effects.

Lien, S., & Ahmed, N. (2011) introduced the method for examining the suitability of using a multi-hole pressure probe for skin friction measurements at different Reynolds Number, and the results were compared with another probe called the Preston probe. Figure 2.41 depicts the velocity profile measured inside the pipe flow and figure 2.42 describes the dynamic pressure profile.

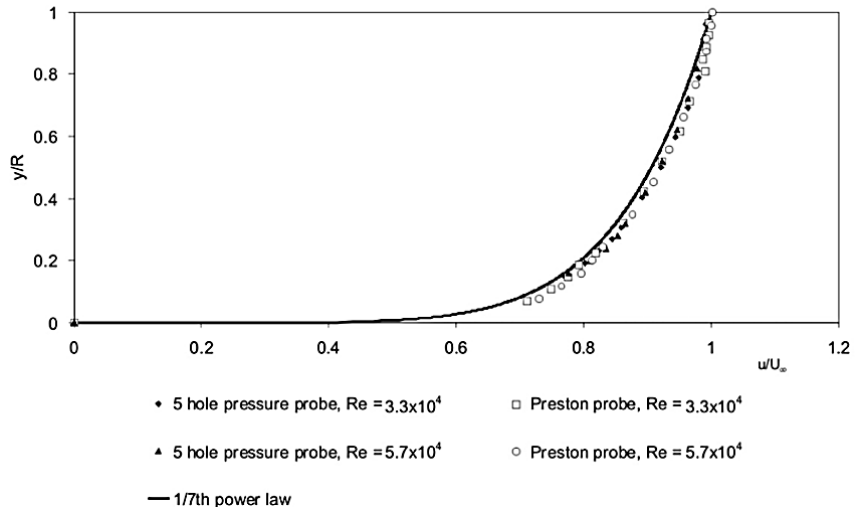

Figure 2.41. Velocity profiles in the pipe obtained using the five-hole probe and compared the Preston probe Lien, S., & Ahmed, N. (2011)

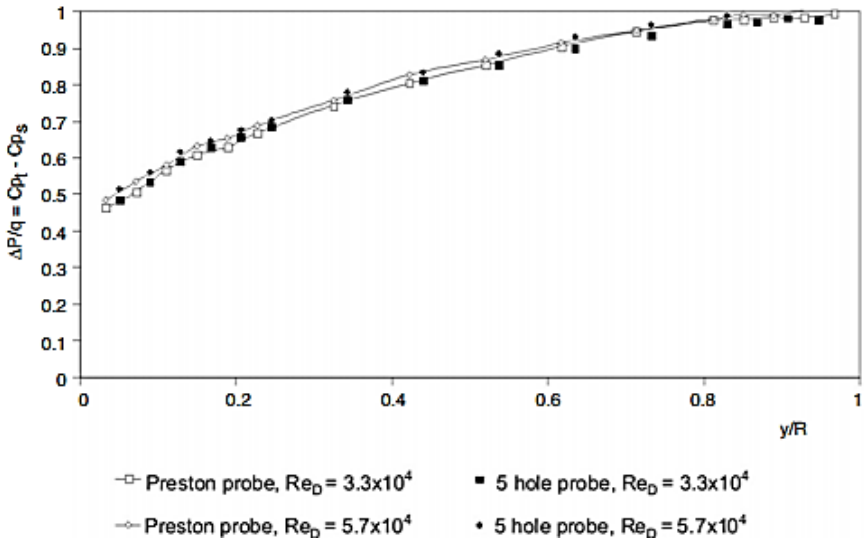

Figure 2.42. Comparison of local dynamic pressure in the pipe obtained using the five-hole probe and the Preston probe Lien, S., & Ahmed, N. (2011)

Even though the study was carried out in pipe flow, it did not consider what would be the results of another probe with a different shape. Furthermore, the research focuses on only single-phase airflow and not for water tunnel flow. Also, the study does not consider the use of CFD to integrate and improve the accuracy of experimental results.

Christopher, C., Shinder, I., & Michael, R. (2013) introduced a study on the effect of turbulence on a multi-hole pressure calibration. When calibrating the multi-hole pressure probe, hysteresis was found in specific ranges of air velocity, pitch angle and yaw angles. In the worst cases, this hysteresis caused a calibration error of about 30%. The experimental study demonstrates that the presence of hysteresis was because of the flow instability associated with flow separation. The pitch and yaw responses of the multi-hole probe were quite complicated, and hence accurate calibrations require thousands of measurable points. Since there are no precise models, calibration data are to be distributed as tables rather than using calibration factors that are dynamic pressure-related, as is the case for standard Pitot tubes and other S-shape or L-shape probes. Figure 2.43 depicts the probe used for this particular study.

Figure 2.43. Cone-shaped five-hole Pitot tube with 9.5mm diameter Christopher, C., Shinder, I., & Michael, R. (2013)

The results show a strong hysteresis in pressure differences measured during calibration when air velocity increases, as depicted in figure 2.44. The hysteresis was characterised by the calibration factor C_i ratio, shown in equation (2.34) as:

$$C_i \equiv \frac{\Delta p_{IUT,i}}{\Delta p_{standard}} \tag{2.34}$$

Where $\Delta p_{IUT,\ i}$ is the pressure difference between the centre-hole and the i^{th} off-axis hole of the Instrument Under Test (IUT), $\Delta p_{Standard}$ is the differential pressure measured by a standard Pitot tube at the laboratory inside the test section. The standard Pitot tube monitors the standard air velocity measurements. The installation location in the test section is one meter away from the IUT and rightly in the same cross-sectional plane of the wind tunnel.

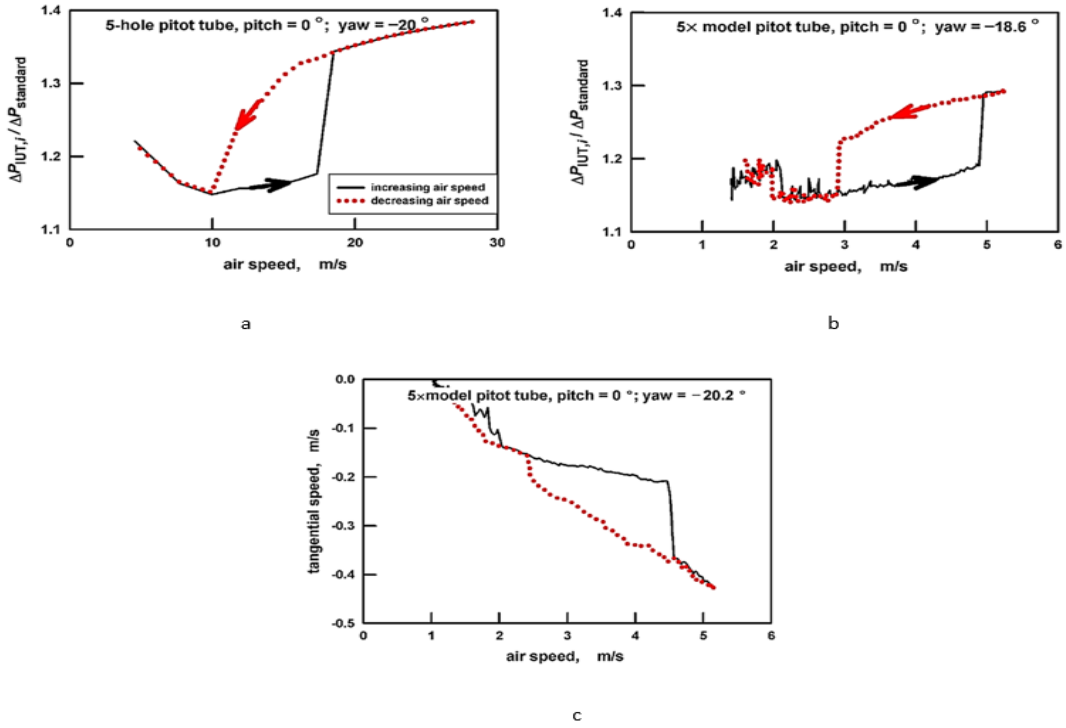

Figure 2.44. Characterisation of observed hysteresis for at different pitch and yaw angles for different air velocity Christopher, C., Shinder, I., & Michael, R. (2013)

As seen in figure 2.44, the air velocity decreases as the flow structure in the recirculation zone gradually approaches the structure before the transition. To test the role, if any, played by the multi-hole holes themselves, 45^{o} , thus displacing the holes out of air circulation area, rotated the probe. The counterflow velocity exhibited the same behaviour. Hence, the hysteresis is not caused by the pressure holes but was created by the geometry of the probe itself. The presence of hysteresis is because of flow transition connected with the recirculation zone. The change is sensitive to the condition surrounding the recirculation zone. A light bump of the probe when the velocity is increasing can cause the transition to occur at a lower velocity. Similarly, by increasing the amount of turbulence present in the wind tunnel, the hysteresis will disappear and the shape of the calibration curve in the region near the hysteresis changes.

2.9 State of the Art Approach to Multi-hole Pressure Probes

The purpose of calibrating a multi-hole pressure probe is to establish the mapping relationship between pressure differences and flows properties. Due to the economic and robust nature of the

multi-hole pressure probes for three-dimensional velocity measurements, there are ongoing research and numerous applications of the probes. Some states of the art approach to multi-hole pressure probe are identified in this study to understand the recent works and how they are carried out for reference purposes.

Hsin-Hung, L., Iosif, I.S., John, D.W., & Michael R.M. (2014) proposed the calibration method of multi-hole Pitot tube for the application of ANFIS. The probe considered in this study is the conical and hemispherical five-hole pressure probes as depicted in figure 2.45.

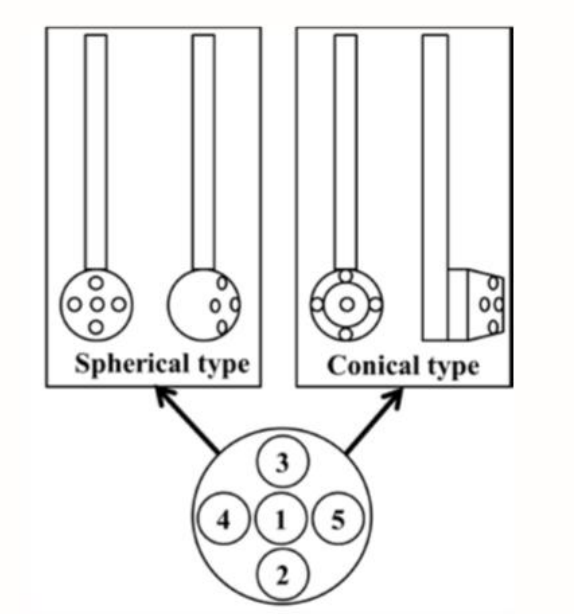

Figure 2.45. The configuration of five-hole Pitot tube Hsin-Hung, L., Iosif, I.S., John, D.W., & Michael R.M. (2014)

The calibration method is Adaptive-Network, and Fuzzy Interference System (ANFIS) based. This powerful technique integrates the benefits from the reasoning of fuzzy logic and the skill of the neural network. This method involved constructing a set of fuzzy logic if-then rules that have tuneable function parameters and then use Neural-Fuzzy systems and a set of rules to process dataset obtained from the probes. The calibration procedures for this method are summaries in the flowchart depicts in figure 2.46 and figure 2.47 depicts the velocity map generated by the probe using its non-dimensional pressure quantities for pitch and yaw angle planes.

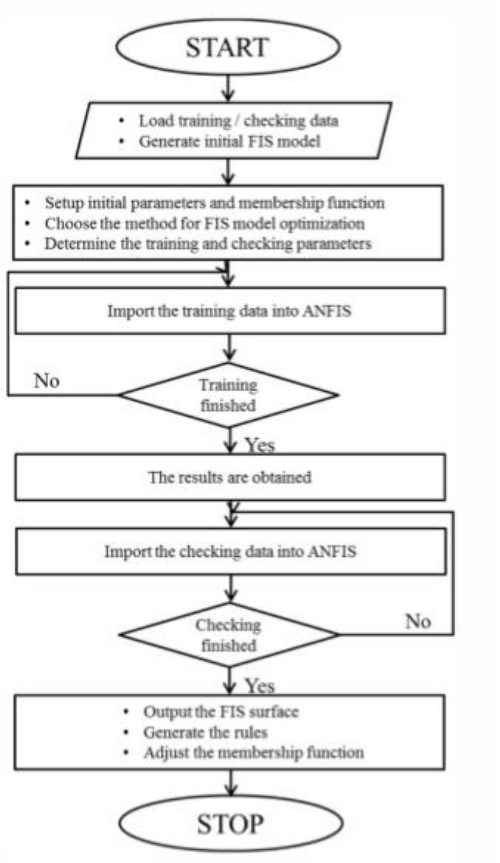

Figure 2.46. ANFIS calculation procedure Hsin-Hung, L., Iosif, I.S., John, D.W., & Michael R.M. (2014)

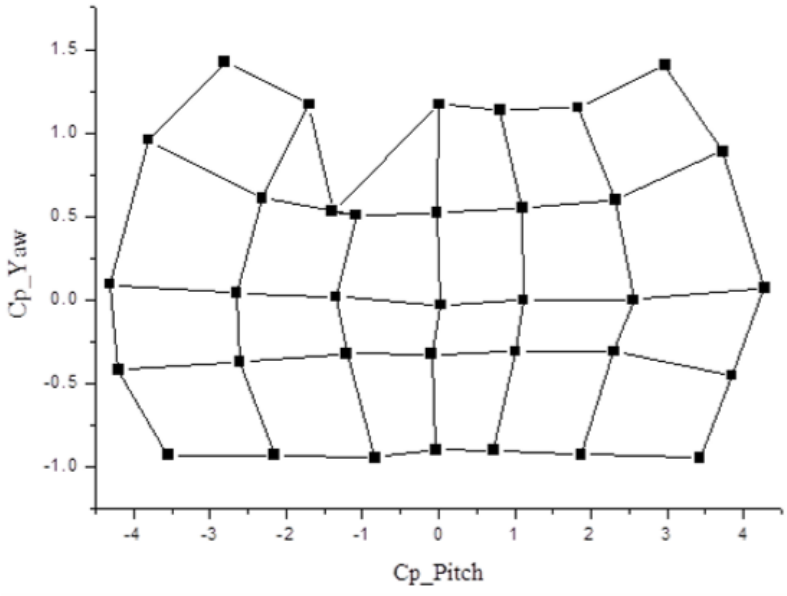

Figure 2.47. Air velocity Hsin-Hung, L., Iosif, I.S., John, D.W., & Michael R.M. (2014)

In this study, it was reported that the distribution of velocity begins to distort after flow angles are over 30^{o} , this is demonstrated in figure 2.47. Therefore, the study has been carried out for $\pm 30^{o}$.

Furthermore, it was reported that the method is efficient for flow measurement at this angle because the error is less than $7.2x10^{-3}$ before the flow stabilises. Due to the programmability of the method adopted to calibrate the probe, ANFIS it can be integrated with real-time data acquisition system in wind tunnel, an extensive database consisting of flow properties, flows angles and non-dimensional pressure coefficients can be efficiently established.

Additionally, it reduces calibration time. However, this method cannot extend the calibration angle beyond the $\pm 30^{o}$ set for the calibration. This limitation is where the CFD is strong and has an advantage over other integration methods. Furthermore, this method is only carried out for wind tunnel flows and not in any hydraulic system. Therefore, the accuracy of this method in any hydrodynamic systems cannot be guaranteed.

Jason, T., & Cengiz, C (2014) proposed a time efficient adaptive gridding approach and improved calibrations in five-hole probe measurements. The main aim was to introduce an automated system of calibration that eliminates the manual traversing of the probe in the test section, thereby reducing the human error that may arise from manual traversing. The calibration block diagram for the method used in this proposed method is depicted in figure 2.48.

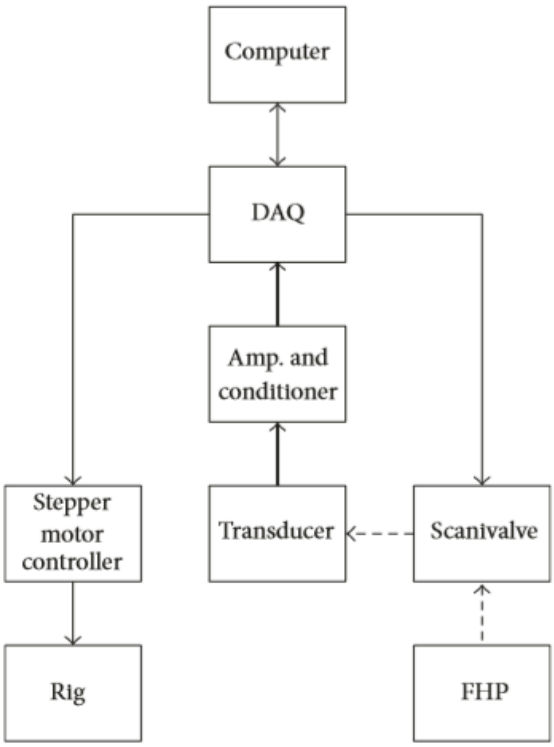

Figure 2.48. The calibration block diagram for five-hole probe measurements Jason, T., & Cengiz, C (2014)

The reason for this approach was to reduce the time it takes to calibrate a multi-hole pressure probe, improve the spatial resolution of measurements in selected high gradient areas such as boundary layers, wakes, tips vortices and secondary flow dominated zones, and improve general measurement accuracies.

The calibration approach used a single transducer that is connected to a scanivalve Corp. 48 channel mechanical pressure selector. The specific electrical commands to stop and reset the scanner are provided by the digital output D/A of the DAQ for pressure data set to be collected. After which a direct interpolation data reduction approach was used to analyse the data and provide results as shown in figure 2.49 is the carpet map of the probe.

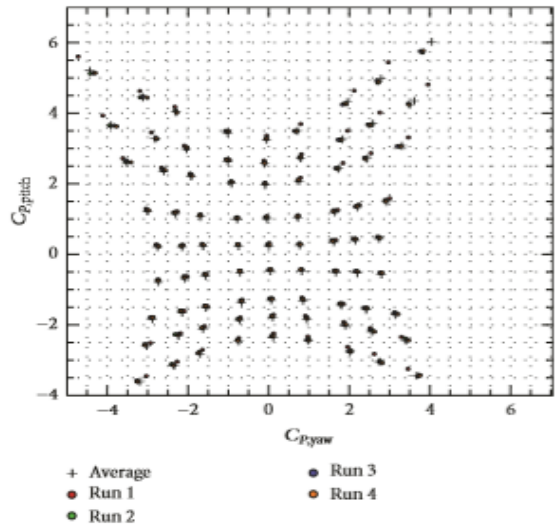

Figure 2.49. Average values (crosses) with data spread of four runs Jason, T., & Cengiz, C (2014)

The carpet map as shown was obtained four times in subsequent runs to establish the repeatability of the calibration process. The centre of each cross represents the average value, while the four points surrounding each cross represents the data collected from each run. Nearly all aspects within the ±20° range have good grouping and are close to the average value. In the outlying regions of the calibration, those greater than ±20° , the gathering is not as tight and initial alignment errors are exacerbated. Furthermore, the star-shaped carpet map is not perfectly symmetrical because a dimensionally perfect and balanced pressure probe is very difficult to manufacture because of the small nature of the probe and the inherent machining imperfection.

Calculations of Cp_{Pitch} and Cp_{yaw} are found directly using equation 2.34 and 2.35. The results are used to interpolate pitch and yaw angles values with the help of data represented in figure 2.50 that is a typical averaged carpet map produced by the automated calibration approach.

$$Cp_{pitch} = \frac{p_5 - p_4}{p_1 - \bar{p}} \tag{2.34}$$

$$Cp_{pitch} = \frac{p_2 - p_3}{p_1 - \bar{p}} \tag{2.35}$$

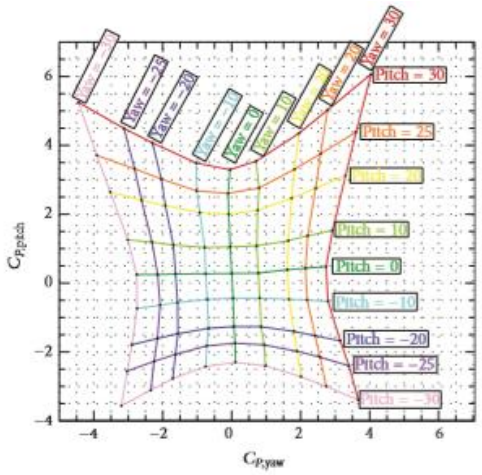

Figure 2.50. Coefficients of pitch angle versus coefficients of yaw angles at variable yaw angles of ±30 for 81 calibration pints Jason, T., & Cengiz, C (2014)

The variation in Cp, $_{total}$ concerning pitch and yaw angle are represented in figure 2.51. Interpolation is carried out to find Cp, $_{total}$ using t using equation (2.36).

$$Cp_{pitch} = \frac{p_2 - p_{total}}{p_1 - \bar{p}} \tag{2.36}$$

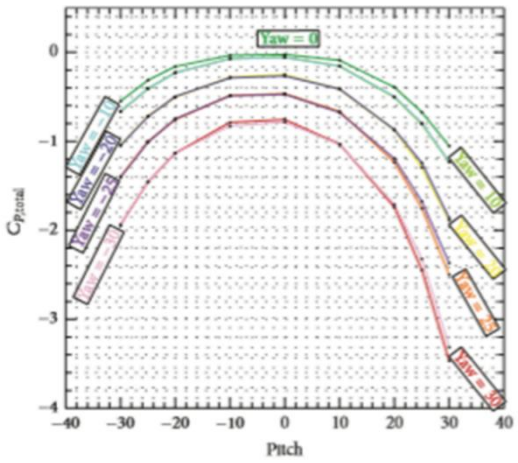

Figure 2.51. Coefficients of total pressure versus pitch of ±40 at a variable yaw angle of ±30 for 81 calibration pints Jason, T., & Cengiz, C (2014)

Figure 2.52 represents the Cp, static as a function of pitch and yaw angle. The non-dimensional Static pressure of the probe can be recovered using equation (2.37).

$$Cp_{pitch} = \frac{p - p_{static}}{p_1 - \bar{p}} \tag{2.37}$$

where $\bar{P} = \frac{p_2 + p_3 + p_4 + p_5}{4}$

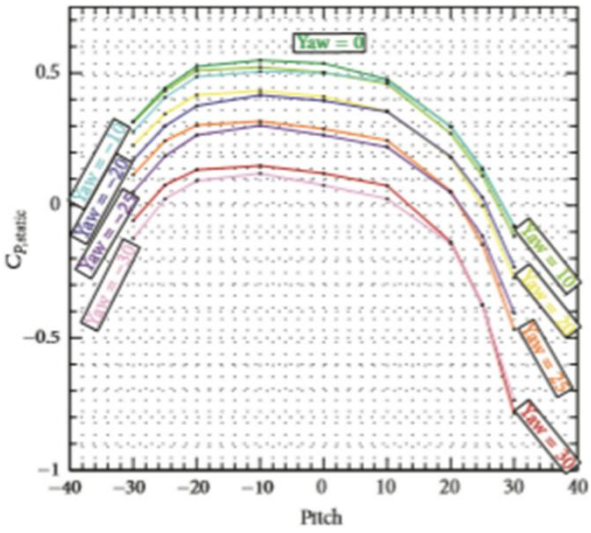

Figure 2.52. Coefficients of static pressure versus pitch angle of ±40 at a variable yaw angle of ±30 for 81 calibration points Jason, T., & Cengiz, C (2014)

The mechanical scanning approach with one transducer adopted in this study reduces measurements uncertainty by cancelling out thermal shift and calibration error the sensor might measure. It also reduces the total cost of the system but comes up with increased management time for the calibrations and measurements. Furthermore, the pressure probe was only for ±20^{o} , and nothing is suggesting extending the angle for more substantial flow.

Aschenbruck, J., Hauptman, T., & Seume, J.R. (2015) introduced the study of the influence of a multi-hole (five-hole hemispherical) pressure probe on the flow field in the axial turbine. It is essential to predict gas turbine flow field using CFD to improve jet engines continuously. The results of the CFD simulations are validated with pressure probe measurements. The probe was intended to predict flow field between the turbine blade rows, but as the probe is positioned in the flow passage, it disturbs the flow field. Therefore, this study investigated the influence of a multi-hole pressure probe on the flow field in a multistage axial air-turbine to measure airflow velocities experimentally, and the results were compared to the outcome of CFD simulations. These simulations were carried out with and without the probe in the flow passage to investigate the effect of the probe the flow field numerically. The shape and schematics of the probe are depicted in figure 2. 53.

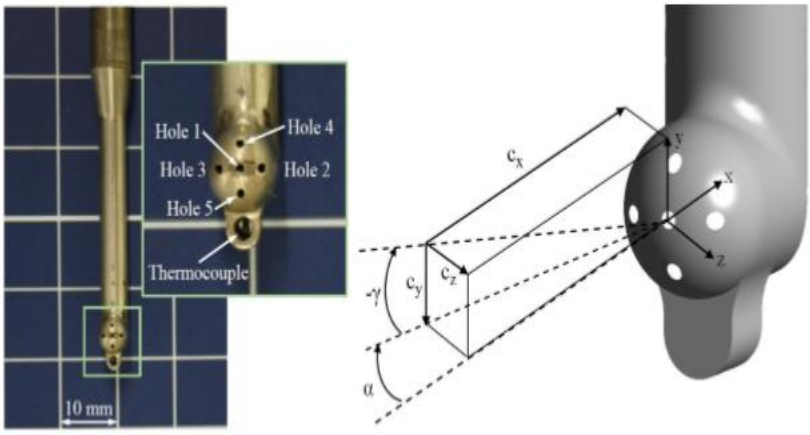

Figure 2.53. Five-hole pneumatic probe numeration and definition of pitch and yaw angles Aschenbruck, J., Hauptman, T., & Seume, J.R. (2015)

The total and static pressures of the flow can be determined by analysing the five pressure values sensed by the probe. For this analysis a calibration of the probe is necessary, to do this the probe was used to measure pressure at various Mach numbers at different pitch and yaw angles (α and y). This was carried out by rotating and tilting the probe around pressure hole 1. After the pressure probes were measured in the calibration duct, the calibration coefficients were determined as a function of Mach number and flow angles α and y. These coefficients are defined as yaw, pitch angle coefficients, and total and static coefficients.

For yaw angle coefficient, $$YAC = \frac{p_2 - p_3}{p_1 - (p_2 + p_3 + p_4 + p_5)/4} \quad (2.38)$$

For pitch angle coefficient, $$PAC = \frac{p_4 - p_4}{p_1 - (p_2 + p_3 + p_4 + p_5)/4} \quad (2.39)$$

For total pressure coefficients, $$TAC = \frac{p_t, p_r - p_1}{p_1 - (p_2 + p_3 + p_4 + p_5)/4} \quad (2.40)$$

For statistic pressure coefficient, $$SAC = \frac{Pp_r - (p_2 + p_3 + p_4 + p_5)/4}{p_1 - (p_2 + p_3 + p_4 + p_5)/4} \quad (2.41)$$

P is the flow of true local static pressure.

Their coefficients were used to analyse the flow measurement analysis in an iterative process, as the flow angles depend on the Mach number. Figure 2.54 depicts the free jet region of the calibration duct where pressure values were sensed.

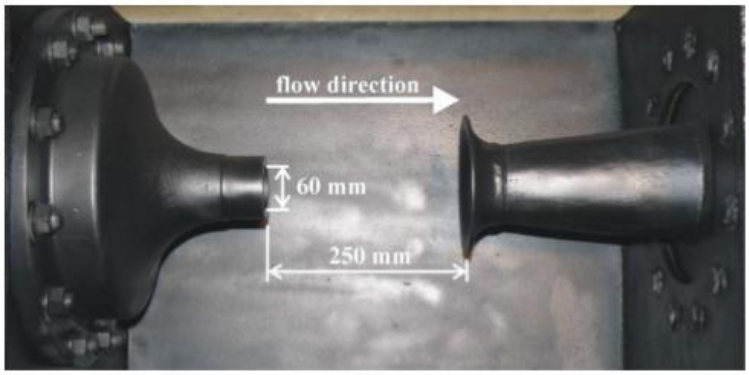

Figure 2.54. The free jet region of the calibration duct Aschenbruck, J., Hauptman, T., & Seume, J.R. (2015)

The experimental calibration of the aerodynamic probes took place in the low-speed calibration channel of the turbomachinery and fluid dynamics system (TFDS). This channel is operated in an open loop. The maximum Mach number is Ma = 1. The probe was positioned one nozzle diameter downstream of the convergent nozzle outlet. The first of the probe positioned at the centre line of the free jet for all calibration positions. The experimental calibration was conducted for a pitch angle of $\gamma = \pm 15^{o}$ in step 3^{o} and for yaw angle $\alpha = \pm 12^{o}$ in 3^{o} step. These positions were then calibrated for Mach numbers between 0.1 and 0.6 in 0.1 steps. The total pressure p_t, and the static pressure p_s for the total and static pressure coefficients are measured with Prandtl Pitot tube at the axial probe location for reference values. Figure 2.55 depicts the numerical calibration setup.

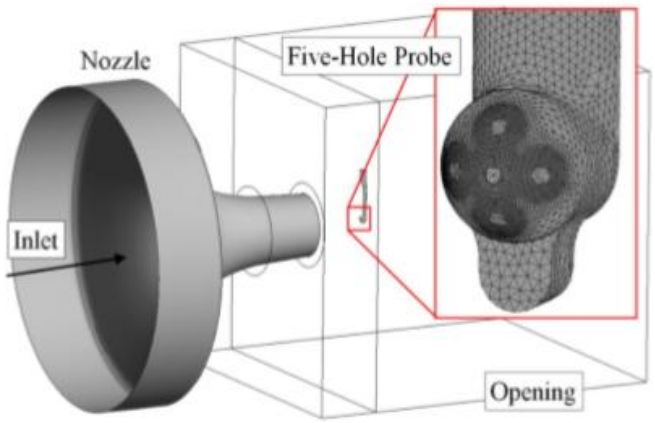

Figure 2.55. A numerical model of high-velocity calibration channel with five-hole pressure probe Aschenbruck, J., Hauptman, T., & Seume, J.R. (2015)

The numerical calibration was carried out with a model of the high-speed-calibration channel shown in figure 2.55. The model of the calibration channel was simplified by modelling only the

nozzle and replacing the bell mouth with a volume defined as a boundary with ambient static pressure. Besides the calibration channel, the five-hole pressure probe was also simplified, by covering the pressure holes and the pressure holes with the wall. However, the probe was modelled with its characteristics shape, to ensure negligible modelling error between simulations and experiments. The modification of the pressure probe reduces the computational effort in the mesh generation. However, the geometry was still complicated. Thus, the probe mesh must be generated with an unstructured mesh using hexahedral elements. The meshes for the numerical calibration have a grid quality with a minimum angle of 26^{o} and maximum aspect ratio below 1700. The total number of grid points in approximately 1.15million.

The boundary condition of the nozzle inlet was set to a constant total pressure corresponding to the specific Mach number. The numerical calibration is carried out for two Mach number Ma = 0.2 and Ma =0.4 with varied pitch and yaw angles. These Mach numbers were selected because these are the relevant values in the experimental stage of the axial turbine for the investigated operating point. The outflow of the nozzle is homogenous and undisturbed. The probe is located in the middle axis of the free jet. The numerical calibration was conducted for a pitch angle of $\gamma = \pm 5^{o}$ in step 5^{o} and for yaw angle $\alpha = 0^{o}$ to 15^{o} in 5^{o} step. The negative yaw angles are neglected because of the symmetrical geometry of the probe. The pitch and yaw angles range were deemed fit to capture the occurring flow angles in the turbine.

Figure 2.56 shows the numerical and experimental results of the calibration plot for the case of Ma = 0.2. This Mach number shows similar results when compared to higher velocities. The error bars of the experimental indicate 95% confidence interval. The YAC has the same characteristic depending on the yaw angle in the range of $\alpha = \pm 15$ and is in good agreement between numerical and experimental results. It can be noticed that the TPC shows good accordance of the statistical and experimental calibration data and differs only slightly. However, the diagram of the TPC coefficient shows a higher deviation at a yaw angle of 12.5^{o} . This difference is not in the 95% confidence interval. Linear behaviour is also visible in the results of the PAC calibration coefficient subjected to the pitch angle. Both the numerical and experimental results show linearity but differ by a constant offset. The results of the statistical calibration of the SPC coefficient are not by the preliminary results and show differences in dependence on the pitch angle.

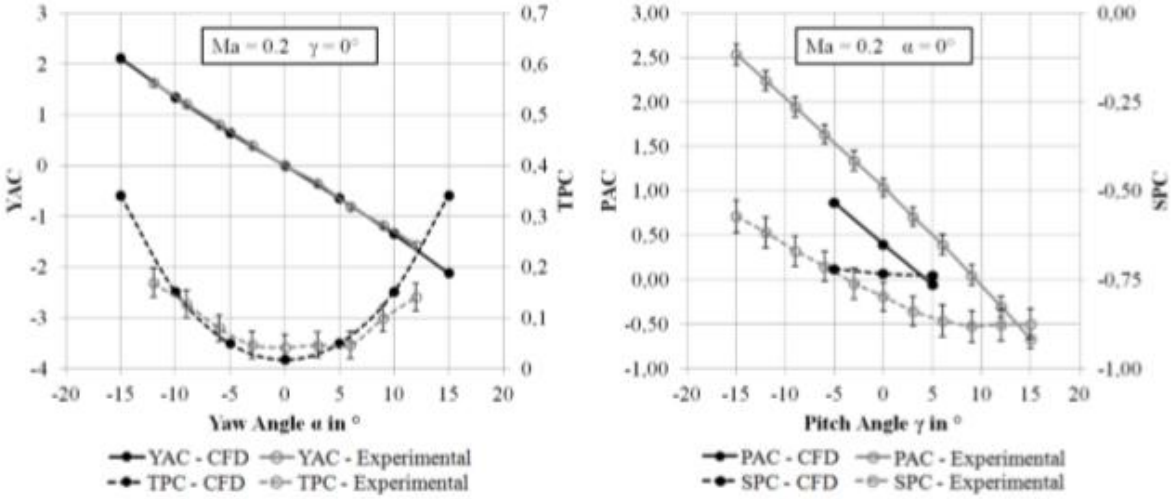

Figure 2.56. Numerical and experimental calibration coefficients for Ma = 0.2 Aschenbruck, J., Hauptman, T., & Seume, J.R. (2015)

The simulations with the probe were compared with the experimental data of the measurements in the turbine to verify numerical results as shown in figure 2.57.

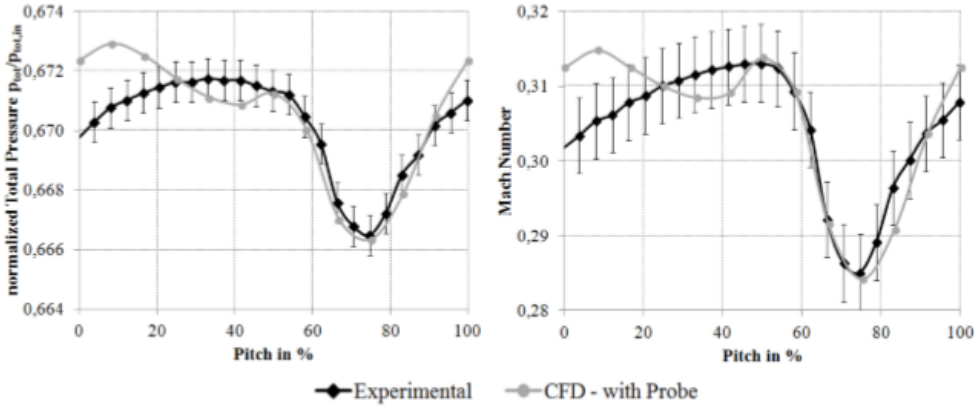

Figure 2.57. Comparison of experimental and numerical results Aschenbruck, J., Hauptman, T., & Seume, J.R. (2015)

The normalised total pressure and Mach number are plotted in figure 2.57. The experimental results agree well with the numerical results with the probe in the area of 50% to 90% of the pitch. In this area, the wake is region predicted accurately by the CFD. The differences are in the 95% accuracy intervals, which are indicated by the error bars

The results presented here is accurate for the application. Even though the results show in figure 2.56 demonstrates good agreements between CFD calibration and experimental calibration

especially for YAC and TPC, for high accuracies the numerical results alone are unreliable because it could not reproduce flow separation accurately. The reason for the offset at the PAC and the difference at the SPC between numerical and experimental results could not be determined. An attempt to doing this may result from a modelling error between the simplified model and the real probes geometry. Furthermore, there is disagreement between numerical and experimental results in the flow region with low total pressure gradients, between 0 to 50% pitch as shown in figure 2.57. There was no integration of CFD and experimental result to improve this limitation.

Remigiusz, J., Jaroslaw, M., & Jacek, P. (2017) introduced the use of multi-hole pressure probe positioning for exhaust emissions measurements. Emission of harmful compounds in the exhaust gases depends on the operating conditions of the engine and its technical requirements. In this type of environments, multi-hole pressure probe is the best choice for such measurements. The research was carried out is a turbofan, twin shaft engine with a hydraulically adjustable nozzle. It is equipped for the three-stage low-pressure compressor and a ten-stage high-pressure compressor. The combustion chamber is annular. Figure 2.58 depicts the cross-section of the engine Pratt and Whiney F100-PW-299 used for the research.

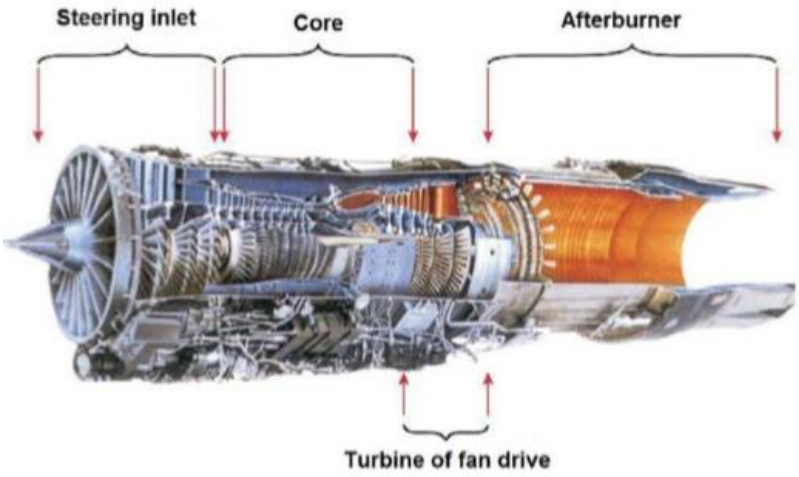

Figure 2.58. Cross-section of the engine Pratt and Whiney F100-PW-299 Remigiusz, J., Jaroslaw, M., & Jacek, P. (2017)

The engine is fitted with anti-icing system, wherein the heating of the engine inlet is managed by air taken from the relief valve at the fifth compressor stage. The study uses analyser Semtech DS (Sensor Emission Technology) depicts in figure 2.59 to measure the concentration of the exhaust compounds such as carbon monoxide, hydrocarbons, nitrogen oxides and carbon dioxide, according

to required characteristics of measurements contained in table 2.3 before using the multi-hole probe to measure samples of the exhaust.

Figure 2.59. Gas analyser Semtech DS Remigiusz, J., Jaroslaw, M., & Jacek, P. (2017)

Table 2.3. Characteristics of the Semtech-DS analyser Remigiusz, J., Jaroslaw, M., & Jacek, P. (2017)

Compound	Measurement method	Accuracy % of the range
CO	NDIR, range 0÷10%	±3.0
HC	FID, range 0÷10 000 ppm	±2.5%
$NO_x = (NO + NO_2)$	NDUV, range 0÷3000 ppm	±3.0%
CO_2	NDIR, range 0÷20%	±3.0%
O_2	Electrochemical analyzer, range 0÷20%	±1.0%

The exhaust gases were introduced to the analyser via a cable, whose temperature was 191° C, required to measure the hydrocarbon concentration in the flame ionisation analyser. After cooling the flue gas to a temperature of 4° C. The process of measuring nitrogen oxides, carbon dioxide, and carbon monoxide is depicted in figure 2.60.

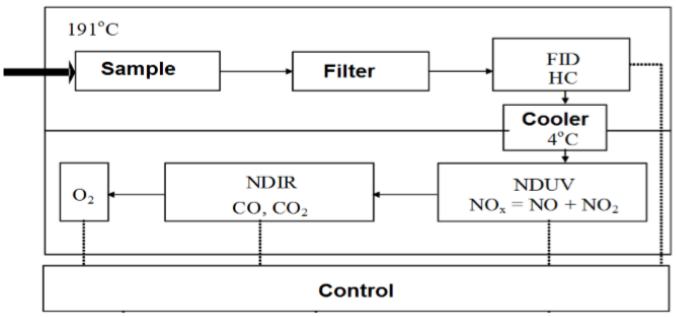

Figure 2.60. The block diagram of Semtech-DS analyser Remigiusz, J., Jaroslaw, M., & Jacek, P. (2017)

The methodology for measuring the emissions of gas turbine engines involves measuring the concentration of exhaust gas in a sample obtained from the exhaust gas stream flowing through a specially designed multi-hole probe following the stated rules set by ICAO.

- The probe, which makes contact with the gas sample, must be made of stainless steel or other non-reactive material.
- All holes of the probe must be of the same diameter.
- The design of the probe must be such that at least 80% of the pressure acting on the probe should be through the holes.
- The number of exhaust gas intake must not be less than 12.
- The surface of the probe must be close to the outlet of the engine as permitted by the engine performance, but in any case, it must be less than 0.5mm of the nozzle.
- There must be a need to demonstrate to the certification authorities that the proposed probe and its placement in the system will provide a representative sample for each particular engine state

The use of a multi-hole pressure probe in this study allows obtaining an average sample of exhaust gases. The average value of the collected sample gas is related to the fact that, as the distance from the exhaust gas axis increases, a decrease in the concentration of the exhaust constituents can be observed. It depends on the design of the engine, including the cooling method of cooling and separation of the engine parts from the hot exhaust gases and the associated turbulence flow in the exhaust stream. The resulting exhaust sample sensed at the holes of the probe for different concentrations of compound are mixed and therefore and used to estimate the average concentration value of pollutants. Consequently, it is desirable to measure the level of contaminants in the exhaust-outlet area without a dilution effect. By performing such measurements, it is possible to estimate the actual gas composition and use additional information to determine exhaust gas mass flow and exhaust emissions

The study was conducted to evaluate changes in the concentration of pollutants in the exhaust gases relative to the distance from the measuring point from the exhaust flow axis. A special test bench was prepared to allow the probe to be changed during engine operation. The experiment was carried out by performing a typical engine test on the engine dyno at the minimum value of thrust. During the study, concentrations were measured in four positions of the probe. The distance between the

measuring points was about 250 mm. The last measuring point was 750 mm from the exhaust flow axis. The analysis of changes in the concentration of the compounds was performed based on carbon dioxide concentration. Figure 2.61 depicts the test section, figure 2.62 depict the results obtained at various measurement positions, and figure 2.63 depicts the comparison of results.

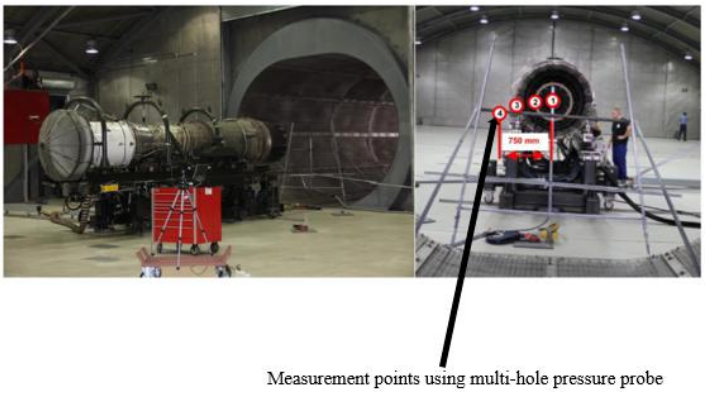

Figure 2.61. The test stands and measurement points Remigiusz, J., Jaroslaw, M., & Jacek, P. (2017)

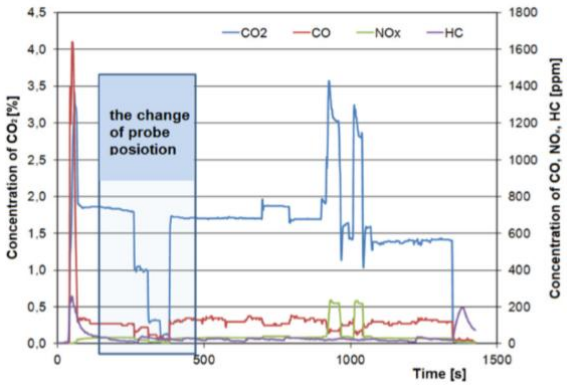

Figure 2.62. Concentrations of pollutants measured by the multi-hole pressure probe while changing the gas sampling position Remigiusz, J., Jaroslaw, M., & Jacek, P. (2017)

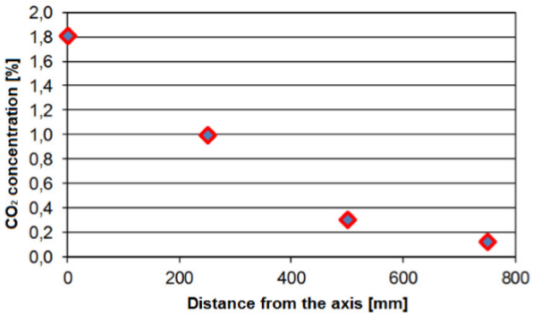

Figure 2.63. The concentration of carbon dioxide as a function of the distance from the axis of the exhaust flow Remigiusz, J., Jaroslaw, M., & Jacek, P. (2017)

Conclusively, the measurement results confirm the phenomenon of the mixing of gases in the outer areas of the exhaust stream flowing from the nozzle. Therefore, it can be assumed that the measurement of pollution must be carried out in the axis of the exhaust using a single-hole pressure probe. The results obtained show a substantial change in the concentration of pollutants in the exhaust gases, which are dependent on the distance from the axis of the flowing stream of exhaust gases. Changes recorded at two nozzle diameters indicate a strong exhaust gas fluctuation and a significant dilution zone. It can, therefore, be concluded that the measurement of the concentration of harmful compounds in the measurement procedures for the assessment of the ecological properties of turbine engines should be implemented in the axis of the exhaust gas flow using a single-hole probe. However, with the use of a five-hole probe with accurate calibration methods, the ecological properties of the turbine engine including the three-dimensional velocities can be obtained and compare to CFD for proper analysis.

Elisabeth, S.S., Ewoud, J.J.S., Bart, R., Christopher, D.W., & Qiping, C. (2017) introduced incremental non-linear dynamic inversion and multi-hole pressure probes for disturbance rejection control of fixed-wing micro air vehicles (MAV). In this study, two methods are proposed to improve the disturbance rejection performance of the MAV. The incremental non-linear dynamic inversion (INDI) control and phase-advanced pitch probes. INDI uses the angular acceleration measurements to counteract disturbances. Multi-hole pressure probes measure the incoming flow angle and velocity ahead of the wind to react to guests before an inertia response occurs. The performance of INDI response is compared to a traditional proportional integral derivative (PID) controller with and without the multi-hole pressure probes.

Pantelidis, K., & Hall, C.A (2017) introduced the Reynolds number effects on the aerodynamics of small compressors. It was intended to develop an improved understanding of the loss variation with Reynolds number, ReD in such a compressor. Some experiments of scaled-up single stage axial compressor were conducted across a range of Re 10^4 to 10^5. The flow field was measured at the rotor inlet; rotor exit and stator exit using full area traverse with a miniaturised five-hole probe. Furthermore, three-dimensional computations of the same compressor stage were conducted to investigate how useful steady fully turbulent RANS CFD, with the Spalart Allmaras turbulence model, is for this low Re regime. For this purpose, a small-scale axial compressor was designed experimentally and numerically, where the choice of Φ and Ψ were selected to achieve high efficiency. The low- speed rig used for the experiment is shown in figure 2.64.

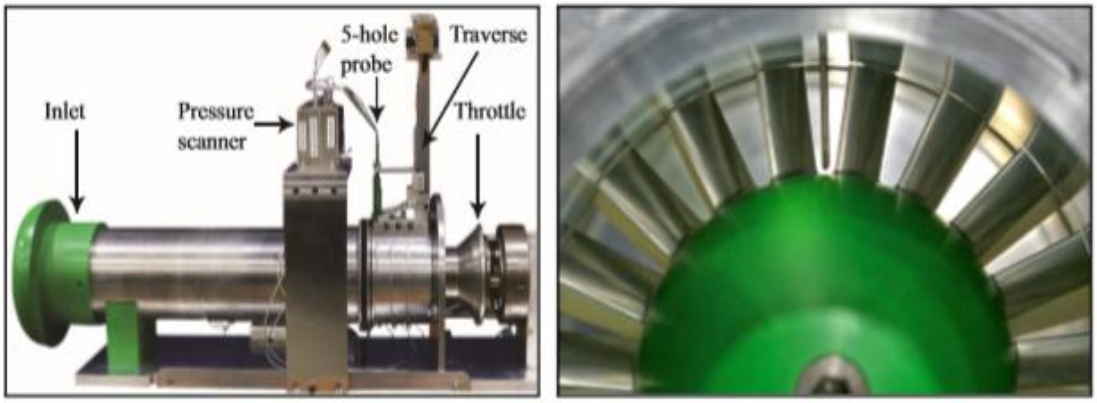

(a) Test rig illustrating the proximity of the pressure scanner to the 5-hole probe

(b) The 5-hole probe positioned at rotor inlet (station 1)

Figure 2.64. Experimental rig setup Pantelidis, K., & Hall, C.A (2017)

The miniature five-hole probe was constructed with an outer diameter of 4.4% of the blade span. This was connected to a 16-channel pressure scanner that was mounted nearby. This was done to achieve a fast measurement settling time, 1.3sec, with high accuracy. The probe was calibrated Dominy and Hodson method to generate a calibration map with a wide range, pitch = ±25° and yaw = ±35° . Figure 2.65 shows a schematic showing the traverse location of the probe in the test rig.

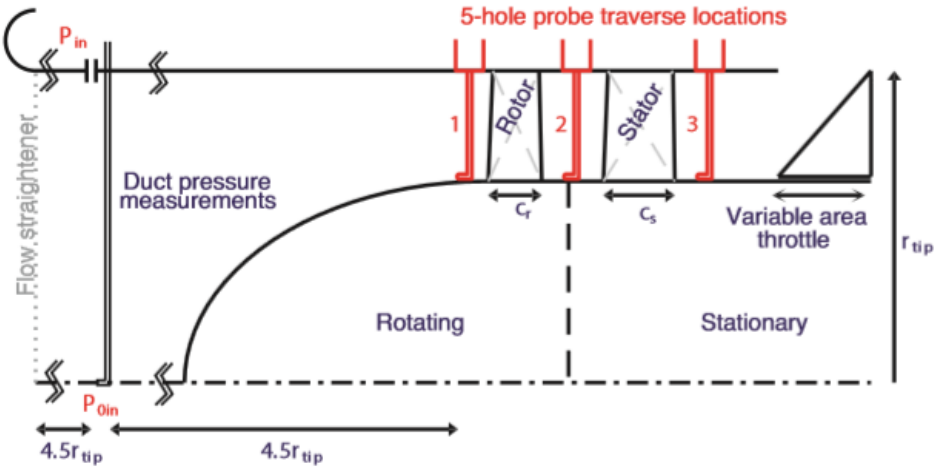

Figure 2.65. Rig schematic showing traverse locations Pantelidis, K., & Hall, C.A (2017)

A variable area motorised throttle at the stage exit controlled the flow coefficients, and the operating Re of the rig was adjusted through setting the rotational speed. Area traverses using a five-hole probe were completed at three stations, with up to 1000 measurement positions being

taken. To achieve the overall characteristic of the static compressor pressure rise the throttle was gradually closed stating at the fully open position.

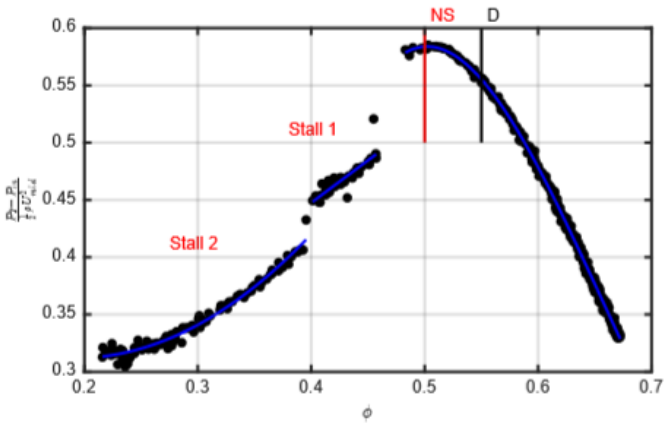

Figure 2.66. Static pressure rise characteristic measured at Re_D, showing Φ_D and Ψ_{NS} Pantelidis, K., & Hall, C.A (2017)

Two regions of stall can be observed at the peak. Stall 1 was expected to be part span (tip) stall cell and stall 2, a full span stall as shown above. Figure 2.66 depicts the probe traverse results at the design (D) and the near stall (NS) flow coefficient, which is the last continuously stable operating point.

The aerodynamic measurements made by the five-hole probe at ReD = $6x10^4$ in the duct are presented in figure 2.67. Emphasis is given to the flow properties measured by the probe, velocity, flow angle, pressure loss distributions of rotor and stator at two flow coefficients $\Phi_D = 0.55$ and $\Phi_D = 0.50$ as shown in figure 2.66.

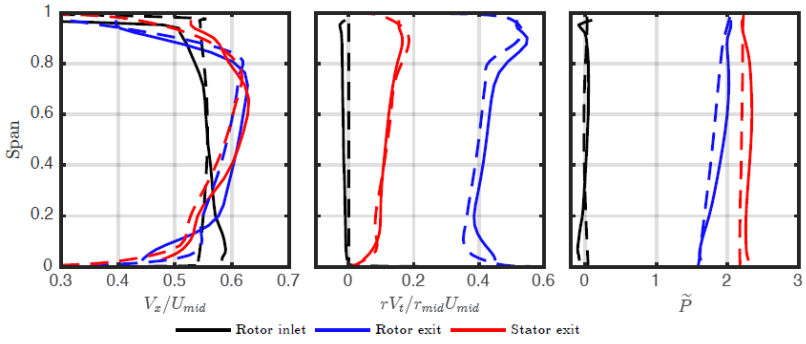

Figure 2.67. Span wise axial velocity distribution at rotor inlet, exit and stator exit Pantelidis, K., & Hall, C.A (2017)

Experimental measurements are shown in solid lines, and computation measurements are shown in dash lines span-wise for pitch angle-averaged, distribution of properties at ReD and Φ_D for different traverse stations of the probe. At the rotor inlet, there is a velocity gradient that is induced by the stream coverture above the rotor conenose. At the rotor exit, there is both a hub and casing velocity deficit characteristic of small corner separation and a large tip clearance flow. At the stator exit, the hub deficit has increase indicating a more significant corner separation, whereas at the tip there is a velocity recovery.

Reinaldo, A., Gomes, Julia, K., & Reinhard, N. (2018) introduced the development and implementation of a technique for five-hole probe measurements downstream of the linear cascade. The focus of this study is to develop a measurement method that combines other way and extend it allows for fast or transient five-hole measurements at strongly varying flow conditions by varying the Reynolds number as well as with steady and periodically unsteady inflow. This method enables reducing measurement time by up to 90% with compressing measurement accuracy. For the effectiveness of the technique, it was applied for flow measurements downstream of a compressor cascade with the attached and stalled flow. Figure 2.68 depicts the experimental setup, a high-speed cascade wind tunnel of the Institute of Jet Propulsion at the forces university Munich. The main components of the facility are a six-stage axial compressor, a settling chamber with laminar coolers and the nozzle. These parts are enclosed inside a pressure chamber where the static pressure can be changed between 3000Pa and 120,00Pa.

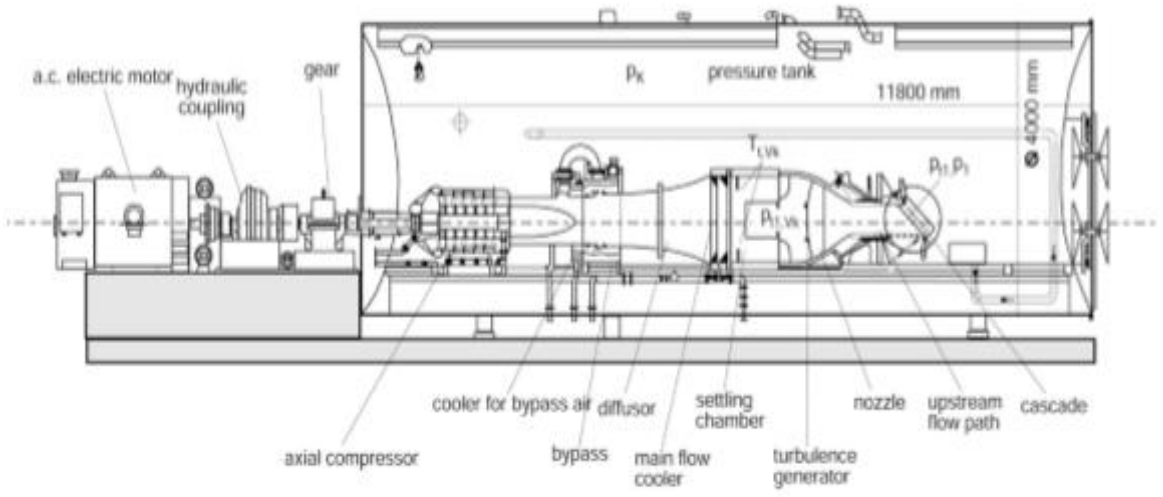

Figure 2.68. High-speed cascade wind tunnel Reinaldo, A., Gomes, Julia, K., & Reinhard, N. (2018)

The Mach number and Reynolds number of the flow are varied independently from each other **t**o control the compressor speed and the cooling of the air. The Mach number range at the nozzle exit lies within $0.1 \leq Ma \leq 1$, and the scope of the Reynolds number based on nozzle exit conditions derived by the geometric scale is approximately $2x10^5 m^{-1} \leq Re/l \leq 16x10^6 m^{-1}$. A 1.3MW electric motor drove the compressor, and a hydraulic coupling controls the speed. These components are placed outside the pressure chamber.

The determination of settling time for pressure measurement probe was the focus of this work. The settling time is essential whenever there is a noticeable time lag between pressure changes at the measurement location and the actual measurement device. The settling time is defined as the time needed for the measured pressure to level 99.9% of the initial pressure difference $P_1 - P_{0,}$ this is expressed in equation (2.42).

$$Ps = 0.999 \times p_1 + 0.001 \times p_1 \tag{2.42}$$

Using the probe for measurements in the downstream of the linear compressor cascade with moderate turning and a Mach number at the outlet of approximately 0.3. Measurements were taken at two Reynolds numbers, a medium 150,000 at which low profile loss is generated and low Reynolds number of 50,000 where the stalled flow was present. Also, for periodically unsteady inflow, the method was tested, and the result is depicted in the figure.

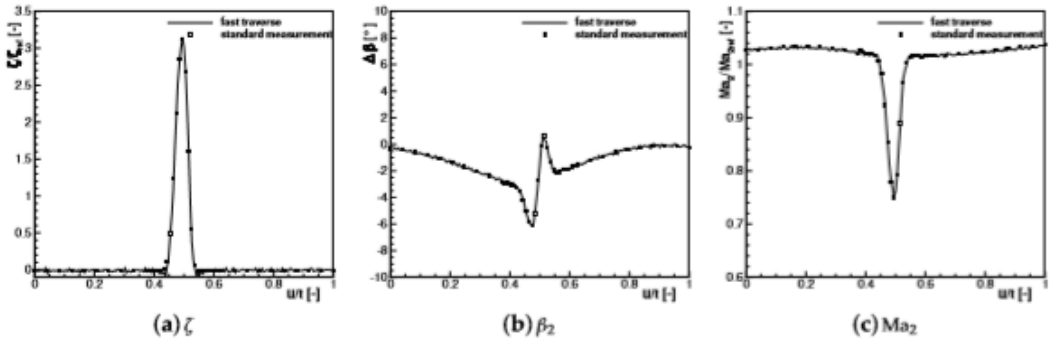

Figure 2.69. Flow properties measured downstream of the cascade with the standard and fast traverse technique for medium Reynolds number and steady inflow Reinaldo, A., Gomes, Julia, K., & Reinhard, N. (2018)

Figure 2.69 shows the results from a traverse at medium Reynolds number and steady inflow conditions. It shows the normalised profile losses (a), the flow angle (b), and the normalised Mach number as a function of the relative pitch wise position. The results of transient measurements

shown in figure 2.69 are from traversing velocity of 2m/sec. The same operating point was measured with a traversing velocity of 1m/sec. It was also observed that for medium and low Reynolds number, the measurement time decreases using the pressure probe developed for this study decreases the measurement. The total time needed is normalised by the time required at the low Reynolds number with the standard technique.

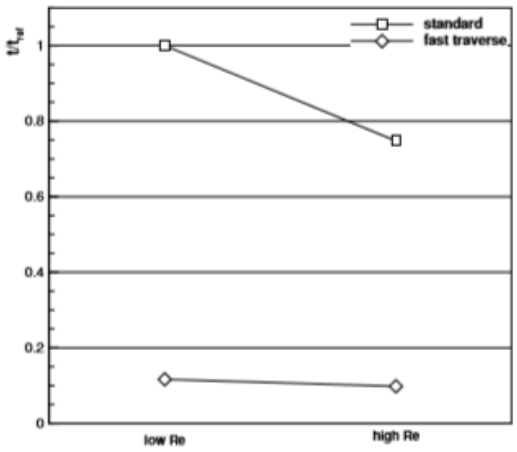

Figure 2.70. Entire measurement time necessary for a complete traverse measurement Reinaldo, A., Gomes, Julia, K., & Reinhard, N. (2018)

In figure 2.70, it can be seen that both standard and the new method of measurement are compared, and the process decreased the total time needed for one traversed by up to 90%. For a better estimate of the time saved, the typical overall measurement time for a standard traverse at low Reynolds number is approximately 45minutes.

The method and technique developed for the measurement of the high-speed cascade wind tunnel have been tested and has provided good results, the results are only one direction as it is limited to 50,000 and 150,000 Reynolds numbers. Furthermore, nothing is suggesting how to make the accuracy stronger like using CFD or integrating CFD into experiments.

Marcel, B., & Reinhard, N. (2018) developed an adaptive manufactured miniaturised wedge probe optimised for two-dimensional transonic wake flow measurements. Transonic measurement is known as challenging and several requirements and constraints arising in this flow regime. T meet this challenge, a new multi-hole pressure probe in the type of miniaturised wedge probe was developed. The miniaturised wedge probe was calibrated for high subsonic and low supersonic Mach numbers and different pitch angles at low ambient pressure conditions. This method

introduced some improvements of the probe calibration as well as using the base pressure hols for static pressure reference in the flow. Figure 2.71 depicts the design of the type of multi-hole pressure probe used for these particular experiments.

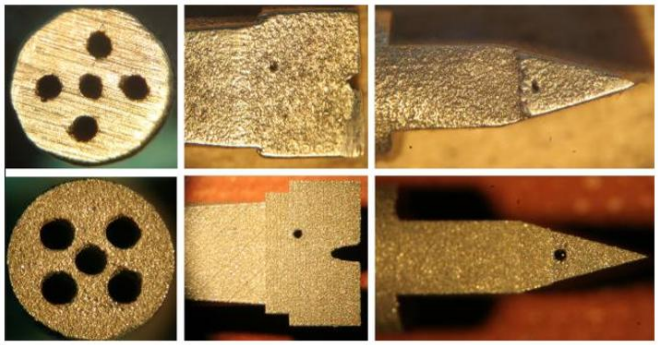

Figure 2.71. Raw sintered pressure probe head built with a layer thickness of 10µm Reinaldo, A., Gomes, Julia, K., & Reinhard, N. (2018)

The aim of the probe is to the exit flow quantities of transonic turbines cascade at mid-span (two-dimensional flow) in a high-speed cascade wind tunnel. The cascade wind tunnel is placed inside a pressure tank. The ambient pressure can be reduced down to 3.5kPa to obtain engine relevant Reynolds numbers during the test. It was reported that at low-pressure conditions, the settling time of the probe increases significantly, this was noted in the design process.

The probe was calibrated for Mach numbers between 0.5 and 1.6 and pitch angled of ±16° at the wind tunnel. Since the probe was intended to be used in low ambient pressure environment during measurements, the calibration was performed at the lowest possible ambient pressure of 12kPa. This resulted in Reynolds numbers based on the wedge thickness (1.3mm) between $1.8x10^3$ and $9.3x10^3$. Direct interpolation technique was used for data reduction as a method to evaluate the measured pressure from the probe; From the five pressure taps (labelling in figure 2.72) at the probe head, the non-dimensional probe quantities are derived as shown in equation (2.43 and 2.44). They are closely related to its special flow quantity Mach number and pitch flow angle respectively.

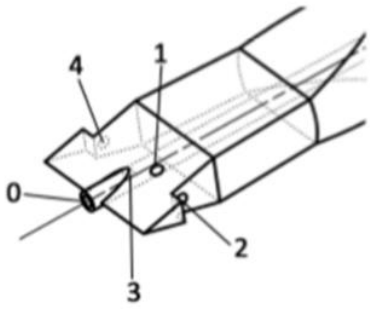

Figure 2.72. Position and labelling of the pressure taps at the multi-hole wedged probe head Reinaldo, A., Gomes, Julia, K., & Reinhard, N. (2018)

$$k_{Ma} = \frac{\Delta p}{p_0} \tag{2.43}$$

$$k_{\alpha} = \frac{p_3 - p_1}{\Delta p} \tag{2.44}$$

Δp is the quantity related to the dynamic pressure of the flow. Either, it can be derived with the pressure from the wedge face (wf) or with the base pressure (bp) holes as shown in equation (2.45) and (2.46).

$$\Delta_{pwf} = p_0 - \frac{p_1 - p_3}{2} \tag{2.45}$$

$$\Delta_{pbp} = p_0 - \frac{p_2 - p_4}{2} \tag{2.46}$$

The advantages of using the base pressure holes for referencing the dynamic pressure can be seen in the characteristic of the Mach number parameter k_{Ma} plotted over the Mach number at zero flow incidence depicted in figure 2.73.

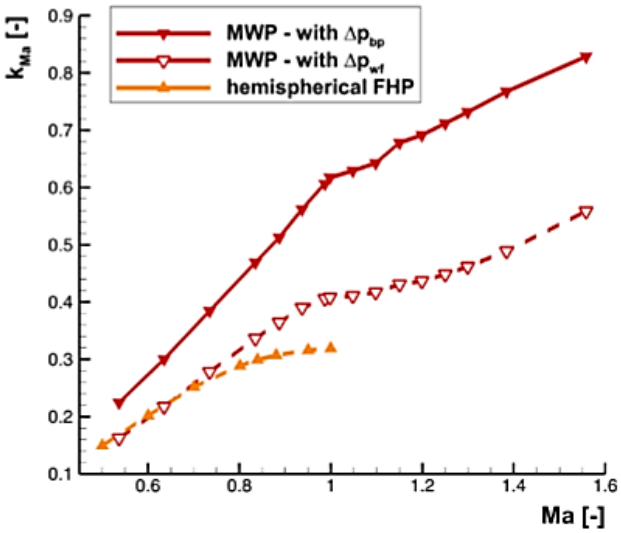

Figure 2.73. Mach number parameter at zero occurrences Reinaldo, A., Gomes, Julia, K., & Reinhard, N. (2018)

Figure 2.73 shows the characteristic of a five-hole pressure probe. It shows there is a decrease at Ma = 0.8 and the pronounced plateau is reached towards sonic flow velocity even though the slope of the characteristic is barely increasing above Mach 1. The sharp instead of blunt probe head geometries are preferable in the transonic flow regime, so this can be enhanced to increase the velocity to desired conditions.

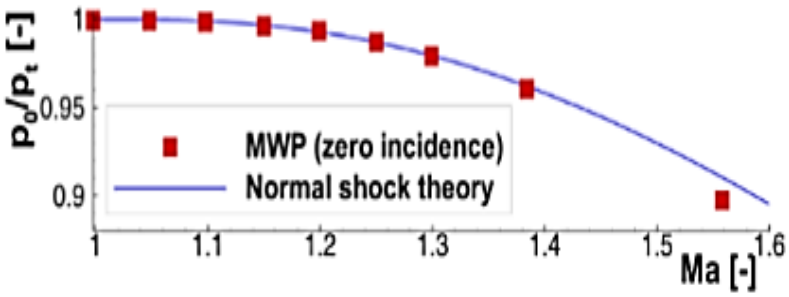

Figure 2.74. Total pressure measurement in sonic flow at zero incidences measured using a multi-hole wedged pressure probe compared to standard shock theory Reinaldo, A., Gomes, Julia, K., & Reinhard, N. (2018)

Figure 2.74 shows that the multi-hole wedged pressure probe. As expected, the pressure procurements with the Pitot tube p_0 of the MWP in subsonic flow agree very well with the total pressure in the flow at zero incidences. In supersonic flow, p_0 matches the theoretical total pressure ration downstream and upstream of a standard shock, which is expected.

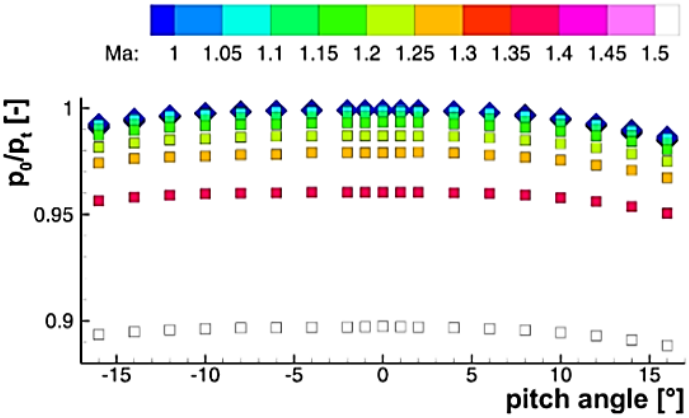

Figure 2.75. Flow angle sensitivity of total pressure measurements values of subsonic flow Reinaldo, A., Gomes, Julia, K., & Reinhard, N. (2018)

Due to the high ratio of the inner and outer diameter of the used Pitot in this study, the total pressure measurements are less affected by pitch angle variations, cf. All subsonic measurements, in blue diamond's lying above each other, showing similar flow angle dependency. For pitch angles of $\pm 10^{o}$ of the pressure reading of p_0 is less than 1% erroneous to the real total pressure of the flow. In the supersonic flow regime, the shape of the plots is similar to the subsonic ones, but the shock losses are observable. Nevertheless, the deviation of the pressure readings of p_0 is similar less affected by flow incidence angles in supersonic flow regimes. Since the Mach number parameter k_{Ma} of the multi-hole wedged pressure probe did indicate whether supersonic or subsonic is present, the actual total pressure of the flow can be uniquely assigned to the measured p_0. Furthermore, incidence angles in the yaw direction between $\pm 2^{o}$ assumed to be negligible effects were observed on the measurements of the multi-hole, which was tested for all Mach numbers and pitch angles. Therefore, the probe was found to be well-suited for real profile loss measurements and obtaining exit flow quantities in turbine cascade applications particularly in transonic exit flow conditions. The study also shows that the characteristic of the pitch angle parameter showed an approximately linear trend. Figure 2.76 illustrates the results for three different Mach numbers.

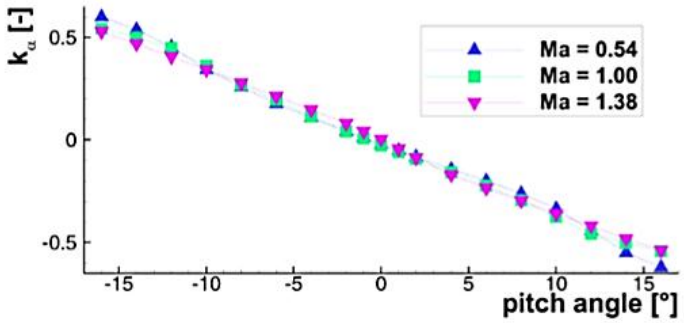

Figure 2.76.Characteristic of the pitch angle parameter k_α for three different Mach numbers Reinaldo, A., Gomes, Julia, K., & Reinhard, N. (2018)

It can be noticed undoubtedly that the characteristic is almost independent of the flow Mach number and the slope is practically constant over the entire calibrated pitch range.

Although the study carried out here, prove that the use of a multi-hole pressure to measure flow in wind tunnel can be accurate if proper calibration procedure is followed. However, there was no emphasis on velocity or higher Mach number and only very little was mentioned of the probe yaw angle. Further, there was no report suggesting using them in any hydraulic flow to test for its suitability and accuracy.

Marcel, B., Martin, B., & Reinhard, N. (2018) studied the challenges of five-hole probe measurements at high subsonic Mach numbers in the wake of transonic turbine cascades. The objective was to evaluate the Mach number measurements of a five-hole pressure probe in wake flow of a transonic turbine cascade at engine relevant Reynolds numbers by comparing them to results of particle image velocimetry (PIV). The PIV measurements were performed with an inserted five-hole pressure probe to investigate the influence of the probe on the wake flow field. The high-speed test facility used for this study is the same as shown in figure 2. 68 and table 2.2 shows the operating condition for these investigations.

Table 2.4. Operating condition range of the high-speed test facility

Reynolds number	$2x10^5 m^{-1} \leq Re/l \leq 1.6x10^7 m^{-1}$
Mach number	$0.2 \leq Ma \leq 1.05$
The ambient pressure inside the tank	$3.5kPa \leq pc \leq 1.2$ MPa
Free stream turbulence level at the inlet place	$0.4\% \leq T_{u1} \leq 7.5\%$

The operating point of the turbine cascade is defined by the theoretical exit flow Mach and Reynolds number ($M_{a2,th}$, $Re_{2,th}$) assuming an isentropic flow through the cascade. The theoretical exit flow Mac number is derived by equation (2.47).

$$M_{a2,th} = \sqrt{\frac{2}{\gamma-1} \times \left[\left(\frac{p_t 1}{p_c}\right)^{\frac{\gamma-1}{\gamma}} - 1\right]} \tag{2.47}$$

Where the total pressure p_t1 upstream and the static pressure p_c downstream of the cascade. Combining these parameters with the total temperature T_{t1} at the cascade inlet and the chord length l the theoretical exit flow Reynolds number can be calculated using equation (2.28).

$$R_{e2,th} = \sqrt{\frac{\gamma}{R}} \times \frac{l}{C_1} \times \frac{M_{a2,th} \times p_c \times \left(\frac{T_{tl}}{1+\left(\frac{\gamma-1}{2}\right)\times M_{a2,th}{}^2} + C_2\right)}{\left(\frac{T_{tl}}{1+\left(\frac{\gamma-1}{2}\right)\times M_{a2,th}{}^2}\right)} \tag{2.48}$$

C_1 and C_2 are the Sutherland constant. It was reported that a Reynolds number based on the dimensions of the five-hole probe $Re_{2,th}$ was more suitable for this work can be calculated analogous using equation 2.48 by using the probe head diameter d_p instead of the profile chord length l. The experiments were carried out at for two different exit flow Mach numbers of the turbine at probe Reynolds numbers of 6,500 and 13,000 and a constant total temperature T_{tl}= 303.15K.

The data reduction method for the five-hole probe calibrations before measurements are described in equation (2.49) through (2.52). From the five-hole pressure holes at the probe head cf, the non-dimensional probe coefficients can be derived. They are very closely connected with its particular flow quantity Mach number, pitch and yaw angles.

$$k_{Ma} = \frac{\Delta p}{p_0} \tag{2.49}$$

$$k_{\alpha} = \frac{p_3 - p_1}{\Delta p} \tag{2.50}$$

$$k_{\gamma} = \frac{p_4 - p_2}{\Delta p} \tag{2.51}$$

Where Δp is the quantity equivalent to the dynamic pressure, which is defined by equation (2.52).

$$\Delta p = p_0 - \frac{p_2 - p_4}{2} \tag{2.52}$$

Figure 2.77 depicts the schematic and pressure hole labelling of the probe. The finite distance between the pressure holes at the probe head causes measurement errors, especially inflows with large gradients. A spatial interpolation algorithm can reduce the mistake of not measuring each pressure at precisely the same position in the flow.

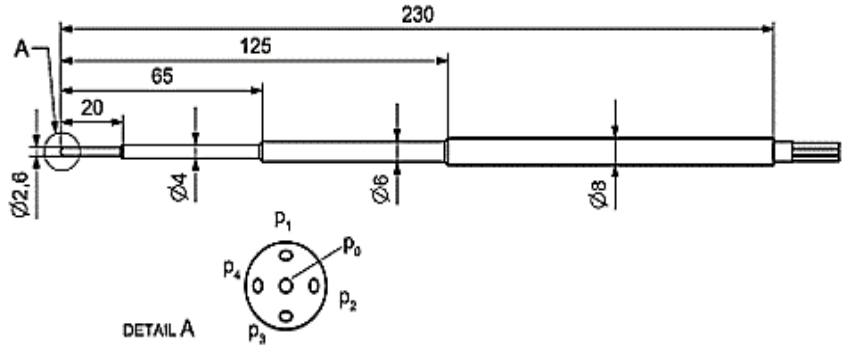

Figure 2.77. Five-hole pressure probe with a spherical head for pneumatic wake traverse Reinaldo, A., Gomes, Julia, K., & Reinhard, N. (2018)

The absolute velocity field was converted using equation (2.53) to compare the velocity quantities from the PIV measurements with the measured Mach number from the five-hole probe,

$$M_a = \sqrt{\frac{U^2}{\gamma R T_{tl} - \frac{\gamma - 1}{2} \times U^2}} \tag{2.53}$$

The experimental setup for this study is shown in figure 2.78, and the results of the ensemble-averaged PIV measurements of the lowest and figure 2.79 shows the highest investigated exit flow Mach number.

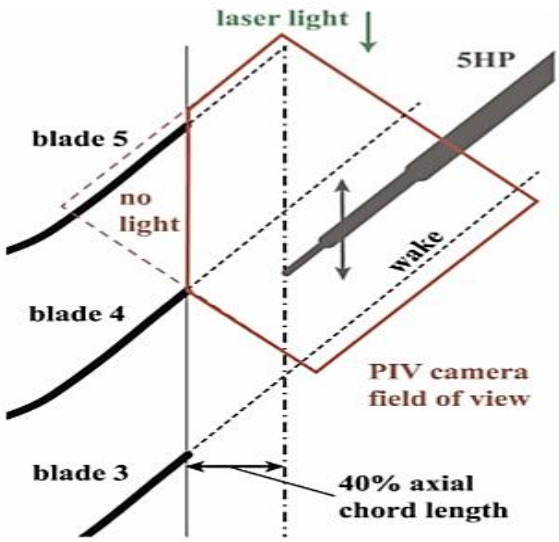

Figure 2.78. Experimental setup of five-hole (5HP) and PIV field of flow view in the cascade wake at midspan Reinaldo, A., Gomes, Julia, K., & Reinhard, N. (2018)

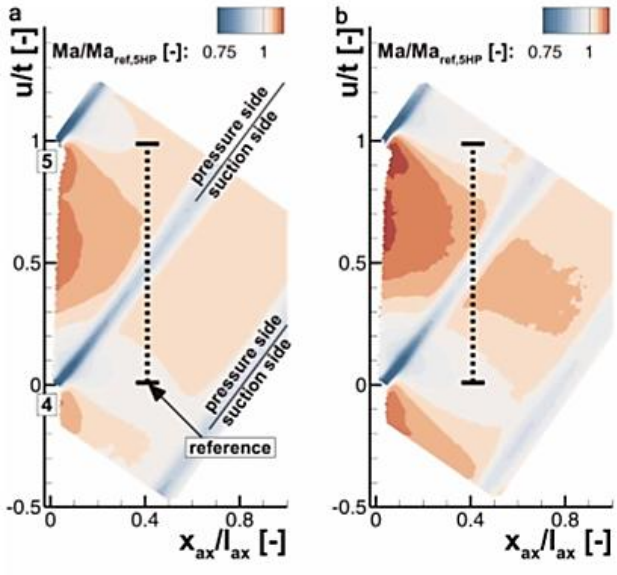

Figure 2.79. Mach number field calculated from PIV normalised with the reference Mach number of the five-hole probe (dash lines shows 5HP wake traverse path) Reinaldo, A., Gomes, Julia, K., & Reinhard, N. (2018)

The data is normalised with the Mach number $M_{aref,5HP}$ at the five-hole probe (5HP) wake traverse position u/t = 0 separately for each case. The dashed line shows the traverse path of the pressure probe over one blade pitch at 40% axial chord length downstream of the cascade outlet plane. As can be seen, the suction side flow from the adjacent blade interacts with the wake of the edge four, which is typical for transonic turbines.

Moreover, the influence increase with high velocity on the suction side(right figure). The resulting high-velocity variation (i.e. static pressure gradients) is merging with the steep total pressure gradients from the blade wake. It can be seen from the measurement fields that the average flow field downstream of the cascade outlet plane is subsonic in all investigated case and no supersonic flow regime are noticeable which is the requirement for applying the five-hole probe, merely calibrated for subsonic flows.

Data points along $x_{ax}/lx_{ax} = 0.4$ were extracted from the PIV flow field to compare them to the five-hole probe(5HP) wake traverse over one blade pitch. Linear interpolation was applied between the grid points. The results are depicted in figure 2.80 by a normalised Mach number plot for the three investigated operating locations. The reference point Mach number M_{aref} is chosen separately for each graph at its first pitch position u/t = 0 for qualitative comparison.

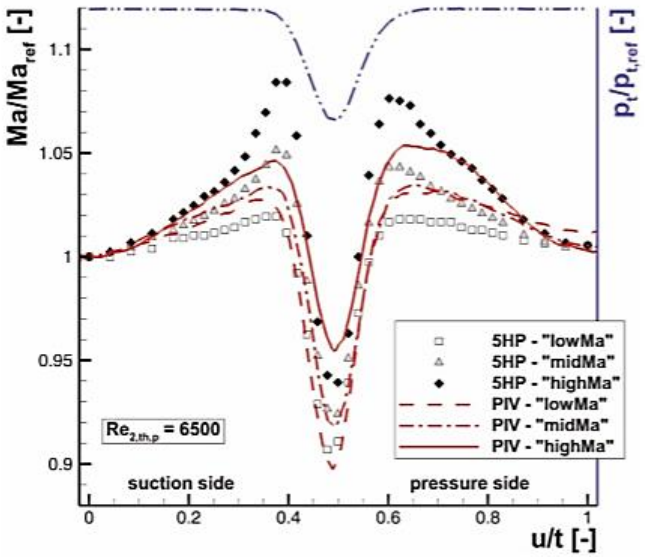

Figure 2.80. Normalised Mach number plot of the five-hole probe (5HP) and converted PIV measurements at $x_{ax}/lx_{ax} = 0.4$ Reinaldo, A., Gomes, Julia, K., & Reinhard, N. (2018)

The double dash-dotted blue line shows the qualitative normalised total pressure distribution along the traverse path measured with the five-hole probe. The extension of the pressure wake is similar for all investigated operating points. The reference Mach numbers from the five-hole probe and PIV at the same operating point deviate in the range of 1% to 2.5%.

A good agreement of the probe and the PIV measurement can be found in the first and last 30% of the pitch-wise traverse, where no total pressure gradient is present in the flow field. Accelerated

flow is available in both the five-hole probe and PIV measurement on each side of the wake. This positions approximately at u/t = 0.4 and 0.6 coincided directly with the insertions of the probe's traverse path and strong wake flow gradients. Figure 2.80 generally presents the trend that the five-hole pressure probe overestimates the Mach number compared to PIV in the area of high-pressure gradients. This effect increases as the shear layer become thinner, and the wake gradient gets stronger with rising exit flow Mach number. Furthermore, it must be stated that the flow Mach number evaluated by the five-hole pressure probe is subsonic at all positions and in all investigated cases. Therefore, the five-hole pressure probe did not reach the constraints of its calibration range.

Although the influence of a five-hole pressure probe has been established in this study, however, there is a significant challenge for this type of probe head in such applications. The strong gradients are arising from a merge of the blade wake and the transonic suction side flow field of the adjacent turbine blade. The complex flow gradients caused a different pressure distribution on the probe head compared the one at free stream conditions during the probe calibration. The decreasing sensitivity of the probe close to Mach 1 fostered an overestimation of the Mach number, especially in high subsonic flows. Therefore, excellent care need to be taken in interpreting the Mach number measurements of round head shaped five-hole pressure probes in gradient flows with Mach > 0.8.

Eny, Y.J., Zeng, Z., & Gordon, L. (2018) introduced the calibration of a seven-hole pressure probe in a low-speed wind tunnel. The focus of this study was to calibrate a small seven-hole pressure probe designed to be utilised in the new wind tunnel of the Embry-Riddled Research Park. The seven-hole pressure probe was designed to measure flow angularity, which has better sensitivity than most five-hole pressure probe. However, the seven-hole pressure probe requires finer and more specific calibrations. The probe consists of seven small diameter holes, with an outer diameter of 3.1750mm and ID of 0.3048mm. A 16-channel pressure transducer was used to measure the pressures from the seven pressure holes of the probe simultaneously, and the calibration was carried out at $\pm 10^{o}$ at an interval of 0.5^{o} pitch and yaw angles resulting in a test matrix of 41-by-41 measurement points. Figure 2.81 depicts the probe and its calibration set-up, while figure 2.83 depicts the calibration facility.

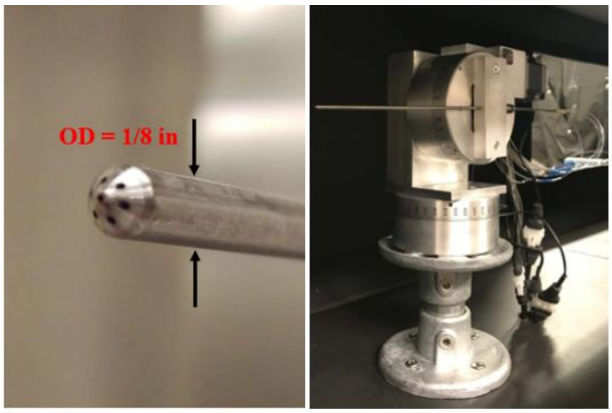

Figure 2.81. Seven-hole probe mounted on motorised rotary tables Eny, Y.J., Zeng, Z., & Gordon, L. (2018)

Figure 2.82. ERAU Boundary layer wind tunnel Eny, Y.J., Zeng, Z., & Gordon, L. (2018)

The experimental setup used a subsonic boundary layer wind tunnel, a new facility built in 2017, is 6706 x 6706mm cross-section and has a test section located 1219.2mm from the inlet.

The calibration theory was based on the data reduction technique derived from pressure coefficients defined based on the differences of the opposite pressure hole according to figure 2.83.

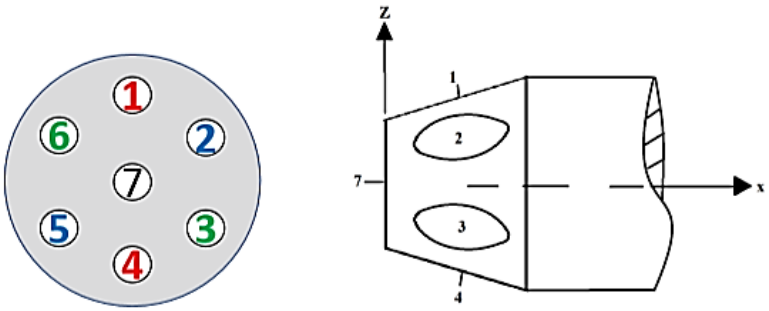

Figure 2.83. Front and side view of seven-hole pressure probe Eny, Y.J., Zeng, Z., & Gordon, L. (2018)

Figure 2.83 shows the definitions of the pressure holes with the centre hole, the forward facing pressure hole. The probe consists of seven stainless steel tubes that connect the probe to pressure transducers. Using the orientation and positions of the pressure holes, the calibration coefficients as expressed in equations (2.54) through equation (2.56) are defined.

$$C_{\alpha 1} = \frac{p_4 - p_1}{p_7 - p_{1-6}} \tag{2.54}$$

$$C_{\alpha 1} = \frac{p_3 - p_6}{p_7 - p_{1-6}} \tag{2.55}$$

$$C_{\alpha 3} = \frac{p_2 - p_5}{p_7 - p_{1-6}} \tag{2.56}$$

The angle pitch and yaw coefficients are defined using equation (2.57) and (2.58) and figure 2.84 depict the calibration coefficients, while figure 2.85 depicts the carpet map.

$$C_{\alpha} = \frac{1}{3}(2C_{\alpha 1} + C_{\alpha 2} - C_{\alpha 3}) \tag{2.57}$$

$$C_{\beta} = \frac{1}{\sqrt{3}}(C_{\alpha 2} + C_{\alpha 3}) \tag{2.58}$$

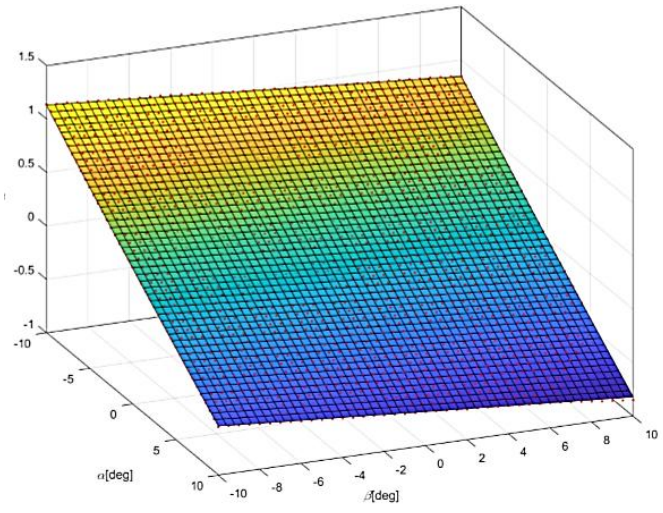

Figure 2.84. Seven-hole pressure probe calibration coefficients Eny, Y.J., Zeng, Z., & Gordon, L. (2018)

Figure 2.84 shows that the seven-hole pressure probe has demonstrated calibration accuracy with relative superiority and maintains even intervals of point distribution overall while showing massive points. The calibration map shown in figure 2.85 suggests that the probe configuration would lead to a relatively large standard error when calibrating within a 15° pitch angle, which is the operational range of the tunnel, as it has a wide interval between points that are somewhat unevenly distributed when the angle exceeded 5°.

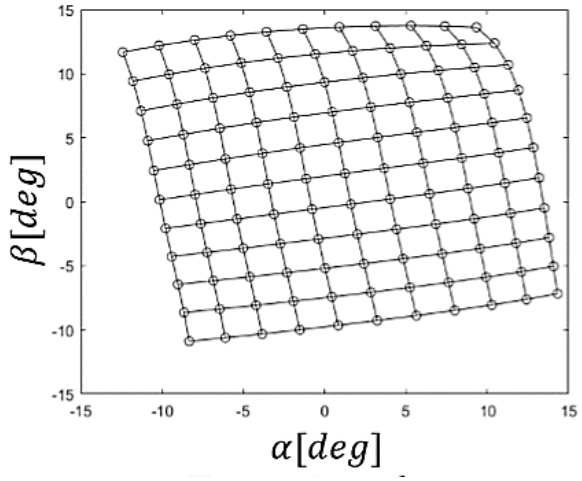

Figure 2.85. Seven-hole calibration carpet map Eny, Y.J., Zeng, Z., & Gordon, L. (2018)

Figure 2.85 shows the response of the individual five pressure hole. They are representative of pressure distribution obtained from the perimeter holes for the seven-hole pressure probe. It indicates the range of pitch and yaw angle for various sensing holes of the probe. It is characterised by the dimensionless pressure coefficients defined in equation (2.57) and (2.58).

The images shown in figure 2.84 and 2.85 have proven that the probe calibration has established accurate coefficients and map that have demonstrated that the calibration performed as expected. However, the probe was only calibrated for low pitch and yaw angles. Further, nothing was showing that the probe could measure wind tunnel flow quantities with accuracy because there was nothing to prove that. Also, nothing was suggesting that the pitch and yaw angled could be extended or that the probe could perform differently in another flow field or regime.

2.10 Summary

Flow diagnosis is a common phenomenon in engineering applications, such as the wind tunnel flow, of hydraulic pipelines, gas turbines and jet engines, oil supply in pipes, etc. Analysis and

design process for such a system requires the velocities, pressures, and concentration of each phase in air and water flows or air-water two-phase flows. The measurement of fluid flow velocities and pressure in air or water systems is an area of significant research. Some areas of recent experimental techniques for measuring air and water flow parameters through complex geometries involve the use of Pitot tubes and multi-hole pressure probes with specific calibration methods and techniques. According to the literature review, despite all the progress reported over the years, these techniques and methods have their limitations that need to be improved to extend the use of multi-hole pressure probes to other kinds of fluid and flow systems. For example, a Pitot static pressure tube is mainly used for airflow applications and is limited to measure velocity magnitude only. Besides, there might be errors introduced in measurements if the Pitot-static pressure tube is yawed beyond 5º from the flow velocity vector.

The multi-hole pressure probe is a cost-effective, robust and accurate instrument for three-dimensional velocity and pressure measurements in a wide range flowfield. For steady-state measurements, the five-hole probe is capable of resolving flow angularities up to 75° and predict the flow conditions with high accuracy. Although powerful, measurement techniques such as Laser Doppler Velocimetry (LDV), Hot Wire Anemometry (HWA), and Particle Image Velocimetry (PIV) have some disadvantages compared to multi-hole pressures probes. Laser Doppler Velocimetry (LDV) and Particle Image Velocimetry (PIV) require the use of costly components, such as expensive lasers and optical equipment to obtain accurate flow measurements, and it is often hard to get good results outside the laboratory environment. Furthermore, these techniques require sophisticated hardware and software that need seeding, especially for optical measurements if particle levels are low and the inability to cope with significant levels of vibration due to the optics requiring careful alignment.

Since multi-hole pressure probes are intrusive flow diagnostic instruments, concerns of the probe interference with the flows it is trying to measure always arise. For instance, in the case of leading-edge vertical flows over delta wings, the presence of a pressure probe in the neighbourhood of the vortex core can influence premature vortex breakdown. Hence, there is a strong need to miniaturise the probe size, thus reducing interference. Furthermore, the probe size miniaturisation offers a high spatial resolution, for measurements in high-shear flows. Also, when measuring near a surface, a distance of at least four probes diameters should be maintained to avoid wall effects. However, pressure probe miniaturisation presents fabrication as well as frequency response challenges.

Regarding fabrication and manufacturing, the probe head surface quality is essential for accurate measurements. For two different calibration surfaces, smoother surface typically leads to higher prediction accuracies. The typical interpolation techniques use smooth continuous functions to model the calibration surface locally. The smoothness of the calibration surface depends on the head quality. Maintaining the same relative head surface roughness becomes a fabrication challenge as the probe diameter decreases.

In a different challenge, as the probe diameter decrease at the head, the tubing frequency response decreases. As the size of the probe is miniaturised in hope to reduce flow interference, the frequency response of the probe deteriorates. The decrease in the frequency response of the probe often causes an increase in the wait times in flow mapping experiments using the probe. The wait time is the time that the probe, after it moves to a new measurement location in the flow field, has to wait before data acquisition can be performed, for the pressure at the probe pressure transducers to reach steady state. However, deterioration of the probe frequency response limits its ability to resolve temporary flow information in unsteady flows. The probe requires to be calibrated before it can be used for flow measurements to overcome these limitations and those mentioned above, Numerous calibration, data reduction algorithms and procedures have been developed over the years for steady and unsteady flow measurements. One of the approaches relates the flow velocity magnitude and incidence angle to a theoretical model, such as a potential flow model. Based on the conceptual model, the pressure holes are related to the flow incidence and velocity magnitude. However, this method is not accurate especially for the small probe, where manufacturing imperfections are inevitable.

It would be disadvantageous if analytical procedures determined the calibration characteristics of a multi-hole probe. For hemispherical probes geometry, a potential flow solution can predict the pressure distribution and the corresponding calibration characteristics to reasonable accuracy. However, due to manufacturing inaccuracies and operating range and accuracy requirements encountered in the laboratory or flow field conditions, calibrations are required for probes of this simple geometry. For conical probes or prismatic geometry, analytical procedures of any type are difficult. These complex geometries, characterised by an abrupt change in contour, are subject to viscous effects, which are not modelled by current computational methods. Therefore, until now the only generally acceptable way of calibration is the conventional method of calibration that uses

complex computational mathematical equations to represent characteristics of the probe response to a known flow field.

For non-nulling operational mode, it is apparent that the calibration characteristic must include data that represent pressure difference in both pitch and yaw planes, as well as the difference between measured correct local total and static pressures. These pressure differences known as pressure coefficients must be defined so that they are independent of velocity and are a function of only flow angularity. Apart from the errors associated with complex computational mathematics, which limits accuracies in measurements, the current calibration and use of pressure probes for flow measurements have failed to capture full flow filed and meaningful results when stretched beyond the particular angles and fluid for which they are meant to measure.

Presently, the knowledge of multi-hole probes for measurement is limited to the conventional methods of calibration that define the probe to be used in one particular flow field because the probe cannot exceed its calibrated average velocity, pitch and yaw angles. Furthermore, because the conventional calibration method is subjected to cumbersome mathematics coupled with imperfections associated with miniaturised design and fabrications, it lacks the precision needed for effective and accurate measurements. However, with the advancement of knowledge and technology, it is now possible to develop sophisticated but straightforward calibration methods and techniques to measure flow field with larger flow angles with reasonable accuracies and precisions for optimum process operations at different flow rates.

Another practical option that could capture the full flow field of air or water with increased accuracy is the use of experimental calibration data integrated with computational fluid dynamics (CFD). This method increases measurement accuracy and extends the probe angle further thereby allowing it to measure flow parameter in three-dimensional flow fields, as seen in many process applications. A novel calibration method of a multi-hole pressure probe, other than what is currently available, would need to be developed, that will have direct application to the industry. With this, the multi-hole pressure probe will be able to measure flow velocities, and pressures in air and water flow with greater flow angles without limitations and with reasonable accuracy other than those presented in the works of literature.

Although there are several works regarding the use of the multi-hole probes pressure probe in various configurations such as a three-hole probe, four-hole probe, five-hole and seven-hole

pressure probes to measure properties of three-dimensional flows in multiple systems. However, it is still mainly being characterised by errors and measurement inaccuracies, and there has never been any study where CFD methodology has been integrated with experimental calibration study or any other method to extend calibration range and increase measurement accuracy in the wind tunnel measurement.

Until date, although many works have been carried to study the flow properties of air and water flows using various instruments to monitor the features of both media, there is minimal literature that has included evaluation of probe head effect on calibration and measurement accuracy. Use of combined experimental and numerical investigations to quantify the impact of shape is another facet of the present work that has a direct impact on design, development, and selection of pressure probes for a suitable application. Furthermore, calibration of multi-hole pressure probes for use in the wind tunnel and hydraulic pipeline flows has not adequately been measured. In many industrial applications, the pipe flows can be three-dimensional (flexible pipes, bends, helical pipes). The calibration for such work needs to be correctly developed.

The main area of the present research is the integration of experimental and CFD calibration methods of multi-hole pressure probes for flow measurement in wind and pipeline flow systems. Integrating the use of CFD with an innovative approach in the calibration of multi-hole pressure makes it possible to analyse different problems that are difficult and dangerous experimentally. The purpose of CFD in this study reduces time and money in the design of the new calibration methods as computers become more powerful for easier industrial applications

This research provides the possibility to simulate, generate pressures from the probes in pitch and yaw angle direction and generates graphs and contours that give an understanding of the results. Due to experiments constraints, data are collected at a limited number of locations within the experimental test sections, but CFD allows data to be collected at any place of interest within the flow domain, and interpret its performance through a set of flow parameters within the test sections. The Computational Fluid Dynamics (CFD) numerical simulations of the probes in this study introduced the opportunity to study data, compared data, and analyse data for different calibration conditions in both wind tunnel and hydraulic pipeline flows. The five-hole pressure probes designed and fabricated in this study are cost-effective, easy to be applied to fluid flow systems, and possess simple algorithms of data acquisition and analysis.

Chapter 3 Experimental Apparatus and Instrumentation Setups

The study of five-hole pressure probes requires many pieces of equipment and Computerized Data Acquisition Systems (DAQ). The following sections describe the detailed design of the probes, the construction, and calibration of the experimental apparatus that have been used in this research study and the setup and verification of the DAQ systems.

Two primary facilities are required to carry out the calibrations and measurements using a five-hole pressure probe. These are Wind tunnel airflow facility for external flow experiments, and water single-phase loop for pipeline flow experiments. On these facilities, several reference measurements devices are used including manometer for measuring air flow velocity (from pressure values), turbine meters for measuring liquid (water) flow rate, and data acquisition for acquiring data from the probes and reference measurement devices. Furthermore, to accurately position the probe in the wind tunnel and pipe, and move them to predetermined positions, a traverse mechanism is used. The next sections describe all these setups and their functions in detail.

3.1 Experimental Methodology

The methodologies used in the calibration of the five-hole probes are described in the following sections.

3.1.1 Probe Development and Fabrication

Typically, for local measurements, the probe diameter range used is about 5mm. The construction of the probes was carried out in two phases, the fabrication of internal features and external features. The external elements define the geometry of the probe in the flow domain, whereas the interior elements define the pressure tubes that transmit pressure from the probe head to the pressure transducers from which the data are collected Wysocki, M., & Drobniak, S. (2001). Figure 3.1 depicts the physical structure of a five-hole pressure probe.

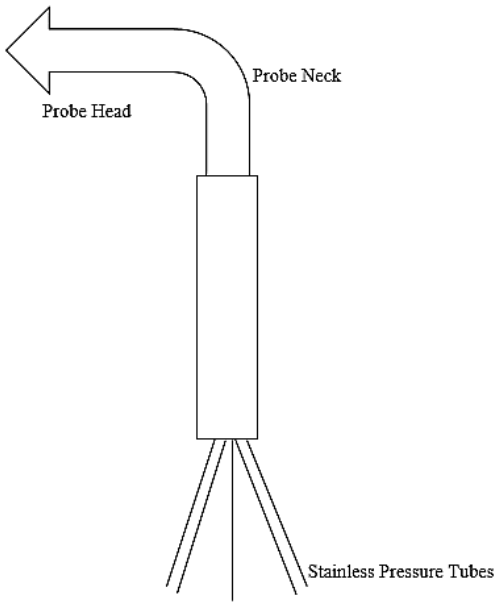

Figure 3.1. Schematic layout showing physical parts of the five-hole pressure probe

The external features of the probe comprise the head, which is made of brass, but the smallest tubes (1.5mm in diameter) inside each of the probe hole for pressure transmission to transducers are made of stainless steel. Three parameters define the probe head geometry and features; these are the diameter, which is 5mm, the shape (conical and hemispherical heads), and the pressure holes (5 in number in each probe head). The first section (Base part of L section probe, Figure 3.2) to the probe precisely matches the outside diameter of the probe head and is typically up to 20mm widths long

Rex Klopfenstein Jr. (1998). If there is a need, further extensions can be added to the probe stem to create a very long probe for particular applications like the case of the current investigation. The probe is mounted on a mechanism to allow it to rotate corresponding to yaw and pitch angles Seshadri, V., Gandhi, B., & Singh, S. (2001).

The two different head shapes used in this study are the 45° chamfer cone and the hemispherical shape. The head shapes are depicted in schematically in figure 3.2. The head shapes are depicted as constructed in figure 3.3.

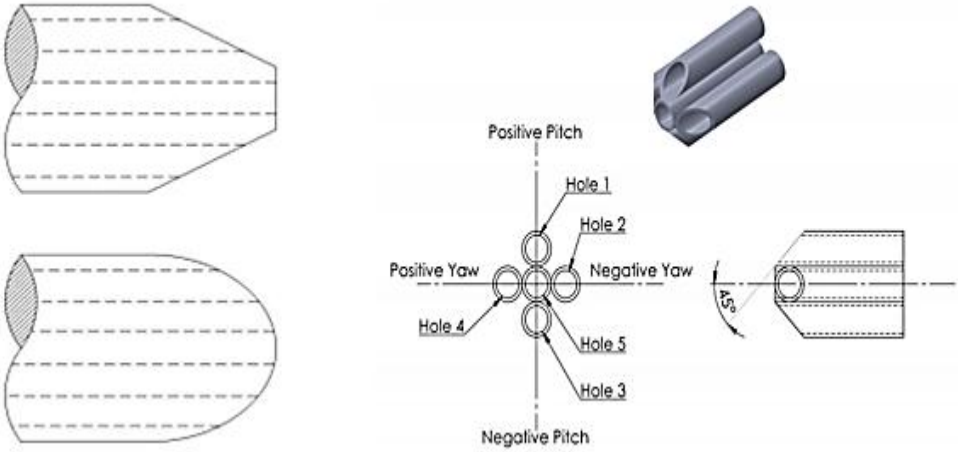

Figure 3.2. Schematics drawing of conical and hemispherical probe heads

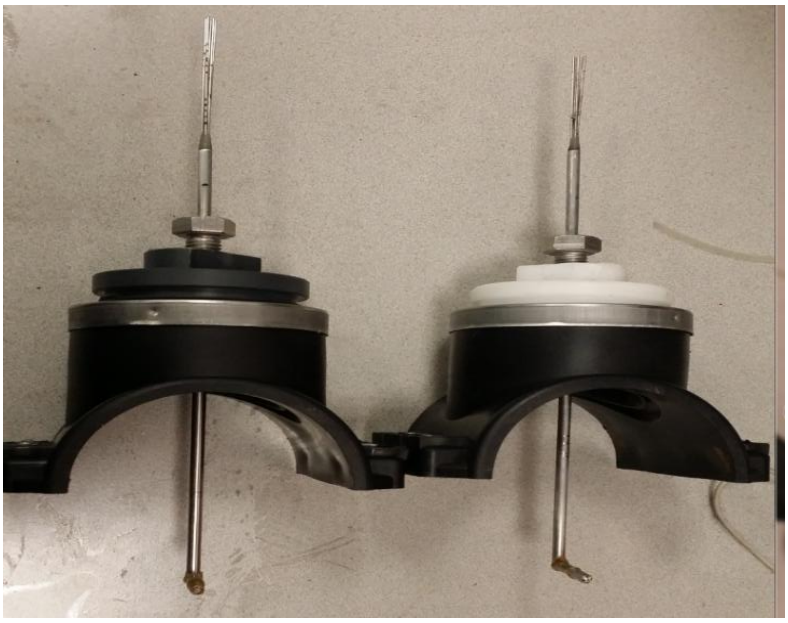

Figure 3.3. Assembly of conical and hemispherical heads five-hole pressure probe

The calibration of the five-hole pressure probe requires an orientation mechanism that enables rotation of the probe about its head in two planes perpendicular to each other. The probe orientation mechanism allows ±25° for pitch and yaw rotation inside the test section.

3.1.2 Experimental Apparatus

The three main pieces of equipment used in the present study are the wind tunnel, flow loop, and the rotary traverse. The wind tunnel and the flow loop are used to generate calibration flow, while the rotary traverse is used to position the probes at known angles to the stream.

3.1.3 Calibration Wind Tunnel Flows

Pneumatic pressure probes are useful tools for multi-dimensional velocity measurements. With recent developments in measuring and sensing equipment, high-resolution electronic sensors are readily available for transduction of physical quantities like pressure and temperature. These sensors replace the original measuring equipment like multi-tube manometers that limit the sensitivity and accuracy of the multi-hole pressure probe. Measuring instruments are no longer a

bottleneck for the effective implementation of these instruments. The accurate measurement of velocity and its direction now requires the optimisation of the design parameters of these probes.

The optimisation of pressure probes is complicated because it involves repeated design and testing of some geometric parameters such as the diameter of the probe head, the shape of the head, the shaft size, the shape of the shaft and the distance between the probe head and probe shaft. This process has been numerically analysed by studying the flow field in and around the probes to contributed to the effective design and fabrication of the probes. The resulting geometric modifications significantly increased the sensitivity and accuracy of the pressure values measured during the calibration process as well as the use of probes for measurements. This work led to the choice and types of multi-hole pressure probes used in this research study.

3.1.4 Flow Description

The wind tunnel was set in operation and allowed to run for at least ten minutes before data collection was initiated from the probe to ensure that transient start-up effects and mild aerodynamic heating of the internal components would not influence airflow. Furthermore, the probe traverse system is moved in a single step in each angular direction to ensure that polarity is set correctly for the first calibration setup and to ensure each procedure of the calibration processes work perfectly for the experiments (Figure 3.4).

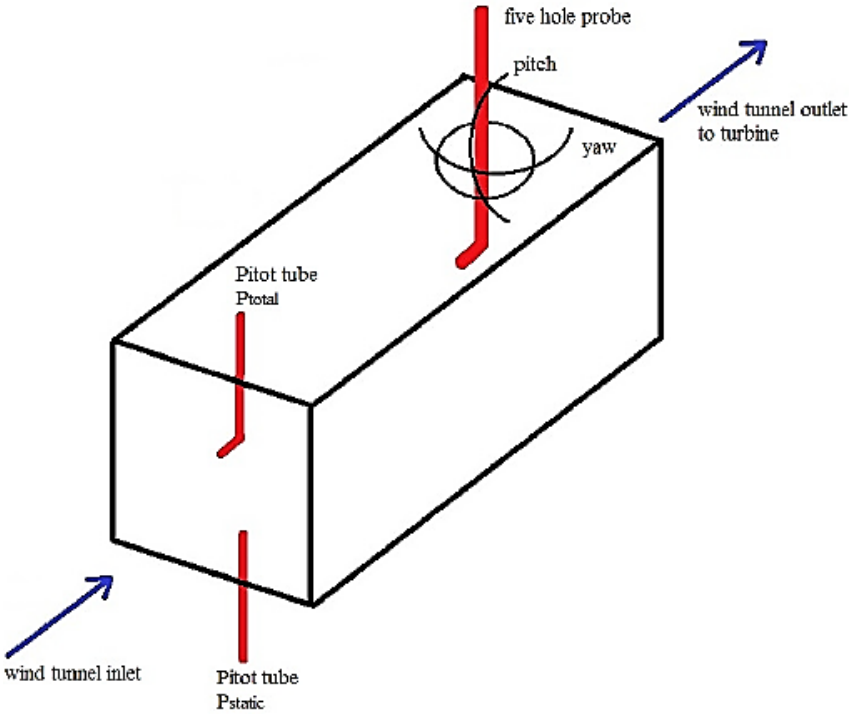

Figure 3.4. CAD schematic of the wind tunnel experimental setup

The performance of the five-hole pressure probe with four holes symmetrically placed on the surface and one at the tip for conical and hemispherical probes are calibrated in a three-dimensional airflow on an open circuit subsonic wind tunnel. The difference in total and static pressures of the flow using Pitot tube pressure tapping installed on the top and bottom walls of the wind tunnel test section produced dynamic pressure that was then used to calculate the velocity magnitude of the flow. The five-hole pressure probe calibrations were carried out at a constant magnitude velocity of 15m/sec, the same inlet velocity for wind tunnel CFD simulations.

A proper reference position in the test section of the wind tunnel is required to generate the correct calibration charts, and it is the position at which the centreline of the probe head should be aligned parallel to the oncoming flow direction to correct the misalignment errors. After the scale is set to this position, the pressure reading from the sides holes are measured, and the probe orientation is changed until these readings are equal to each other. The pitch and yaw angles of the probe are incremented by 5^{o} increments in the range of $\pm 25^{o}$ using the probe orientation mechanism. The pressure sensed by the probe holes is separately recorded for each pitch and yaw angle setting given to the probe concerning its position. The reference position of the probe is maintained throughout the calibration, and it was taken as zero position for the yaw and pitch angles. The flow field in the wind tunnel is constant and known throughout the investigation Vijay, R. (2004).

3.1.5 Wind Tunnel Instrumentation

Figure 3.5 depicts the instrumentation design of the DAQ systems used in acquiring pressure data from the pressure probe. The DAQ instrumentation includes a data acquisition device and seven pressure transducers electronically connected to the DAQ devices responsible for obtaining datasets.

3-5(a). Inside view of the DAQ Systems

3-5(b). Outside view of the DAQ System

Figure 3.5. Data acquisition (DAQ) systems design

This DAQ system is connected with other electronic devices, which includes the digital multimeters that give the real pressure values measured by the probes while the DAQ device interpreted the analogue data into digital data and sent to a computer. A complete instrumentation setup for pressure datasets measurement in the wind tunnel is depicted in figure 3.6.

The probe is mounted facing the stream direction at the pitch and yaw angles of 0° inside the wind tunnel test section to measure pressure datasets. Furthermore, a Pitot tube mounted in the wind tunnel test section is needed to measure the dynamic pressure of the flow was installed at a distance of 100mm from upstream of the test section, while the probe is located at the centre of the test section at a distance of 500mm from the Pitot tube within the test section.

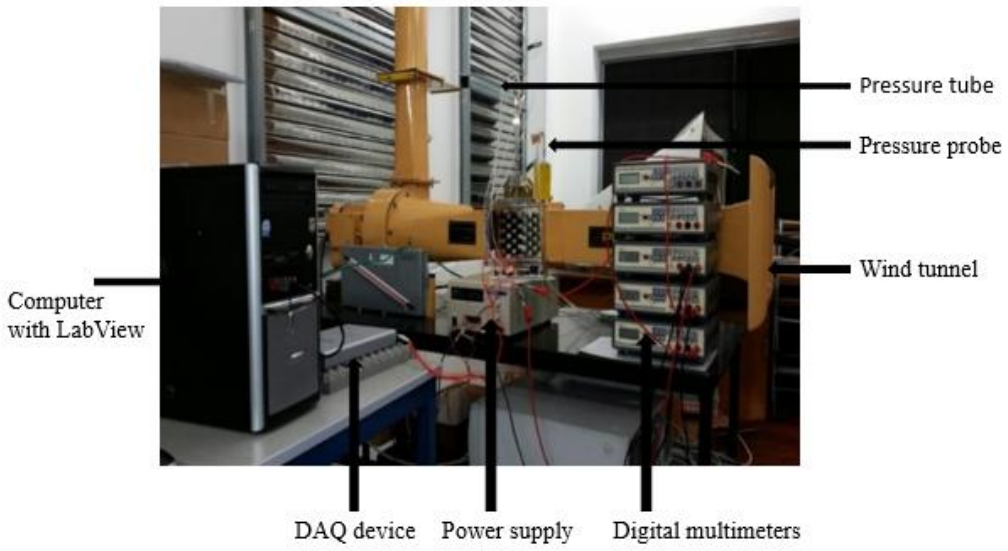

Figure 3.6. Instrumentation experimental setup at the University of Huddersfield wind tunnel laboratory

Figure 3.6 depicts the instrumentation facilities for the calibration and experimentation of five-hole hemispherical and conical head pressure probe in the wind tunnel flow is the experimental set up used in this study. The main component of the experimental set up includes a wind tunnel with an air supply, a contraction cone, and a straight test section. Others include a 5V amplifying circuit (see figure 3.5a) systems that measure and transmit pressures from the transducers and data acquisition system. These systems allow for removal and electrical testing of individual transducers. The circuits systems each have fewer wirings, which reduces electrical line loss and resistance. The circuits never resulted in any problems, which makes the whole system very robust for the study. The calibration is carried out in the air coming from the test section. Ambient air is used as a flowing fluid during the calibration.

3.1.6 Wind Tunnel Manual Rotary Traverse

A rotary traverse capable of positioning the probes at known flow angles has been constructed and installed in the wind tunnel. The angular resolution of the calibrator is 1.5° per step in pitch angle and 0.5° yaw angle. The assembled rotary traverse and the probe is depicted in figure 3.7, while figure 3.8 depicted the probe fixed in traverse and mounted on the wind tunnel.

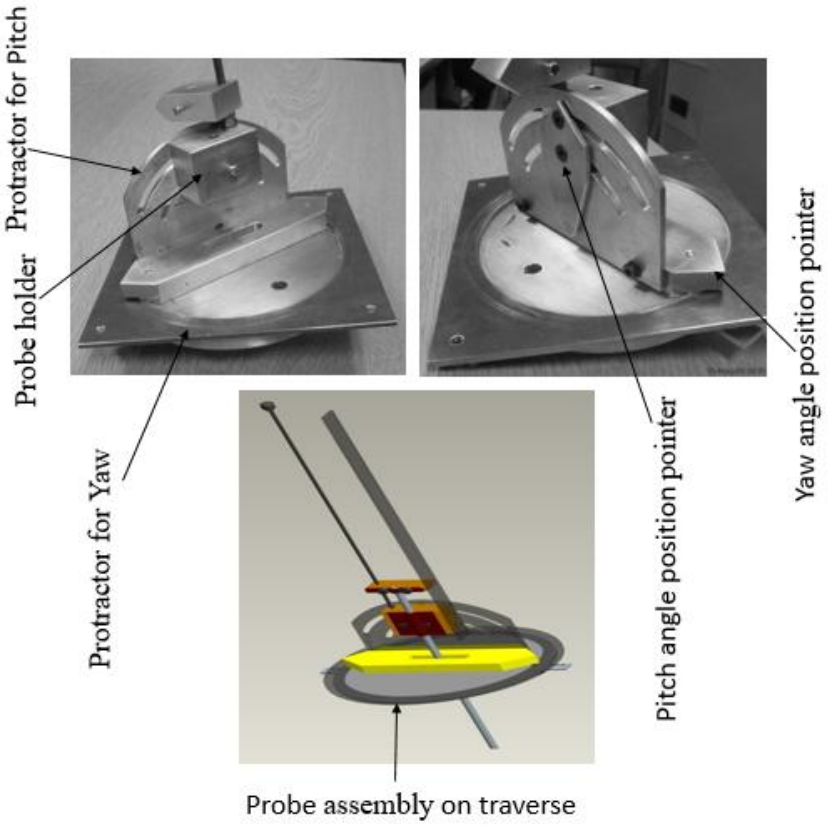

Figure 3.7. Side view of the probe traverse system

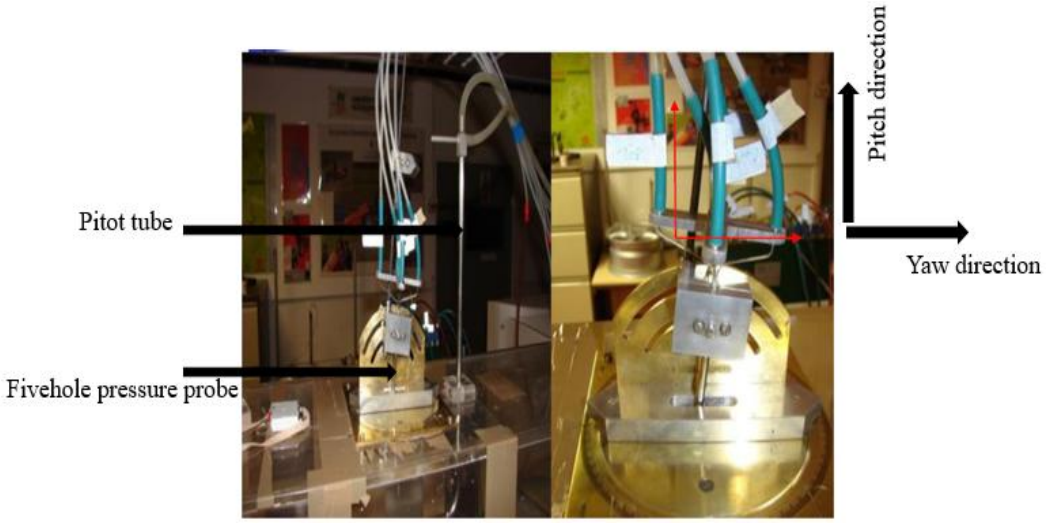

Figure 3.8. Five-hole pressure probe fixed on traverse mounted on the wind tunnel at Huddersfield wind tunnel laboratory

Figure 3.8 depicts the traversing mechanism of the probe mounted on the test section. The probe was adjusted in a way that the head of the probe was located at the intersection of the pitch and yaw axes of rotation to allow the probe position relative to the wind tunnel was kept constant, and any

non-uniformity in the exit velocity profile was reduced. With this mechanism, the manual rotations of the probe in different pitch and yaw angle directions are possible. At each pitch angle, the probe rotates to a particular yaw angle position, and the probe returns five pressure measurements. After that, it rotates to another yaw angle position. This process repeated for seventeen yaw measurements at each pitch angle position.

3.2 Experimental Methods for Pipe Flows

A conveniently accessible part of the pipeline has been selected preferably, where there is a straight horizontal section at least 500mm downstream from any obstruction, bend or section change. The first step of the pipeline is to design a probe traverse mechanism that meets specifications and allows rotation of the probe in its axes. Figure 3.9 depicts this mechanism.

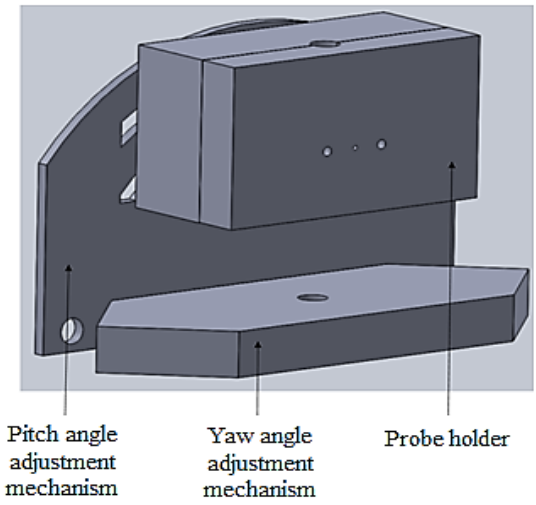

Figure 3.9. Yaw and pitch angle rotation mechanism

Figure 3.9 depicts a traverse mechanism that allows for yaw and pitch setter fabricated from metallic strips and has two degrees of freedom. It can rotate in clockwise and anti-clockwise directions at a fixed pitch and yaw angles. A combination of yaw and pitch can be set between $\pm 25^{o}$ as required in the pipeline with the help of the setter mechanism. There are two parallel holes drilled in the rectangular frame of the yaw movement device in which the probe is inserted into; this allows the probe to be tightened and held firmly. The yaw and pitch setter mechanism is further mounted on a subset of traverse mechanism that allows for a 360^{o} rotation. Figure 3.10 depicts this pitch and yaw setter mechanism.

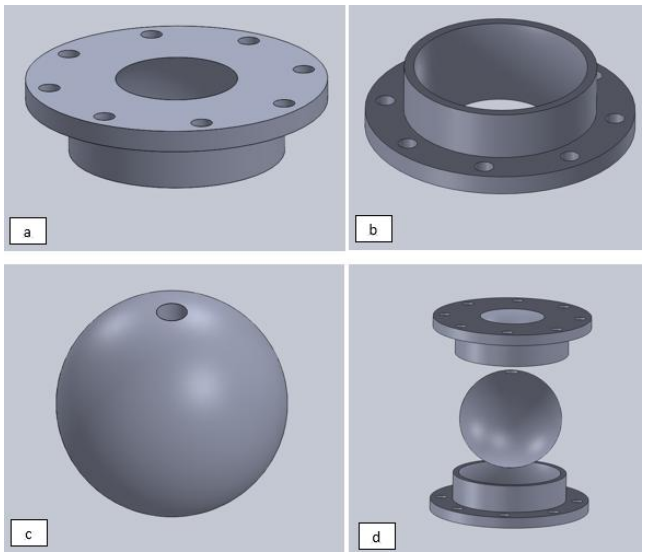

Figure 3.10. Probe traverse mechanism (a) top flange (b) bottom flange (c) rotating sphere and (d) assembly of the traverse mechanism

The transverse mechanism positions the probe on pitch and yaw directions during calibration and experimental investigation. The two flanges consist of a base that holds the sphere on each side. The flanges allow the sphere to rotate in clockwise, anti-clockwise and vertical directions to make a 360^{o} movement that allows the yaw and pitch setter to rotate the probe in desired directions. The traverse mechanism is finally tight fixed on the double clamp saddle as shown in figure 3.11.

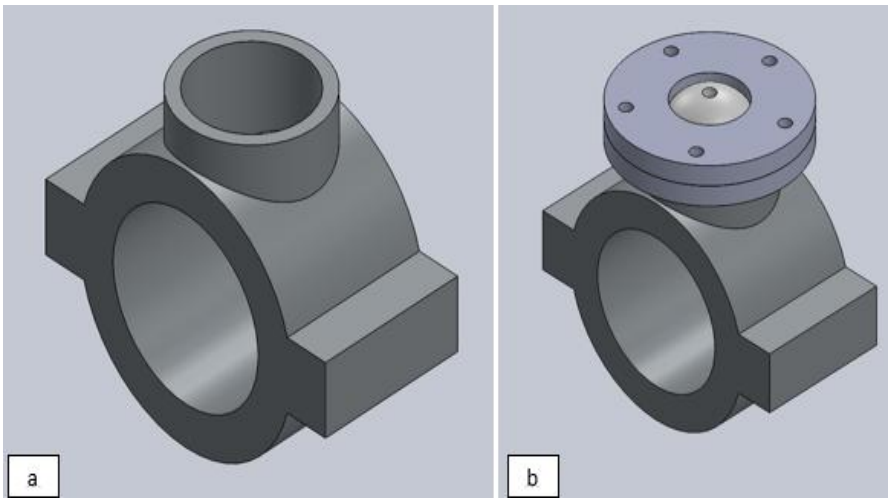

Figure 3.11. Traverse mechanism fixed in double clamp saddle (a) double clamp saddle (b) traverse mechanism tight-fixed in double clamp saddle

This traversing system where the hydraulic pipeline investigations took place using the conical and hemispherical head five-hole probes is shown 3.11(b). The section is tight fixed on the 101mm

radius, 1800mm long hydraulic pipeline and allow for probes to be moved pitch and yaw planes as shown in figure 3.12.

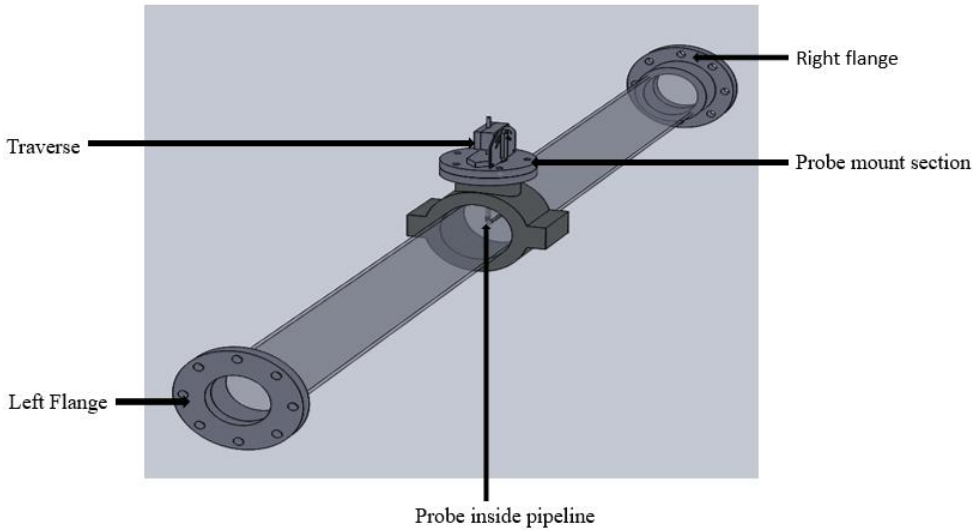

Figure 3.12. CAD diagram of hydraulic pipeline calibration setup design

The orientation mechanism contains an O-ring that prevents water leakages. The probe is positioned in a way that allows its head at the centre of the pipeline section far from the pipe walls to minimise boundary layer and pipe wall effects. The calibration device has provisions to change the pitch and yaw angle in the range of $\pm 180^{o}$ at an interval of 5^{o} .

3.2.1 Pipeline Flow Description

A proper reference position in the test section of the pipeline flow is required to generate correct calibration charts as well as to make correct measurements at different angular positions inside the pipeline. The reference position is at the position in which the probe head is aligned parallel to the oncoming flow direction inside the pipeline. This choice was to facilitate calibration process, compensate and correct pitch and yaw misalignment errors. After the scale is set to this position, the pressure reading from the sides (pressure hole 1 and pressure hole 3) and (pressure hole 2 and pressure 4) were measured and the probe orientation was changed until these readings were equal to each other. These angular positions are set as the reference position of the probe. Figure 3.13 depicts the full details of the pipeline test section.

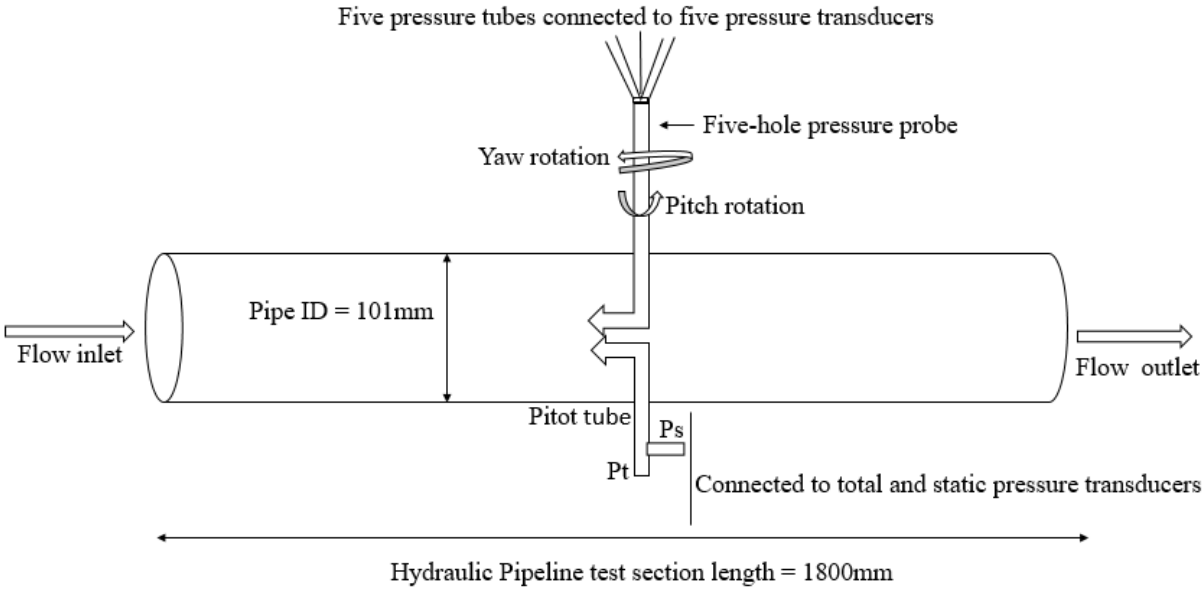

Figure 3.13. Hydraulic pipeline flow experimental design

Figure 3.13 depicts the full experimental section of the pipeline flow. The flow magnitude velocity in the pipeline was set at a constant velocity of 2.12m/sec, which is the highest velocity of the hydraulic pipeline flow measured using a Pitot tube. It is the same inlet velocity used for CFD simulations as explained in chapter 4. The Pitot tube as depicted in figure 3.13 above was used to resolve the velocity magnitude by measuring the total and static pressures of the flow and then applying the Bernoulli equation to obtain the velocity magnitude. The Pitot tube is located directly opposite the five-hole pressure probe head; this is to ensure that the velocities measured by both the five-hole probe and the Pitot tube have reasonable correlation and accuracies.

The reference position of the probe was maintained throughout the calibration, and it was taken as zero position for the yaw and pitch angles. The probe angles are set at 5^{o} increments in the range of $\pm 25^{o}$ and pressures sensed by the probe at each angle was separately recorded and stored for further data processing using the probe orientation mechanism.

3.2.2 Pipe Flow Facilities and Instrumentation

The first thing required before collecting data has been to carry out a bleeding process in the entire test section, which involves injecting air out of the pressure transducers and internal holes of the probe and pressure transmission tubes connected to the probe and the transducers.

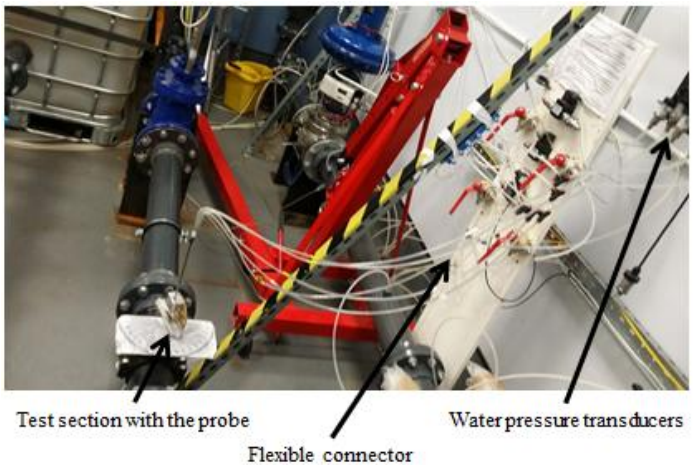

Figure 3.14. Bleeding system set-up at the University of Huddersfield fluid laboratory

Figure 3.14 depicts the bleeding system. The sole aim of installing the bleeding system is to inject air out of the tiny pressure tubes, making sure they contain flowing water at every measurement for accurate data collection. This process requires an eight-channel manifold; one channel of the manifold is connected to the tap using a flexible transparent plastic tube to supply water to the system. The other remaining five circuits of the manifold are connected to the five pressure transmission tubes and interlinked with the pressure transducers. The remaining two circuits are connected to the Pitot tube static and total pressure taps. When the water tap opens, water travels through the transparent plastic tube to the manifold, and the manifold distributes the water to its seven channels and flows into the pressure transmission tubes and the transducers thereby flushing any air in the pipes down to the pipelines. Figure 3.15 depicts the setup of the pipeline flow experiments.

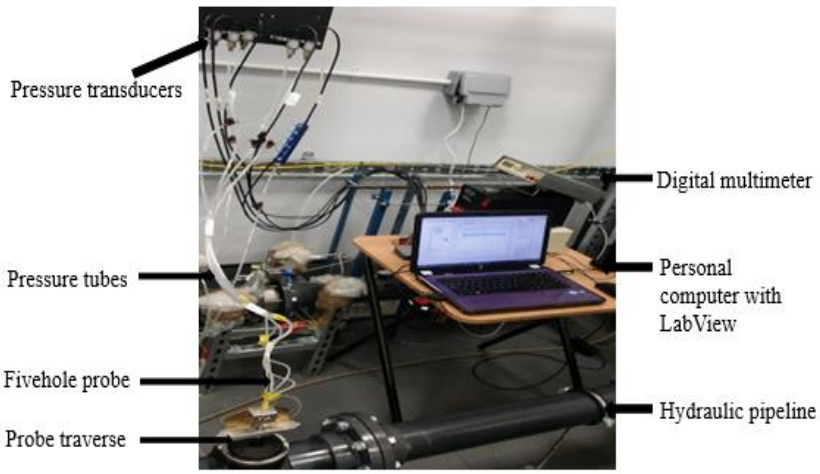

Figure 3.15. Hydraulic Pipeline calibration setup at the University of Huddersfield fluid laboratory

Figure 3.15 illustrates the experimental set up used for the hydraulic pipeline flow study. The main components of the experimental set up include seven pressure transducers, a personal computer with all the necessary software installed, a water supply tank, and the flow control arrangement within the flow loop. The test section and the water tank are made of plastic. The straight test section is made of a transparent straight PVC pipeline. However, their calibration is carried out inside the pipeline with flowing water from the water tank to the test section. Seven single ended pressure transducers were used in the pipeline flow investigations as depicted in figure 3.15. Five transducers were connected to the five-hole probe to measure and return pressure values. The other two transducers were connected to the Pitot tube to measure and return pressure values from the Pitot-static probe. The output of each pressure transducer is connected to the input channels of the Data Acquisition (DAQ) device. The DAQ input is connected to the computer through a USB cable which is used for data collection from the flow, stored, processed and analysed using a LabView programme.

3.3 Data Acquisition

The Data Acquisition (DAQ) device converts the analogue pressure data measured by the transducers into a digital data and transmits it to the computer installed with a LabView platform where it is stored for further processing and analysis. The Data Acquisition (DAQ) used for this investigation is the National Instrument (NI) USB-6002, a full-speed DAQ USB device with eight single-ended analogue input (AI) channels. It also contains 2 analogue output (AO) channels, 13 digital input/output (DIO) channels, and the 32-bit counter. The DAQ board had a resolution of 14-bit and a maximum sampling rate of 100 KS/sec. It has 0-50V allowable input voltage range Vijay, R. (2004).

The DAQ cable provides access for the pressure holes and Pitot tube having numbering systems (P_0, P_1, P_2, P_3, P_4, P_5, and P_6) to the computer. The negative channels have common ground, and the output pins are connected through pressure transmission tubes to the five-hole pressure probe using pressure transducers. The computer programmed processes and analyses the dataset using LabView software program developed and used to control and monitor the activities of the calibration process Vijay, R. (2004).

3.3.1 Calibration Procedures and Data Collection

This section outlines the methods and procedure that was followed for each step of data collection and analysis during the calibration. It includes experimental procedures, computational sequences, and method of error checking, verification, and validation. Furthermore, the sources and estimation of experimental errors and discussed in this section. The collection of preliminary data requires many steps. The following sections explain the detailed procedures that have adopted and followed when collecting raw calibration data from the probes Samantha, S., Alex, T., & David, M. (2014).

3.3.2 Probe Alignment and Connection to Data Acquisition

The five-hole pressure probe was installed in the calibrator of both wind tunnel and flow loop and show in figure 3.5 and 3.7. Many adjustment features of the rotary traverse allowed the location of the probe head to be adjusted to be an intersection with pitch and yaw axis of rotation; this enables the probe head not to translate as it is rotated. Error in the probe head location was estimated as ±0.5mm in the X and Y directions. However, the effect of this error has been ignored because it would not affect the movement of the probe slightly at a different position on the outlet. The velocity gradient at the probe location was minimal enough to neglect the associated error Simon, W. (1990).

Once the probe was installed in the traverse, the traverse was then aligned with the flow. The traverse was positioned such that the probe head was within the wind tunnel plane. The probe was position in such a way that it brought the pitch axis of the probe parallel to the outlet plane. A flat plate-like metal was placed against the wind tunnel, and the traverse was rotated until the yaw axis was parallel to the outlet plane. Once the traverse was aligned, it was then secured with a metal lock. The error in this alignment procedure was about ±0.3° in both pitch and yaw directions Castorph. D., & Raabe, J. (1994).

After aligned the traverse, the probe was connected to the DAQ system. Silicon tubing was used to connect the stainless pressure tubes on the pressure tube side to the pressure transducers. The tubing was connected to the probe, and compressed air is used to blow any condensation out of the lines for the wind tunnel experiment, and water for the hydraulic pipeline experiment. An eight-pressure line was connected to the static hole on the Pitot-static tube to enable collection of reference static pressure data. Once the probe and the static tube were connected to the pressure transducers, the

pressure transducers were read, and the pressure-recorded pressures were taken to be zero offset for the transducers. That reference pressures were used to correction factor that was used to correct all subsequent measurements Akshoy, R.P., Ravi, R.U., & Anu, J. (2011).

3.3.3 Calibration Grid Requirement and Generation

A LabView program was written to control the position of the traverse to accept a sequentially ordered list of pairs of pitch and yaw angles that define the calibration grid. Programming code in LabView was developed to generate these grids. These grids are uniform in pitch and yaw angles. The grid is a function of two parameters, grid spacing, and maximum pitch angle. The grids are generated by moving through the yaw angle from 0° to the defined maximum pitch angle, stepping in the increment of 5°. At each fixed pitch angle, the yaw angle was rotated from ±25°, with 5° increment.

Once the list of the point to be measured had been generated, the list was sorted to minimise the number of movements performed by the traverse. The incremental nature of the calibration means that at low flow angles, a few names of points were duplicated. Duplicated points occurred when a desired progressive change in roll angle translated to less than a full step change in pitch and yaw angles. These duplicated points were taken out from the calibration grid during the sorting process.

The final step in generating a calibration grid, also known as calibration map was to add a number of the point where the traverse would return to 0,0. These reference measurements were necessary for two reasons. Firstly, they were used as a reference point of position during the calibration procedure to visibly confirm that no steps were skipped and that the traverse was returning to precisely 0, 0 at each time. Secondly, they were used to establish the total reference pressure of the flow. With the probe at 0, 0 the probe was aligned with the flow, and the pressure at the measured at the centre hole was the total flow pressure. This measurement process was repeated many times during the process of calibration to ensure that the flow was steady and to reduce random transducers error related to the reference measurements. The result of this process is a map that was uniform in pitch and yaw angles as shown in figure 3.16. The grid has a maximum angle of 25° in pitch and yaw angle axes and a grids spacing of 5°.

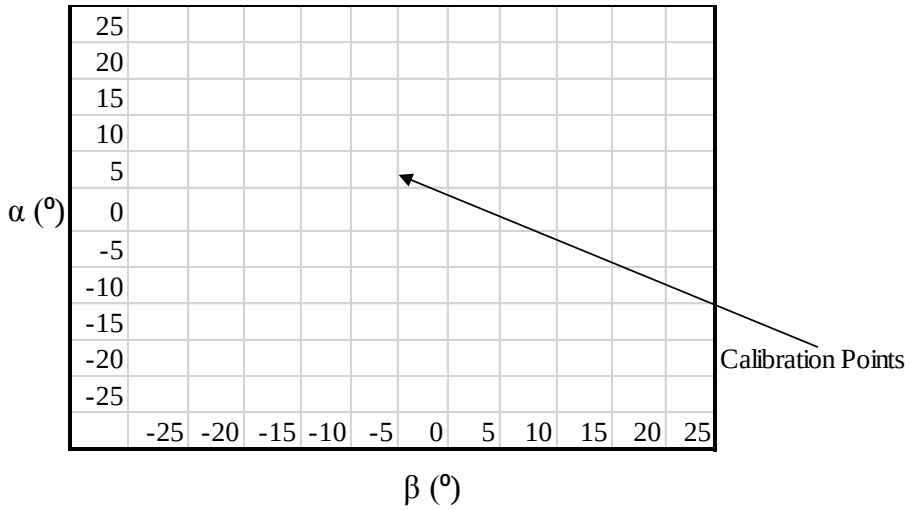

Figure 3.16. Sample calibration grids

The calibration grid shows that a total of 121 calibration points is required to be measured by each probe in a particular calibration that was carried out. The angular range of each probe inside the tunnel and hydraulic pipeline corresponds to traverse in the region of $\pm 25^0$ for both pitch and yaw in this present investigation to exceed the normal flow angle considerably. An increment of 5^0 step was chosen as the resolution for varying the pitch and yaw angles. With other processes seen in the literature, this is common Akshoy, R.P., Ravi, R.U., & Anu, J. (2011).

3.3.4 Operation and Automated Data Collection Setup

The wind tunnel and flow loop were run for at least 20 minutes before data were collected to ensure stabilisation in all the systems, and ensure transient start-up effects and mild aerodynamic and hydrodynamic heating of internal components did not affect the flows. With the flow system warmed up, and the traverse initialised, the automated data collection process was started. After that, the process in figure 3.17 was followed. Figure 3.17 depicts the algorithm of the software development flowchart for the five-hole pressure probes calibration.

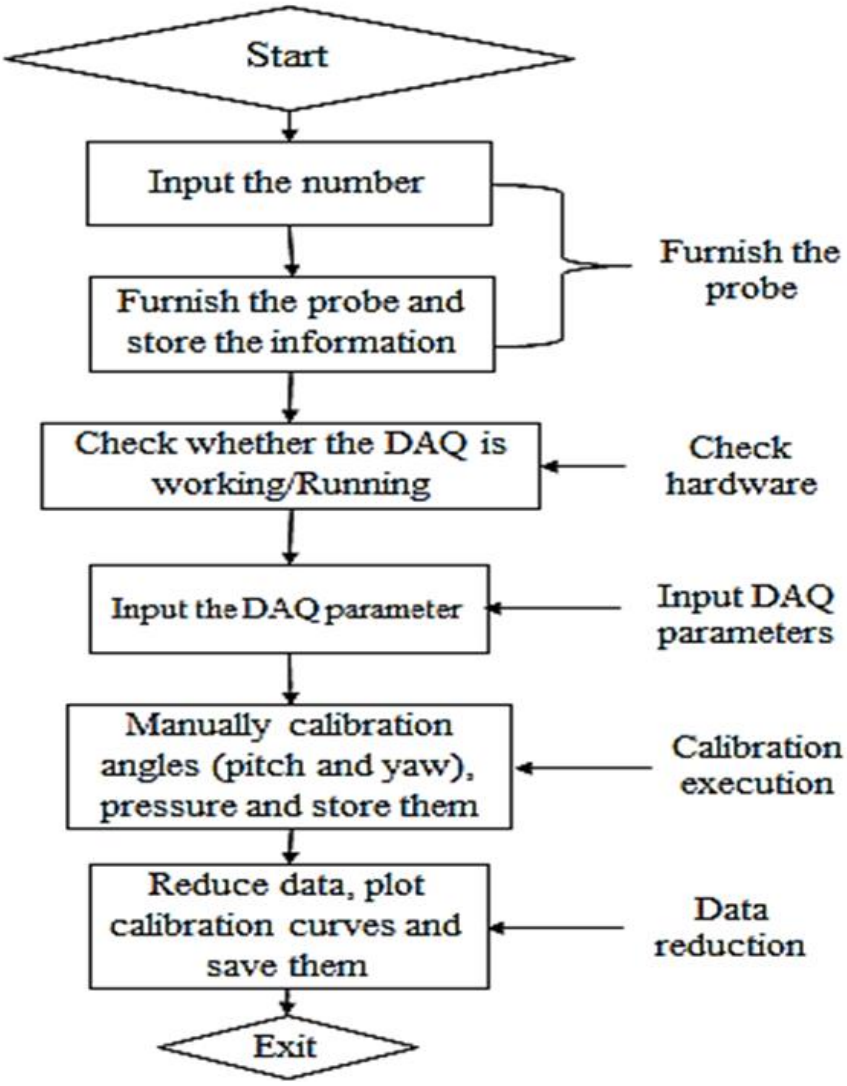

Figure 3.17. Operation of automated data collection procedure based on LabView

LabView platform provides access to software development. LabView is a flexible and user-friendly graphics software program. The stages of the calibration procedure to go through developed for this research study include furnishing the probe, checking the hardware, entering DAQ inputs, executing the calibration and analysing calibration data.

Furnishing the of the Probe

To provide the probe is the first step in the calibration process. This step is to make the probe ready for calibration by entering the necessary information such as the probe type, pressure tap numbers, and angles. It happens once at a time, and this information is stored and during the latter part used to run the LabView program.

Check the Hardware Operating Condition

Before calibration, it is proper to ensure that the probe, the pressure transducers, DAQ device and the computer among other hardware systems communication are operating as required. In this stage, the software judges whether the hardware is performing as expected. Any error in the setup alerts the user by displaying error information on the front panel environment and give instructions to solve the problem.

DAQ Input Parameters

The pressure signals from the transducers as assigned to the DAQ channels displayed on the software platform accordingly. The pressures according to pressure taps 0,1, 2, 3, 4, 5 and 6 has channels numbers assigned as A_0, A_1, A_2, A_3, A_4, A_5 and A_6. The sampling time and frequency are the only common parameters in the calibration of the five-hole pressure probe, and they are set at 1kHz and 1second respectively.

Execution of the Calibration Process

When the five-hole pressure probe is ready for implementation, the angle range of the pitch and yaw angles (α and β) are decided and manually inputted accordingly to furnish the calibration process. At each angular position, the pressures of each hole (P_1, P_2, p_3, P_4, and P_5) are acquired by the DAQ device, and the given pitch angle α and yaw angle β are recorded.

3.4 Generation of Calibration Maps

After collecting data by the probes, the calibration dataset for each sector containing the calibration for all the points that fell into various sectors. The next was to generate a unique set of polynomial coefficients for each sector. The methods and approaches used in the ways are described in the following sections.

3.4.1 Calibration Data Sorting using Sector Scheme

The sector technique divides the entire calibration zone into five parts, one central sector, and four side zones. The zones are chosen based on the highest pressure sensed by the holes, for example, when the centre hole senses maximum pressure, one zone is taken. The first step is to determine the pressure hole that gives the maximum reading and according to the identified sector where the

probe lies. While calibrating the value of P_s and P_t are recorded, and $C_{\alpha,}$ C_β ,$C_{Pstatic,}$ and C_{Ptotal} are thereby calculated for each zone. A full sixth order multiple regression analysis model with two independent variables, $C_{\alpha,}$ C_β, which would predict four different variables ($C\alpha$, C_β, $C_{Pstatic}$, and C_{Ptotal}) depending on the coefficient set selected. The multiple regression model predicts the flow angles α and β explicitly but predicts the static and total pressure implicitly via a pressure $C_{PSTATIC}$ and C_{PTOTAL}, which are defined in each zone. This method of sector division reduces errors because of extrapolation. The sector demarcation angles are chosen such that the zones overlap example, hole 1 is maximum within yaw angles of ±10º at a pitch angle of -3º . The actual data prediction equations for the multiple regression model are defined in section 3.4.5 Akshoy, R.P., Ravi, R.U., & Anu, J. (2011).

The raw calibration data was read line by line in the excel file according to holes of the probes, and sorting criteria are applied to determine the sectors that the calibration data belong. A calibration data would be included in a given sector if the pressure hole of the probe read the highest pressure at a particular given pitch and yaw angle. The warning was that a set of checks must be performed on the data to make sure that the flow in low angle flow, the flow was attached over all the peripheral holes, and in high angle flow, the flow was attached over the centre hole.

The sectoring of pressure data is best represented by the hole of the pressures that recorded the highest pressure. The preliminary calibration datasets are plotted against pitch and yaws as depicted in figure 3.18 and 3.19 for the two tested probes in wind tunnel and hydraulic pipeline.

β (°) \ α (°)	-25	-20	-15	-10	-5	0	5	10	15	20	25
25	4	1	1	1	1	1	1	1	1	1	2
20	4	1	1	1	1	1	1	1	1	1	2
15	4	4	1	1	1	1	1	1	1	2	2
10	4	4	4	1	1	1	1	1	2	2	2
5	4	4	4	5	5	5	5	5	2	2	2
0	4	4	4	5	5	5	5	5	2	2	2
-5	4	4	4	5	5	5	5	5	2	2	2
-10	4	4	4	5	5	5	5	5	2	2	2
-15	4	4	4	3	3	3	3	3	2	2	2
-20	4	4	3	3	3	3	3	3	3	2	2
-25	4	3	3	3	3	3	3	3	3	2	2

Figure 3.18. Preliminary sample calibration sector map generated using a conical probe

Figure 3.18 and 3.19 shows the pitch and aw angle map of sectors chosen by the calibration scheme. The symbol indicates the hole is registering the maximum pressure. The flow angle α and β are taken within ±25. The figure also shows the range of α and β for various sensing holes of the probe. It shows that the top hole (sector 1) covers the most range of α and β among all other holes (sectors). However, at higher angles of α and β the four peripherals holes (sectors) are likely to sense the total pressure, and therefore, the pressure detected by the holes at their locations is maximum. Also, the centre hole or the other holes in this position will become stalled. Figure 3.18 and 3.19 shows that there is an increasing pressure as the holes of the probe is oriented to the flow. Similarly, the curvature of the calibration grid increases as the pressure increases, since the flow is more directly into the hole and exhibit greater dependence upon the inclination of the hole concerning the mean flow.

β (°)	-25	-20	-15	-10	-5	0	5	10	15	20	25
25	1	1	1	1	1	1	1	1	1	1	1
20	4	1	1	1	1	1	1	1	1	1	2
15	4	4	1	1	1	1	1	1	1	2	2
10	4	4	4	1	1	1	1	1	2	2	2
5	4	4	4	5	5	5	5	5	2	2	2
0	4	4	4	5	5	5	5	5	2	2	2
-5	4	4	4	5	5	5	5	5	2	2	2
-10	4	4	4	5	5	5	5	5	2	2	2
-15	4	4	3	3	3	3	3	3	2	2	2
-20	4	4	3	3	3	3	3	3	3	2	2
-25	4	3	3	3	3	3	3	3	3	3	2

α (°)

Figure 3.19. Preliminary sample calibration sector map generated using a hemispherical probe

The error in the boundaries of the calibration map was because of flow unsteadiness and transducer error, as the probes measure pressures in the peripheral holes become equal, transducer uncertainty or little uncertainty in the flow could lead to overlapping in the calibration sector map. This noise shows that there was a need to ensure that the calibration of multi-hole pressure provides results beyond its expected extent. The method that was used to improve the calibration of the results to the degree of each calibration validity.

3.4.2 Calibration Data Sorting Criteria

The first thing to do when carrying out datasets sorting is to identify the hole that records the highest pressure to determine the sector into which the data point should be added. Before adding the data point, an additional check was carried out to ensure that the data point did not violate the assumptions made in the definition of flow coefficients for that sector. An analysis of the probe datasets has shown that it is acceptable to assume that if the centre hole of the probe records the highest pressure in low angles, the flow over the peripherals hole will remain reliably attached to the probe.

There was a possibility of flow separation over the centre hole. Therefore, a test was performed to confirm that the flow over hole five was not separated. The analysis carried out was the same as that shown and implemented by Zilliac, G.G. (1993). The pressure at the centre hole was compared with the pressured recorded in the separated flow downstream side of the probe head. If the pressure at the centre hole is less than the pressure in the separated flow, the centre hole was considered to be recording separated flow, and the point was not included in the calibration. In the present study, no calibration points were rejected because the angles under investigation were limited to ±25° and extended to ±45° pitch and yaw angle, which is well below the five-hole pressure probe working limit of ±50°.

3.4.3 Overlapping Pressure and the Extent of Calibration Sectors Domains

There are two main reasons why it is desirable to ensure each sector of the calibration map is valid a little beyond its expected extents. Firstly, for the arbitrary flow study, if the flow angle is such that the point would be so close to the sector boundary, transducers error may have caused the point to fall into either sector. Secondly, if a calibration point inside a sector is considered, it is possible there would be some parts of the sectors edge that would not have a near-boundary calibration point. Extrapolated polynomials tend to go to infinity outside of their fitted domain, and their derivatives could be unbounded. Therefore, it is possible to obtain high-speed slops and sudden changes. A significant error could be introduced in the areas that are beyond the last calibration point in a sector. However, it could remain within the applicable extent of the sector in the extrapolated polynomial region.

Overlap pressure is defined as a tolerance that is applied when determining the hole of the probe that recorded maximum pressure, and hence the sectors in which to include a calibration. A calibration point is added in the sector if that hole is recorded either the maximum pressure or within the overlap of maximum pressure. It meant that calibration points near sector boundaries could be included in multiple sectors. These relations between overlap pressure and the actual number of the additional point included are unknown. However, it can be determined during the data sorting process.

3.4.4 Determination of Calibration Reference Flow Conditions

The calibration process correlates with the response of the probe to the actual flow conditions. Therefore, it was necessary to measure the free stream flow conditions in the wind tunnel and hydraulic pipeline. The flow reference static and total pressures are measured using a Pitot tube mounted on the wind tunnel and pipeline respectively (see section 3.1.4 and 3.2.1), and these pressure values were recorded at each calibration. As discussed in section 3.1.2, the probe was returned (0, 0) from time to time during calibration. The data sorting procedure involves identifying the reference calibration point (0, 0), determining the sector that recorded the highest pressure at each point, and alternatively, the pressure at the centre hole was used at the total pressure were necessary at all time during the calibration when the traverse is moved to (0,0) Akshoy, R.P., Ravi, R.U., & Anu, J. (2011). These reference flow calibration conditions were recorded to an excel file and sorted for use in the generation of a calibration map as shown in figure 3.18 and figure 3.19.

3.4.5 Calculation of Calibration Coefficients

Once the data is sorted, and files containing the calibration had been generated, the generation of the calibration coefficients sector-wise is straightforward. The equations established by Akshoy, R.P., Ravi, R.U., & Anu, J. (2011) is used to calculate the coefficients. In this method, the influence established by the central hole (P_5) is taken into account in determining these coefficients as shown below in equation (3.1). Multiple linear regression is after that performed, which generated the vector for each of the flow descriptors, namely, pitch and yaw angles, and static and total pressures. This process is repeated for each of the five sectors in all the calibrations.

Zone-1:	Zone-2:	Zone-3:	Zone-4:	Zone-5:
$\overline{P} = \frac{P_4 + P_5 + P_2}{3}$	$\overline{P} = \frac{P_1 + P_5 + P_3}{3}$	$\overline{P} = \frac{P_4 + P_5 + P_2}{3}$	$\overline{P} = \frac{P_1 + P_5 + P_3}{3}$	$\overline{P} = \frac{P_1 + P_2 + P_3 + P_4}{4}$
$D = P_1 - \overline{P}$	$D = P_2 - \overline{P}$	$D = P_3 - \overline{P}$	$D = P_4 - \overline{P}$	$D = P_5 - \overline{P}$
$C_{P_\alpha} = \frac{P_1 - P_5}{D}$	$C_{P_\alpha} = \frac{P_1 - P_3}{D}$	$C_{P_\alpha} = \frac{P_5 - P_3}{D}$	$C_{P_\alpha} = \frac{P_1 - P_3}{D}$	$C_{P_\alpha} = \frac{P_1 - P_3}{D}$
$C_{P_\beta} = \frac{P_2 - P_4}{D}$	$C_{P_\beta} = \frac{P_2 - P_5}{D}$	$C_{P_\beta} = \frac{P_2 - P_4}{D}$	$C_{P_\beta} = \frac{P_5 - P_4}{D}$	$C_{P_\beta} = \frac{P_2 - P_4}{D}$
$C_{P_{total}} = \frac{P_1 - P_{total}}{D}$	$C_{P_{total}} = \frac{P_2 - P_{total}}{D}$	$C_{P_{total}} = \frac{P_3 - P_{total}}{D}$	$C_{P_{total}} = \frac{P_4 - P_{total}}{D}$	$C_{P_{total}} = \frac{P_5 - P_{total}}{D}$
$C_{P_{static}} = \frac{\overline{P} - P_{static}}{D}$	$C_{P_{static}} = \frac{\overline{P} - P_{static}}{D}$	$C_{P_{static}} = \frac{\overline{P} - P_{static}}{D}$	$C_{P_{static}} = \frac{\overline{P} - P_{static}}{D}$	$C_{P_{static}} = \frac{\overline{P} - P_{static}}{D}$

(3.1)

Where P_1, P_2, P_3, P_4, and P_5 are the pressure sensed by the pressure transducers from the individual holes of the probe. $\bar{p}$ is the arithmetic mean of the pressures measured from the four side holes of the probe, i.e. $(P_1+ P_2+P_3+P_4)/4$, Cp_α is the coefficient of yaw, Cp_β coefficient of pitch, Cp_{total} is the coefficient of total pressure, Cp_{static} is the coefficient of static pressure, P_{total} and P_{static} are true local total and static pressures of the fluid flow. Normally, the true local P_{total} and P_{static} are unknown quantities, which solely depend on the flow field. Nevertheless, during the calibration of the probe in wind tunnel and pipeline flows respectively, these are free stream values, so all the four pressure coefficients are determined according to the sector that recorded the highest pressure corresponding to each pitch and yaw angle of the probe.

In other to find the calibration coefficients, various non-dimensional pressure coefficients such as Cp_α, Cp_β, $Cp_{total,}$ and Cp_{static} need to be calculated. The first approach in data reduction analysis is to calculate the average pressure $\bar{p}$ and denominator D for each sector as formulated. The D in these equations in the value that makes the non-dimensional pressure values independent of the flows. This procedure for data reduction and analysis are carried out in special software using the Excel Sheet, which contains nine columns. These comprise of the pitch, yaw, P_1, P_2, P_3, P_4, P_5, P_{total} and P_{static} all data transferred to MS Excel, sorted pitch and yaw wise in rows and P_1 through P_{total} in columns.

The next step is creating the sectoring system. It means identifying pressure with maximum value for each dataset, that is for a combination of pitch and yaw angle when the holes of the probe are facing the upstream flow. Pressures measured by P_1 indicate sector1 and so on to sector 5 (pressure measured by P_5). Additional six columns are added to the Excel file to expand the datasheet and accommodate $\bar{p}$, D, Cp_{total}, Cp_{static}, Cp_α, and Cp_β. The values for these calibration quantities are calculated sector wise using the formulated equations corresponding to the sectors. The actual data

prediction equations for the full sixth order multiple regression model is defined as shown in equations (3.2) through equation (3.5).

$$\alpha\,(An_{\alpha}.A_{\beta}) = a_0 + a_1A_{\alpha} + a_2A_{\beta} + a_3{A^2}_{\alpha} + a_4{A^2}_{\beta} + a_5A_{\alpha}.A_{\beta} + a_6{A^2}_{\alpha}.A_{\beta}\ \ a_7A_{\alpha}.{A^2}_{\beta} + a_8{A^3}_{\alpha} + a_9{A^3}_{\beta} + a_{10}{A^2}_{\alpha}.{A^2}_{\beta} + a_{11}{A^3}_{\cdot\alpha}A_{\beta} + a_{12}A_{\alpha}.{A^3}_{\beta} + a_{13}{A^4}_{\alpha} + a_{14}{A^4}_{\beta} + a_{15}{A^5}_{\alpha} + a_{16}{A^4}_{\alpha}.A_{\beta} + a_{17}{A^3}_{\alpha}.{A_{\beta}}^2 + a_{18}{A^2}_{\alpha}.{A^3}_{\beta} + a_{19}A_{\alpha}.{A^4}_{\beta} + a_{20}{A^5}_{\beta} + a_{21}{A^6}_{\alpha} + a_{22}{A^5}_{\alpha}.A_{\beta} + a_{23}{A^4}_{\alpha}.{A^2}_{\beta} + a_{24}{A^3}_{\alpha}.{A^3}_{\beta} + a_{25}{A^2}_{\alpha}.{A^4}_{\beta} + a_{26}A_{\alpha}.{A^5}_{\beta} + a_{27}.{A^6}_{\beta} \quad (3.2)$$

$$\beta\,(B_{\alpha}.B_{\beta}) = a_0 + a_1B_{\alpha} + a_2B_{\beta} + a_3{B^2}_{\alpha} + a_4{B^2}_{\beta} + a_5B_{\alpha}.B_{\beta} + a_6{B^2}_{\alpha}.B_{\beta}\ \ a_7B_{\alpha}.{B^2}_{\beta} + a_8{B^3}_{\alpha} + a_9{B^3}_{\beta} + a_{10}{B^2}_{\alpha}.{B^2}_{\beta} + a_{11}{B^3}_{\cdot\alpha}B_{\beta} + a_{12}B_{\alpha}.{B^3}_{\beta} + a_{13}{B^4}_{\alpha} + a_{14}{B^4}_{\beta} + a_{15}{B^5}_{\alpha} + a_{16}{B^4}_{\alpha}.B_{\beta} + a_{17}{B^3}_{\alpha}.{B_{\beta}}^2 + a_{18}{B^2}_{\alpha}.{B^3}_{\beta} + a_{19}B_{\alpha}.{B^4}_{\beta} + a_{20}{B^5}_{\beta} + a_{21}{B^6}_{\alpha} + a_{22}{B^5}_{\alpha}.B_{\beta} + a_{23}{B^4}_{\alpha}.{B^2}_{\beta} + a_{24}{B^3}_{\alpha}.{B^3}_{\beta} + a_{25}{B^2}_{\alpha}.{B^4}_{\beta} + a_{26}B_{\alpha}.{B^5}_{\beta} + a_{27}.{B^6}_{\beta} \quad (3.3)$$

$$C_{SP}\,(C_{\alpha}.C_{\beta}) = a_0 + a_1C_{\alpha} + a_2C_{\beta} + a_3{C^2}_{\alpha} + a_4{C^2}_{\beta} + a_5C_{\alpha}.C_{\beta} + a_6{C^2}_{\alpha}.C_{\beta}\ \ a_7C_{\alpha}.{C^2}_{\beta} + a_8{C^3}_{\alpha} + a_9{C^3}_{\beta} + a_{10}{C^2}_{\alpha}.{C^2}_{\beta} + a_{11}{C^3}_{\cdot\alpha}C_{\beta} + a_{12}C_{\alpha}.{C^3}_{\beta} + a_{13}{C^4}_{\alpha} + a_{14}{C^4}_{\beta} + a_{15}{C^5}_{\alpha} + a_{16}{C^4}_{\alpha}.C_{\beta} + a_{17}{C^3}_{\alpha}.{C_{\beta}}^2 + a_{18}{C^2}_{\alpha}.{C^3}_{\beta} + a_{19}C_{\alpha}.{C^4}_{\beta} + a_{20}{C^5}_{\beta} + a_{21}{C^6}_{\alpha} + a_{22}{C^5}_{\alpha}.C_{\beta} + a_{23}{C^4}_{\alpha}.{C^2}_{\beta} + a_{24}{C^3}_{\alpha}.{C^3}_{\beta} + a_{25}{C^2}_{\alpha}.{C^4}_{\beta} + a_{26}C_{\alpha}.{C^5}_{\beta} + a_{27}.{C^6}_{\beta} \quad (3.4)$$

$$D_{TP}\,(D_{\alpha}.D_{\beta}) = a_0 + a_1D_{\alpha} + a_2D_{\beta} + a_3{D^2}_{\alpha} + a_4{D^2}_{\beta} + a_5D_{\alpha}.D_{\beta} + a_6{D^2}_{\alpha}.D_{\beta}\ \ a_7D_{\alpha}.{D^2}_{\beta} + a_8{D^3}_{\alpha} + a_9{D^3}_{\beta} + a_{10}{D^2}_{\alpha}.{D^2}_{\beta} + a_{11}{D^3}_{\cdot\alpha}D_{\beta} + a_{12}D_{\alpha}.{D^3}_{\beta} + a_{13}{D^4}_{\alpha} + a_{14}{D^4}_{\beta} + a_{15}{D^5}_{\alpha} + a_{16}{D^4}_{\alpha}.D_{\beta} + a_{17}{D^3}_{\alpha}.{D_{\beta}}^2 + a_{18}{D^2}_{\alpha}.{D^3}_{\beta} + a_{19}D_{\alpha}.{D^4}_{\beta} + a_{20}{D^5}_{\beta} + a_{21}{D^6}_{\alpha} + a_{22}{D^5}_{\alpha}.D_{\beta} + a_{23}{D^4}_{\alpha}.{D^2}_{\beta} + a_{24}{D^3}_{\alpha}.{D^3}_{\beta} + a_{25}{D^2}_{\alpha}.{D^4}_{\beta} + a_{26}D_{\alpha}.{D^5}_{\beta} + a_{27}.{D^6}_{\beta} \quad (3.5)$$

Where α is the pitch flow angle and β is the yaw angle, while A and B are their corresponding coefficients respectively. Similarly, C_{PS} and D_{PT} are static and total pressure, while C and D are their corresponding coefficients respectively. Equation (3.2) and (3.3) have been used to calculate flow angles using the calibrations coefficients, a_0 to a_{27} generated using the polynomial curve fit coefficients generated earlier, while equation (3.4) and (3.5) have been used to calculate the flow static and total pressures respectively using the calibration coefficients, a_0 to a_{27} corresponding to static and total pressures. For any set of reading used in calculating the flow properties, these coefficients will be different for Aα = pitch angle, B_{β}=yaw angle, C_Sp = static pressure, and Dp_T = total pressure. These four calibration parameters are used to calculate flow velocities of internal and external flows. Furthermore, these expansions can also be expressed in matrix form, indicating that

once the calibration coefficients are known, any number of points (m) can be converted to flow properties using the matrix multiplication shown in equation (3.6) Akshoy, R.P., Ravi, R.U., & Anu, J. (2011).

$$\begin{Bmatrix} X_1 \\ X_2 \\ X_3 \\ \vdots \\ X_m \end{Bmatrix} = \begin{bmatrix} 1 & C_{\alpha_1} & C_{\beta_1} & C_{\alpha_1}^2 & \cdots & C_{\beta_1}^4 \\ 1 & C_{\alpha_2} & C_{\beta_2} & C_{\alpha_2}^2 & \cdots & C_{\beta_2}^4 \\ 1 & C_{\alpha_3} & C_{\beta_3} & C_{\alpha_3}^2 & \cdots & C_{\beta_3}^4 \\ \vdots & \vdots & \vdots & \vdots & \cdots & \vdots \\ 1 & C_{\alpha_m} & C_{\beta_m} & C_{\alpha_m}^2 & \cdots & C_{\beta_m}^4 \end{bmatrix} \begin{Bmatrix} K_1 \\ K_2 \\ K_3 \\ \vdots \\ K_{15} \end{Bmatrix} \tag{3.6}$$

Where, X is one of the flow parameters like α, β, C_{SP}, and D_{TP}. A sample set is set of m data points are taken for each of the given sectors. The Ks are the calibration constants where the subscript identifies the term in the expression, while C_{am} is the calibration coefficients.

This matrix is further simplified in its expression. The independent variable array is a function of angular pressure coefficients only and can, therefore, be calculated directly from the probe data. The vector dependent variable is known during calibration, but this is unknown when the probe is used to measure arbitrary flow. Similarly, the calibration vector is unknown at the time of calibration but need to know when measuring the arbitrary flow. The matrix is expressed in a simplified form as shown in equation (3.7).

$$\{X\} = [C]\{K\} \tag{3.7}$$

Where, [m×1], [A] matrix contains m values of one of the four flow parameters, the [m×27], [C] matrix contains the corresponding expanded pressure coefficient variables, and [K] matrix contains the calibration coefficients. The quantities with the X matrix have been determined for every sector during the calibration. That is, for α = 25° and β = 25°, the value of Aα, or B_β at that corresponding point of C_{SP} and D_{TP}.

From equation 3.6, it is clear that the simple matrix algebra can be used to calculate the calibration vector K, given that flow properties are known during calibration. Also, it is clear that the only data needed to calculate flow properties in an arbitrary flow is the calibration vector. It leads to one of the main advantages of polynomial surface calibration methodology that after the formulation of the polynomial expression the implementation of the probe calibration run-time and computation

expenses and resolving arbitrary flows information is deficient. This method has proven to be capable and reliable in measuring flow angles to within ±1° and flowed pressure to within 2% Jason, T., & Cengiz, C. (2011).

The accuracy of calibrations depends, of course, depend on the density of the calibration grid. The accuracy also depends on the cone chamfer angle for conical probes, at high chamfer angles, the errors tend to be higher. However, the approach is simple to implement and has been shown to be capable of producing accurate flow measurements using CFD based numerical integrated datasets. All the datasets obtained during calibrations have been checked to ensure the effectiveness of the calibration constants obtained. The calibration coefficients have an approximate accuracy level of ±0.5° for both yaw and pitch angles. It is the point where the coefficient of determinations is equal to 1.0000 for all the four calibration parameters of pitch and yaw angles and static and total pressures.

The velocities in three directions are determined using the mathematical expressions shown in equations (3.8) through equation (3.11).

$$|U| = \sqrt{\frac{2(p_{total} - p_{static})}{\rho}} \tag{3.8}$$

$$U_x = |U| \cos(\alpha) \tag{3.9}$$

$$U_y = |U| \sin(\alpha) \sin(\beta) \tag{3.10}$$

$$U_z = |U| \sin(\alpha) \cos(\beta) \tag{3.11}$$

3.5 Conversion of Pressures from Arbitrary Flows to Flow velocity, Direction, and Pressure

The first step deployed in converting arbitrary flow datasets into flow information is first to measure the pressures from the flow, identify which sector(hole) that estimates the highest pressure value, and apply sectoring technique to calculate calibration coefficients. Once this step is done, the calibration coefficients are stored and later used to calculate flow angles and velocity magnitude by using the calibration coefficients (a_0 to a_{27}) calculated during calibrations sector-wise. Any single

measurement contains seven pieces of information, two angle points and five pressure values measured by the five-hole of the probe. From this information, the flow pressures (static and total), and velocities are calculated. Figure 3.20 summarises the procedures of calculating flow velocities from an arbitrary flow using a five-hole pressure probe.

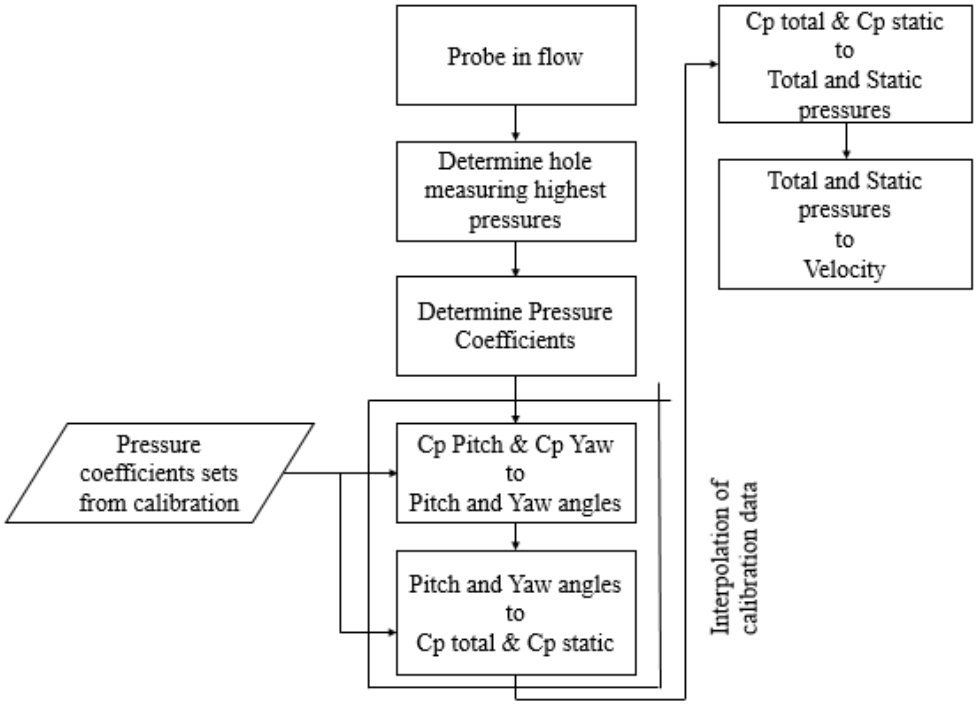

Figure 3.20. Flowchart Representing the Procedure to Determine Flow Parameters

The sector that would be used to convert the datasets is selected using the same criteria that are applied during the sorting process, using the hole recording the maximum pressure. The calibration equations and coefficients for that sector are used to calculate the flow properties. Once the flow properties are calculated and the validity of the pressure datasets confirmed, and datasets were written to an output file.

3.6 Calibration Verification

The calibration verifications are carried out by first generating calibration coefficients for a set of pressure data and process flow information using the coefficients. Flow pressures and angles are then compared to the known actual flow pressures and angles. Errors were computed in three ways. The root means square (RMS) average error has been calculated for each flow parameter individually as shown in equation (3.12 and 3.13) proposed by Zilliac, G.G. (1993).

$$\delta_\theta = \sqrt{\frac{1}{n}\sum_{i=1}^{5}(\theta_{\mathrm{i,calculated}} - \theta_{\mathrm{actual}})^2} \tag{3.12}$$

$$S_E = \frac{\delta_\theta}{\sqrt{n}} \tag{3.13}$$

It is important to mention that all bias errors such as those from pressure transducers, temperature drift, and probe stem deflections are negligible. Hence, they are not included in this error analysis. However, in actual measurement, bias errors can be the dominant error sources, and there is a need to reduce these errors to the barest minimum. One way that was achieved in this study has been first to calibrate all the pressure transducers. It involved reading the A/D counts with zero applied pressure C_Z and then using a known pressure difference h measured by a manometer and further reading the corresponding A/D counts Cref. Therefore, an unknown pressure that is the actual pressure is then determined using equation (2.14) proposed by Zilliac, G.G. (1993).

$$P = \frac{h}{(c_{ref} - c_z)}(c - c_z) \tag{3.14}$$

Equation 3.14 is used to improve further the accuracy of the calibration process which is what the study is about. This is very useful in the study because it separates the effects of the curve fit from pressure transducers errors. The datasets used to generate results and plots are the same as the datasets used to generate the calibration maps. Therefore there are no sources of error other than the error in curve fittings which are aimed to be corrected using CFD based numerical datasets.

3.7 Calibration Validation

Validation of the calibration of the probe was carried out using the same process that was used in section 3.6 because the process of error calculation and presentation was the same. The calculation to validation flow information involved using equation 3.12 to calculate and compare the actual flow information with the calculated flow values under different flow conditions using the calibration datasets. The analysis gave a measure of the net effects of all of the errors related to the calibration errors, including potential uncertainty in the probe traverse, pressure transducer error, and flow loop instabilities, and curve fit error Zilliac, G.G. (1993).

3.8 Experimental Preliminary Results

The variation of the probe pressures at different yaw and pitch angles are plotted at constant pitch angles to ascertain the accuracy of the calibration datasets. For brevity, only sample calibration datasets for second measurements are presented in figure 3.21 through 3.28. Taking data twice and generating sample calibration sector maps in the second run prove repeatability and accuracy. For both conical and hemispherical probes, the pressures datasets exhibit the expected trends without any sudden change. Therefore, the calibration sample datasets are considered accurate and utilised to calculate calibration coefficients and flow parameters.

3.8.1 Experimental Calibration Sample Data Collected in Wind Tunnel Flow

A set of pressure data are collected using conical and hemispherical in the wind tunnel at different pitch and yaw angles planes for the points defined for the calibration. Figure 3.21 presents the coefficients of pressure datasets measured in wind tunnel flow before applying sectoring calibration equations for analysis.

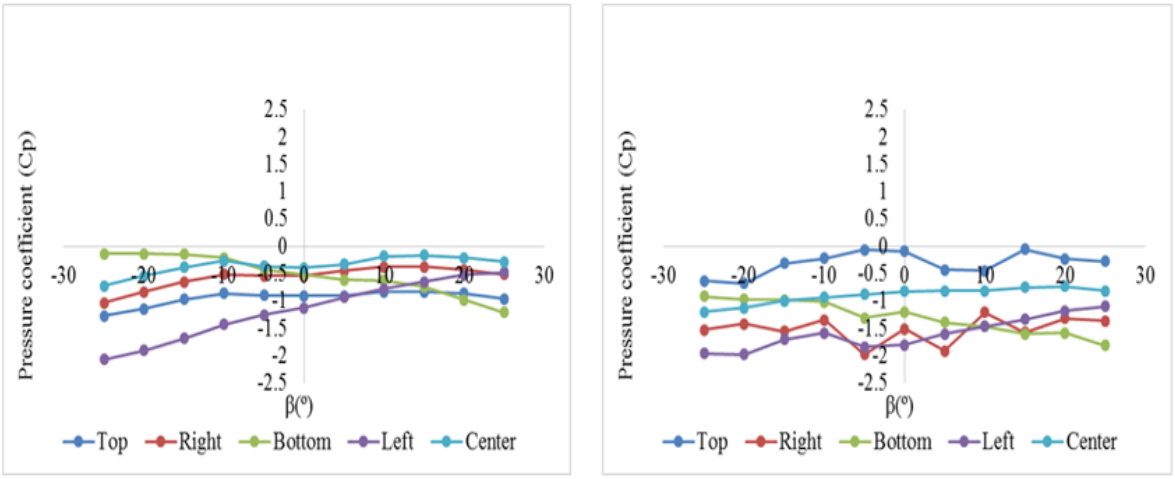

(a) Sample calibration data measured on negative pitch (a) Sample calibration data measured on positive pitch

Figure 3.21. Sample calibration dataset measured by a five-hole conical probe in wind tunnel flow

As shown in figure 3.21, pressure measured by the central hole, P_5 is maximum at positive yaw angles but varies more or less symmetrically about negative yaw angles. The bottom hole, P_3, measured less pressure at positive angles but high-pressure values at negative angles. Similarly, the pressure measured by the top hole, P_1, maintains approximately a coefficient of -1.0000 but drops as

the probe shifts towards negative yaw angles. Furthermore, the right hole of the pressure probe, P_2, measures constant coefficients of about -0.5000 on the positive yaw plane but drops at -10° to about -1.0000. Similarly, the left hole, P_4 measured the least pressure values especially at negative yaw angles but gradually increases at the positive yaw angle planes. Overall, figure 3.21 shows the expected trends of pressures datasets measured by the conical five-hole probe without abnormal values. Therefore, the calibration datasets are found satisfactory.

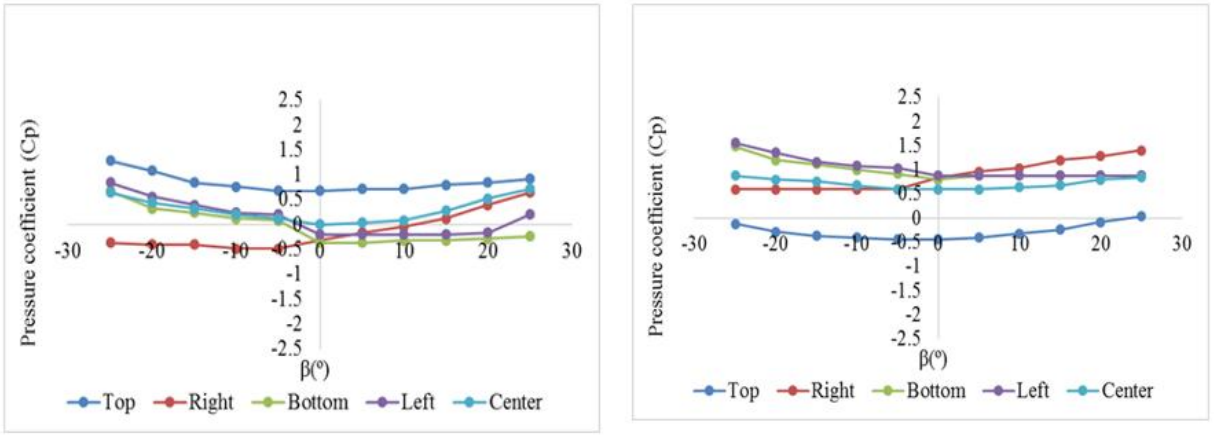

(a) Sample calibration data measured at negative pitch (a) Sample calibration data measured on at positive pitch

Figure 3.22. Sample calibration dataset measured by a hemispherical probe in wind tunnel flow

Figure 3.22 shows that the top hole, P_1 measured maximum datasets at both positive and negative yaw angles planes. Similarly, the right hole, P_2, maintained symmetrical trend at negative to positive yaw angles plane even though it recorded small coefficients below the zero line on negative yaw and just above on the positive yaw planes. The bottom hole, P_3, measured the highest pressure at negative yaw direction but decreased as the probe is traversed in a yaw direction from 0° . The same is for the case for the left hole, P_4, but recorded a sharp high value at 20° yaw angle plane. The centre hole, P_5, maintained a level symmetrical trend in the negative and positive yaw direction, recording all positive coefficients. It can be seen that figure 3.22 demonstrate a well symmetrical trend for all five pressure holes as expected. Therefore, it can be said that the calibration datasets measured by the hemispherical five-hole probe in wind tunnel flow are without abnormality and is found satisfactory for this study.

3.8.2 Comparison of Experimental Wind Tunnel Dataset

Both the dataset measured by the conical and hemispherical five-hole pressure probes have been compared. In each calibration, the probe is traversed from the centre of the calibration section to the end of the opposite wall. A manual traversing mechanism with 1mm measurement resolution along the radial direction and 1° measurement resolution in the yaw plane is used to traverse the probes along the grid points. From figure 3.21 and figure 3.22, it is evident that the non-dimensional pressure measured by both the conical and hemispherical five-hole pressure probes are in good agreement without any change in their particular trend. However, due to some of the errors discussed in the literature, experimental calibration of a five-hole probe cannot be free from error.

3.8.3 Experiment Calibration Sample Dataset Collected in Hydraulic Pipeline Flow

Sets of pressure data are collected using conical and hemispherical in the hydraulic pipeline flow field at different pitch and yaw angle planes for the defined calibration grids. Figure 2.23 shows the pressure calibration dataset measured by the conical probe.

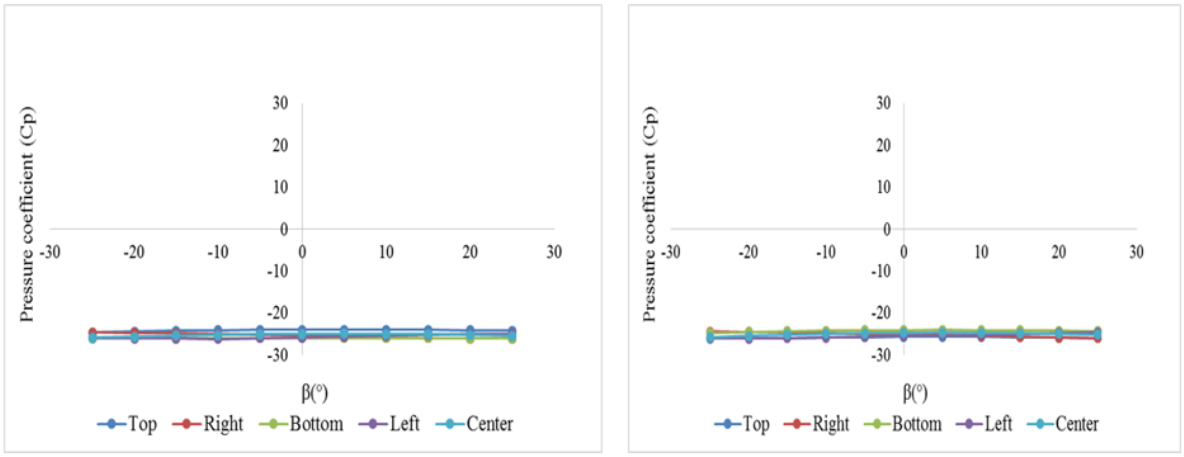

(a) Sample calibration data measured at negative pitch (a) Sample calibration data measured at positive pitch

Figure 3.23. Sample calibration dataset measured by a five-hole conical probe in hydraulic flow

As seen in figure 3.23, it can be concluded that all holes of the conical probe measured calibration datasets at about the same range and maintained a perfect symmetrical trend from negative to positive yaw angle plane of the probe. Therefore, it can be concluded without a doubt that datasets presented by the probe can be used to determine the calibration coefficients satisfactorily.

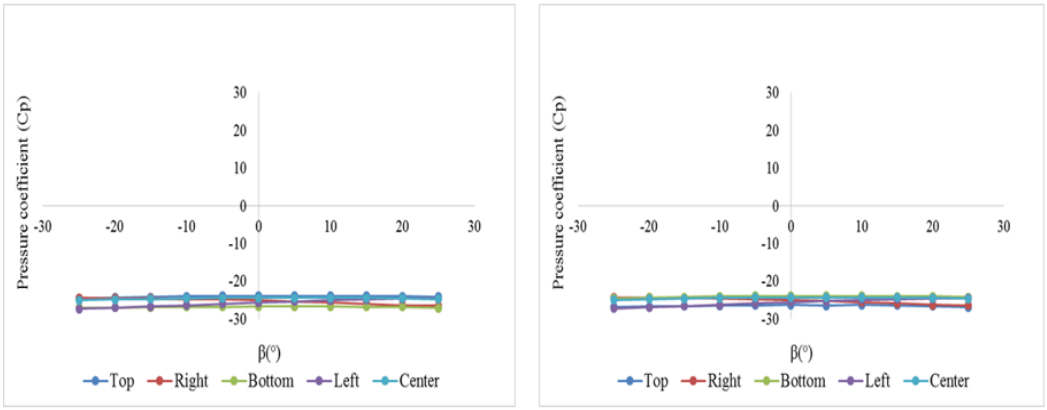

(a) Sample calibration data measured at negative pitch (a) Sample calibration data measured at positive pitch

Figure 3.24. Sample calibration dataset measured by a five-hole hemispherical probe at in hydraulic pipeline flow

As depicted in figure 3.24, having analysed the calibration datasets qualitatively, it can be seen that all five holes of the hemispherical probe measures pressure datasets about the same range for negative and through to positive yaw angle plane. Furthermore, it can be seen that the probe has maintained a perfect symmetrical order of calibration datasets. Therefore, it can be concluded that the pressure datasets met the requirements need for this study and can be to generate trusted calibration coefficients for accurate measurements satisfactorily.

3.8.4 Comparisons of Experimental Hydraulic Pipeline Flow Dataset

A manual motion mechanism with a 1mm measurement resolution along the radial direction and 1° resolution in the plane are used to traverse the probe the same for wind tunnel system. Both the conical and hemispherical probes started taken measures at the centre of the hydraulic pipeline, which is of the zero points of the test section, and yawed away 5° interval in both negative and positive. As the probe approaches the opposite walls, the intervals are reduced, and wall proximity decreases. However, comparing figure 3.24 to 3.25, it can be seen that both pressure probes perform very well in the measurement of pressure dataset in the hydraulic pipeline flow.

3.9 Novel CFD Based Calibration Methods of Conical and Hemispherical of Five-hole Pressure Probes

The CFD based calibration methods of five-hole conical and hemispherical pressure probe for wind tunnel and hydraulic pipeline flow is aimed to improve measurement accuracies in the respective

flow. The CFD calibration methods are classified into three major novel methods. These are CFD based numerical calibration method, CFD based numerical integration method and CFD based extension of calibration range. Figure 3.25 shows a flowchart that summarises the calibration methods while sections 3.9.1 and 3.9.2 describe the systematic approach to achieving the aims and objectives of the study.

The calibration methods use sixth order polynomial curve-fit for data analysis and reduction for accuracy. The goodness of fit or calibration coefficient of determination, which is commonly known as r^2 is expected to be equal to 1.0000 for all calibration coefficients of determination. The curve-fit technique compares estimated data, (θe) and actual data, (θa), and ranges in value from 0.0000 to 1.0000. If the correlation returns 1.0000, it means there is a perfect correlation in the sample data, and suggest there is no difference between estimated and actual data. However, at the other extreme, if the regression analysis returns 0.0000, it means there is no correlation between estimated and actual data, and the regression equation has failed in predicting a y-value.

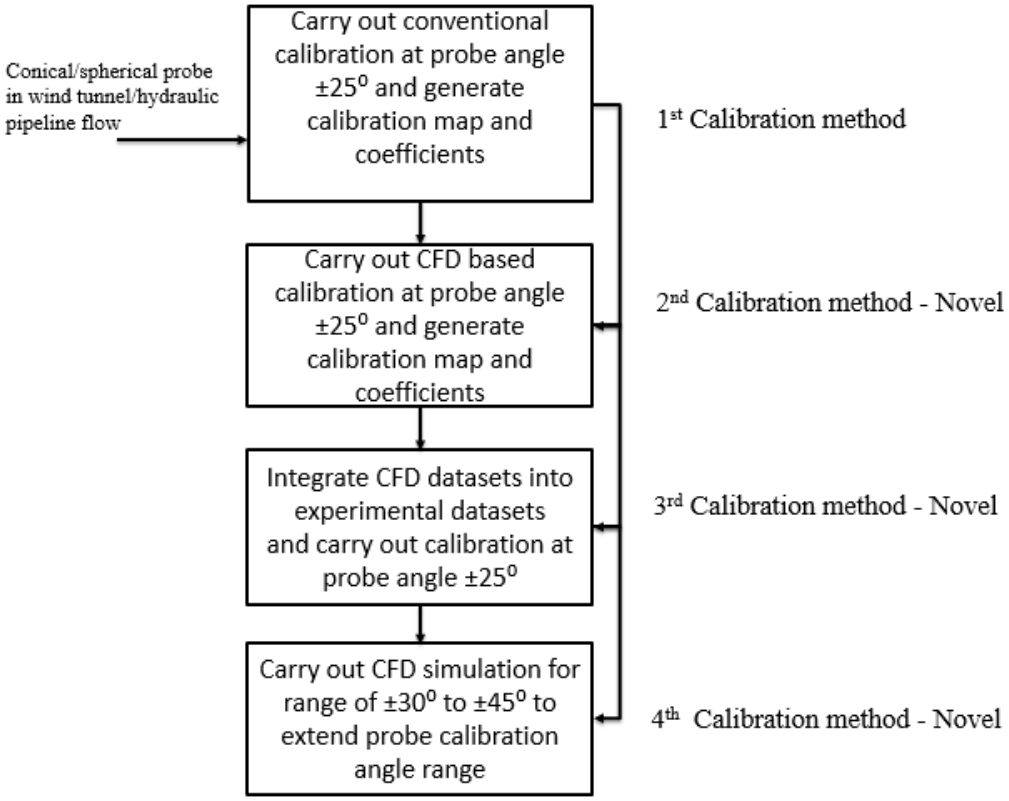

Figure 3.25. A flowchart summarising novel calibration methods

Figure 3.25 summarises the computational fluid dynamic (CFD) based calibration methods proposed for this study. Each calibration method is inter-linked through the use of (CFD) simulations. The steps and procedure of each calibration method are clearly explained in the next sections. The calibration techniques and schemes described in section 3.4 are applied to all the processes. The only thing that differs in the proposed is the means of acquiring pressure datasets and its application within the proposed methods.

3.9.1 Conventional and Novel CFD based numerical Integration Calibration Methods

This section discusses the systematic approach and processes adopted for the calibration of the conical and hemispherical five-hole pressure probes using CFD based techniques. The CFD based calibration methods are sub-divided into four parts. The first part is to carry out the conventional experimental calibration, analyse a dataset, verify dataset by measuring flow properties, and then compare them with known flow fields to validate the method and analyse the performance of the conventional calibration method. The second part is using CFD to simulate the same probe under the same flow conditions, record the pressure (acquire pressure datasets for calibration), analyse and process dataset, verify calibration by measuring flow properties to validate numerical datasets and then compare with known flow fields for accuracy checks.

The third method is to identify the sectors whose r^2 is below 90% in the experimental calibration method, replace that sector/sectors with its CFD based numerical corresponding dataset (this is the integration method) and repeat the calibration processes. Analyse and process CFD based integrated datasets, verify the CFD based integration datasets by measuring flow properties to check the accuracy of measurements and establish the authenticity of the calibration method. The fourth novel calibration method is to extend the calibration angle range of the integration method by using CFD to simulate both pitch and yaw angles of the prob respectively beyond $\pm 25^{o}$ to $\pm 45^{o}$. These require setting the probe to known pitch and yaw angles (α, β) in a steady flow and recording the five-hole pressures (P_{1-5}). The systematic calibration approach and procedures are summarised as follows:

1 Carry out standard experimental calibration. Record the pressures sensed by each hole of the five-hole pressure probe at different pitch and yaw angles are taken as 5^{o} increment in the range of $\pm 25^{o}$.

2 Apply the sectoring technique to sort the pressure dataset according to the hole that covered the highest pressure.

3 Generate the calibration sector map, which indicates the hole of the probe that sensed the highest pressure for a particular pitch and yaw angles.

4 The map generally reveals that the central hole covers the broadest range of pitch and yaw angles among all the five holes.

5 However, at larger pitch and yaw angles, the peripherals holes (hole 1 to 4) are likely to sense the total pressure, and hence the pressure detected by the peripherals holes at their corresponding location is maximum (see figure 3.18 and 3.19).

6 Many asymmetries may be found in the sector map, indicating the non-symmetry associated with the error introduced during manufacturing and those mentioned in the literature.

7 Pressure coefficient normalisation is then applied sector-wise using the equation defined in 3.1 to calculate non-dimensional pressure coefficients

8 Apply a sixth order polynomial curve-fit regression method to analyse the non-dimensional pressure calculated above.

9 Record the calibration coefficient of determination and the calibration constantans (a_0 to a_{27})

10 Use the probe to measure pressure values in an arbitrary flow, identify the sector measuring the highest pressure, apply equation 3.1 and calculate the calibration constants

11 Use the calibration constants to calculate the flow angles and use the flow angles to calculate flow velocities using equations 3.8 to 3.11.

12 Repeat to verify data

13 Validate and compare flow velocity with actual flow field and analyse the difference.

14 Analyse the accuracy of the first calibration method on the steady flow fields.

15 Check whether the calibration coefficient of determinations for each sector is above 90%.

16 Simulate the probe using CFD based approach at the same range of pitch and yaw angles for the second novel calibration method, $\pm 25^{o}$ as did for experiments and acquire the numerical pressure data and repeat step 1 to 15 for the CFD based numerical pressure datasets under same flow conditions.

17 Identify the experimental sector that performs below 90% and replaces that sector with its corresponding CFD numerical pressure datasets in to develop another stronger novel method of calibration known as CFD based Integration Calibration method.

18 Apply step 1 to 15 to the CFD based integration datasets, plot the results, and compare with actual flow fields.
19 Analyse the accuracy level of the CFD based integration calibration method based on the measured flow properties
20 End process and proceed to the CFD based extension of calibration angle range, the fourth novel calibration method

This calibration process must be repeated until the desired angular range is covered to obtain strong datasets, and it not uncommon for the calibration dataset to contain approximately 100 points or more. Figure 3.18 and 3.19 shows the distribution of the calibration points in the pitch and yaw coordinate system for the conical and hemispherical five-hole pressure probes. The first, second and their calibrations are carried out for a maximum angle of $\pm 25^{o}$ in the wind tunnel and hydraulic pipeline located at the University of Huddersfield laboratories. Section 3.9.2 describes the systematic approach to the novel CFD based extension of the range calibration method.

3.9.2 Novel CFD Based Extension of Five-hole Probe Calibration Angle Range

This section describes the CFD based extension of range calibration method and procedures for acquiring numerical calibration datasets beyond $\pm 25^{o}$. The next novel step in this study is to use CFD based simulations to extend each probe angle from $\pm 25^{o}$ to $\pm 45^{o}$ (extension of the integration angles). It is carried for the respective probe to be used for measurements to be carried at wider pitch and yaw angles of $\pm 45^{o}$. The following steps summarise the procedures of the CFD based extension of the range calibration method.

1. Carry out CFD simulation of the probe in their respective flow domain (air and water) for $\pm 30^{o}$ to $\pm 45^{o}$ and acquire pressure dataset sensed at each hole at each combination of pitch and yaw angle for $\pm 30^{o}$ to $\pm 45^{o}$.
2. Integrate all CFD $\pm 30^{o}$ to $\pm 45^{o}$ pressure dataset into CFD based integration calibration datasets generated in step 16 above to develop a novel CFD Extension Calibration Dataset.
3. Apply the sectoring technique to sort the pressure dataset according to the hole that covered the highest pressure.
4. Generate the sector map, which indicates the hole of the probe that sensed the highest pressure for a particular pitch and yaw angles.

5. The map generally reveals that the central hole covers the broadest range of pitch and yaw angles among all the five holes.
6. However, at larger pitch and yaw angles, the peripherals holes (hole 1 to 4) are likely to sense the total pressure, and hence the pressure detected by the peripherals holes
7. Many asymmetries may be found in the sector map, indicating the non-symmetry associated with the error introduced during manufacturing and those mentioned in the literature.
8. Apply pressure normalisation sector-wise using the equations defined in 3.1 to calculate non-dimensional pressure coefficients
9. Apply a sixth order polynomial curve-fit technique to analyse the non-dimensional pressure calculated above.
10. Record the calibration coefficient of determination and the calibration constantans (a_0 to a_{27})
11. Repeat to verify dataset
12. Use the probe to measure pressure values in an arbitrary flow, identify the sector measuring the highest pressure, apply equation 3.1 and calculate the calibration constants
13. Use the calibration constants to calculate the flow angles and use the flow angles to calculate flow velocities using equations 3.8 to 3.11.
14. Validate the calculated flow velocity with actual flow field and analyse the difference
15. Compare the computed flow velocities with real flow field and check the accuracy level of the calibration method in the measured flow properties.
16. Compare the accuracies of the first, second, third and fourth calibration methods.
17. Analyse the performance of the probes in the two flow systems and draw conclusions
18. End process.

3.10 Summary

In this chapter, details of the University of Huddersfield Flow wind tunnel hydraulic pipeline facilities have been presented. The facilities are used for flow quality assurance, multiphase measuring, and control studies. The flow facilities used in this study, as well as their working fluids and the supply circuitries, are also described. The details of the instrumentation used are presented and how data are acquired from the instruments are further discussed. Furthermore, the methodology adopted to perform the experiments are discussed in detail, the operating range of the experiments as well as CFD simulations are clearly defined. Also, the details of the procedures and

equipment for calibration and measure external and internal fluid flow have been carefully described.

Lastly, the preliminary sample calibration results have been analysed to demonstrate the accuracy of the pressure data measured in both external and internal flows that are used in this study. The results for both probes in external and internal flow shows satisfactory results.

Chapter 4 Computational Fluid Dynamics (CFD) Numerical Modelling and Simulations

It has been discussed in chapter 1 that the importance of flow measurement accuracy has been continuously gaining relevance due to its various applications in many industries such as the oil and gas and power sector. Based on the different calibration and measurement method using five-hole probe reviewed in literature chapter 2, the process of integrating experimental with numerical calibration method of calibration of a five-hole pressure probe has presented the opportunity and the potential to significantly improve the calibration and measurement accuracies of flow in internal and external systems.

4.1 Methodological Approach for Comparative Simulations and Analysis of the Five-hole Pressure Probes

Pneumatic five-hole probes are useful tools for multi-dimensional velocity measurements. These instruments can be used in combination for detailed flow mapping in complex applications such as the ones described in section 1.5, flow in around aircraft, velocity measurement inside pipelines etc. However, for accurate measurement of velocity at any application, it is essential that the probe produce accurate measurements. There is a need to perform precise calibration data that can be used to carry out velocity measurements to achieve accurate flow measurements. Although calibration of pressure probes does not always produce accurate results because of the machining inaccuracies, manufacturing inaccuracies, and pressure sensors limitations to measure and capture full flow velocity etc., it is necessary to adopt CFD calibration method in order to overcome these experimental limitations as well as those identified in literature by integrating experimental data with CFD data.

Computational fluid dynamics (CFD) simulations of the five-hole pressure probes are carried out in flow domains fully described with the characteristics of the experimental wind tunnel and hydraulic pipeline. The CFD simulations are carried out using the same flow velocity magnitude described in section 3.1.4 and 3.2.1 for wind tunnel and hydraulic pipeline, 15m/sec and 2.12m/sec respectively as inlet velocities to capture the full measurements in this study. The local flow total and static pressure are used to calculate the flow velocity. Furthermore, the two pressures are used to compute the coefficients of C_{Total} and C_{Static} needed in the calibrations. These two non-dimensional pressure quantities determine the flow velocity magnitude in an arbitrary flow of wind tunnel and hydraulic pipeline. They are demonstrated mathematically in equation (4.1) and equation (4.2) as follows.

$$C_{Ptotal} = \frac{P_{sector} - P_{total}}{D} \tag{4.1}$$

$$C_{Pstatic} = \frac{\bar{P} - P_{total}}{D} \tag{4.2}$$

Where P_{sector} is the pressure under the sector in consideration, D is a parameter that makes the C_{Ptotal} and $C_{Pstatic}$ independent of the flow. Furthermore, the true local P_{total} and P_{static} are the static pressures of the flow measured using a Pitot tube installed in the fluid system. Therefore, all calibrations both numerical and experimental including flow measurements are carried out at the flow rate of the

wind tunnel and pipeline flow velocity measured from using a Pitot tube installed in each system as explained in chapter 3.

A set of calibration data is generated experimentally and used for analysing possible combinations of pressure normalisation and data reduction where a calibration map and calibration coefficients are produced. Using a surface fit method, sector map and coefficients of calibration is generated. The coefficient of determination is commonly known as r^2 and is expected to be close to 1. It compares the measured data (θm) and computed data (θc). If the calibration returns a 1, it shows there is a perfect correlation in the sample, and there is no difference between the measured and the computed values. However, if the coefficients of determination are 0, it means the regression equation has not predicted the acceptable percentage in this study. The sectors in the calibration that CFD data replace probe below the expected percentage of coefficients of determination to achieve the optimum required calibration results for accurate flow velocity measurements. The methodology used in the integration of experimental calibration with CFD simulation method is summarised in figure 3.16.

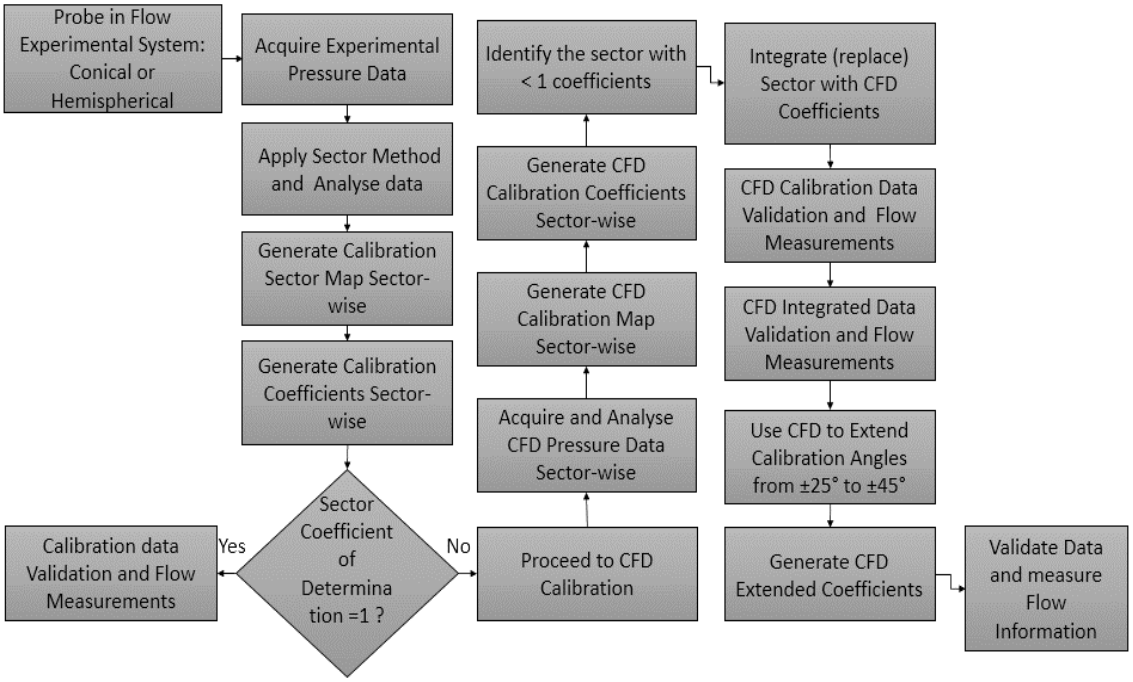

Figure 4.1. CFD Methodology for Probe Simulations

The simple but strong computational fluid dynamic (CFD) technology have been adopted to calculate and simulate the flow parameters measured by conical and hemispherical five-hole pressure probes in air and water having identified the research objectives of this investigation in the

previous chapter. This section presents the CFD innovative methodology used to acquire pressure data from the wind tunnel and pipeline flow domains.

The relevant solver settings and the boundary conditions specified in this investigation are mentioned here. Also, the numerical tests performed for this investigation have been determined. These equations can be found in any CFD related textbooks, and thus, much emphasis is not included in the main body of the present investigation. However, for the completeness of this investigation and readers without in-depth knowledge of Computational Fluid Dynamics, CFD basics have been included. The following sections provide detailed data on numerical modelling used in this present investigation. The CFD package used to achieve this is called Ansys MalateshBarki, Ganesha, T., & Math, M.C. (2014). During the time of this investigation, version 17.0 was the latest version of this package and is therefore used for simulations and analyses. The methodologies adopted for the CFD simulations of the five-hole pressure probes in this study are described in the section below.

4.1.1 Methodology for Comparative Simulation of Five-hole Pressure Probes

Computational fluid dynamics (CFD) is employed to enhance accuracies and eliminate those deficiencies found in experimental calibrations. The CFD method demonstrated in figure 3.17 is the same for both conical five-hole probe and hemispherical five-hole probe.

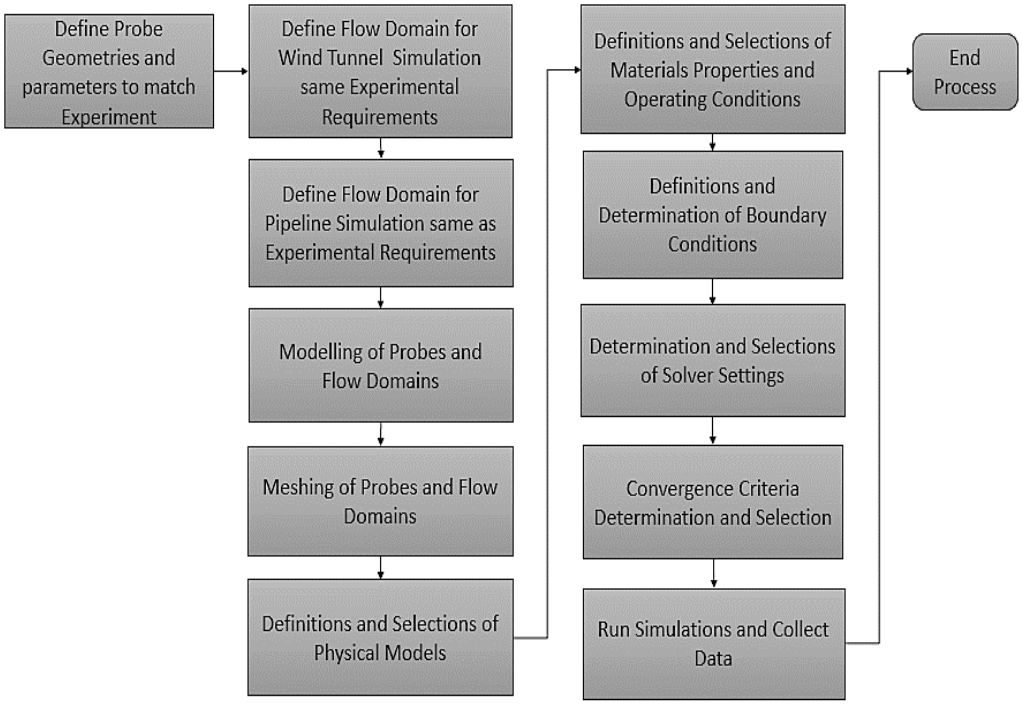

Figure 4.2. CFD Simulations Methodologies

4.1.2 Geometry of the Five-hole Pressure Probe

The flow field around the five-hole pressure probe is simulated mathematically using computational fluid dynamics (CFD). Studying and Solving a set of partial differential equations with predefined boundary conditions are required. Fluent CFD package iteratively solves Navier-stokes equations along with the continuity equation and appropriate auxiliary equations depending on the type of application using control volume formation Naveenji, A., Malavarayan, S., & Kaushik, M. (2010). In this work, the conservation equations of mass and momentum have been solved sequentially with two additional transport equations for turbulent flow. Two types of multi-hole pressure probes that have been chosen for this study are the five-hole conical probe and five-hole hemispherical probe. They are of the same geometry, the same dimension in pressure hole size, shaft length and stem. The experimental and numerical studies involved in the study have been carried out for both probes respectively. Figure 3.18 depicts the geometry and dimensions of the five-hole conical probe.

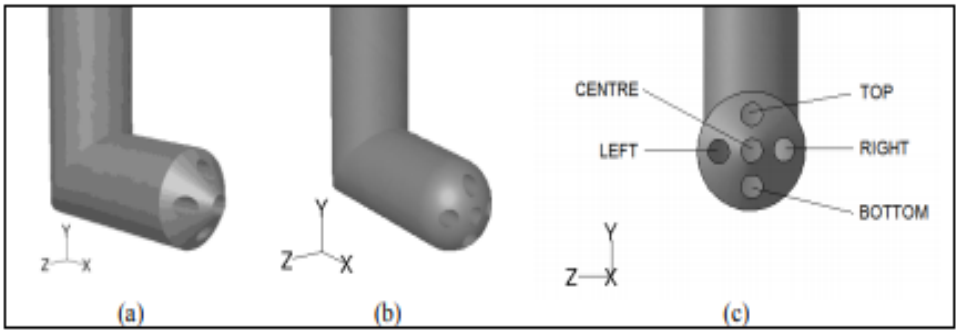

Figure 4.3. CFD pressure probes schematics: (a) Conical head probe; (b) Hemispherical probe; and Pressure tap designation

The physical domain represents the flow around the five-hole probe. The flow approaches the probe from upstream of the domain. The dimensions of the physical flow domain are depicted in figure 3.18. The probe model was imported into a three-dimensional flow domain created in solid works design modeller. The Computational fluid dynamics (CFD) was used to simulate the flow field around the probe. The simulation involves a set of partial differential equations and boundary conditions. Fluent 17.0 is the computational fluid dynamics package used to iteratively solve Navier-stokes equations along with the continuity equations and the appropriate auxiliary equations depending on the type of control volume formulation R´egert, T., & Lajos, T. (2007). The conservation equations for mass and momentum have been solved with two additional transport equations for steady turbulent flow for this study.

4.1.3 Flow Field Conditions

The physical domain represents the flow around the five-hole probe. The flow approaches the probe from upstream of the domain. The dimensions of the physical flow domain are depicted in figure 3.18. The probe model was imported into a three-dimensional flow domain created in solid works design modeller. The Computational fluid dynamics (CFD) was used to simulate the flow field around the probe. It involves a set of partial differential equations and boundary conditions. Fluent 17.0 is the computational fluid dynamics package used to iteratively solve Navier-stokes equations along with the continuity equations and the appropriate auxiliary equations depending on the type of control volume formulation Rauch, R., & Batira, D. (1991). The conservation equations for mass and momentum have been solved with two additional transport equations for steady turbulent flow for this study.

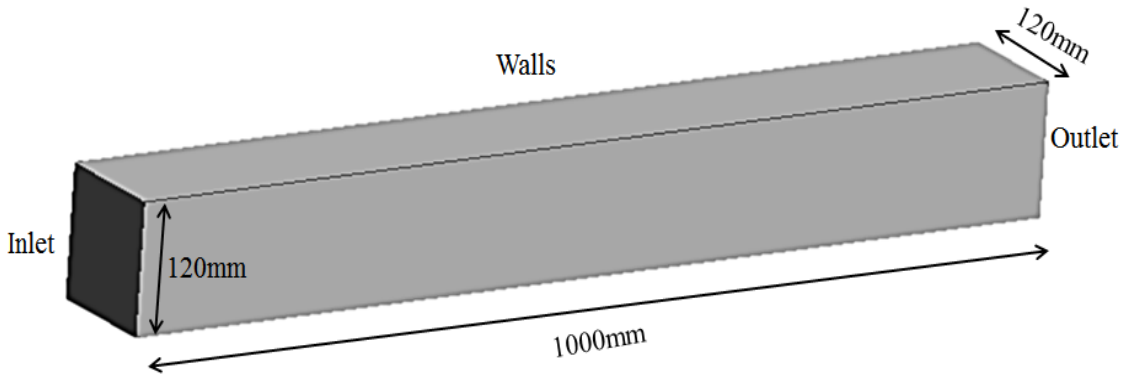

Figure 4.4. Wind Tunnel Flow domain

The geometry of the flow domain is modelled to represent the wind tunnel used to carry out the experiments in this research. The geometry has been created in five different steps. The first part is called the inlet of the tunnel, the second is the test section (the probe body with holes), the third is the tunnel outlet, and the rest are walls. It has been deliberately made so because of the implementation of the boundary conditions of the resolver. The flow domain is designed and modelled to match the experimental setups for accurate results. The length of the flow domain is 1000mm, the height and width are 120mm from the inlet. The probe is placed at the centre of the domain, which is the 500mm upstream, 500mm downstream of the flow domain, 7mm from top and 50mm from the bottom. The arrangement of the probe in flow domain is spatially sufficient to prevent the downstream-imposed 101325Pa ambient atmospheric pressure that stops an upstream effect of pressure field and to prevent the interference of the domain wall boundary layer with the flow field of the model Rauch, R. Batira, D. (1991).

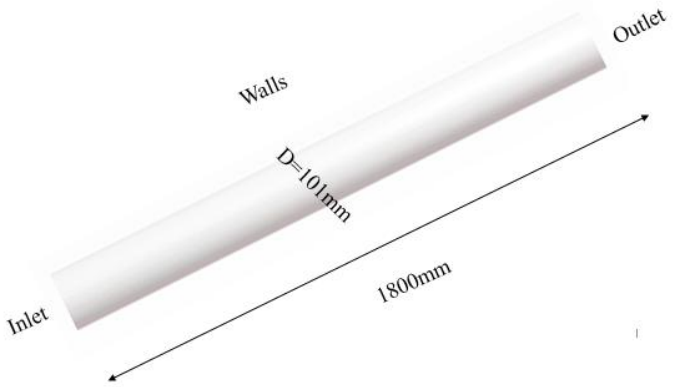

Figure 4.5. Hydraulic pipeline Flow domain

The geometry of the pipeline flow domain used for the numerical studies of the five-hole pressure has been modelled to represent the flow pipeline used in the experimental studies of the research. The model contains the water inlet, a water outlet, and the pipe walls. The CFD simulation setup and the probe positioning is the same as explained in section 3.3.1.

4.2 Numerical Formation

The flow simulation of the five-hole pressure probe models in this study has been carried out using the CFD package fluent 17.0. A set of partial differential equations with predefined boundary conditions is required. Fluent uses the finite volume method to solve the time-averaged Navier-stokes equations and is known for its robustness in simulating many fluid dynamic phenomena. The finite volume method consists of three stages namely; formal integration of the governing equations of the fluid flow over all the finite control volumes of the solution domain, discretisation which involves the substitution of a variety of finite-difference-type approximations for the terms in the integrated equation representing flow processes such as convection, diffusion, and sources. It converts the integral equation into a system of algebraic equations, which can then be solved in the third stage using iterative methods. The first stage of the process is the control volume integration. This step distinguishes the finite volume methods from the CFD methods. The statements resulting from this step express the conservation of the relevant properties for each finite cell volume Malviya, V., Mishra, R., Palmer, E., & Majumdar, B. (2007).

4.2.1 Mass conservation

The mass conservation equation as demonstrated below is valid for compressible and incompressible flows. The source term S_m is the mass added to the continuous phase from the disperse the second phase because of vaporisation of liquid bubbles and any user-defined source Malviya, V., Mishra, R., Palmer, E., & Majumdar, B. (2007).

$$\frac{d\rho}{\delta t} + \text{div}(\rho \mathbf{u}) = 0 \qquad (4.3)$$

4.2.3 Momentum Conservation

Conservation of momentum in the ith direction in an inertial (non-accelerating reference frame is given by the expression shown in equation (4.4) through equation (4.7).

y- momentum:

$$\frac{d(\rho u)}{\delta t} + di(\rho\, v\mathbf{u}) = -\frac{d\rho}{\delta x} + div(\mu\, grad\, u) + S_{Mx} \quad (4.4)$$

y- momentum:

$$\frac{d(\rho v)}{\delta t} + di(\rho\, v\mathbf{u}) = -\frac{d\rho}{\delta y} + div(\mu\, grad\, v) + S_{My} \quad (4.5)$$

z- momentum:

$$\frac{d(\rho v)}{\delta t} + di(\rho\, v\mathbf{u}) = -\frac{d\rho}{\delta z} + div(\mu\, grad\, w) + S_{Mz} \quad (4.6)$$

internal energy equation of state:

$$\frac{d(\rho i)}{\delta t} + di(\rho i\mathbf{u}) = -pdiv\,\mathbf{u} + div(k\, grad\, T) + \phi + S_i \quad (4.7)$$

Where p = p (ρ, T), i = i (ρ, T), and for perfect gas, p = ρRT and i= C_vT.

4.2.3 Meshing of the Flow Domain

Meshing is the process of breaking down a flow domain into several parts, where each part is called a mesh element. The fluid flow governing equations are solved iteratively on these elements. It is therefore important to use appropriate meshing parameters, which include the shape and size of the elements Rauch, R., & Batira, D. (1991). There are many different types of mesh element shapes available, each having its advantages. In the present study, because of the small sizes of the holes in comparison with the overall dimensions of the wind tunnel or the pipe, a polyhedral meshing scheme has been used to carry out numerical simulations. Hence, the flow domain has been divided into some polyhedral sections, as shown in figure 3.19. It can be seen that the meshing size in the vicinity of the holes is significantly smaller than the rest of the flow domain, to capture the complex flow phenomena, in the vicinity of the holes, with reasonable accuracy.

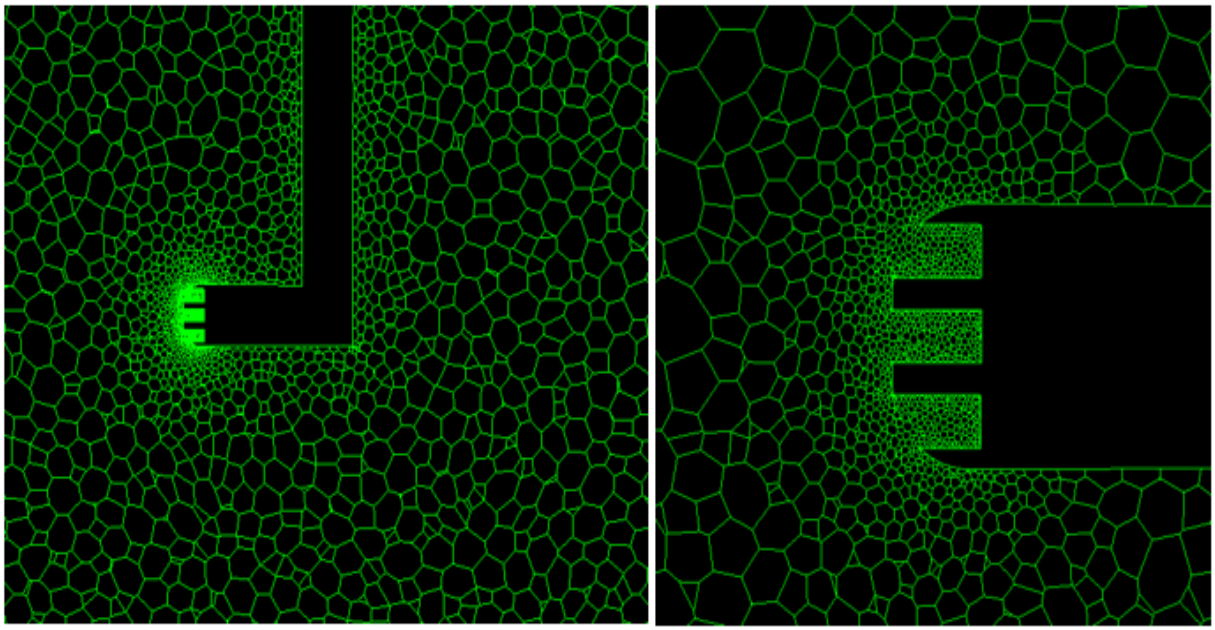

Figure 4.6. The meshing flow domains

4.2.4 Selection of the Physical Models

The flow velocity within the pipeline and the wind tunnel is such that the compatibility effects in the flow domain can be ignored. Hence, a pressure-based solver is used to diagnose the air and water flow in pipelines and wind tunnel using a five-hole probe. The fluid density remains constant in this model and the primary fluid flow parameter being solved iteratively is the pressure within the flow range Shih, T., Liou, W., Shabbir, A., Yang, Z., & Zhu, J. (1995).

The flow in the pipeline and wind tunnel, which are currently in operation, are designed in such a way that they can achieve a fully developed fluid flow. Thus, for a specific pump power and continuous air or water capacity, the pipeline and wind tunnel flows can be considered as steady flows. Hence, a steady state solver is used to diagnose fluid flows in the pipeline and wind tunnel in the present investigation.

Further to the above settings, it is also necessary to model the turbulent flows. It is because the studies carried out in this investigation centres on the turbulent flow of the hydraulic pipelines and wind tunnel. The condition for the external and internal flows such as the ones considered in this work is investigated to be turbulent as Reynolds number is higher than 4000. Thus, the respective streams are turbulent, and a turbulence model is needed to numerically predict the flow parameters

of the turbulence in the pipeline and wind tunnel with acceptable accuracy Barth, T. J., & Jespersen, D. (1989).

Many turbulence models are available in the commercial CFD package, and one of them has been adopted in the present investigation. Each turbulence model has its advantages and disadvantages; this can be found in any CFD book. As far as pipeline and tunnel flows are concerned, because of formation of flow separation of the flow caused by high yaw and pitch angles, the k-ω model is selected for modelling turbulence in the pipeline and tunnel. The main reason for choosing the k-ω model is because of its superiority in precisely and accurately modelling the wake regions and extreme pressure gradients that are expected to occur between the probe and pipe or tunnel walls. It has also shown that the k-ω turbulence model predicts changes in flow parameters with reasonable accuracy Ventikatakrishnan, V. (1993).

k-ω is a two-equation model, divided into two types. The first type is called the standard k-ω model, while the second type is called Shear-Stress Transport k-ω turbulence model. In the present investigation, the SST k-ω model is selected because a mixing function both multiplies the standard k-ω model and the transformed k-ε model, and both models are combined. The mixing function is designed to be one in the near wall area, this activates the standard k-ω model and zero away from the surface, and this, in turn, activates the transformed k-ε model. Furthermore, the definition of turbulent viscosity is modified to take account of the transport of turbulent shear stress Munson, B. R., Young, D. F., & Okiishi, T. H. (2002).

These properties make the SST k-ω model more accurate and reliable for a broader class of fluid flow such as negative pressure gradient flows etc. than the standard k-ω model. Other modifications include the addition of a cross-diffusion term in the ω equation to ensure that the model equations behave appropriately in both near wall areas and the far field areas Shih, T. H., Liou, W.W., Shabbir, A., Yang, Z., & Zhu, J. (1995).

4.2.5 Material Properties and Operating Conditions

The current investigations using the probes to diagnose fluid flow have been carried out in two different media, water for pipeline flow simulation and air for wind tunnel flow simulation. The fluid medium within the pipe has been defined to be liquid-water with a density of 998.2kg/m^3 and the dynamic viscosity of 0.001003kg/m-sec. The fluid medium within the wind tunnel has been

defined to be gas-air with a density of 1.225kg/m^3 and the dynamic viscosity of 0.001789kg/m-sec. One set of investigations was carried out in boundary layer condition using hemispherical and conical head probes respectively, and the other set of the investigations was carried out in standard operating condition using hemispherical and conical probes respectively too.

4.2.6 Boundary Conditions

The boundary conditions that are defined for the investigations are listed in table 3.1.

Table 4.1. Boundary condition and definitions

Boundary	Definition	Units
Hydraulic pipeline inlet	Velocity inlet	2.12m/sec
Wind tunnel inlet	Velocity inlet	15m/sec
Pipe/Tunnel outlet	Pressure Outlet	Pa,g
Pipe/Tunnel wall	Stationary Wall	-

The operating conditions that are given to the solver are the operating pressure of 101325Pa defined at the outlets of each flow system, inlet velocity of 15m/sec for the wind tunnel flow, 2.12m/sec for the hydraulic pipeline flow, these velocities match the experimental velocities (see section 3.1.4 and 3.2.1). Gravitation acceleration is negligible because the investigations are carried out in the horizontal wind tunnel, and hydraulic pipeline flows.

4.2.7 Solver Settings

Application-based solver settings are required to diagnose the flow domain numerically using the five-hole pressure probe. These settings are as follow:

1 Pressure-velocity coupling
2 Gradient
3 Spatial discretisation

The Navier-Stokes equations are solved iteratively. It refers to the linear dependence of fluid flow velocity on pressure and vice versa. In this current investigation, the Semi-Implicit Method for Pressure-Linked Equations (SIMPLE) algorithm for pressure-velocity coupling is included as it converges the solution faster and is very precise for flows with simple flow geometry, such as spheres, cylinders, and the like Shih, T. H., Liou, W.W., Shabbir, A., Yang, Z., & Zhu, J. (1995).

The SIMPLE algorithm provides an approximate calculation of the velocity field using the momentum equation. The term of the pressure gradient is calculated from the preceding iteration or the initial assumption of the pressure distribution. The pressure equation is formulated and solved to obtain a new pressure distribution. The velocities are corrected, and a new set of conservative flows is calculated.

Gradients are necessary for constructing scalar values at cell faces, for calculating secondary diffusion conditions and velocity derivatives. The Green-Gauss Node-based gradient estimation has been used in this study. This is because this scheme reconstructs the precise value of the linear function at the node around the cell-centred values of arbitrary unstructured meshes by solving a specified minimization problem and preventing the spatial accuracy of the second order Shih, T H. Liou, W.W., Shabbir, A., Yang, Z., & Zhu, J. (1995),

The CFD solver saves the discrete values of scalars in cell centres. However, for convection conditions, face values are required and must interact with cell centre values, which is achieved by using an upwind spatial discretisation scheme. The up winding means that face value results from quantities in the cell upstream or downstream relative to normal velocity direction. In the current investigation, for pressure, momentum, turbulent kinetic energy, and turbulent dissipation rate, the second-order upwind scheme is used. Using the second order upwind scheme increases, the accuracy of the results obtained Bendell, E. (2005).

4.2.8 Convergence Criteria

It is often necessary to converge the solution. The convergence of solution shows that the solution has achieved a stable state and the variations in the flow parameters concerning iterative solver have ceased. Therefore, only a converged solution can be considered as one that predicts a solution to a flow problem with a reasonable accuracy Anderson, J.D. (1995).

The default convergence criterion for continuity, velocities in three dimensions and turbulence parameters in Ansys 17.0 is 0.001. It means that if there is a change in continuity, velocity in three dimension and turbulence parameters falls to the fourth place after the decimal point, then the solution is considered to be converged. However, in many practical applications, the default criterion may not necessarily show that changes in the solution parameters have finished. Therefore,

it is often appropriate to monitor the convergence instead of depending on the default convergence criteria.

In the current investigation, the static pressure on the inlet and outlet faces of the pipeline was monitored throughout the iterative process. The solution is considered to be converged when the static pressure in both the inlet and outlet faces has become stable. Therefore, in this case, a durable solution can be that the pressure fluctuation has completely died out or have become cyclical with the same amplitude in each cycle.

After numerically simulating and acquiring pressure values from the probes in the wind tunnel and hydraulic pipelines domain respectively, the novel calibration methods described in section 3.9 are applied. The performances of the conical and hemispherical pressure probes have been analysed for the results. A detailed discussion of these results is provided in the subsequent sections for gauge pressures.

4.3 Preliminary Results

Just like the foundation laid in section 3.8, the CFD numerical pressure datasets are plotted in this section to verify and established the accuracy of the CFD numerical datasets. The variations of the pressures measured by both probes at different yaw and pitch planes have been plotted. The CFD base simulations are carried out at the same velocity where the probe is calibrated in the experimental setup. For brevity, only sample calibration dataset is presented in figure 4.8 through 4.13. For both conical and hemispherical probes, the pressures characteristics shown here exhibits expected trends without sudden changes. Therefore, the calibration data is utilised to calculate calibration coefficients and flow parameters.

4.3.1 Sample Dataset Collected in CFD Wind Tunnel Flow Domain

A set of data were collected using conical and hemispherical in the wind tunnel computational domain at different angles, and different calibration grid are presented in this section. Figure 4.7 depicts the CFD dataset collected at different pitch and yaw angle plane of the conical five-hole pressure prob. The analyses are carried out using pressure coefficients to describe the behaviour of the calibration sample datasets and to compare them with the ones collected experimentally.

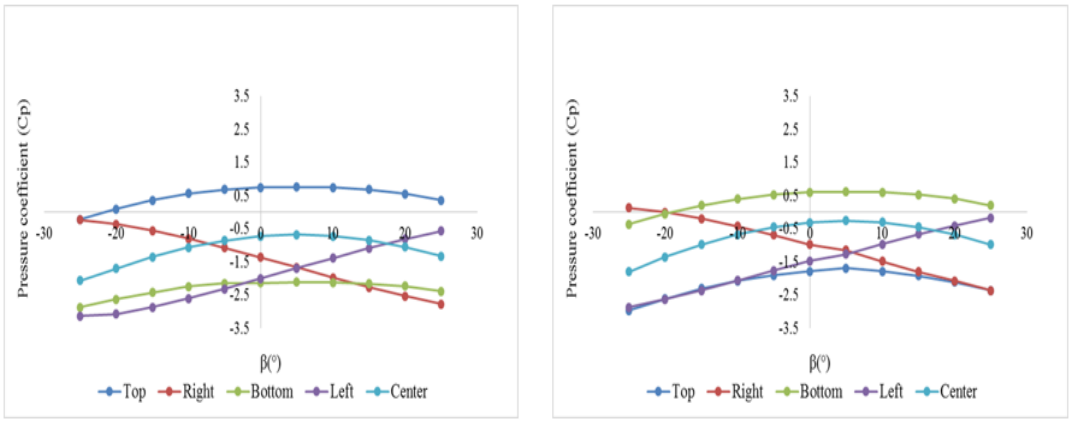

(a) Sample calibration data measured at negative pitch (a) Sample calibration data measured at positive pitch

Figure 4.7. Sample calibration dataset measured by five-hole conical in CFD wind tunnel domain

Top hole, P_1, measured the maximum pressure value at both positive and negative angles but toggled at 10° to -20° . Similarly, the centre hole P_5 measured the second highest pressure but decreased -20° . Also, the bottom hole P_3 measured the highest pressure at -25° and 20° , but decreased from -10° to 25° . It means that the pressure measured by P_3 at high positive angles decreased, as the probe is traversed towards the positive plane of the yaw angle. Also, hole P_2 alternates high and low when the probe is traversed from negative to positive yaw angle planes. Finally, the left hole, P_4 measured lowest pressure values for negative yaw directions, but it gradually increased, as the probe is traversed towards positive yaw direction. As shown in the graph above, the pressure values measured by the probe demonstrate the expected trends of the calibration datasets at without any unreasonable trends. Hence, compared to 3.21, the CFD dataset shows satisfactory distribution and can be used to determine calibration coefficients Taylor, J.R. (1997) and Nowack, C.F.R. (1970).

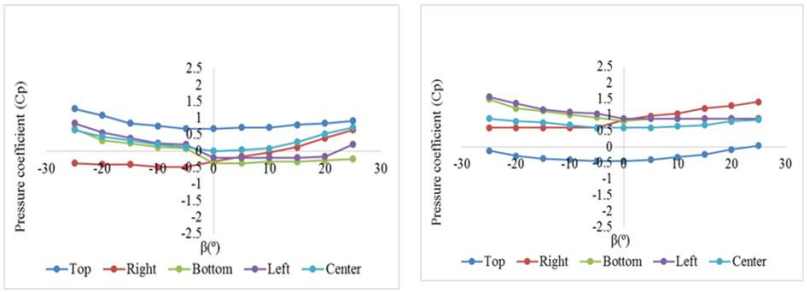

(a) Sample calibration data measured at negative pitch (a) Sample calibration data measured on at positive pitch

Figure 4.8. Sample calibration dataset measured by a five-hole hemispherical probe in CFD wind tunnel Domain

As demonstrated in the top hole, P_1 measured the lowest pressure at this probe orientation. Similarly, the right hole, P_2, maintained symmetrical trend but recorded small pressure compare to positive yaw angles where it recorded the highest pressure compare to the rest of the holes. The bottom hole, P_1, measured the highest pressure at negative yaw direction but maintained a steady trend as the probe is traversed towards positive yaw direction. The same is the case for the left hole, P_4, and the centre hole, P_5. The trend of the plot presented in figure 4.8 shows a symmetrical trend as expected for all the pressure sensed by both the centre hole and the peripheral holes. In comparing this to figure 8.7, it can be concluded without a doubt that the calibration datasets measured by the hemispherical five-hole probe using CFD based numerical method in the wind tunnel flow domain has produced strong pressure datasets that can be satisfactory to determine calibration coefficients Dominy, R. G., & Hodson, H. P. (1993).

4.3.2 Sample Data Collected in CFD Hydraulic Pipeline Flow Domain

Sets of pressure data are collected using conical and hemispherical in the hydraulic pipeline flow domain at different pitch and yaw angles of the calibration grid. Figure 4.9 shows the CFD numerical pressure dataset measured in hydraulic pipeline flow using conical five-hole pressure. The analyses are carried out using pressure coefficients to describe the behaviour of the CFD numerical sample data.

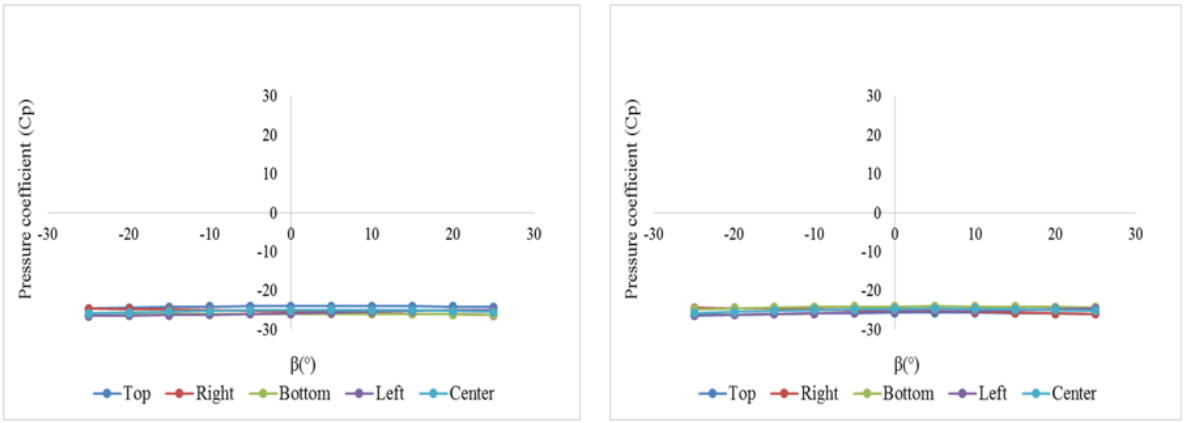

(a) Sample calibration data measured at negative pitch

(a) Sample calibration data measured at positive pitch

Figure 4.9. CFD sample calibration dataset measured by a five-hole conical probe in the hydraulic pipeline flow domain

Figure 4.9 depicts the plot of the calibration datasets collected in the CFD hydraulic pipeline flow domain for the conical five-hole pressure probe. This analysis is to determine the qualitative

accuracy of the CFD numerical calibration dataset of the flow domain. The process of determining calibration coefficients have been used to analyse the CFD pressure sample datasets, and the result shows that the numerical datasets measured the conical five-hole probe maintain a symmetrical and orderly tendency from a negative deviation to a real plane of the probe.

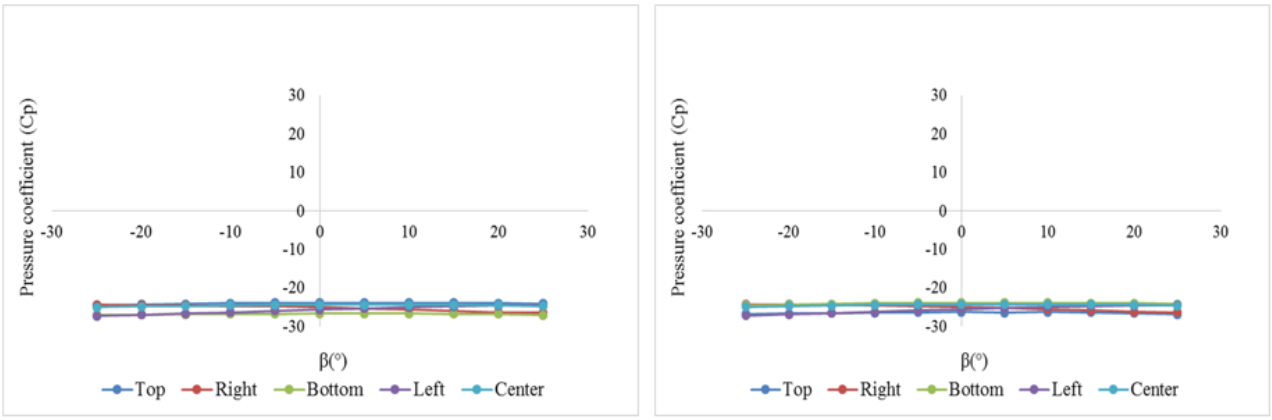

(a) Sample calibration data measured at negative pitch (a) Sample calibration data measured at positive pitch

Figure 4.10. CFD sample calibration dataset measured by a five-hole hemispherical in CFD hydraulic pipeline flow domain

Figure 4.10 depicts the simulation datasets measured using the hemispherical five-hole probe in the CFD hydraulic pipeline domain. This analysis is carried out to determine the quality of the simulation datasets. By qualitatively analysing the data, it can be concluded that the hemispherical five-pit probe not only maintains a symmetrical trend in all angle plane of the probe but also maintains an orderly tendency, which has proven accurate for this study. In comparison, it can be seen that both the conical and hemispherical five-hole pressure probe have the same characteristics and behaviour and have performed accurately. Therefore, these data meet all satisfactory requirements needed in this study to be used to calculate reliable calibration coefficients capable of improving measurement accuracies Lamb, H. (1932).

4.5 Summary

This chapter has described in details the numerical schemes and solution algorithms of the software employed for the computational fluid dynamic (CFD) investigations. The approaches and procedures including technical detailed and operational constraints that have been used in this study have also been discussed in details.

Model geometries, mesh characteristic, boundary condition, and solver setup have been described. The calculations are based on a finite-volume scheme and the standard k-ε model for dissipation of turbulent kinetic energy. Grid density, turbulence modelling, wall function approach and convention parameters have been investigated using parametric analysis. This reason for this is to improve the overall accuracy of the CFD predictions. The preliminary results obtained from CFD simulations for both conical and hemispherical five-hole probe are also analysed and presented for further analyses.

Lastly, the conical and hemispherical five-hole pressure probes have been simulated and measure pressure data in both wind tunnel and hydraulic pipeline CFD flow domains acquired for calibration analyses. For each simulation, the probe is located at the centre of the flow domain, whether it be wind tunnel or hydraulic pipeline. The CFD pressure datasets presented in the figures above show that both probes did very well in sensing pressure values in the flow domains. In comparison to the experimental data shown in section 3.8, the CFD pressure datasets have maintained symmetric trend with strong characteristic capable of improving the overall accuracy of measurements.

Chapter 5 Development of a Novel Calibration Method for Conical Head Five-hole Pressure Probes in Wind Tunnel Flows

In this chapter, the results of the conical five-hole calibration and measurements in wind tunnel flow are shown. These include the air experiments at flow angle α and β ±25 to ±45 in a horizontal wind tunnel with airflow at a flow velocity, U=15m/sec for practical applications of the probes (see chapter 3). This chapter includes results from numerical experiments at the same flow conditions.

As mentioned earlier, there is a need to develop a calibration method that is quicker, more accurate and more flexible. In this chapter, an integrated CFD based calibration method for conical head five-hole pressure probes has been developed. The results obtained after carrying out experiments, and performing CFD simulations, for the cases discussed in the previous chapter, have been presented and analysed in this chapter. Detailed qualitative and quantitative analyses of the results have been carried out on a conical head five-hole pressure probe, in wind tunnel flows. A method for the extension of the probe's calibration range, which is the primary outcome of this methodology, is also included in this chapter.

5.1 Introduction

The main aim of this chapter is the development of an integrated calibration method for conical head five-hole pressure probes, operating in external flow conditions, like wind tunnels. For this purpose, firstly, the conventional method of calibrating a multi-hole pressure probe (as discussed in chapter 3) has been used that is experiments based. The inaccuracies and the limitations of the conventional method have been identified. The accuracy of the traditional method of calibration has been enhanced through the use of Computational Fluid Dynamics (CFD) based techniques. Hence, the same probe has been calibrated using CFD dataset. Based on the comparison of the two datasets (experimental and CFD), an integrated calibration method has been developed. Last but not least, the main limitation of the conventional calibration method, i.e. restricted a range of application and had been removed by developing a bigger database that includes extended numerical dataset

5.1.2 Conventional Method of Calibrating a Five-hole Pressure Probe

As discussed in chapter 3, the conventional method of calibrating a five-hole pressure probe is the one commonly known as a non-nulling method, which is based on the sectoring technique. The pressure data on all the five holes of the probe is recorded at an air velocity of 15m/sec, for a range of pitch (α) and yaw (β) angles. This velocity is calculated by measuring the total and the static pressures of the flow using a Pitot tube, however, because the is no measurement of the static and total pressure in the CFD simulations, the velocity is integrated into CFD calibration to calculate the total and static coefficients. The range of pitch and yaw angles is $\pm 25^{o}$ due to the size of the tunnel, to allow enough space between the probe and the wind tunnel wall to reduce wall effect on the measured pressure values. The sectors are then identified based on the maximum pressure recorded at a particular hole for a specific α and β values. Furthermore, the total and static pressure data is also recorded. Once all the five sectors (corresponding to the five holes of the probe) have been identified, a pressure normalising technique is then applied to the pressure data from the sectors.

The pressure normalising technique defines the non-dimensional pressure coefficients for all the five sectors of the probe. The details of the pressure normalising technique have already been discussed in chapter 3. After that, a dataset reduction algorithm is applied to the pressure dataset, using a sixth order polynomial curve-fitting regression technique. The dataset reduction method generates the calibration coefficients and the coefficients of determination (r^2). These calibration

coefficients are used in equations like equation (3.1) to determine the flow parameters of interest. A flow chart summarising the conventional method of five-hole pressure probe calibration is presented in figure 5.1.

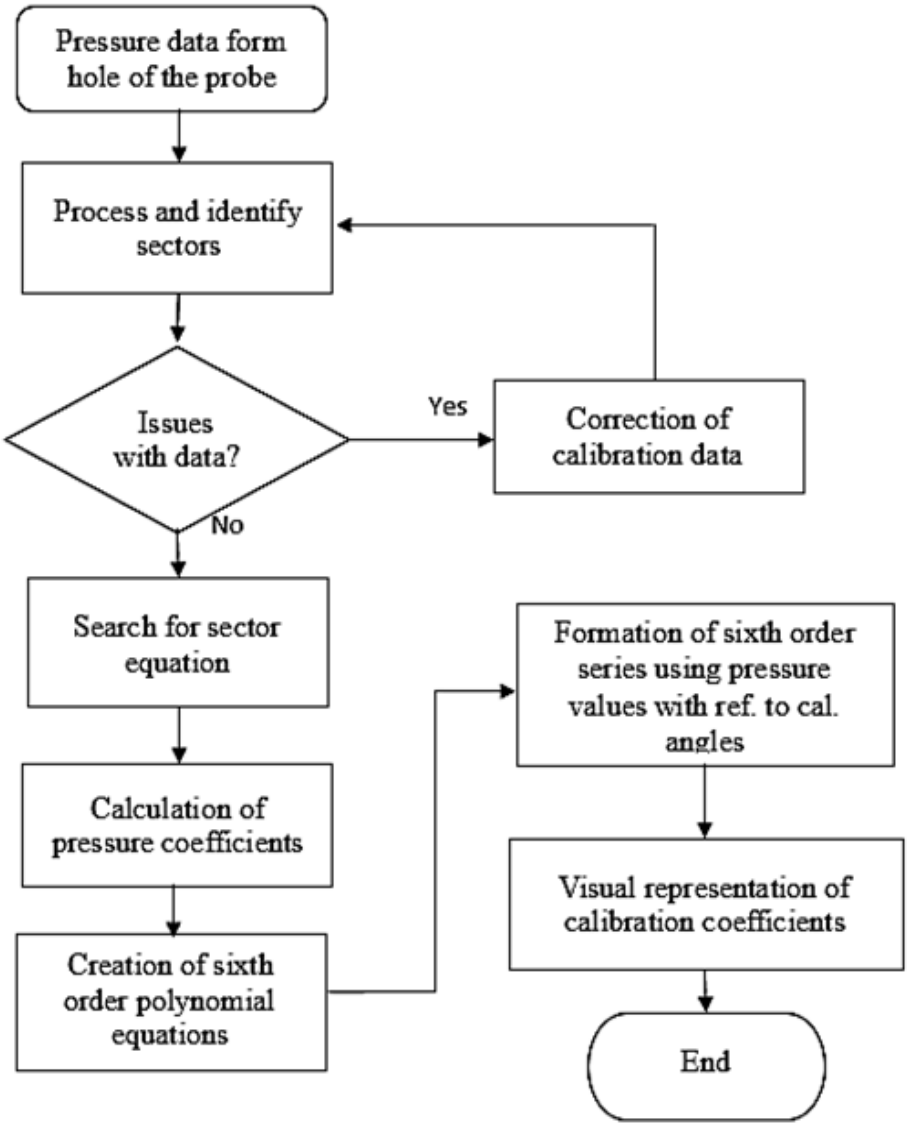

Figure 5.1. A flowchart of the conventional calibration method

The experimental calibration is carried out to find where there is a defect in the process and using CFD numerical pressure dataset; the defect is corrected. First, the pressure probe is positioned at the centre of the wind tunnel, and pressure dataset is recorded pitch and yaw and wise. These datasets are sorted to identify which hole of the register highest to the least pressure values within the calibration grid to generated sector map of the calibration as the pressure distribution within the holes. Thereafter, sector equations are used to calculate and analyse the non-dimensional pressure

quantities of the calibration parameters. The next step is to apply sixth order curve-fit polynomial analysis to the non-dimensional pressure values to generate the calibration constants. Analyse the coefficient and identify the sector that needs to be replaced with CFD numerical dataset.

5.1.3 Experimental Calibration of a Conical Head Five-hole Pressure Probe

A five-hole pressure probe, the details of which have already been discussed in chapter 3, has been calibrated using the conventional method of calibration. The conventional method of calibrating the pressure probe has been used on the experimental pressure data obtained on the probe's holes. The experiments have been performed in a wind tunnel facility; hence, the flow regime is external flow. One of the main concerns while calibrating a five-hole pressure probe is to obtain a high-quality calibration/sector map with minimum errors. Theoretically, the calibration map should be accurate, repeatable and of an appropriate resolution, although this is hardly the case due to many error sources associated with the calibration procedures, such as geometric imperfections associated with the probe, misalignment, measurement errors, human errors etc. It is therefore recommended carrying out the calibration at least three times to obtain a stable and accurate sector map that will guarantee the repeatability of the calibration dataset.

At an air velocity of 15m/sec, the probe has been rotated in the yaw direction, at a particular pitch angle. The yaw angles range covered $\pm 25^{o}$, with readings taken at 5^{o} increments. The same has been carried out then at another pitch angle. The range of pitch angles covered is $\pm 25^{o}$, with readings taken at 5^{o} increments. The pressure data of all the five holes, including the static and total pressure data, has been recorded four times in subsequent runs, to establish the repeatability of the calibration process. Average gauge pressure values, summarised in appendix 5.1a, have then been considered for further processing.

It can be seen in appendix 5.1a that for $\alpha = -25^{o}$, the highest pressure is recorded at the bottom hole of the probe in the range of $\beta = -25^{o}$ to -10^{o} . From $\beta = -5^{o}$ to 25^{o} , the centre hole registers the highest pressure for same pitch angle α. The sectors have been identified based on the highest pressure a particular hole registers. For example, for all the combinations of α and β angles, whenever the centre hole registers the highest pressure, all those data points are grouped to form sector 5. Similar is the case with the other holes, i.e. sector one for top hole, sector two for right hole, sector three for the bottom hole and sector four for the left hole. The sector map for the conical head five-hole pressure probe is shown in figure 5.2, indicating the holes that register

maximum pressure for a particular pitch (α) and yaw (β) angles. This method has been depicted to improve the accuracy of measurements Akshoy, R. P., Ravi, R.U., & Anu, J. (2011).

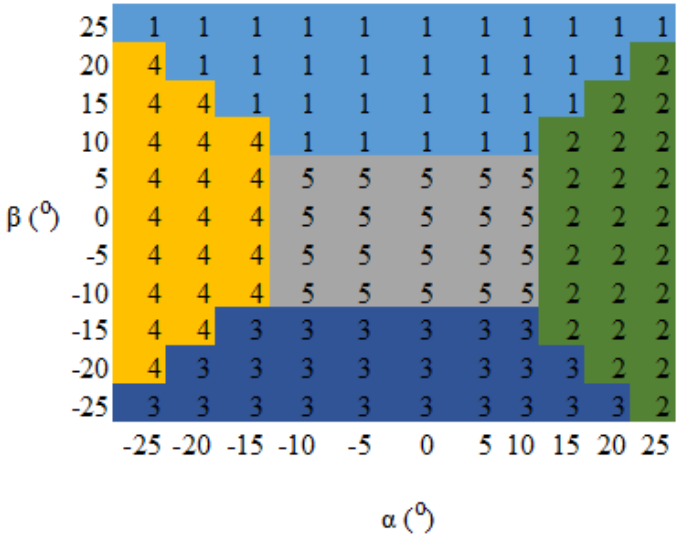

Figure 5.2. Experimental sector map for wind tunnel calibration

Figure 5.2 is the calibration sector map of the five-hole pressure probe. The y-axis of the map represents the pitch angle plane of the probe, while the x-axis represents the yaw angle plane of the probe. At each combination of pitch and yaw angles, the probe measures five different pressure values. Therefore, for a combination of pitch and yaw angle in calibration range of ±25^{o} , the pressure probe attempts to demonstrate the schematic numbering of its five holes according to the pressure it measures in the flow field. As shown, the area covered the top hole (sector 1) of the probe is represented by a number (1), while the areas covered serves by the number (3) are the calibration grid points covered by the bottom hole (sector 3) of the probe during calibration.

Similarly, the area covered by the number (2) demonstrates the calibration grid covered by the left hole (sector 4), while the areas covered by the number (2) shows the calibration grids covered by the right hole (sector 2) of the probe during calibration. Also, the centre areas covered by the number (5) shows the grid points covered by the centre hole (sector 5) in the entire calibration process. As the probe is positioned against the oncoming flow, in a combination of different pitch and yaw planes, the probe senses gauge pressure values that became the calibration dataset.

It can be seen in that the centre hole (sector 5) registers maximum pressure from pitch angle α=-10^{o} to 10^{o} and at yaw angles (β) in the range of -10^{o} to 5^{o} . Similarly, the top hole (sector 1)

registers the highest pressure for a value of α from -25º to 25º and at βin the range of 10º to 25º . However, at higher pitch angles (beyond ±10º), the yaw angle range becomes narrower. It is the case with the bottom hole (sector 3). The side holes (sectors 2 and 4) register maximum pressure corresponding to α=15º to 25º and -15º to -25º respectively, where the yaw angle ranges from -20º to 20º for both the holes. It can be further noticed that the sector map is not although mostly symmetrical because a dimensionally perfect and balanced five-hole pressure probe is very difficult to manufacture due to the small size of the probe and inherent machining imperfections.

After identifying the sectors, the next step is to convert the pressure data of the sectors into the calibration coefficients. The calibration coefficients are obtained using sixth order polynomial curve fitting technique. A flowchart showing the systematic approach involved in converting the pressure data into the calibration coefficients and calibration constants is depicted in figure 5.3. These steps are followed for all the proposed calibration method in this study.

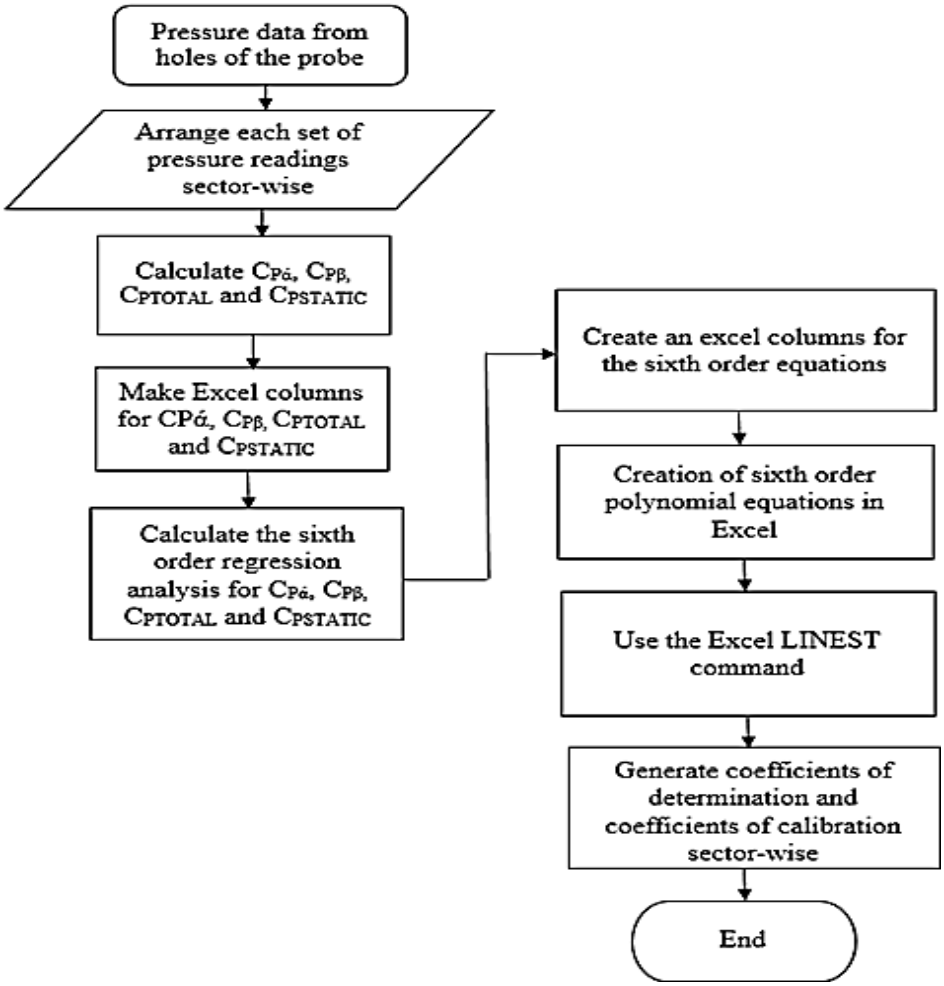

Figure 5.3. A flowchart of pressure conversion to calibration coefficients

The resulting calibration coefficients are recorded for further processing. Calibration coefficients, representative of sectors 1 and 5, are summarised in appendix 5.1b and 5.1c.

The accuracy of the calibration coefficients is gauged using a coefficient of determination (r^2). It compares measured values against the computed values and ranges from 0.0000 to 1.0000. If it records a value of 1.0000, this shows that there is a perfect correlation in the sample, or in order words, there is no difference between the measured and the computed pressure values. On the other hand, if the coefficient of determination is 0.0000, there is no correlation between the measured and the calculated pressures. Hence, this value is, expected to be very close to 1.0000 theoretically but most difficult to achieve experimentally. However, due to the issues above with the pressure measurements and the manufacturing of the probes, a coefficient of determination equal to 1.0000 is difficult to achieve (refer to section 3.9 for a detailed explanation). The coefficients for determination for all the sectors have been summarised in table 5.1.

Table 5.1. Experimental coefficients of determination

Calibration parameters	Sector 1 (r^2)	Sector 2 (r^2)	Sector 3 (r^2)	Sector 4 (r^2)	Sector 5 (r^2)
Pitch angle (°)	0.9401	1.0000	0.6925	1.0000	0.7575
Yaw angle (°)	0.7924	1.0000	0.9898	1.0000	0.8649
Total pressure (Pa)	0.9998	1.0000	0.9978	1.0000	0.9084
Static pressure (Pa)	0.9998	1.0000	0.9976	1.0000	0.9117

It can be seen in table 5.1 that within sectors 2 and 5 (i.e. right hole and the centre hole) a perfect correlation with the measured pressure data has been achieved., For sectors 1 and 3, the correlation is entirely accurate, except for the yaw angle in the case of sector 1 and pitch angle in the case of sector 3. Similarly, for sector 4, significant discrepancies in correlating both the pitch and the yaw angles can be noticed. In the present study, a correlation of more than 90% has been considered adequate for correlating the measured and the calculated coefficients, and any correlation below 90% is not acceptable for calibration. It is expected that the measurements based on these correlations will not yield accurate dataset for actual flow measurements. Therefore, additional high accuracy dataset is needed that can be used alongside the measured dataset, to develop correlations that have better validity by incorporating data obtained using CFD based numerical simulations.

It is generally accepted that these coefficients of determinations must perform excellently well for accurate velocity measurement, however, due to the manufacturing process and procedures that five-hole probes it is difficult to achieve this result 100% without bulky computational

mathematical models. This research has attempted to perform pressure measurements computationally with the same experimental conditions and replace those malfunctioning pressures in an attempt to achieve calibration coefficient of determinations with 100% accuracy using the same dataset analysis and pressure normalisation proposed by Akshoy, R. P., Ravi, R. U., & Anu, J. (2011) to avoiding bulky computational mathematics.

The Accuracy of the pitch and yaw angles calibration parameters is greatly influenced by the low resolution of the manual traversing device; this is by far the dominant source of error when it comes to pitch and yaw determination. Table 5.2 demonstrates that the set of pressure coefficients that have been used to generate the calibration coefficients of determinations gives some errors that need to be replaced for both flow angles before using the data to determine flow velocity that is acceptable. It is essential at this point to note down that some coefficients shown in figure 5.2 will be retained (showing >90% correlation), while the rest of them will be replaced by the strong CFD based coefficients, to improve the accuracy of the calibration method.

A comparison of flow velocity components at 15m/sec average flow velocity has been carried out between the actual velocity values and the velocity values using the calibration coefficients obtained to access the validity of the calibration. The actual velocity components have been obtained for a known flow field, i.e. at -25^{o} in pitch angle direction and at various yaw positions. This comparison is shown in figure 5.4. It can be seen that there are significant differences in the velocity components between the actual and the calibration results. For example, the average x-component of the flow velocity from the calibration equation is 10.3% lower than the actual flow velocity in x-component.

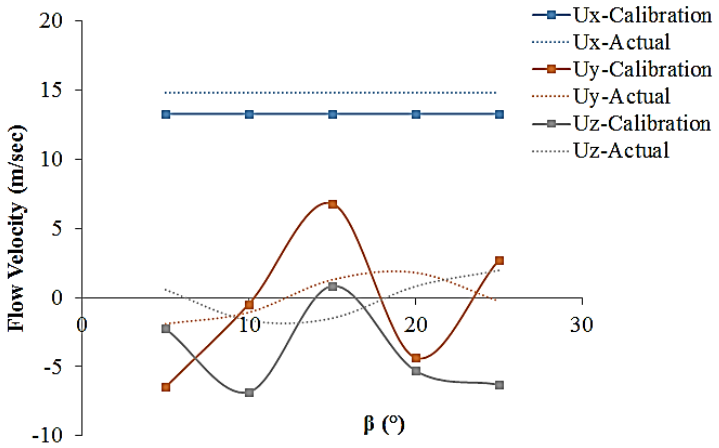

Figure 5.4.Validation of the experimental calibration dataset

Figure 5.4 further demonstrates the strength of the wind tunnel calibration data in estimating external flow information. The measured flow angle and velocity have been compared with known values of flow angle and velocity for the calibration dataset. The figure indicates that the probe measurements for $\theta<25^{o}$ has a pitch error of 0.5^{o}, and yaw angle error within 1.2^{o}. The errors in the trend for velocity are because of wall proximity and turbulence intensities in the flow.

5.1.4 Experiment Measurements Error Analysis

Error analysis is helpful in this regard, where the following parameters are a useful combination. The statistical results shown in table 5.1 reveal that the goodness of fit (r^2) values in the computation of pitch and yaw angles and total and static pressures. Where there is less value compare to the other, the focus is made on better prediction, and this is where CFD is used. The exact uncertainty of velocity and pressure measurement is not just a function of the curve-fits, which are dependent upon the probe design, but upon the accuracy of the five pressure measurements.

The error analysis carried out here using equations (5.1) based on the pressure normalisation techniques and dataset reduction methods chosen for this study, and therefore, it is considered as computational errors which have huge connections with the experimental accuracy of the five-hole pressure probe and experimental errors involved during dataset generations. Table 5.2 shows the summary of all combinations of pressure and data reduction technique and measurements

$$\delta_{\theta} = \sqrt{\frac{1}{n}\sum_{i=1}^{5}(\theta_{\mathrm{i,calculated}} - \theta_{\mathrm{actual}})^2} \tag{5.1}$$

Table 5.2. Uncertainties and standard errors in measurement for conical five-hole pressure probe

Statistical parameters	Pitch angle (^{o})	Yaw angle (^{o})	Total pressure (Pa)	Static pressure (Pa)	U	U_x	U_y	U_z
Standard error	0.1173	0.2614	0.0052	0.0042	0.0095	0.1307	0.7183	7

Table 5.2 represents the computed errors from the error analysis for all the flow parameters measured using the conical five-hole pressure probe in wind tunnel flow. In general, it is possible to notice that the error in y and z-component velocities is quite high compared to others. The reason

for this is that the conventional calibration method could not be able to maintain the level accuracy that is expected in modern measurements. Another fact notice here is that the errors on the yaw angle of the flow are a bit higher than the pitch angle.

The reason for this can be identified with the higher uncertainty generated by the manual yawing mechanism of the traverse system. Furthermore, the accuracy in the method can be noticed in the total and static pressure measurements. Although the recorded errors in y and z component velocities are high, however, the probe has performed averagely well in predicting flow parameters of the wind tunnel system.

5.2 Numerical Simulation of the Calibration Process for a Conical Five-hole Probe

A numerical approach has been applied, using the same method as an experimental approach, to carry out the numerical calibration of a conical head five-hole pressure probe. Airflow within the wind tunnel has been simulated at 15m/sec (see chapter 4), which is the velocity magnitude of the wind tunnel flow has been used as inlet velocity for CFD simulations under the same flow conditions. The pressure dataset on the five holes of the probe have been recorded for processing (see section 3.9 and figure 5.3 for the approach of calculating calibration coefficients and constants) and the results obtained are shown in the following sections.

5.2.1 Flow Field Analysis around a Conical Head Five-hole Probe

The interaction between the pressure probe geometry is quite complex. It is required to understand this interaction to ascertain whether the measurements are accurate. The static gauge pressure and flow velocity magnitude variations in the region of the conical head five-hole pressure probe have been shown in figure 5.5. The flow parameters variations shown in the figure corresponds to in lent flow velocity magnitude of 15m/sec, at $\alpha = \beta = 0^{o}$. It can be noticed that the presence of the probe disrupts the flow within the wind tunnel. As the probe offers resistance to the flow, the static gauge pressure is higher on the front section of the probe, while due to flow separation, the static gauge pressure is low at the probe's leeward side. Some distance downstream the probe, the static gauge pressure recovers. Hence, the effect of the probe on the static gauge pressure is limited to the distance downstream where the pressure recovers. It is worth noticing that the static gauge pressure is highest at the holes of the probe. It can also be seen that the effect of the stem of the probe is very

limited near the sensing head and hence it can be assumed that probe insertion is not affecting the flow pattern drastically at the measurement location.

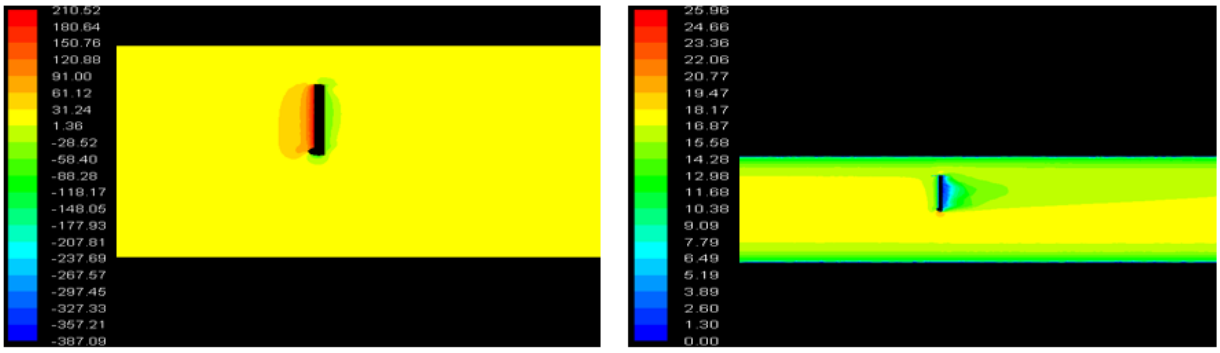

(a) Flow static gauge pressure (b) Flow velocity magnitude

Figure 5.5. Variations in (a) flow field static gauge pressure and (b) flow field velocity magnitude in the vicinity of the probe at α=β=0º

Figure 5.5(b) depicts that the velocity field is significantly affected by the presence of the five-hole pressure probe. The probe can be seen to disrupt the flow field quite some distance downstream the probe, in the wake region of the probe. At the surface of the probe, and the holes, because of the no-slip boundary condition, the flow velocity magnitude is zero. It is worth noticing that although the average flow velocity is 15m/sec, due to resistance to the flow offered by the probe, the flow accelerates up to 17.4m/sec at the periphery of the conical head of the probe. However, at these measurement locations, the flow field appears undisturbed Malviya, V., Mishra, R., & Palmer, E., (2015).

5.2.2 Effect of Flow Angle on the Flow Field around the Conical Head Five-hole Probe

As discussed earlier that the non-nulling calibration method involves rotating the probe in both pitch and yaw directions, it is essential to analyse the flow field associated with the probe at a non-zero angle. Hence, figure 5.6 depicts the variations in the static gauge pressure and the flow velocity magnitude in the vicinity of the conical five-hole pressure probe at 15m/sec average flow velocity, and at $\alpha = 0^{o}$ and $\beta = 25^{o}$. It can be seen in figure 5.6(a), in comparison with figure 5.5(a), that the highest static gauge pressure is 90.5Pa, which is about 70% less than observed in case of $\alpha = \beta = 0^{o}$. Hence, the pressure variations in the case of $\beta = 25^{o}$ are significantly less than at $\beta = 0^{o}$. Moreover, it can be seen that the effect of the probe is limited to a much shorter distance downstream of the probe. In particular, near the sensing head now different pressure distribution

can be seen as the velocity vector is now making an angle with sensing plane. It an indication that the simulation is capturing the effect of three-dimensional velocity field very accurately.

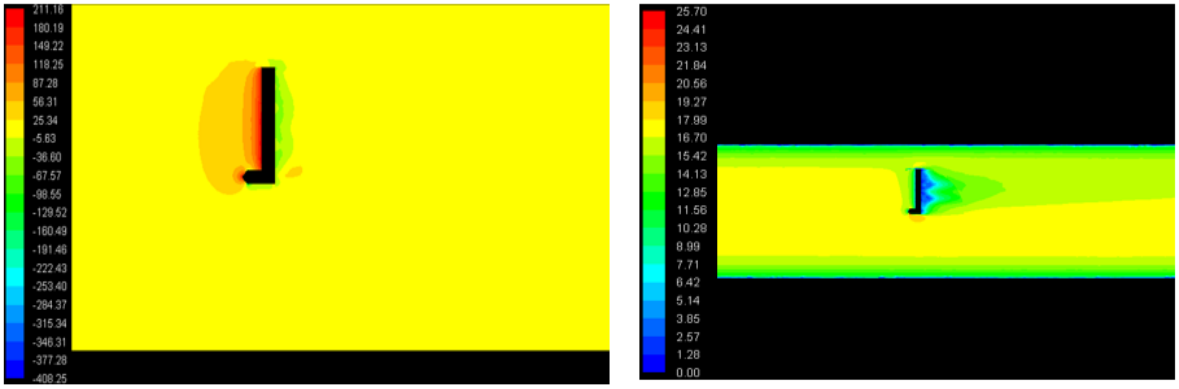

(a) Flow static gauge pressure (b) Flow velocity magnitude

Figure 5.6. Variations in (a) flow field static gauge pressure and (b) flow field velocity magnitude in the vicinity of the probe at $\alpha=0^{o}$ and $\beta=25^{o}$

In comparing the flow velocity magnitude variations between figures 5.6(a) and 5.5(b), it can be seen that the effect of the presence of a probe is restricted to a much smaller region. The highest flow velocity magnitude is 4% higher than observed in the case of $\beta=0^{o}$ Malviya, V., Mishra, R., & Palmer, E., (2015).

5.2.3 Justification for using Numerical Simulations for Calibration

The numerical simulations have been used in the present study to enhance the accuracy of measurements. As seen in figure 5.4, there are significant differences between the actual flow velocity measurements and the one obtained through the calibration process. These differences exist because the coefficients of calibration (in table 5.1) are not entirely appropriate for use and involve many errors. Moreover, using numerical techniques, a large number of numerical experiments can be carried out in a relatively shorter period, which adds to the benefits of numerical simulations over real-world experiments. It is further supported by the fact that although there are inherent geometric imperfections in the probes, numerical techniques generate geometrically perfect models, hence, reducing the errors associated with the manufacturing characteristics of the probes.

In any calibration methodology, it is expected that the variable for which calibration is being carried should have first order effects. All other error contributing variables should be minimised. In this regard, CFD simulations can be useful to bridge the gaps in experimental calibration dataset,

strengthen the experimental calibration dataset and eliminate unwanted effects from the experimental calibration datasets.

The most obvious benefit of using numerical simulations for the calibration of five-hole probes is that numerical simulations can depict the interaction between the flow and the probes, which is very difficult to achieve through experimental methods. Furthermore, using CFD numerical simulations, higher accuracy in calibrations and measurements results can be obtained in this study. Hence, the use of CFD numerical simulations in the calibration of five-hole pressure probes can prove to be extremely useful as far as enhancing the accuracy of the probes calibration datasets and calibration coefficients for realistic measurements is concerned.

5.2.4 Calibration of the Conical Probe CFD Numerical Data

A conical five-hole pressure probe has been numerically simulated using advanced Computational Fluid Dynamics (CFD) based techniques, in a wind tunnel. Both the conical pressure probe and the wind tunnel walls have been modelled as no-slip boundaries, mimicking the real-world conditions. Integrating real-world application in to CFD datasets for calibration and measurement purposes only, the average flow velocity of 15m/sec measured in the wind tunnel measured using a Pitot tube has been kept the same in the calibration of numerical dataset, as in the case of experiments outlined in section 5.1.3, for useful comparison and accurate calibration purposes. The primary goal here is to obtain highly precise calibration coefficients using controlled CFD numerical simulations datasets. The accurate CFD based numerical calibration coefficients will replace the erroneous experimental coefficients. The process of replacing CFD dataset with experimental datasets is known as the novel calibration method for improved accuracy of the measurements of fluid flows, which is the first novel calibration method in this study.

Similar to the experimental calibration process, the pressure data corresponding to the holes of the probe have been recorded. The pressure values have been converted into non-dimensional pressure coefficients using the approach in figure 5.3. Data reduction technique, same as before, has then been applied on these coefficients to form the sixth order polynomial equation as described in figure 5.3. The sector map from the numerical calibration is shown in figure 5.7. The numerically obtained sector map is the same as in the case of the experimental sector map of figure 5.2. However, a close examination of the pressure data summarised in appendix 5.2a and 5.2b, corresponding to sectors 1 and sector 5 of the conical five-hole pressure probe, depict that the pressure values are significantly

different. The primary reason for these differences in the pressure values is the fact that numerical simulations have been performed in a much more controlled manner as compared to real-world experiments, where many errors come into play, such as human errors, measurement errors etc. Hence, it is expected that the coefficients of determination from numerical simulations will be much closer to 1.0000 as compared to the coefficients of determination from the experiments Hale, M.R. (1967).

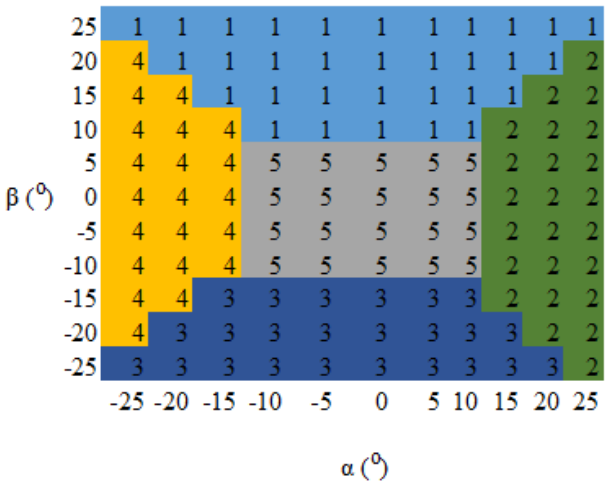

Figure 5.7. CFD based numerical sector map for wind tunnel calibration

Figure 5.7 depicts the calibration map generated numerically by the conical five-hole pressure in a wind tunnel flow. The y-axis of the map represents the yaw plane of the probe, while the x-axis represents the pitch angle plane. As shown in the figure, the areas marked by the number one (1) are the grids points covered by the top hole (sector 1) of the probe during calibration, while the area marked by the number three (3) are the grids covered by the bottom hole (sector 3) of the probe. Furthermore, the areas marked by number four (4) are the grids points of the calibration map covered by the left hole (sector 4), while the areas marked by number two (2) are the grids covered by the right hole of the probe (sector 2). Also, the centre area of the calibration map marked by number (5) is the area in the grid covered by the centre hole (sector 5) of the probe.

The top hole of the conical five-hole probe as shown in the figure above has the top hole (sector 1) registers the highest pressure from $\alpha = -25^{o}$ to 25^{o}, while at yaw axis, $\beta = 10^{o}$ to 25^{o}, however, at higher pitch angles (beyond $\pm 10^{o}$), the yaw angle range becomes narrower. The same is true with the bottom hole (sector 3). The side holes (sectors 2 and 4) register maximum pressure from $\alpha = 15^{o}$ to 25^{o} and -15^{o} to -25^{o} respectively, where the yaw angle registers pressure from $\beta =$ -

20° to 20° for the holes right hole (sector 2) and β = -25° to 20° for the left hole (sector 4). Furthermore, it can be seen that the centre hole (sector 5) registers maximum pressure from pitch angle α = -10° to 10° at yaw angles (β) of -10° to 5° . It can be noticed that the conical five-hole probe sector map is not perfectly symmetrical even though it was numerically generated. It is because a dimensionally perfect and symmetrical five-hole pressure probe is very difficult to design and perfectly placed inside the flow domain due to human factors.

As expected, the coefficients of determination from the numerical simulations for all the sectors are 1.0000 as summarised in table 5.3. Hence, the calibration carried out using numerical simulations is much more accurate than from the experiments. However, many factors do affect the accuracy of the numerical data as well. The factors include the choice of the turbulence model used, appropriateness of the boundary and operating conditions, accuracy of the material properties (especially the density of the fluid at a particular temperature), the convergence criteria employed etc. Because all these affecting parameters have already been taken care of in the present study, most of the coefficients of determination are equal to 1.0000. However, based on the user's experience, and the time constraints for calibrating probes, the accuracy of the calibration process can vary significantly. Hence, a careful balance should be maintained between experiments and the numerical simulations (see section 3.9 for a detailed explanation).

Table 5.3. CFD based numerical coefficients of determination

Calibration parameters	Sector 1 (r^2)	Sector 2 (r^2)	Sector 3 (r^2)	Sector 4 (r^2)	Sector 5 (r^2)
Pitch angle (°)	1.0000	1.0000	1.0000	1.0000	0.9999
Yaw angle (°)	1.0000	1.0000	1.0000	1.0000	1.0000
Total pressure (Pa)	1.0000	1.0000	1.0000	1.0000	1.0000
Static pressure (Pa)	1.0000	1.0000	1.0000	1.0000	1.0000

In comparing table 5.1 to 5.3, it can be seen that the CFD based numerical calibration produce a far more accurate result than the experimental calibration. Therefore, numerical pressure data for sector 1, 3, and five have been integrated into experimental pressure data of sector 1, 3, and 5 because it achieved the required accuracy level for coefficients of determination. It is carried out to improve the overall experimental calibration accuracy. These integrated data are used to generate new sets of calibration data that required applying the calibrations procedures stated above to produce new sets of calibration coefficients; this is carried out in section 5.3. Figure 5.8 depicts the validity of the CFD based numerical calibration dataset that was used to measure wind tunnel flow velocities to

confirm and validate the accuracy of the numerical calibration method. The measurements were carried out and compared against a known flow field. It can be seen that the numerical calibration results are significantly accurate flow velocity measurements, for the three velocity components considered in the present study, as compared to the experimental calibration results above in figure 5.4.

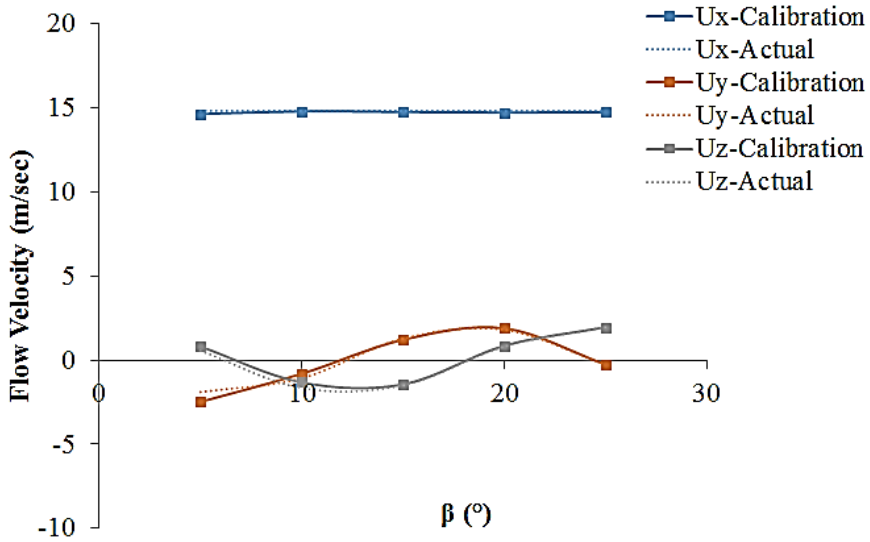

Figure 5.8. Validation of the CFD based numerical calibration dataset

The calibrated probe was used for the measurement of flow velocity components in the principles directions of cylindrical polar coordinates, (x, y, z) and the static pressure in wind tunnel flow field. The determined values of the velocity components were measured concerning actual and calculated flow angles. The y-axis of the graph represents flow velocity, while the x-axis represents flow angles. The x- component velocity measured using calibrated data shows a very accurate value in comparison with the x-component velocity measured using actual value. It can be seen that there is about 98% accuracy in both data, this demonstrates the accuracy of the numerical calibration method as also shown in table 5.3. Furthermore, y-velocity components and the z-velocity components also show good agreements with each other in the region of about 95% accuracy for both calibrated and actual data. In comparison to figure 5.4, it can be seen that figure 5.8 produce better accuracies in all velocities for actual and calibrated values. Figure 5.8 is proof that the conventional calibration method of the five-hole pressure probe can be significantly improved using CFD numerical data.

5.2.5 Numerical Measurements Error Analysis

The error analysis was performed for all parameters measured by the conical probe in wind tunnel flows formula and principle stated in section 5.1.4. The results are shown in table 5.4.

Table 5.4. Standard errors in measurement for conical five-hole pressure probe

Statistical parameters	Pitch angle (°)	Yaw angle (°)	Total pressure (Pa)	Static pressure (Pa)	U	U_x	U_y	U_z
Standard error	0.0302	0.0018	0.005	0.004	0.0029	0.1073	0.5010	0.2421

As seen in table 5.4, compared to table 5.2, the CFD based numerical calibration has increased the accuracy of measurement by reducing y- component velocity error to 0.5010m/sec, similarly, the z-component velocity error has been reduced to 0.2421m/sec. Compare pitch and yaw measurement; both parameters have increased their accuracies to almost 100%. The effect of CFD based calibration have a tremendously positive influence on a five-hole probe calibration and measurements can be felt here as established in this table.

5.3 Development of an Integrated Calibration Method for Conical Head Five-hole Probe

Although numerical simulations provide useful results, it will not be appropriate to use simulation-based calibration method for real-life applications without proper integration with real-life systems. Experimental data provide a valuable reference for the development of calibration methodology for real-life applications. As discussed above, the experimental calibration coefficients that showed a correlation of less than 90% (sector 1, 3, and 5) have been replaced by more accurate numerical calibration coefficients as shown in table 5.5. Hence, a novel calibration method is developed here that integrates the advantages of both the experiments and the CFD based numerical simulations. The steps involved in the integrated calibration method are as follows:

1. Carry out experiments and record pressure data measured by the holes of the five-hole conical probe with required probe orientations
2. Identify the sectors of the probe with fewer correlations (<90%) of calibration coefficients of determinations
3. List down the calibration coefficients and the coefficients of determination

4. Note down those calibration coefficients where the coefficient of determination is less than 90%
5. Carry out CFD numerical based simulations under the same conditions as experiments; record the pressure data measured by the holes of the probe.
6. Apply calibration procedure such as pressure normalisation and data reduction techniques
7. Generate a calibration map and determine calibration coefficients and calibration coefficients of determination sector-wise.
8. Validate the probe readings by using the calibration data to calculate wind tunnel flow velocities and compare with actual flow velocities.
9. Identify the calibration sectors that need to be replaced with the numerical dataset and list down the coefficients of determination that needs to be replaced.
10. Highlight the calibration coefficients that corresponds to the less accurate experimental calibration coefficients.
11. Replace the less accurate experimental calibration coefficients by, the more accurate CFD based numerical calibration coefficients.
12. Validate the velocity measurements from the integrated calibration method against a known velocity field.

The CFD based integration procedure and activities are summarised in the flowchart shown in figure 5.9.

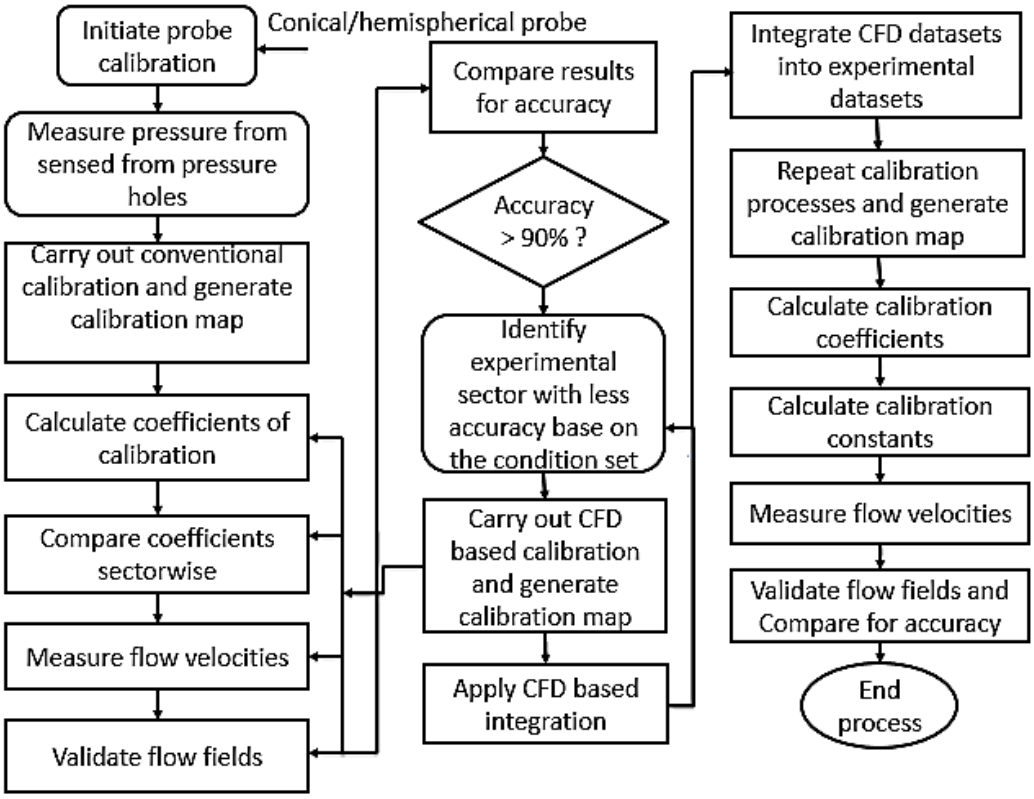

Figure 5.9. A flowchart summarising the novel CFD based integration calibration method in wind tunnel flow

The focus in the flowchart is to identify the experimental sector that is less accurate in predicting the calibration coefficients of determination. Any sector whose calibration coefficient is less than 90% accurate experimentally is replaced with CFD pressure dataset of the same sector, after which the probe is recalibrated using these experimental and numerical integrated datasets.

The calibration sector map of the integrated calibration method is shown in figure 5.10 having gone through the methodology of the integrated process. Based on the new/integrated calibration sector map, the integrated coefficients of calibration have been calculated and summarised in appendix 5.3a and 5.3b corresponding to sectors 1 and sector 5. It must be noted that as the less accurate sectors identified in case of experimental calibration (table 5.1) were sectors 1, 3, and 5, hence, the calibration coefficients of both these sectors have been replaced by the numerical calibration coefficients corresponding to the same sectors. Thus, the calibration coefficients are shown in appendix 5.3a and 5.3b.

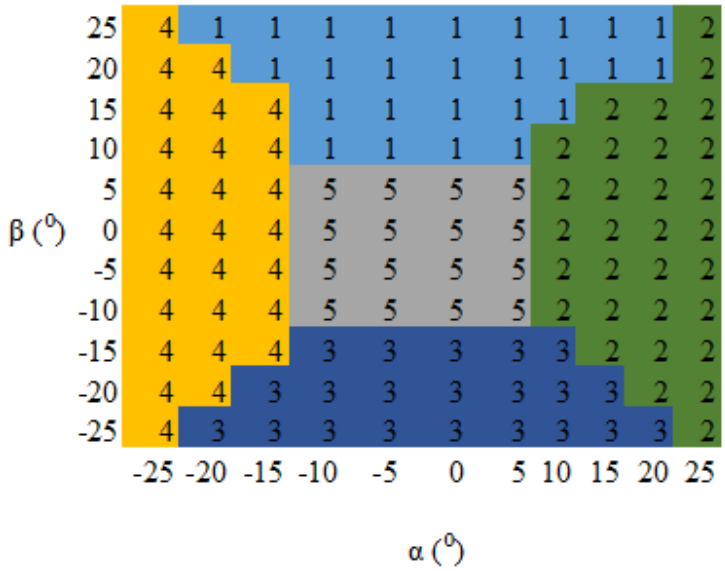

Figure 5.10. CFD based integrated sector map for wind tunnel calibration

Figure 5.10 depicts the calibration map generated by the CFD based integrated datasets of the five-hole probe in a wind tunnel flow. The y-axis of the sector map represents the yaw angle plane, while the x-axis represents the pitch angle plane. The areas marked by the number one (1) are the grids covered by the top hole (sector 1) during the calibration pressure measurements. Similarly, the characterized by the number three (3) are the grids in the calibration map covered by the bottom hole (sector 3).

Furthermore, the areas covered by number four (4) are the grid points covered by the left hole (sector 4) in the calibration map. It the same for the areas marked by number two (2), it is the grids points covered by the right hole (sector 2) of the probe during calibration. The centre area of the calibration map marked by number five is an area in the grid points covered by the centre hole (sector 5) of the probe.

The top hole of the probe as shown in figure 5.9 above has the top hole (sector 1) registers the highest pressure from $\alpha = -20^{o}$ to 20^{o}, while at yaw axis, $\beta = 10^{o}$ to 25^{o}, however, at higher pitch angles (beyond $\pm 10^{o}$), the yaw angle range becomes narrower. It is the same with the bottom hole (sector 3). The side holes (sectors 2 and 4) register maximum pressure from $\alpha = 10^{o}$ to 25^{o} and $\alpha = -15^{o}$ to -25^{o} respectively, where the yaw angle registers pressure from $\beta = -25^{o}$ to 25^{o} for the holes right hole (sector 2) and $\beta = -25^{o}$ to 25^{o} for the left hole (sector 4). Furthermore, it can be seen that the centre hole (sector 5) registers maximum pressure from pitch angle $\alpha = -10^{o}$ to 5^{o} at yaw angles (β) of -10^{o} to 5^{o}. It can equally be noticed that the conical five-hole probe sector

map is not perfectly symmetrical even though it was generated using an integration data of experimental and numerical results. The non-symmetrical shape of the calibration sector map is because of a combination of human factors in the experimental calibration process as well as the CFD based numerical method mentioned above.

Based on the CFD based integrated calibration pressure datasets, the calibration coefficients of determination have been calculated, as summarised in table 5.5. It can be seen that those coefficients of determination, which were identified in the experimental calibration section as less accurate (<90%), are now 1.0000 (highlighted in table 5.5), based on the integration of the CFD numerical data into the experimental data. Hence, the integrated calibration model developed here is significantly more accurate and reliable than the conventional method of calibration of conical five-hole pressure probes (see section 3.9 for a detailed explanation).

Table 5.5. CFD based integrated coefficients of determination

Calibration parameters	Sector 1 (r^2)	Sector 2 (r^2)	Sector 3 (r^2)	Sector 4 (r^2)	Sector 5 (r^2)
Pitch angle (°)	0.9401	1.0000	1.0000	1.0000	0.9999
Yaw angle (°)	1.0000	1.0000	0.9898	1.0000	1.0000
Total pressure (Pa)	0.9998	1.0000	0.9978	1.0000	0.9084
Static pressure (Pa)	0.9998	1.0000	0.9976	1.0000	0.9117

Based on the results shown in table 5.5, it is wise to mention here that the sectors that are replaced by the integration process are sector 1, sector 3 and sector 5. Comparison table 5.5 to table 5.1, it can be seen that all calibration parameters for all five sectors of the probe have now achieved more than 90% accuracy for all four parameters. The accuracy of the calibration method is demonstrated further in figure 5.10 where the integrated calibration data have been used to calculate and compare flow velocities with actual measurements of a known velocity field.

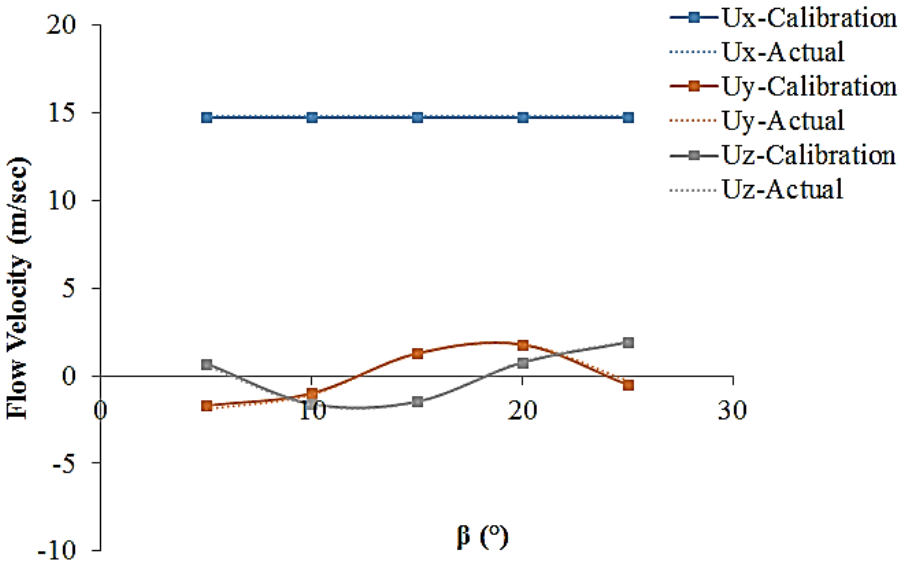

Figure 5.11. Validation of the CFD based integrated calibration dataset

By integrating numerical calibration data with experimental data, a new set of calibration data was generated. The probe was used in wind tunnel flow to measure and calculate velocity components as shown in figure 5.10 having applied the calibration method described above, as shown in figure 5.11, the probe was mounted on the horizontal wind tunnel and measurements were taken at various angles. The velocities were calculated and compared with actual values. It has been demonstrated that there is a very agreement in all components velocities with about 99% accuracy for x, y, and z components. By comparing figure 5.11 to 5.4, and 5.8, it is evident that by integrating numerical data into experimental data, a new set of pressure data that can produce almost 100% accuracy is achievable using five-hole probes, and this has been shown clearly here.

It can be seen that the difference between the actual and calibration based flow velocity measurements is less than 1%. Hence, the integrated calibration method is more accurate than the conventional method of calibrating five-hole pressure probes. It should be noted down here that although the integrated calibration method has been shown to be more accurate than the conventional method of calibration, the range of calibration is still limited, i.e. for $\alpha = \beta = \pm 25^{o}$; this severally limits the usefulness and applicability of the integrated calibration method. This limitation has been removed in the present study by extending the range of calibration for five-hole pressure probes. The extension of the angular calibration range has been carried out using datasets from CFD numerical simulations, which is discussed in detail in the next section. For a detailed description of the CFD based integrated method, see section 3.9.

5.3.1 Integration Measurements Error Analysis

This section discusses the error analysis of using CFD based integrated datasets to measure wind tunnel flows using a conical five-hole probe. The same formula and principle applied to section 5.1.4 and section 5.2.5 have been adopted to carry out this analysis. Table 5.6 shows the error analysis for each wind tunnel flow parameters measured using the equations generated for CFD based integrated calibration method of the conical five-hole pressure probe.

Table 5.6. Uncertainties and standard errors in measurement for conical five-hole pressure probe

Statistical parameters	Pitch angle (°)	Yaw angle (°)	Total pressure (Pa)	Static pressure (Pa)	U	U_x	U_y	U_z
Standard error	0.0302	0.0018	0.005	0.004	0.0029	0.1073	0.0181	0.1421

In comparing table 5.6 to table 5.4 and table 5.2, it can be seen that the accuracy of measurements established here based on the error analysis applied has shown that integrating CFD based numerical dataset to experimental dataset measurement accuracy with approximately 100% can be achieved for measurements of wind tunnel flow parameters. Furthermore, it has been established in this chapter that the sources of errors mentioned above can be tackled using CFD based calibration techniques in many ways that will boost measurement operations and design of lymphatic vessels.

5.4 Extension of the Calibration Angle Range

As discussed earlier, the range of the integrated calibration method developed here is limited that restricts the applicability of the five-hole pressure probe. The experimental calibration method up to flow angles of 25^0 limits the likely range of application of the probe. It is expected to encounter unknown velocity fields having larger flow angles. Hence, it is necessary to develop a calibration methodology that can take care of a wide range of flow fields. Therefore, numerical simulation data has been generated for $\alpha = -30^0$ to -45^0 and from 30^0 to 45^0, and $\beta = -30^0$ to -45^0 and from 30^0 to 45^0 (see section 3.9). The calibration data for $\alpha = \pm 25^0$ and $\beta = \pm 25^0$ is considered the same as in the integrated method. The flow static gauge pressure and flow velocity magnitude variation in the region of the conical head five-hole pressure probe at a high angle, $\alpha = 0^o$ and $\beta = 45^o$ have been shown in figure 5.12. It can be seen in figure 5.12(a), in comparison with figure 5.5(a), that the highest static gauge pressure of the flow is 85.7Pa. It means that at high flow angle, the probe measures less pressure Malviya, V., Mishra, R., & Palmer, E., (2015).

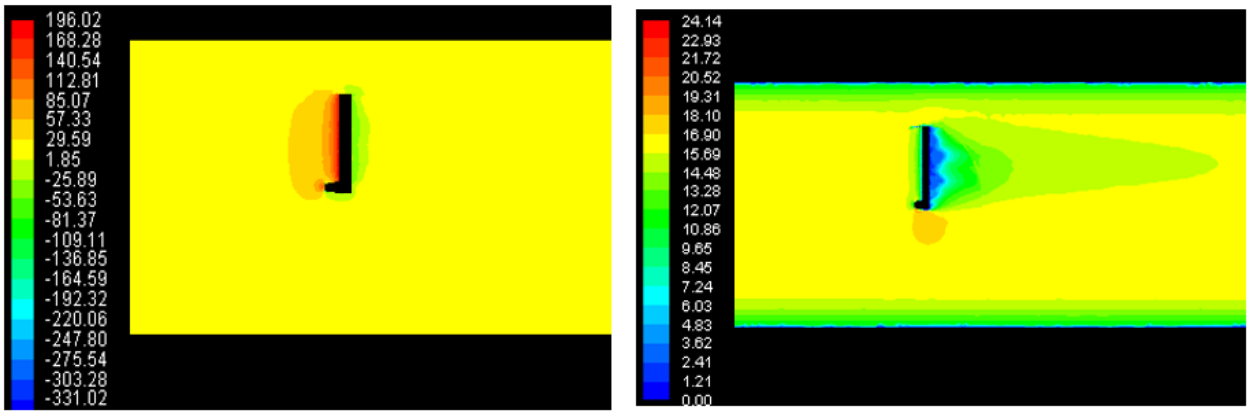

Figure 5.12. Variation in (a) flow field static gauge pressure and (b) flow field velocity magnitude in the vicinity of the $\alpha=\beta=45^{o}$

These simulations are carried out to establish the flow interaction with the probe at high flow angles. In comparison, with the flow velocity magnitude variations between figure 5.5(b) and figure 5.6(b), it can be seen the effect of the presence of the probe is even smaller. The highest flow velocity magnitude is about 4% than observed in the case of $\beta=0^{o}$ and $\beta=25^{o}$. With this established, the CFD based extension pressure data can then be integrated into the CFD based integration dataset to carry out full calibrations for the conical five-hole pressure probe. In the region of the sensing head, just like the case of the $\beta=0^{o}$ and $\beta=25^{o}$, different pressure distribution can be seen as the velocity vector is now making an angle with the sensing plane. It indicates that the simulation at higher flow angles captures the effect of three-dimensional velocity field as expected. The calibration method follows the procedures and process described in figure 5.13 in section 5.4.1.

5.4.1 CFD based Calibration of Extension of Range

Having numerically acquired pressure dataset for the extension of angle range calibration method through CFD simulations of the probe at higher flow angles under the same flow conditions as experiments, in this section, the novel procedures followed in this study to achieve the aims and objectives of this chapter is discusses. In this section, a novel extension of calibration range is developed that merges the advantages of both numerical simulations and the integration methods. The steps involved in the CFD based extension of the range calibration method for a conical five-hole pressure probe are shown in figure 5.13. The sectoring scheme, the method of data analysis and the technique of defining non-dimensional pressure are the same as the other precious developed methods.

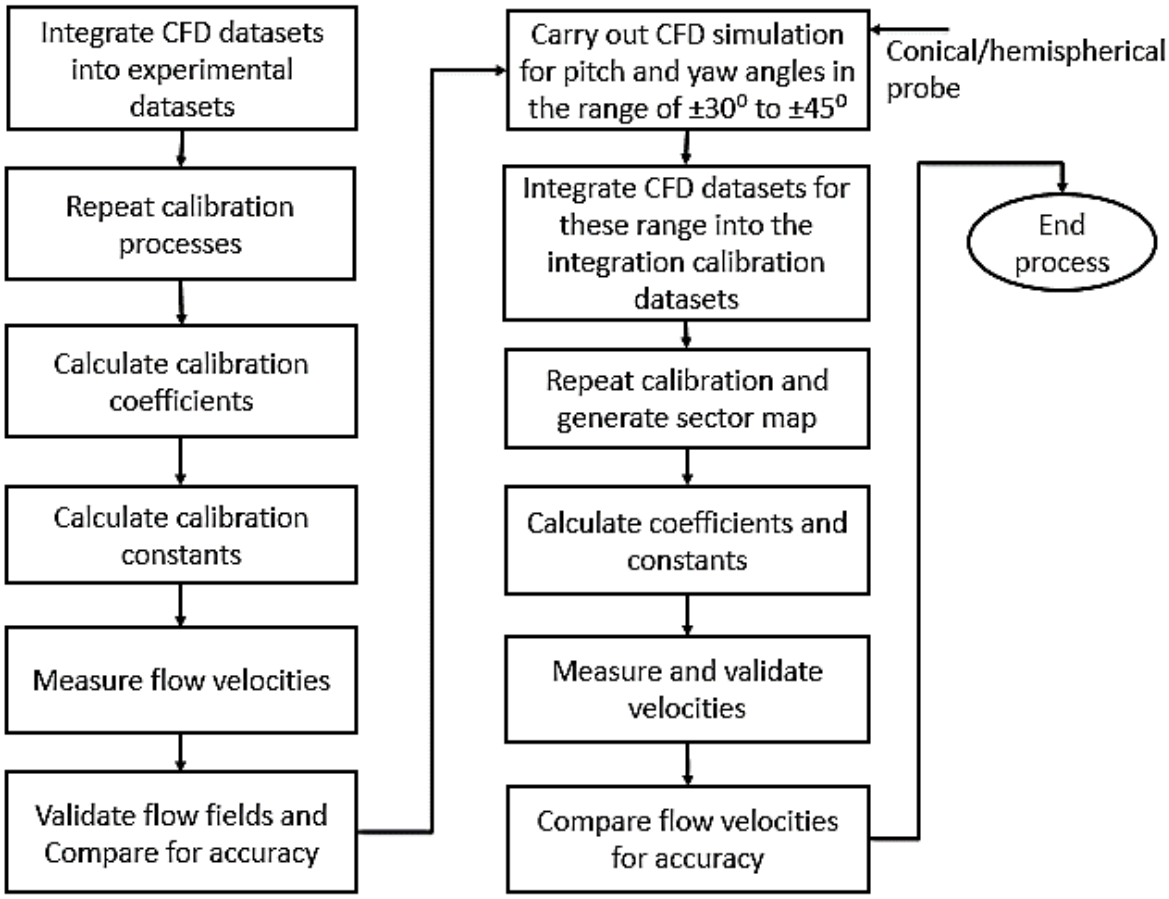

Figure 5.13. A flowchart summarising the novel CFD based extension of a probe angle range calibration method for the wind tunnel flow

The extended calibration sector map is shown in figure 5.14. The data/sectors shown in the box are the ones that have been taken from the integrated method, while the data outside the box is based on CFD based extended numerical simulations. Again, the pressure dataset on the holes of the conical five-hole pressure probe has been recorded, along with the static and total pressure. This data has been converted to non-dimensional pressure coefficients using data reductions techniques. Then, based on the sixth order polynomial curve fitting method, the calibration coefficients, corresponding to the different sectors of the probe, have been calculated. The calibration coefficients for sectors 1 and five are shown in appendix 5.4a and 5.4b. It can be seen that the extended calibration coefficients are significantly different from experimental, numerical and integrated calibration coefficients Parameswanran, V., Jategaonkar, R., & Press, M. (2002) and Akshoy, R.P., Ravi, R.U., & Anu, J. (2011).

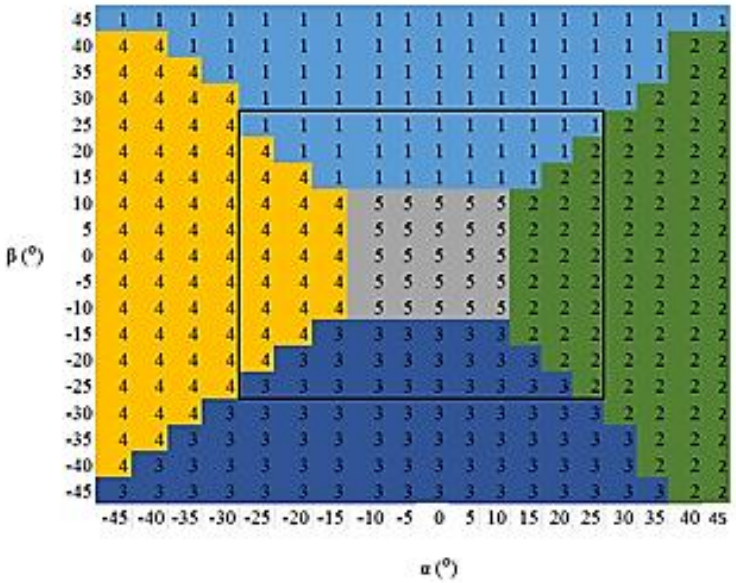

Figure 5.14. CFD based extended calibration sector map for wind tunnel calibration

In this figure, each colour with the number they cover represents each hole of the probe. Number 1 represents the top hole, number 3 represents the bottom hole, while number 2 and 4 represent right and left holes respectively. The area of the calibration map covered by the sky blue colour represents the top hole of the probe just as demonstrated by the probe numbering in the schematic as shown in chapter 3, and it shows the points where pressure was measured in the grid at each combination of pitch and yaw angle. The areas covered by the dark blues are the areas where pressure was measured by the bottom hole in each combination of pitch and yaw angles.

Similarly, the yellow areas show the area in the calibration map covered by the left hole, while the green shows the area covered by the right hole in the calibration grid. The area in grey remains the grid covered by the centre hole. It is important to note here that the entire region of the calibration map marked by a thick line represents the calibration map generated using the integrated datasets as shown in figure 5.9. Therefore, the extension of the calibration angle was carried out from ±30° to ±45° . Having established the calibration sector map of the CFD based extension of the range method, it is equally important to further demonstrate the accuracy of the method by calculating and tabulating the coefficients of determination Kim, S. H., & Kang, Y. J. (2009).

The top hole of the probe as shown in figure 5.11 above has the top hole (sector 1) registers the highest pressure from α = -45° to 45° , while at yaw axis, β = 15° to 45° , however, at higher pitch angles (beyond ±15°), the yaw angle range becomes narrower. Similarly, the bottom hole

(sector 3) registers the highest pressure from $\alpha = -45^{o}$ to 35^{o}, while at yaw axis, it has at $\beta = 15^{o}$ to -45^{o}, however, at higher pitch angles (beyond $\pm 15^{o}$ the yaw angle narrows). The side holes (sectors 2 and 4) register maximum pressure from $\alpha = 15^{o}$ to 45^{o} and $\alpha = -15^{o}$ to -55^{o} respectively, where the yaw angle registers pressure from $\beta = -45^{o}$ to 40^{o} for the holes right hole (sector 2) and $\beta = -40^{o}$ to 40^{o} for the left hole (sector 4). Furthermore, it can be seen that the centre hole (sector 5) registers maximum pressure from pitch angle $\alpha = -10^{o}$ to 10^{o} at yaw angles (β) of -10^{o} to 10^{o}. Just like figure 5.9, 5.7 and 5.2, it can equally be noticed that the conical five-hole probe extended sector map is not perfectly symmetrical even though it was generated by numerically extending the integration data of experimental and numerical results. It is because of a combination of human factors in the experimental calibration process as well as the numerical method mentioned in section 5.2.4 and section 5.3.

Table 5.7 summarises the coefficients of determination for all the five sectors of the conical five-hole pressure probe, for the extended range calibration data. It can be noticed that the coefficients of determination for all the different calibration parameters, and in all the five sectors, are above 90%. Hence, the extension in the range performed for the conical five-hole pressure probe has been reasonably accurate (see section 3.9 for a detailed explanation).

Table 5.7. CFD based extension of range coefficients of determination

Calibration parameters	Sector 1 (r^2)	Sector 2 (r^2)	Sector 3 (r^2)	Sector 4 (r^2)	Sector 5 (r^2)
Pitch angle (^{o})	0.9079	0.9949	0.9098	0.9807	1.0000
Yaw angle (^{o})	0.9979	0.9415	0.9967	0.9591	1.0000
Total pressure (Pa)	0.9869	0.9983	0.9987	0.9906	1.0000
Static pressure (Pa)	0.9875	0.9777	0.9995	0.9974	1.0000

Table 5.7 demonstrates the accuracy of the extended calibration method as all of the coefficients of determinant for all four-calibration parameters is more than 95%. By comparing table 5.7 to table 5.3 and table 5.5, it can be seen that the accuracy introduced by the CFD numerically integrated data has been maintained throughout this calibration processes. This accuracy is further confirmed in the measurement of flow information using the extended calibration data.

5.1.4 Comparison of Statistical Parameters

The statistical results achieved in the study by using the pressure normalisation and data reduction technique introduced by Akshoy, R. P., Ravi, R. U., & Anu, J. (2011) show significant

improvements in both calibration data and flow in flow measurements. Using sixth order regression analysis, the average values of the calibration coefficient of determination (r^2) parameters for all sectors exhibit the usefulness of the sector scheme, the pressure normalisation, and the data reduction technique. The average statistical results for all four types of calibration method carried in this chapter are shown in table 5.8.

Table 5.8. Statistical summary comparison of all combinations of pressure normalisation and data reduction techniques

Four adopted Calibration methods	Data reduction techniques	Statistical parameters	Pitch Angle (Degree)	Yaw Angle (Degree)	Total pressure (Pa)	Static pressure (Pa)
Experimental calibration method	Polynomial Curve-fit (Sixth order regression)	R^2	0.8780	0.9294	0.9812	0.9818
Numerical calibration method	Polynomial Curve-fit (Sixth order regression)	R^2	1.0000	1.0000	1.0000	1.0000
Integrated calibration method	Polynomial Curve-fit (Sixth order regression)	R^2	0.9880	0.9979	0.9812	0.9818
Extension of calibration range method	Polynomial Curve-fit (Sixth order regression)	R^2	0.9587	0.9790	0.9949	0.9924

As demonstrated in table 5.8, the uncertainty of pressure coefficients is a function of not only the curve-fits, which are dependent upon the probe design and manufacturing but the accuracy of the five pressure measurements. The error analysis carried out here is to compare these values is based on the pressure normalisation techniques and dataset reduction method chosen for this study. Therefore, the differences in the table are considered computational errors. It has no connection with the experimental accuracy of the instrument or experimental errors involved during dataset generation. Table 5.8 shows the statistical summary of all combinations of pressure normalisation and dataset reduction techniques used in this present study. According to table 5.8, the uncertainty is less only for the pitch angle in the experimental method of calibration. However, the pitch, yaw, total, and static pressure maintained a high level of accuracy over 95% in the sector. Similarly, the

numerical results achieved up to 100% for all sectors. The same is true for the integrated calibration method and the extension of the range calibration method.

5.5 Summary

The most important thing with calibrating a conical five-hole pressure probe is producing graphs and maps with reduced errors. Ideally, the calibration map should remain the same every time the probe is calibrated. However, there are many sources of errors, which this study attempt to reduce. The main reason for the errors in the calibration changes in calibration flow quality that can be caused by laboratory disturbances or unwanted air currents during a calibration. Another source of error can occur when the probe is first aligned with the flow. The flow was initially aligned manually, which is a source of human errors. In the calibration, five pressure sensors were used to sample pressure from all five-pressure measurement points. Five tubes where used for the five holes of the probe and two channels were required for the Pitot probe which gives the wind tunnel magnitude velocity, total pressure and static pressure in the test section. The method presented here helped eliminate most of these calibration errors.

In this chapter, a calibration of the conical five-hole probe is carried out in a wind tunnel located at the University of Huddersfield Laboratory. In the wind tunnel calibration, it was found that the probe gives correct readings at the centre position of the test section because of the fully developed flow at the centre of the duct. Near the walls of the test section, the effect of the boundary layer predominates, and therefore the probe was not tested at such location. The probe used for the calibration was tested for different positions of yaw and pitch angle. From the results stated above, it can be seen and said that the best suitable range of yaw and pitch angle for measurements of pressure is $\pm 25^{o}$ for and $\pm 45^{o}$ the extended method of calibration.

This chapter presents a new method of conical five-hole pressure calibration and measurement in wind tunnel flow that attempts to eliminate the errors stated. The new method is based on integrating experimental pressure data with numerical pressure data to obtain new integrated pressure data for increased calibration and flow measurement accuracies. Looking at the experimental calibration method in section 5.1.3 table 5.1, because of the source of errors stated above the experimental calibration could not produce coefficients of determination up to 90%. By integrating both numerical pressure data with experimental data, calibration coefficients of

determination with above 90% have been achieved and replaced the ones that performed below expectation in the experimental method of calibration. The integration techniques presented in this chapter have been tested in wind tunnel flows and have resulted in flow measurement accuracy of up to 93%. In fact, due to the accuracy of the calibration method, measurements accuracy has been shown to be up to 95% using the integrated calibration data. The highlight contents, general discussions and the results presented in this chapter are summarised as follows:

1. The results presented in this chapter are derived from the methodology and experimental setup previously discussed in chapter 3 and 4.
2. The results presented in this chapter are in correlation to their relevance to the overall aims and objective of the study
3. The conventional method of calibrating five-hole pressure probes has severe limitations, resulting in significant errors in the calibration process. The contributing factors, to these errors, are geometrical imperfections of the probe, human errors, measurement errors, flow instability, misalignment of the probe etc.
4. These errors can be minimised through the use of numerical simulations of a conical five-hole probe. The calibration results depict that the numerically obtained calibration coefficients are significantly more accurate than the experimental calibration results, due to the controlled nature of the numerical simulations.
5. There are, however, some inherent limitations within the numerical solvers as well, such as an accurate representation of the boundary and operating conditions, convergence issues etc.
6. Hence, a novel integrated calibration method has been developed that takes into account both the experimental and numerical data. The numerical dataset replaces only the less accurate experimental calibration coefficients. The integrated calibration method has been shown to be more superior in accuracy than the conventional calibration method.
7. The range of the integrated calibration method is however limited, which restricts its usefulness. The calibration range of the conical five-hole pressure probe has been extended by using further numerical data, beyond the conventional range. This extended data has then been integrated with the integrated calibration method developed earlier.
8. The non-null calibration method, specifically the sector technique is advantageous where the rotation of the probe is not possible.
9. For larger flow angles, sector technique appears to be the best option of calibration scheme.

10. For flow angles within $\pm 25^{o}$, five-hole probe in non-null calibration technique is very useful.
11. The data reduction technique yielded and accuracy of $\pm 5^{o}$ in both pitch and yaw angles and accuracy of ±5m/sec in velocity.
12. The key success of the calibration methods is the ability to define velocity invariant pressure coefficients, which are the ratio of a two-pressure difference, taking the pressure sensed by the centre hole into account. This type of pressure normalisation technique takes care of the flow separation caused by the probe when inserted in the flow field.
13. The pressure normalisation technique used in this study overcomes great flow separation when it encounters flow greater than $\pm 43^{o}$. It also limits the effect of double-value and velocity dependent at high flow angles and flow velocities.

The calibration techniques and methods described in this chapter are for a conical five-hole, multi-function pressure probe for air data used in wind tunnel flows. For wind, the tunnel test, configuration design of the five-hole pressure probe has been performed by applying CFD based simulations for optimised calibration methods based on simulation results. The calibration equations and coefficients developed for this process have been used to calculate flow information and compared against known flow fields to validate the performance of the probe calibrated through the wind tunnel test. Furthermore, another comparison of the calibrated results using the present methods and the actual flow field has also been expressed in pitch and yaw and angles and compared against each other sector-wise.

The calibration maps with points spaced at 5° pitch and yaw angles show that the probe in each calibration methods sufficiently resolves the response and pressure distribution across all sectors. The resolution between sectors was sufficient to determine and represent the essential features of the conical five-hole pressure probe response. Also, all coefficients resulting from the calibrations show therefore that the polynomial curve-fit accurately model the physical reaction of the probe by using CFD base methods as demonstrated in the flow velocity measurements presented in this chapter. The techniques presented in this chapter can be used to measure another flow system such as compressor and turbine cascades and allow for measurement accuracy of up to 90% noticeably. In fact, due to the spatial resolution of the flow, the accuracy can be increased for particular applications, for example, when measuring complete outflow planes.

After carrying out detailed calibration based analyses on a conical head five-hole pressure probe, the next step is to investigate the effect of the probe head's shape on the calibration process. Thus, the next chapter presents the calibration of a hemispherical five-hole pressure probe in like manner.

Chapter 6 Effect of the Head Shape of Five-hole Pressure Probes on the Calibration Process in Wind Tunnel Flows

In this chapter, the results of the hemispherical five-hole calibration and measurements in wind tunnel flows are shown. These include the air experiments at flow angle α and β ±25 to ±45 in a horizontal wind tunnel with airflow at a flow velocity magnitude of U=15m/sec. This chapter includes results from numerical experiments at the same flow conditions. At each flow condition, the hemispherical probe is used to measure the local flow velocities of air.

The effect of the shape of a hemispherical five-hole probe has been investigated in this chapter. For this purpose, a hemispherical five-hole pressure probe has been manufactured (for experimental testing) and modelled (for CFD based numerical testing) for wind tunnel flows. The hemispherical five-hole pressure probe has been calibrated both experimentally and numerically, and comparisons have been drawn against the conical five-hole pressure probe described in chapter 5. A Computational fluid dynamic (CFD) based integrated calibration method has been developed for hemispherical five-hole pressure probes, using a dataset from numerical simulations. The development of an extended range calibration method using a CFD based approach is the highlight of this chapter.

6.1 Introduction

The main aim of this chapter is to analyse the effects the shape a five-hole pressure probe has on its calibration process parameters and the accuracy of the measurement. Hence, the calibration process, similar to the one presented in chapter 5, has been carried out on a hemispherical head five-hole pressure probe. Comparisons have been made against the calibration results of the conical five-hole pressure probe. For the sake of useful comparisons, all the operating conditions (like external flows (wind tunnel), average flow velocity in experiments and boundary conditions in numerical work) have been kept the same. A detailed qualitative and quantitative comparison has been made between the two probe heads. Moreover, a comparison of the flow fields associated with the two probes is presented in this chapter.

6.2 Experimental Calibration of a Hemispherical Head Five-hole Pressure Probe

A hemispherical five-hole pressure probe has been calibrated using the conventional method of calibration, similar to the one presented in chapter 5 for a conical five-hole probe. Extensive wind tunnel testing has been carried out at an average flow velocity of 15m/sec, and pitch and yaw angle range of $\pm 25^0$. The pressure data on all the individual holes of the probe has been recorded. Although the experiments have been carried out in a controlled manner, there can be some factors affecting the accuracy of the measurements, such as misalignment of the probe, human error, probe machining imperfections etc. Hence, for repeatability of the pressure data, the pressure data of all the five holes, including the static and total pressures, has been measured four times in subsequent runs. The average pressure values on the holes of the hemispherical head five-hole pressure probe have been used to develop the sector map for the probe, as shown in figure 6.1 (see section 3.9). The sector map for the hemispherical head five-hole pressure probe is a representation of the holes registering the highest pressure values at given α and β angles. In comparison, with figure 5.2, it can be seen that the sector map of a hemispherical head five-hole pressure probe is similar to the one obtained for a conical head five-hole pressure probe. Hence, for the given flow conditions, the same holes on both probes register highest pressures values. It also means that qualitatively, both hemispherical and conical five-hole pressure probes behave similarly as far as global parameters are concerned Hale, M. R. (1967) and Akshoy, R. P., Ravi, R. U., & Anu, J. (2011).

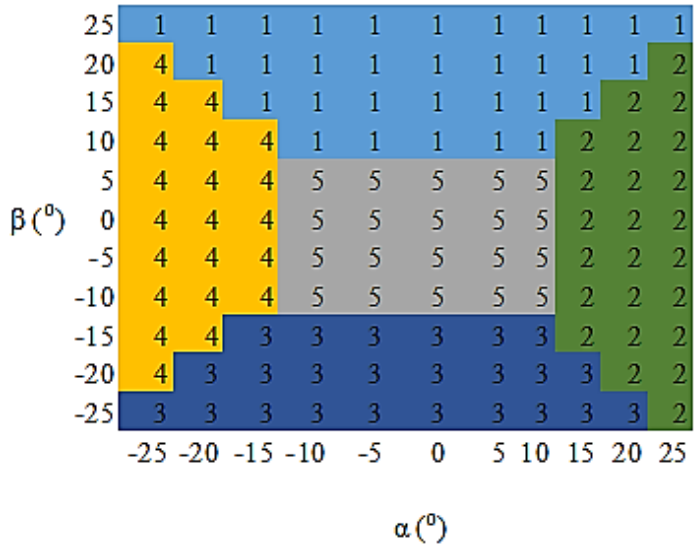

Figure 6.1. Experimental sector map for wind tunnel calibration

Figure 6.1 depicts the calibration map generated by the hemispherical five-hole probe in a wind tunnel flow. The y-axis of the calibration map represents the yaw angle plane, while the x-axis represents the pitch angle plane. The areas marked by the number one (1) are the grids covered by the top hole (sector 1) during calibration, and the fields marked by the number (3) are the grids points covered by the bottom hole (sector 3). Furthermore, the fields marked by number four (4) are the grids points covered by the left hole (sector 4), and the fields marked by number two (2) are the grids points covered by the right hole (sector 2) of the probe. The centre area characterised by number 5 is the grid point of the calibration map covered by the centre hole (5) of the hemispherical five-hole pressure probe.

It can be seen that the top hole (sector 1) registers the highest pressure from $\alpha = -25^{o}$ to 25^{o} at $\beta = 10^{o}$ to 25^{o}, however, at higher pitch angles (beyond $\pm 10^{o}$), the yaw angle range becomes narrower. It is the case with the bottom hole (sector 3). The side holes (sectors 2 and 4) register maximum pressure from $\alpha = 15^{o}$ to 25^{o} and -15^{o} to -25^{o} respectively, where the yaw angle ranges from $\beta = -20^{o}$ to 20^{o} for both the holes. Furthermore, it can be seen that the centre hole (sector 5) registers maximum pressure from pitch angle $\alpha = -10^{o}$ to 10^{o} at yaw angles (β) of -10^{o} to 5^{o}. It can be noticed that the sector map is not perfectly symmetrical. It is because a dimensionally perfect and balanced five-hole pressure probe is very difficult to fabricate due to the small nature of the probe and inherent machining imperfections because of human factors.

Based on dataset reduction techniques, and using a sixth order polynomial curve fitting method, the calibration coefficients for all the sectors of the hemispherical five-hole pressure probe have been

calculated. For effective comparison purposes with conical five-hole pressure probe, the calibration coefficients for sectors 1 and five have been presented herein appendixes 6.1a and 6.1b. In comparison with appendix 5.1b and 5.1c, it is notably seen that the calibration coefficients of the hemispherical head five-hole pressure probe, for the corresponding sector/s, are significantly different from the calibration coefficients of the conical head five-hole pressure probe. It suggests that although the qualitative aspects of the calibration of both the probes are similar, quantitatively, both these probes perform in an entirely different manner. Thus, the probe head affects the measured pressure values even for the same velocity field.

To validate the accuracy of the calibration coefficients of the hemispherical five-hole pressure probe, the coefficients of determination, for all the sectors of the probe, and for the different calibration parameters, have been computed. These coefficients have been summarised in table 6.1. It can be seen that the sectors 2, 3, and 5 show a perfect correlation, i.e. r^2 =1.0000 for all calibration parameters. The correlations in sector 4 are also above 90%, which is the threshold of correlation acceptance considered in the present study. Therefore, only one correlation, i.e. pitch angle in sector one shows a coefficient of determination of 63%, which needs to be replaced by a more accurate correlation, which will be obtained using numerical data, as done in case of the conical five-hole pressure probe (see section 3.9 for a detailed explanation).

Table 6.1. Experimental coefficients of determination

Calibration parameters	Sector 1 (r^2)	Sector 2 (r^2)	Sector 3 (r^2)	Sector 4 (r^2)	Sector 5 (r^2)
Pitch angle (º)	0.6373	1.0000	1.0000	0.9698	1.0000
Yaw angle (º)	0.9172	1.0000	1.0000	0.9341	1.0000
Total pressure (Pa)	0.9754	1.0000	1.0000	0.9673	1.0000
Static pressure (Pa)	0.9646	1.0000	1.0000	0.9669	1.0000

In comparison, with table 5.1, it can be noticed that the overall coefficients of determination for the hemispherical five-hole pressure probe are higher compared to those of conical five-hole pressure probe. Moreover, in the case of conical five-hole pressure probe, four different coefficients of determination were being replaced by the numerical data. In the case of a hemispherical five-hole pressure probe, however, there is only one coefficient of determination value that needs to be replaced by CFD numerical coefficients. Hence, quantitatively, the hemispherical five-hole pressure probe performs better and shows superior calibration results compared to the conical five-hole pressure probe.

The validation of a hemispherical five-hole pressure probe's calibration method, in a wind tunnel, flows, using conventional calibration method (i.e. non-nulling method), is shown in figure 6.2. It can be seen that there are significant differences between the actual velocity components (especially Uy and Uz) and the velocity components obtained from the conventional calibration method for a hemispherical five-hole pressure probe. To compare the traditional calibration methods of the hemispherical and conical five-hole pressure probes, figure 6.3 depicts the variations of the three components of velocity measured using the calibration equations for both the probes.

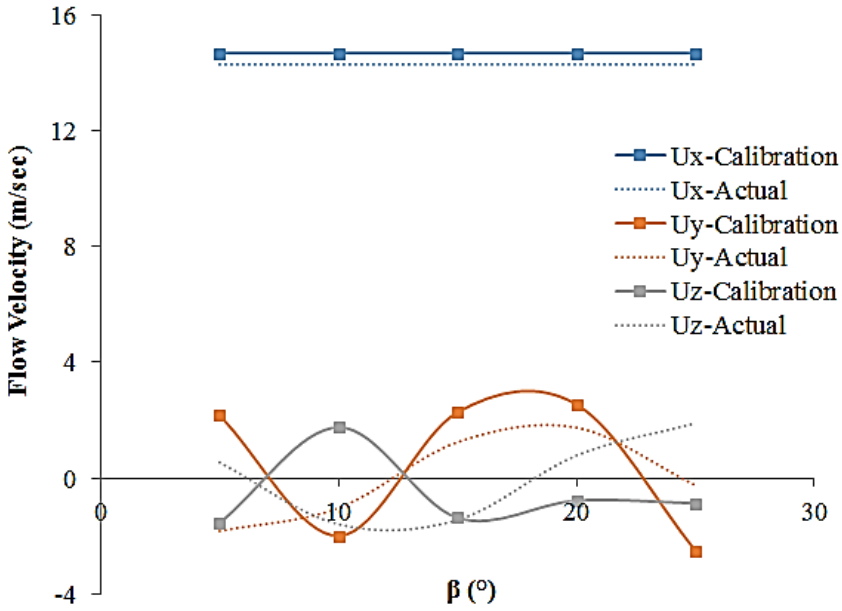

Figure 6.2.Validation of the experimental calibration dataset

Experiments were carried out using the hemispherical five-hole probe in wind tunnel flows to validate the calibration results. This validation was carried out against know flow information to monitor the performances of the new flow information measured by the probe. At each flow condition, the probe has been used to measure local axial, radial and azimuthal air velocities. The wind tunnel axial velocity measured using calibration data is in the range of 14.5m/sec, while the actual axial velocity is 15m/sec. In comparing this, it can be seen that the calibration data has approximately 95% accuracy in the wind tunnel flows. Similarly, radial and azimuthal velocities maintained a similar trend as the actual velocities. However, the accuracies are not up to 90%. It is such improvements that this study tries to introduce. This improvement is introduced by integrating CFD numerical calibration data with experimental data, and this is validated in the wind tunnel flows as explained in section 6.4. However, the calibration data generated through the calibration of

conical and hemispherical probes have been used to measure the flow of wind tunnel flows to compare the performance of both probes in a wind tunnel flow. The results for these probes are shown in figure 6.3.

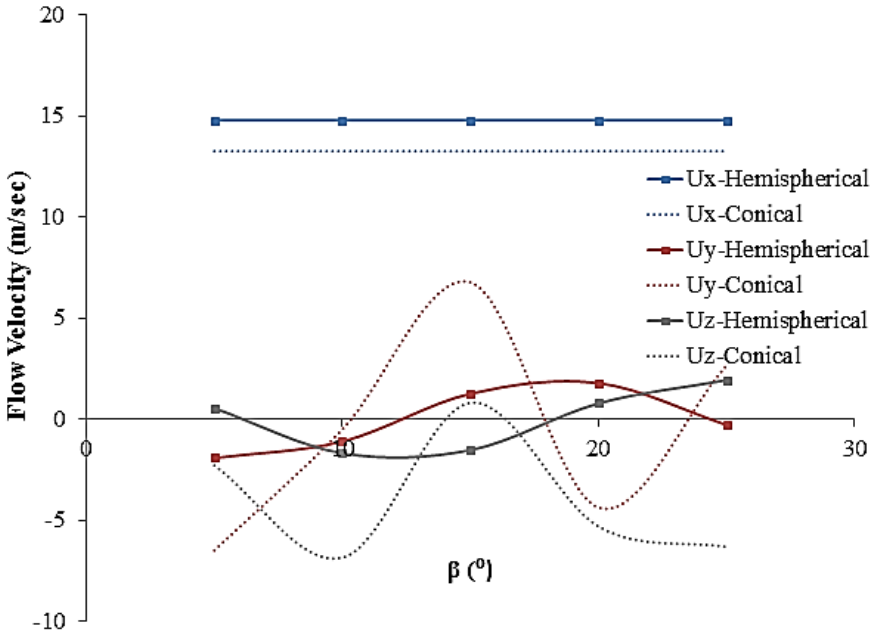

Figure 6.3.Comparison of the experimental calibration dataset for conical and hemispherical probes

It can be seen that, on average, the axial component of velocity, measured using a hemispherical five-hole pressure probe, is 11.5% higher than measured using a conical five-hole pressure probe. Similarly, radial and azimuthal components of velocity, measured using a hemispherical five-hole pressure probe, are 92% and 101% lower than measured using a conical head five-hole pressure probe. A comparison of figures 6.2 and 5.4 also suggests that using the conventional calibration method, the conical five-hole pressure probe measurements of y and z components of velocity were significantly higher than the actual values. In case of the hemispherical five-hole pressure probe, although there is still a significant difference between the actual and the measured values of y and z velocities, the difference between them is considerably less than for a conical five-hole pressure probe. Hence, using the conventional method of calibration, the hemispherical five-hole pressure probe is appreciably more accurate than a conical five-hole pressure probe in external flows.

6.2.1 Experimental Measurements Error Analysis

Error analysis has been performed to determine the uncertainty of the present hemispherical five-hole probe flow angles (pitch and yaw), pressure (total and static) and velocities determination. The

analysis includes included uncertainty of the probe calibration, uncertainty in the measurement of flow angles, total and static pressures, velocity magnitude and 3D velocity components using the calibrated hemispherical five-hole pressure probe in wind tunnel flow. Following a standard error analysis procedure, an estimate of the total precision error in measurement has been made using equation (6.1).

$$\delta_{\theta} = \sqrt{\frac{1}{n}\sum_{i=1}^{5}(\theta_{i,calculated} - \theta_{actual})^2} \quad (6.1)$$

All bias errors such as pressure transducers, temperature drift and probe stem deflection have been neglected, therefore; they are not included in the analysis. These errors have been taken care of by the data-sorting scheme adopted in this study and data analysis (pressure normalisation scheme) used to define pressure coefficients. The uncertainty in the hemispherical five-hole probe measurement of velocity in an unknown flow field is dependent on the errors accumulated during the probe calibration process and also the errors associated with the actual measurements using the calibrated probe. Table 6.2 shows the uncertainty of measurement estimated for the probe.

Table 6.2. Standard errors in measurement for a hemispherical five-hole pressure probe

Statistical parameters	Pitch angle (°)	Yaw angle (°)	Total pressure (Pa)	Static pressure (Pa)	U	U_x	U_y	U_z
Standard error	0.3181	0.3358	0.0508	0.0432	2.5545	0.5003	4.0322	3.2361

The uncertainty in the velocity magnitude determination is directly impacted by the accuracy of the flow angle determination. As discussed in the calibration procedure section in chapter 3, the velocity magnitude can be determined by interpolating for C_{PTOAL} and $C_{PSTATIC}$ at the measured flow angle and then using these values to compute the velocity magnitude. Therefore, these parameters are interrelated, and error in one can affect the other. The errors associated with the interpolation of the calibration data is dependent on the degree of non-linearity of the calibration data and truncate error of the interpolation scheme. The degree errors can be estimated by applying the interpolation process to a model equation which is based on the calibration data. As shown in table 6.2, the error associated with the velocity of the flow is high compared to the flow angles and pressure.

6.3 Numerical Simulation of a Hemispherical Head Five-hole Pressure Probe

Before moving on to the calibration of the five-hole pressure probe, the flow field analysis in the region of the hemispherical five-hole pressure probe has been carried out. The flow field analysis presented here makes use of the static gauge pressure and the variations of the velocity magnitude, as shown in figure 6.4. For effective comparison purposes with the conical five-hole pressure probe, the range (i.e. maximum and minimum values) of these variations has been kept the same. The flow parameters variations shown in the figure corresponds to the highest average flow velocity of the wind tunnel, 15m/sec (see chapter 4) at $\alpha = \beta = 0^0$. It can be seen that the presence of a hemispherical five-hole pressure probe disturbs the uniformity of the flow within the wind tunnel. As the probe offers resistance to the flow, the static gauge pressure is higher on the front section of the probe, while it is low downstream the probe. In comparison, with figure 5.5(a), the static gauge pressure variations for both the probes are similar in magnitude; hence, the pressure field for both the probes is identical. Same is the case for the flow velocity magnitude variations shown in figure 5.5(b), although the highest recorded velocity magnitude in case of the hemispherical five-hole pressure probe is 5% higher than the conical five-hole pressure probe.

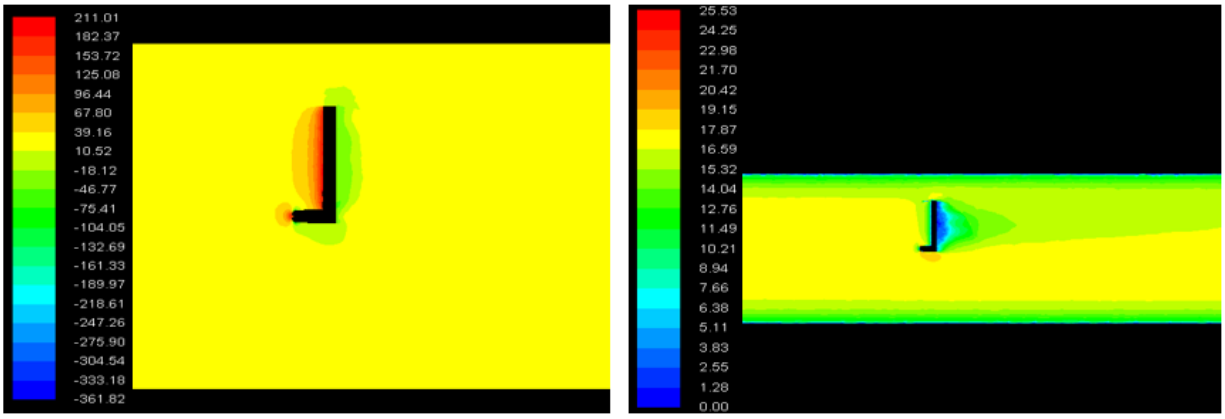

(a) Flow static gauge pressure

(a) Flow velocity magnitude

Figure 6.4. Variations in (a) flow field static gauge pressure and (b) flow field velocity magnitude in the vicinity of the probe at $\alpha=\beta=0^{o}$

The CFD choice to simulate the probe using the maximum flow velocity of the wind tunnel helps is to establish that the variation in gauge pressure, velocity magnitude and determine the extent to which measurements can go and not exceed. This analysis proves the accuracy of using the probe, calibration equations and coefficients to measure flow information in a wind tunnel fluid flow at 15m/sec. Therefore, because of this validation, it is concluded that the probe can be accurately

calibrated and measure fluid flow in the region of 5m/sec to 15m/sec with high accuracy in the wind tunnel flow Malviya, V., Mishra, R., & Palmer, E., (2015). Because of this finding, the next section explains the calibration and measurements results of the hemispherical five-hole probe in a wind tunnel flow.

6.3.1 Calibration of the Hemispherical Probe CFD Numerical Data

As discussed in the previous section that the coefficient of determination for the pitch angle in sector one needs to have a value of more than 0.9000 (i.e. 90%), numerical simulations have been carried out to improve the accuracy of the conventional calibration method. The CFD bases numerical setup is the same as in the case of a conical head five-hole pressure probe i.e. the numerical testing has been carried out in a wind tunnel facility, at an average flow velocity of 15m/sec same as experimental calibration, for a range of pitch and yaw angles in order to capture the whole wind tunnel practical characteristics. It has been carried out to design and develop a numerical calibration method for a hemispherical five-hole probe that can be used to carry out flow measurements. The pressure data on the five holes of the probe has been recorded for processing (see section 3.9).

The pressure data on the holes of the hemispherical five-hole pressure probe has been recorded. It has then been used to form the sector map of the probe, as shown in figure 6.5. The numerically obtained sector map is the same as in the case of the conical five-hole pressure probe (figure 5.7). Hence, again, qualitatively, both the probes perform similarly. The calibration coefficients for sectors one and five of the hemispherical five-hole pressure probe have been summarised in appendixes 6.2a and 5.2b. Comparison of these tables with appendixes 5.2a and 5.2b indicate that the calibration coefficients of both the probes are significantly different from each other.

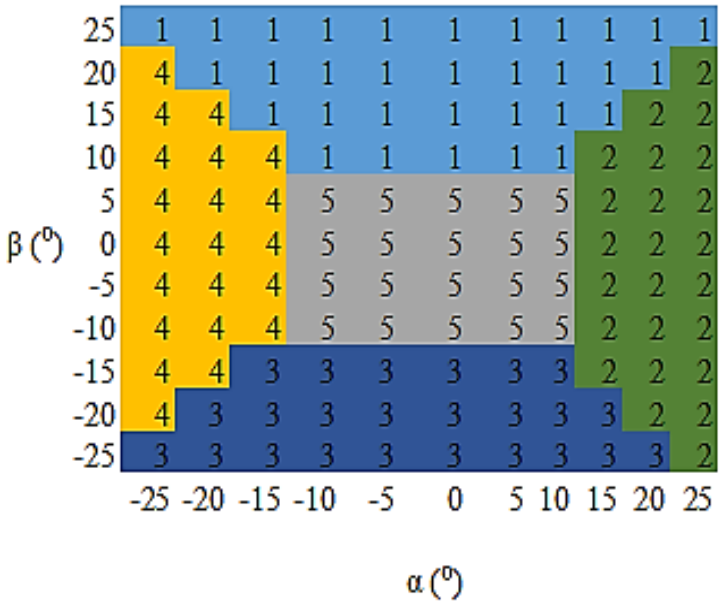

Figure 6.5. CFD based numerical sector map for wind tunnel calibration

Just like figure 6.1, figure 6.5 depicts the calibration map generated numerically for the hemispherical five-hole probe in the wind tunnel flow. The y-axis of the calibration map represents the yaw angle plane, while the x-axis of the calibration map represents the pitch angle plane. At each particular pitch and yaw angle the probe measures five pressure values, this is repeated for ±25° for both pitch and yaw plane, and the pressure is used to generate the map. The areas marked by the number 1 (sector 1) are the grids covered by the top hole of the probe during pressure measurements.

Similarly, the areas marked by the number 3 (sector 3) are the grids covered by the bottom hole. Also, the areas marked by number 4 (sector 4) are the grids covered by the left hole. It the same for the areas marked by number 2 (sector 2). The centre area of the calibration map marked by number 5 are the grid points covered by the centre hole (sector 5) of the probe.

It can be seen that the top hole (sector 1) registers the highest pressure from α = -25° to 25° at β = 10° to 25° , however, at higher pitch angles (beyond ±10°), the yaw angle range becomes narrower. Similarly, the bottom hole (sector 3) registers the highest pressure from α = -25° to 20° at β = -15° to -25° , however, at higher pitch angles (beyond ±10°), the yaw angle range becomes narrower. The side holes (sectors 2 and 4) register maximum pressure from α = 15° to 25° for the right hole (sector 2) and α = -15° to -25° for the left hole (sector 4) respectively, where the yaw angle ranges from β = -25° to 20° for the right hole (sector 2) and β = -20° to 20° for the left hole (sector 4). Furthermore, it can be seen that the centre hole (sector 5) registers maximum

pressure from pitch angle $\alpha = -10^{o}$ to 10^{o} and at yaw angles, it registers the highest pressure from $\beta = -10^{o}$ to 10^{o}. It can be noticed that the sector map is not perfectly symmetrical, it is because a dimensionally perfect and balanced five-hole pressure probe is very difficult to fabricate due to the small nature of the probe and inherent machining imperfections because of human factors.

Based on the calibration coefficients for a hemispherical five-hole pressure probe, the coefficients of determination have been computed for all the sectors of the probe as shown in table 6.3, and for all the different calibration coefficients considered in the present study. Table 6.3 is another way to demonstrate the accuracy of the CFD numerical calibration in wind tunnel external flow (see section 3.9 for a detailed explanation). Notice the portion highlighted in table 6.1 and table 6.3; the CFD numerical simulation has increased the accuracy of the experimental result by 37%. Similarly, for sector 1 and 4 of the CFD simulation calibration have improved the accuracy of those sectors by approximately 10%.

Table 6.3. CFD numerical coefficients of determination

Calibration parameters	Sector 1 (r^2)	Sector 2 (r^2)	Sector 3 (r^2)	Sector 4 (r^2)	Sector 5 (r^2)
Pitch angle (^{o})	1.0000	0.9999	1.0000	1.0000	1.0000
Yaw angle (^{o})	1.0000	0.9889	1.0000	1.0000	1.0000
Total pressure (Pa)	1.0000	0.9988	1.0000	1.0000	0.9999
Static pressure (Pa)	1.0000	0.9988	1.0000	1.0000	0.9999

In comparison to the overall calibration performance of both conical and hemispherical probes in the wind tunnel external flow as demonstrated in table 5.1 and 6.3 respectively, it can be seen that all the coefficients of determination are almost 99%, which shows perfect correlations and acceptable results for this study. Although these coefficients, in case of a conical five-hole pressure probe, were more accurate (only one value of 99% and all the rest were 100%), the error in r^2 values for a hemispherical five-hole pressure probe is 1%, which is negligible in this study. Hence, the numerical calibration of a hemispherical five-hole pressure probe is significantly more accurate than the experimental calibration in the wind tunnel external flows. However, numerically, the conical five-hole pressure probe performs somewhat better with 1% accuracy.

The validation of the CFD numerical calibration dataset of a hemispherical five-hole pressure probe has been carried in a wind tunnel external flow to measure airflow velocities. The outcome of the validation results is presented in figure 6.6.

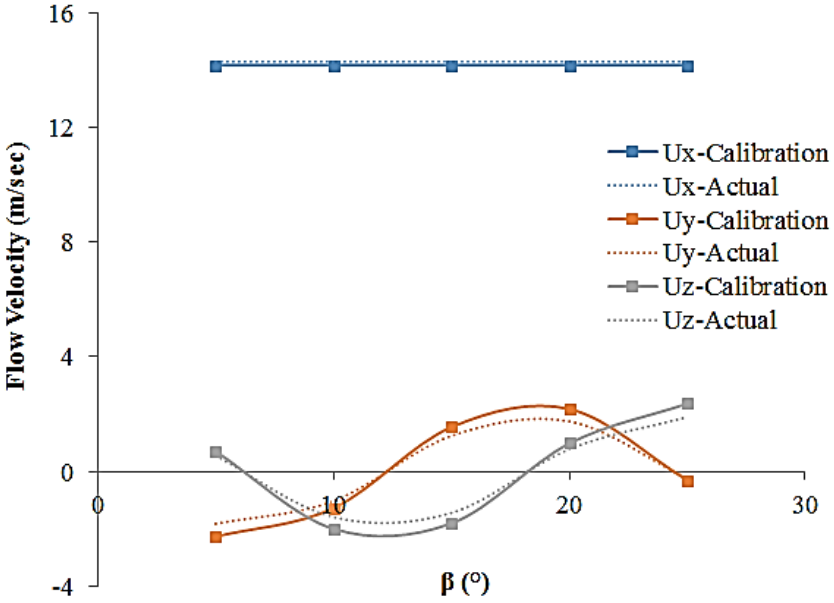

Figure 6.6. Validation of the CFD based numerical calibration dataset

It can be seen in figure 6.6 that the velocity components measured using the CFD based numerical calibration equation for a hemispherical five-hole pressure probe is wind tunnel external flows. As demonstrated in this figure, there is close agreement with that measured experimentally for a known flow field and the velocities measured using CFD based numerical calibration equations. Figure 6.6 shows almost 99% accuracy in the axial direction of the flow velocity. Furthermore, the radial and azimuthal velocities (y and z directions), using a hemispherical five-hole pressure probe, on average, shows about 90% accuracies respectively. Also, the accuracy this study is trying to improve in measurements using five-hole probes through the use of CFD simulation and calibration have been demonstrated in this section, from calibration coefficients to validation of the calibration data using numerical calibration equation.

In comparison, numerical validation results of the two probes the velocity have been computed and presented in figure 6.7. The comparison is also aimed at comparing the performance of both conical and hemispherical pressure probes in wind tunnel external flow. The comparison analysis is carried out to compare the axial, radial and azimuthal velocities of both probes, based on this a comparable conclusion of which probe performed better than the wind tunnel flow is drawn.

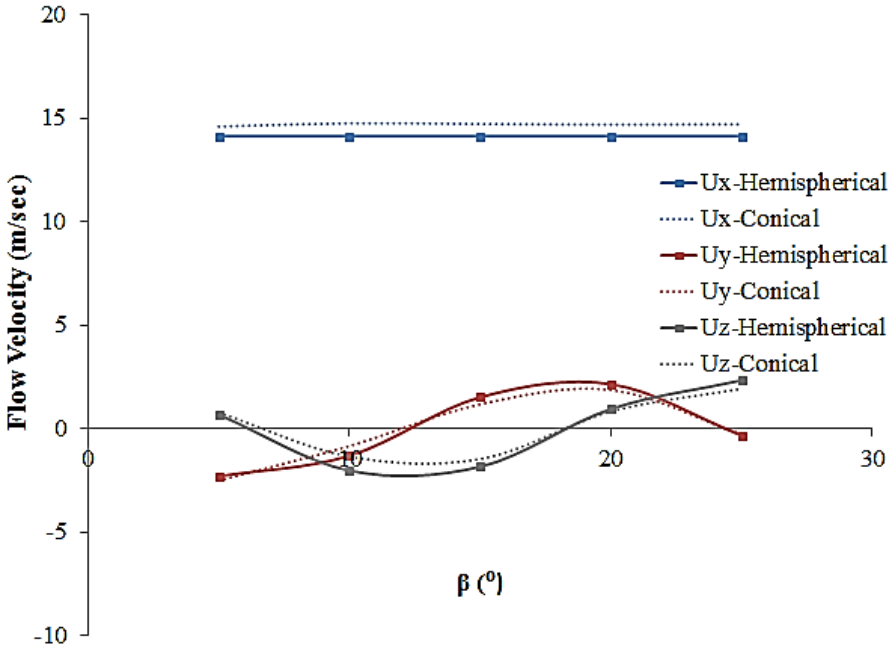

Figure 6.7. Comparison of the CFD based numerical calibration datasets for the two probe heads

Figure 6.7 depicts the comparison of flow information measured by both conical and hemispherical probes using numerical calibration equation. It can be seen that the axial component of velocity measured using a conical five-hole pressure probe is 5% higher than measured using a hemispherical five-hole probe. Similarly, radial and azimuthal velocities, measured using a conical five-hole probe, are 0.5%, while the hemispherical five-hole probe is 0.1% higher than the azimuthal velocity measured using a conical head five-hole pressure probe. Figure 6.7 also suggests that using the CFD numerical calibration method, the conical five-hole probe measurements for axial velocity performed approximately better but the hemispherical five-hole pressure probe measurements for of the radial and azimuthal velocities produce significant accuracy slightly higher in the region of ±2m/sec. In case of the conical five-hole pressure probe, although there is still a significant difference between the axial velocities measured by the two probes, the difference between them is considerably less than for hemispherical five-hole pressure probe. Therefore, using the CFD numerical calibration methods, both conical and hemispherical five-hole probe is appreciably within the same range of accuracy in the range of approximately 1.1%, 3.5% and 3.8% lower.

6.3.2 Numerical measurements Error Analysis

The same principle explained in section 6.2.1 and equation 6.1 have been used to calculate and estimate the error in measurements using the CFD based numerical calibration dataset for the hemispherical five-hole probe. The calculated error values of the five-hole probe measurement are summarised in table 6.4.

Table 6.4. Uncertainties and standard errors in measurement for a hemispherical five-hole pressure probe

Statistical parameters	Pitch angle (°)	Yaw angle (°)	Total pressure (Pa)	Static pressure (Pa)	U (m/sec)	U_x (m/sec)	U_y (m/sec)	U_z (m/sec)
Standard error	0.0281	0.0008	0.0507	0.2903	0.0015	0.0626	0.3908	0.1366

In comparing table 6.4 to table 6.2, it can be seen that the CFD based numerical calibration has increased the flow measurement by decreasing the velocity magnitude error to 0.0015m/sec. Thereby decreasing the error found in three-dimensional velocities to approximately 0.5m/sec. Similarly, table 6.4 shows that the accuracy of flow angles and pressure have equally increased. The accuracy recorded to prove that CFD based numerical calibration can improve measurement accuracy by eliminating the angularity variation of the wind tunnel flow across the test section of the probe calibration through changes in the free stream direction relative to the robe. It is possible because the probe maintained a perfect position (near the tunnel centreline) during the calibration process in the CFD flow domain. Ambient condition changes do not affect the flow measurement directly since the flow angles are determined from the pressure coefficients, which are the ratio of the pressure difference.

The next section explains the method of integrating experimental and CFD numerical dataset to generate a new set of calibration data that aims at improving the wind tunnel flow experimental measurement as depicted in figure 6.3. The following section discusses the method and procedures in details both qualitative and quantitatively.

6.4 Development of an Integrated Calibration Method for Hemispherical Head Five-hole Pressure Probe

The experimental calibration of the hemispherical five-hole pressure probe resulted in a coefficient of determination of 63% for pitch angle in sector one, which is below the threshold of accuracy set in the present study. The numerical coefficient of determination for the same is however perfect (i.e.

100%). This means that the pitch angle measurements using the numerical calibration method are far more accurate than the experimental calibration measurements of the same. Hence, the numerical calibration method has been integrated with the experimental calibration to develop a novel, more accurate calibration method for hemispherical five-hole pressure probes.

After the replacement of the less accurate experimental calibration coefficients for the pitch angle with the more accurate numerical coefficients, the sector map of the integrated calibration method has been developed, as shown in figure 6.8. The sector map for the hemispherical five-hole pressure probe is more symmetrical compared to the integrated sector map of the conical five-hole pressure probe in figure 5.10 (see section 3.9 and figure 5.9 for the summary of the processes).

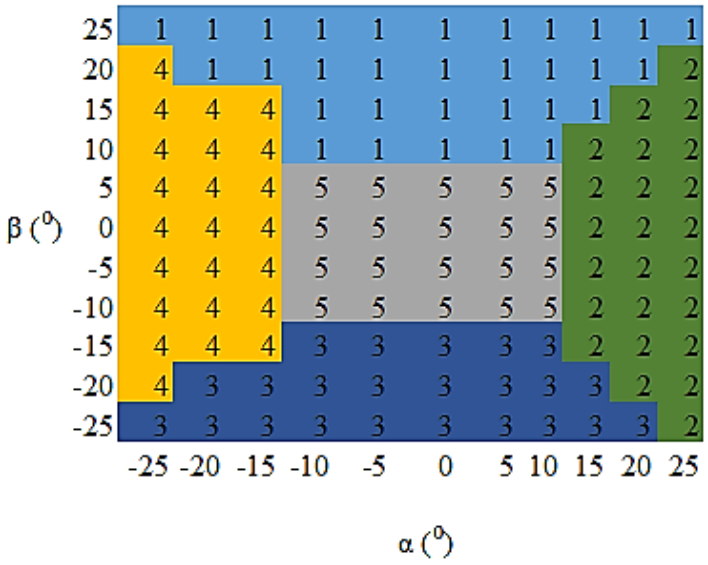

Figure 6.8. CFD based integrated sector map for wind tunnel calibration

Figure 6.8 depicts the calibration sector map generated by integrating CFD base numerical calibration dataset into experimental calibration dataset to eliminate most computational and experimental errors. The y-axis of the calibration sector map represents the yaw plane, while the x-axis represents the pitch plane. The areas with number one in the calibration map are the grid points covered by the top hole (sector 1) of the probe.

Similarly, the area marked by the number 3 are the grids points covered by the bottom hole (sector 3). Also, the fields marked by number 4 (sector 4) are the grids points covered by the left hole. It is the same for the regions marked by number 2 (sector 2). The centre area of the calibration map is the grid point covered by the centre hole (sector 5) of the probe.

It can be seen that the top hole (sector 1) registers the highest pressure from $\alpha = -25^{o}$ to 25^{o} at $\beta = 10^{o}$ to 25^{o}, however, at higher pitch angles (beyond $\pm 10^{o}$), the yaw angle range becomes narrower. Similarly, the bottom hole (sector 3) registers the highest pressure from $\alpha = -25^{o}$ to 20^{o} at $\beta = -15^{o}$ to -25^{o}, however, at higher pitch angles (beyond $\pm 10^{o}$), the yaw angle range becomes narrower. Furthermore, the right holes (sectors 2) register maximum pressure from $\alpha = 15^{o}$ to 25^{o} and $\alpha = -15^{o}$ to -25^{o} for the left hole (sector 4) respectively, where the yaw angle ranges from $\beta = -25^{o}$ to 20^{o} for the right hole (sector 2) and $\beta = -20^{o}$ to 20^{o} for the left hole (sector 4). Also, it can be seen that the centre hole (sector 5) registers maximum pressure from pitch angle $\alpha = -10^{o}$ to 10^{o} and at yaw angles, it registers the highest pressure from $\beta = -10^{o}$ to 5^{o}. Even though the probe registered pressure data evenly, it can be noticed that the sector map is not perfectly symmetrical because of inherent machining imperfections.

The calibration coefficients corresponding to sectors one and five of the hemispherical five-hole pressure probe have been summarised in appendixes 6.3a and 6.3b. Again, in comparison with the conical five-hole pressure probe in chapter 5, the calibration coefficients of the hemispherical five-hole probe, for corresponding sectors, are significantly different. The coefficients of determination of the integrated calibration method have been presented in table 6.5 (see section 3.9 for a detailed explanation).

Table 6.5. CFD based integrated coefficients of determination

Calibration parameters	Sector 1 (r^2)	Sector 2 (r^2)	Sector 3 (r^2)	Sector 4 (r^2)	Sector 5 (r^2)
Pitch angle (^{o})	1.0000	1.0000	1.0000	0.9698	1.0000
Yaw angle (^{o})	0.9172	1.0000	1.0000	0.9341	1.0000
Total pressure (Pa)	0.9754	1.0000	1.0000	0.9673	1.0000
Static pressure (Pa)	0.9646	1.0000	1.0000	0.9669	1.0000

It can be seen that the coefficient of calibration for pitch angle, in sector 1, is now 1.0000 as against the 0.63 in table 5.1 as highlighted in table 6.3, hence, improving the accuracy of measurements using a hemispherical five-hole pressure probe. The integration of CFD numerical calibration data into experimental calibration data is to overcome the limitations of experimental calibration such sudden change in flow characteristics due to laboratory disturbances or unwanted air conditions during calibration or measurements that could cause an error and give less computational errors in calculating flow information. It is worth to mention that the sector replaced by the CFD numerical datasets is sector 1. Having integrated the CFD numerical datasets into the experimental datasets, it

can be seen that table 6.5 have achieved calibration coefficients of determination with more than 97% accuracy averagely.

The validity of the integrated calibration of a hemispherical five-hole pressure probe is presented in figure 6.9. To further study and validate the performance of the CFD based integrated calibration method in wind tunnel flow, the CFD based integrated calibration equations are used to study the velocity distribution of the flow. Flow information measured and calculated using in the integrated calibration equations is compared against know flow fields. This performance study is demonstrated in figure 6.9.

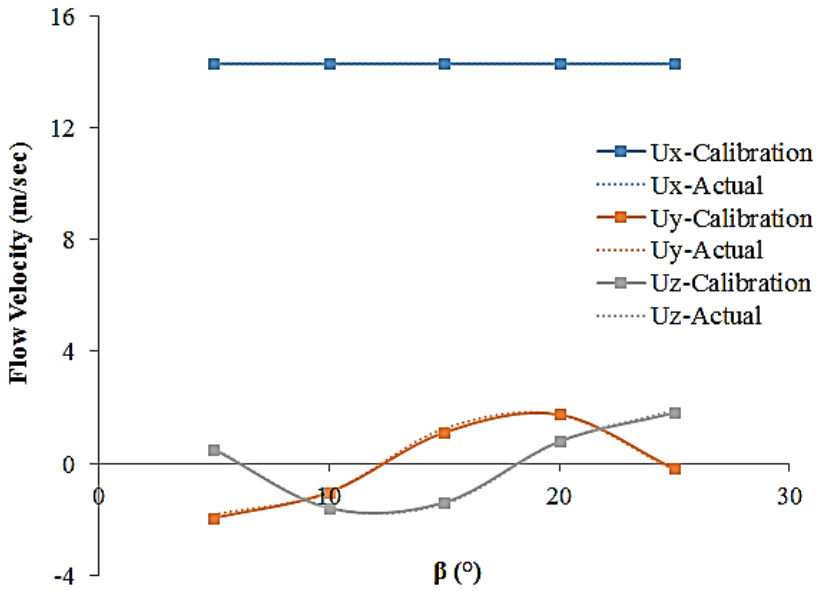

Figure 6.9. Validation of the CFD based integrated calibration data

It can be seen clearly without a doubt that the velocity components of the flow measured using the integrated calibration equation, for a hemispherical five-hole pressure probe, are matching perfectly with the actual velocity components measured for a known flow field (same as before). Hence, the integrated calibration method carried out for the external flow is more accurate than the conventional calibration method. Figure 6.9 shows that the axial velocity produces a ±15m/sec accuracy and a ±5° accuracy in pitch and yaw angle. Similarly, the radial and azimuthal velocities show an accuracy of 100% respective in the wind tunnel flow.

Figure 6.9 demonstrates the comparison of the CFD numerical based integrated calibration methods for both conical and hemispherical probes in the wind tunnel flow. This analysis is carried out to demonstrate the calibration method for different probes and to test their performance.

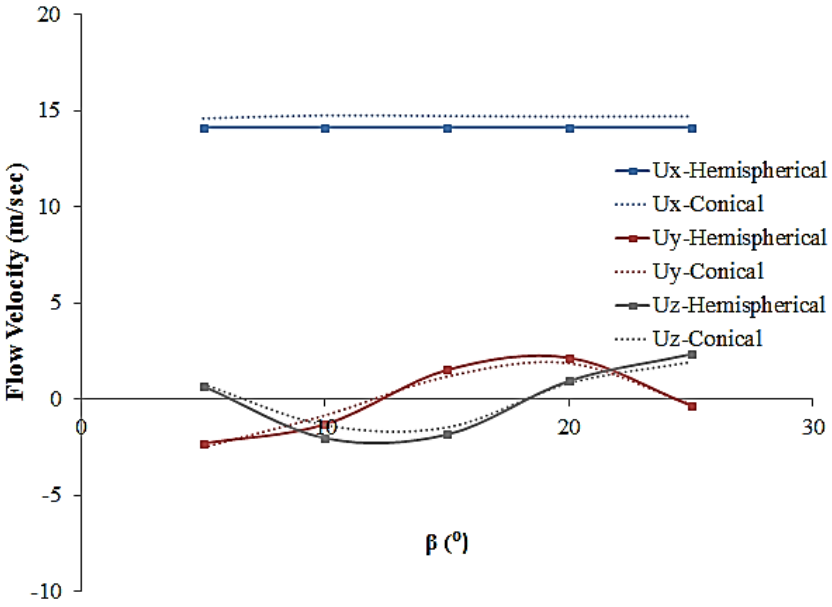

Figure 6.10. Comparison of the CFD based integrated calibration dataset for the two probes

Figure 6.10 depicts the contrast of the performance of the integrated calibration method in wind tunnel flow to measure and study velocities using both conical and hemispherical five-hole probe. It can be seen that the axial component of velocity measured using a conical five-hole pressure probe is 5% higher than measured using a hemispherical five-hole probe, which is 5% less.

Similarly, radial and azimuthal velocities, measured using a conical five-hole probe, are 0.5% accurate, while the hemispherical five-hole probe is 0.2% higher than the azimuthal velocity measured using a conical head five-hole pressure probe. Figure 6.10 shows that the CFD numerical integrated calibration method shows better performance for the conical five-hole probe measurements for axial velocity than the hemispherical five-hole probe. It can be seen that the velocities measured (in axial, radial and azimuthal), using a hemispherical five-hole pressure probe are 2.3%, 3.9%, and 4.8% lower, on average, then the conical five-hole pressure probe.

The next section explains a novel CFD based extended calibration method for the hemispherical five-hole probe using CFD to simulate and extend the calibration range of the integrated calibration method by generating a new set of pressure data from $\pm 30^{o}$ to $\pm 45^{o}$ and then calculate new calibration set of equations that to measure flow at larger flow field. The following section discusses the CFD numerical based extended calibration method and procedures in details both qualitatively and quantitatively.

6.4.1 Integration Measurements Error Analysis

Applying the same principle and equation in section 6.2.1 and equation 6.1, the error analysis for the CFD integration calibration method of the hemispherical probe is summarised in table 6.6.

Table 6.6. Uncertainties and standard errors in measurement for conical five-hole pressure probe

Statistical parameters	Pitch angle (^{o})	Yaw angle (^{o})	Total pressure (Pa)	Static pressure (Pa)	U (m/sec)	U_x (m/sec)	U_y (m/sec)	U_z (m/sec)
Standard error	0.0181	0.0110	0.0507	0.2903	0.0015	0.0626	0.3908	0.1366

By comparing to table 6.4 and table 6.2, the CFD based integrated numerical data into experimental calibration data have the ability to decreased flow angle measurement error to approximately within 0.0291^o . Similarly, the error in flow total and static pressure are within 0.3410Pa. Furthermore, the errors in velocity measurements have been reduced to almost within 0.5915m/sec. The error and uncertainty analysis established in the section for the probe calibration prove that the calibration method developed in this study is capable of predicting wind tunnel flow parameters within the accuracy required accuracy for optimum operation of fluid systems.

6.5 CFD based Extended Calibration Method

As discussed earlier, the range of the integrated calibration method developed here is limited that restricts the applicability of the five-hole pressure probe. Hence, numerical simulation data has been generated for $\alpha = -30^0$ to -45^0 and from 30^0 to 45^0, and $\beta = -30^0$ to -45^0 and from 30^0 to 45^0. The calibration data for $\alpha = \pm 25^0$ and $\beta = \pm 25^0$ is considered the same as in the integrated method. The static gauge pressure and flow velocity magnitude variations in the region of the hemispherical head five-hole pressure probe at a high angle flow angle have been shown in figure 6.11.

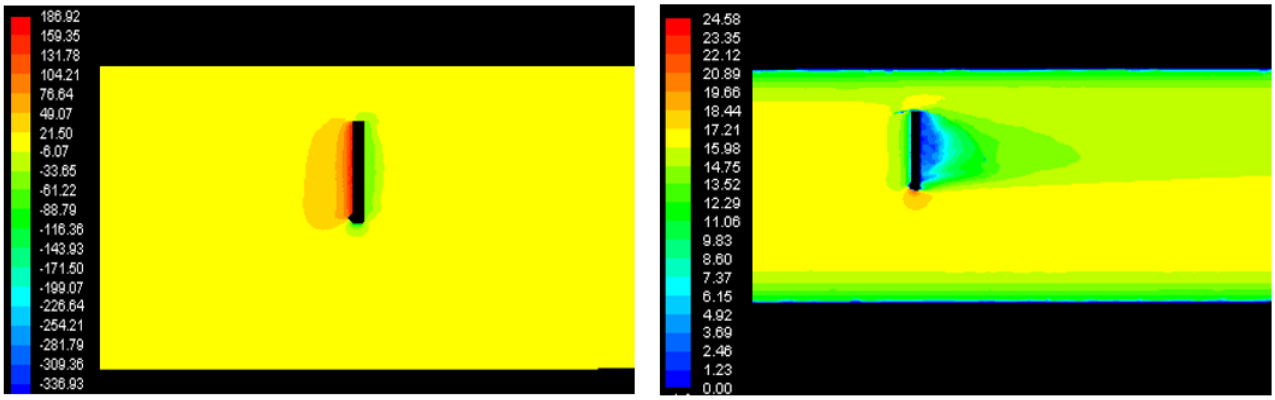

(a) Flow static gauge pressure

(b) Flow velocity magnitude

Figure 6.11. Variation in (a) flow field static gauge pressure and (b) flow field velocity magnitude in the vicinity of the probe at $\alpha=\beta=45^0$

Figure 6.11 shows the flow static gauge pressure and velocity magnitude variations at high flow angles. The effective comparison with the conical five-hole pressure probe for the same high angle flow, the range of these variations has been kept the same. The flow parameters shown in the figure corresponds to the wind tunnel average flow velocity at $\alpha = 0^{o}$ and $\beta = 45^{o}$. It can be seen that the presence of the hemispherical five-hole pressure probe causes flow separation, although uniformly in the wind tunnel. This results in high static gauge pressure at the front region of the probe but decreases downstream the probe. In comparison, with figure 5.12(a), the static gauge pressure variation for the conical and the hemispherical five-hole pressure probe have similar characteristics. Therefore, both probes produce similar flow field at high flow angles. Similarly, the flow velocity magnitude shown in figure 5.12(b) shows that the hemispherical five-hole pressure probe produced slightly higher velocity magnitude of approximately 4.5% than the conical five-hole pressure probe Malviya, V., Mishra, R., & Palmer, E., (2015).

The flow around the conical head and hemispherical head probe have been studied in the wind tunnel system using CFD methods as shown in chapter 5 and 6. The static pressure around the probe for both head shapes has been presented with velocity contours along the flow axis upstream and downstream of the probes. Although the influence of both head shapes on static pressure and flow velocity are similar, the extent of disruption is significantly different. To a distance of about two and a half diameters downstream of the probe, the conical five-hole probe shows to have a much higher disruptive influence on the flow field. It is demonstrated by the higher values of the static pressure within the region of flow first contact with the conical probe, which indicates a high

level of flow divergence. The average static pressure is about 5.5% higher for conical probe compared to the hemispherical probe. It is supported by the generally slightly higher value of the velocity magnitude for the conical probe. The influence of the hemispherical probe on the flow is typically minimal. As the flow travels downstream, the effect of the probe, the flow is considered marginal. It is demonstrated by the decrease in velocity magnitude, as it becomes less 0.7% averagely than the free stream velocity from upstream to downstream.

Although these influences can further be reduced by reducing the size of the probes, however, the conical probe will always have a more significant effect on the flow field for similarly sized probe shapes. The lower impact of the hemispherical probe will subsequently improve the accuracy of measurements. Furthermore, because of the lower level of flow disruption caused by the hemispherical probe, it is possible to use a denser distribution of probes of this type compared to the conical probe. Although it is can be seen that the hemispherical pressure probe has significant advantages over the conical pressure probe in complex three-dimensional flow applications, however, both pressure probes can be accurately calibrated using the novel methods proposed in this study and used to measure and validate flow properties with reasonable accuracies as already established up until this section. The sections below describe further results of the extension of calibration range.

6.5.1 Calibration of CFD based extended datasets

Applying the procedures described in the flowchart shown in figure 5.13 and the steps outlined in section 3.9, the extended calibration sector map for the hemispherical head five-hole pressure probe is has been generated as shown in figure 6.12. The sector datasets within the thick box are the same as in the integrated calibration method. In comparison, with the conical head five-hole pressure probe's extended calibration sector map in figure 5.14, it can be seen that both these sector maps are identical, confirming the qualitative similarities between the two probes. This further indicates that qualitative analysis, without the quantitative analysis, of the five-hole pressure probes, is not enough to analyse the calibration processes in detail Parameswanran, V., Jategaonkar, R., & Press, M. (2002) and Akshoy, R. P., Ravi, R. U., & Anu, J. (2011).

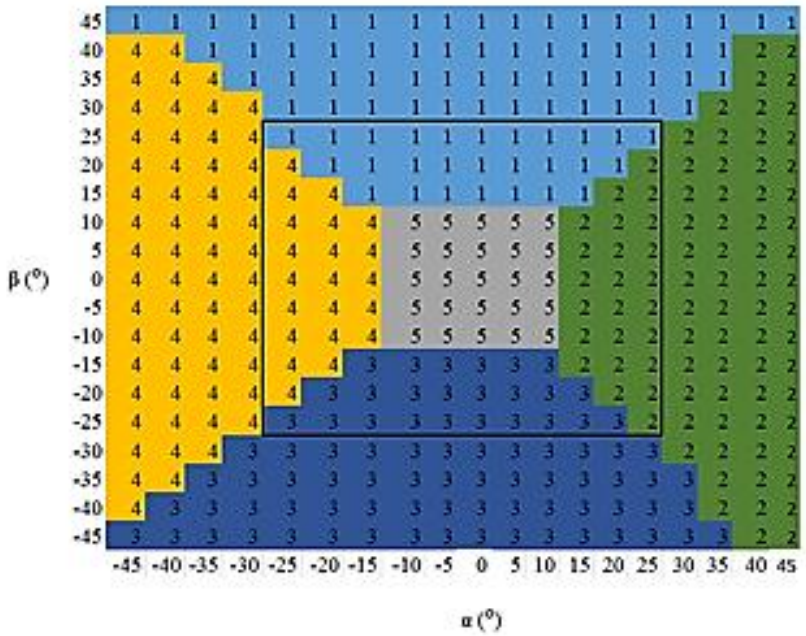

Figure 6.12. CFD based extended sector map for wind tunnel calibration

Figure 6.12 depicts the calibration map generated using CFD numerically extended pressure datasets of the hemispherical pressure five-hole probe in a wind tunnel flow indicating five separate sectors. The calibration map can sometimes be used to find the best suitable range of pitch angle and yaw angle during calibration. It shows the relationship between pressure data and flow angles. The y-axis of the map represents the yaw, while the x-axis represents the pitch. The areas marked by the number 1 (sector 1) are the grids covered by the top hole.

Similarly, the area marked by the number 3 (sector 3) are the grids covered by the bottom hole. Furthermore, the fields marked by number 4 (sector 4) are the grids covered by the left hole. It the same for the area marked by number 2 (sector 2). The centre area of the calibration map marked by 5 are the areas in the regions in the calibration grid covered by the centre hole (sector 5) of the probe during the extension of range calibration.

The top hole of the probe as shown in figure 6.12 above has the top hole (sector 1) registers the highest pressure from $\alpha = -45^{o}$ to 45^{o} , while at yaw axis, $\beta = 15^{o}$ to 45^{o} , however, at higher pitch angles (beyond $\pm 15^{o}$), the yaw angle range becomes narrower. Similarly, the bottom hole (sector 3) registers the highest pressure from $\alpha = -45^{o}$ to 35^{o} , while at yaw axis, it has at $\beta = -15^{o}$ to -45^{o} , however, at higher pitch angles (beyond $\pm 15^{o}$ the yaw angle narrows). The right holes (sectors 2) register maximum pressure from $\alpha = 15^{o}$ to 45^{o} and $\alpha = -15^{o}$ to -55^{o} for the left hole

(sector 4) respectively, where the yaw angle registers pressure from $\beta = -45^{o}$ to 40^{o} for the holes right hole (sector 2) and $\beta = -40^{o}$ to 40^{o} for the left hole (sector 4). Furthermore, it can be seen that the centre hole (sector 5) registers maximum pressure from pitch angle $\alpha = -10^{o}$ to 10^{o} at yaw angles (β) of -10^{o} to 10^{o} . Just like figure 6.1, 6.5 and 6.8, it can equally be noticed that the hemispherical five-hole probe extended sector map is not perfectly symmetrical even though it was generated by numerically using CFD by extending the integrated. The unbalanced nature of the map is because of human factors mainly from the alignment of the probe in the flow.

Based on the sixth order polynomial curve fitting method, the calibration coefficients, corresponding to different sectors of the hemispherical five-hole pressure probe have been computed. The calibration coefficients for sectors one and five have been presented in appendixes 6.4a and 6.4b. In comparison, with appendixes 5.4a and 5.4b for a conical five-hole pressure probe, it is clear that the calibration coefficients of the hemispherical five-hole pressure probe are significantly different in both these sectors, and for all the different calibration parameters considered in the present study.

Table 6.7 summarises the coefficients of determination for all the five sectors of the hemispherical five-hole pressure probe, for the extended range calibration data. It can be seen that the coefficients of determination for all the different parameters, and in all the five sectors, are => 90% (see section 3.9 for explanations and figure 5.13 for process summary). Hence, the extension in the calibration range of the hemispherical five-hole pressure probe has been reasonably accurate.

Table 6.7. CFD based extension of range coefficients of determination

Calibration parameters	Sector 1 (r^2)	Sector 2 (r^2)	Sector 3 (r^2)	Sector 4 (r^2)	Sector 5 (r^2)
Pitch angle (^{o})	0.9965	0.9975	0.9909	0.9964	0.9999
Yaw angle (^{o})	0.9967	0.9976	0.9907	0.9968	1.0000
Total pressure (Pa)	0.9988	0.9986	0.9986	0.9987	0.9998
Static pressure (Pa)	0.9986	0.9986	0.9986	0.9986	0.9999

It can be seen that in table 6.7 that the coefficient of the extended calibration method for all calibration parameters, in all sectors of the probe has achieved more than 95% accuracy. Table 6.7 is another proof that the CFD based integration and extension calibration methods are capable of improving the accuracy of hemispherical five-hole probe calibration and measurements of fluid flows.

The validity of the CFD extended calibration method of the hemispherical five-hole pressure probe is presented in figure 6.13. To further study and validate the performance of the CFD extended calibration method in wind tunnel flow, the probe has been used to measure fluid flow and applied calibration equations generated from the CFD extended calibration to calculate and study flow the velocity distribution. Figure 6.13 depicts the validity of the extended calibration data against a known flow field in the wind tunnel flow, having an average flow velocity of 15m/sec and $\alpha = 45^{o}$.

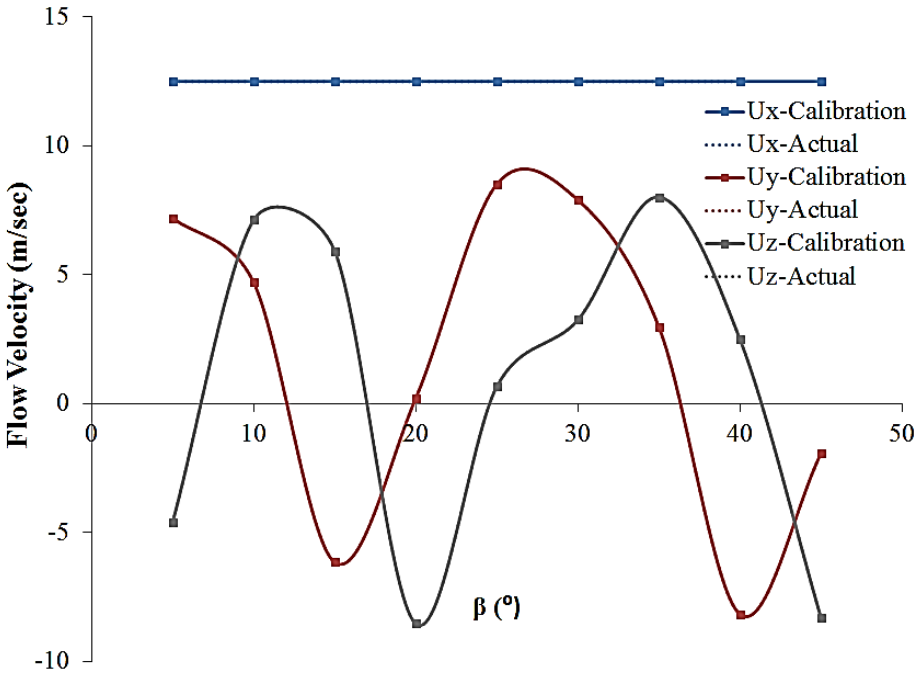

Figure 6.13. Validation of the CFD based extended calibration dataset

It can be seen that the extended calibration data is capable of predicting the three components of the flow velocity with reasonable accuracy. The extended calibration method developed here is not just accurate, but also applicable to a wider range of measurements, which is the highlight of this method.

It can be seen that the axial velocity maintained 100% accuracy equal to the axial velocity of the known flow. Similarly, radial and azimuthal velocities equally have a 100% measurement accuracy concerning flow angles. Figure 6.13 further shows that the CFD based extended calibration method command accurately established performances for five-hole probe calibration and flow measurements for all three components velocities as well as flow angles.

6.5.2 Extension Measurements Error Analysis

The validity of figure 6.13 is tested by performing measurement uncertainty and error analysis of the CFD based extension calibration method of the hemispherical five-hole pressure probe at an unknown flow field. The investigation is carried out on the flow parameters measured by the probe. If the uncertainty analysis proves accurate, the deviation of the velocity measurement should agree with the predicted precision errors. The importance of error analysis is that once accuracy is established, measurements made by the probe can be validated using any other instruments. The error analysis is carried out using equation 6.1 as determined in section 6.2.1. The predicted error values of the hemispherical five-hole probe measurements are summarised in table 6.6. The analysis is carried out on flow angles, total and static pressure, and velocities.

Table 6.8. Uncertainties and standard errors in measurement for a hemispherical five-hole pressure probe

Statistical parameters	Pitch angle (º)	Yaw angle (º)	Total pressure (Pa)	Static pressure (Pa)	U (m/sec)	U_x (m/sec)	U_y (m/sec)	U_z (m/sec)
Standard error	0.0658	0.0121	0.5131	0.0441	0.0011	0.0030	0.0614	0.0465

By comparing table 6.8 to table 6.6, it can be seen that each step of the CFD based calibration increases measurement accuracy in every flow parameter of the wind tunnel flow. The CFD based extension of calibration has reduced measurement error approximately to within 0.0389º pitch and yaw angle, and 0.4770Pa for total and static pressures. Similarly, measurement error has equally reduced to 0.1326m/sec for flow velocities. Again, it has been established in table 6.8 that the CFD calibration can be used to extend a five-hole probe calibration angle and still maintains high measurement accuracies of the flow parameters.

Error analysis has been performed for all measurements carried out in this chapter using the hemispherical five-hole pressure probe to determine the uncertainty of the probe. The error is the difference between the true values and predicted values of the flow parameters. Since the true values are unknown, estimates of the error must be made. Uncertainty is determined as a possible value of that error, known as experimental error. In this chapter, the uncertainty of the flow angles, pressures and velocities for the hemispherical probe has been examined and tabulated for each of the calibration method presented in this chapter.

6.6 Summary

In this study, the hemispherical five-hole pressure probe has been experimentally and numerically studied regarding calibration and fluid flow measurements. The novel techniques, requiring the calibration and measurement of a hemispherical pressure five-hole probe, have been developed for measuring velocities of air in external (wind tunnel) flows. For the wind tunnel test, numerical calibration was performed by applying a CFD analysis and an optimisation technique base on CFD integration and extension calibration methods. The probe was used to measure and calculate flow information and compare with known flow filed to validate the performance of the probe calibration. The techniques have been established to be accurate for both calibration and fluid flow measurements. A measurement study has been carried out using the novel calibration methods developed in this chapter to investigate the distribution of the flow local axial, radial and azimuthal air velocities in a horizontal wind tunnel. The performance of CFD based numerical calibration method has been investigated. For a range of flow conditions, the following key results have been observed.

1. The results presented in this chapter are derived from the methodology and experimental setup previously discussed in chapter 3 and 4.
2. The results are presented in correlation to their relevance to the overall aims and objective of this study.
3. The qualitative comparison of the conventional calibration process between hemispherical and conical five-hole pressure probes has indicated that both these probes perform similarly.
4. Significant differences in the quantitative analyses have been noticed, which suggests that the conventional calibration of hemispherical five-hole pressure probes is more accurate than of conical five-hole pressure probes.
5. The flow fields associated with the hemispherical five-hole probe has minimal differences in comparison with the flow field of the conical five-hole probes.
6. An integrated calibration method for hemispherical five-hole probes has been developed, based on the calibration data from well-validated numerical simulations, for a range of fluid flow operational parameters.
7. The extended calibration method for the hemispherical five-hole probes greatly enhances the usefulness and applicability of such probes for accurate flow velocity immurements in wind tunnel flows.

8. The CFD based integrated calibration method of the hemispherical five-hole probe has been found to have increased the accuracy of velocity measurements by 5% in the wind tunnel flow
9. The CFD based extended calibration method has been found to have a calibration accuracy of over 95% in the wind tunnel flow
10. The CFD extended measurements of the five-hole hemispherical probe have increased the accuracy of flow angles by $\pm 3^{o}$ in the wind tunnel flow
11. The CFD extended measurements of the five-hole hemispherical probe have increased the accuracy of flow velocities by ±1.3m/sec in the wind tunnel flow
12. It has been demonstrated that the key to success of many probe calibration techniques is the ability to define velocity invariant pressure coefficients, which are the ratio of two pressure differences. This type of normalisation is successful for conical five-hole pressure probe in the wind tunnel flow
13. The probe calibration is conceptually simple and is essentially a variation of a time-tested probe technique.

Although these results could have been predicted qualitatively in advance, the novel calibration and measurement methods described herein allows flow velocity measurements with efficiency and at large flow field using CFD numerical calibration methods. It has been found that calibration data decrease close to the walls but increases at the centre of the test section. Furthermore, it has been found that the hemispherical five-hole probe and the calibration methods developed in this chapter could improve the velocities of airflows by overall values of 1.5m/sec and flow angle by $\pm 2.7^{o}$ respectively.

After carrying out detailed investigations on the effects of the head shape of a five-hole pressure probe, the next step is to investigate the effect of the fluid properties on the calibration process of five-hole pressure probes. Thus, the next chapter presents the calibration of both the conical and hemispherical head five-hole pressure probes in a hydraulic pipeline.

Chapter 7 Effect of the Flow Regime and Fluid Properties on the Calibration of Five-hole Pressure Probes

The effect of the flow regime and fluid properties on the calibration of a five-hole pressure probe has been investigated in this chapter. For this purpose, both conical and hemispherical five-hole pressure probes have been extensively tested, both experimentally and numerically, in a hydraulic pipeline flow. The conventional calibration for both the probes has been carried out and compared against each other in the same flow. A computational fluid dynamic (CFD) based integrated calibration method has been developed for both the probes, to increase the accuracy of fluid flow measurements. The calibration range has been extended using CFD based numerical methods.

7.1 Introduction

The main aim of this chapter is to analyse the effects of flow regime and flow properties on the calibration of a multi-hole pressure probe. Hence, the calibration process, similar to that presented in chapters 5 and 6, has been carried out on both the conical and hemispherical five-hole pressure probes in hydraulic pipelines flows. Comparisons have been made against the calibration results of the corresponding five-hole pressure probes in the hydraulic pipeline flows. Detailed qualitative and quantitative comparisons have been made for measuring flow velocities by the two probes using both the calibration methods in the same media. Moreover, a comparison of the flow behaviour near both the probes in low and high angle flows has been included in this chapter.

7.2 Experimental Calibration of Five-hole Pressure Probes

Conical and hemispherical five-hole pressure probes have been calibrated using the conventional method of calibration. Extensive hydraulic pipeline testing has been carried out at an average flow velocity of 2.12m/sec, and pitch and yaw angle range of $\pm 25^0$. The pressure datasets on all the individual holes of the probe have been recorded. Although the experiments have been carried out in a controlled manner, there can be some factors affecting the accuracy of the measurements, such as misalignment of the probe, human error arising from manual traversing of the probe, probe-machining imperfections etc. Hence, for repeatability of the pressure datasets, the pressure datasets on all the five holes of each probe, including the static and total pressures, has been measured four times in subsequent runs (see section 3.9).

The average pressure values on the holes of the conical and hemispherical five-hole pressure probes have been used to develop the calibration sector maps for the probes as depicted in figure 7.1 and 7.2. The calibration sector map is a representation of the holes registering the highest pressure values at a given pitch (α) and yaw (β) angles. In comparison, it can be seen that the calibration sector maps in hydraulic pipeline flows are slightly different for both the probes. In case of a conical five-hole pressure probe, both the sectors 2 and 4 cover a wider range of yaw angle plane. Similarly, in case a hemispherical five-hole pressure probe, both the sectors 2 and 4 cover a wider range of pitch angle plane. Hence, overall, although the sector maps for both the probes are similar, there are differences in the range of angles at which the corresponding holes record highest-pressure values Lamb, H. (1932) and Akshoy, R. P., Ravi, R. U., & Anu, J. (2011).

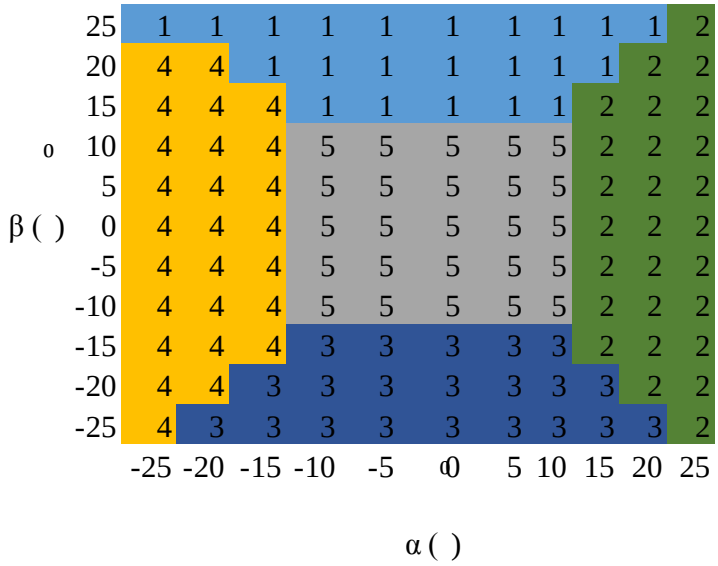

Figure 7.1. Experimental sector map for conical five-hole pressure probe for hydraulic pipeline calibration

Figure 7.1 depicts the calibration map generated by the data measured by the conical five-hole pressure probe in a hydraulic pipeline flow. The y-axis of the map represents the yaw, while the x-axis represents the pitch. The areas marked by the number one (sector 1) are the grids covered by the top hole for pressure measurement. Similarly, the areas marked by the number 3 (sector 3) are the grids covered by the bottom hole. Furthermore, the areas marked by number four (sector 4) are the grids covered by the left hole. Similarly, the areas marked by h number two (sector 2) are the grid covered by the right hole. Also, the centre area of the calibration map marked by the number 5 is the grid covered by the centre hole (sector 5) of the probe.

It can be seen that the top hole (sector 1) registers the highest pressure from $\alpha = -20^{o}$ to 25^{o} and $\beta = 15^{o}$ to 25^{o}, however, at higher pitch angles (beyond $\pm 15^{o}$), the yaw angle range becomes narrower. Similarly, the bottom hole (sector 3) registers the highest pressure from $\alpha = -20^{o}$ to 25^{o} and $\beta = -15^{o}$ to -25^{o} but at higher pitch angles (beyond $\pm 15^{o}$, the yaw angle range becomes narrower. Furthermore, the right holes (sectors 2) register maximum pressure from $\alpha = 15^{o}$ to 25^{o} and $\alpha = -15^{o}$ to -25^{o} for the left hole (sector 4) respectively, where the yaw angle ranges from $\beta = -25^{o}$ to 25^{o} for the right hole (sector 2) and $\beta = -25^{o}$ to 20^{o} for the left hole (sector 4). Also, it can be seen that the centre hole (sector 5) registers maximum pressure from pitch angle $\alpha = -10^{o}$ to 10^{o} and at yaw angles, it registers the highest pressure from $\beta = -10^{o}$ to 10^{o}. Although the calibration map generated by the data measured from the pipeline flow using the conical probe shows that the holes are evenly distributed, it can be noticed that the sector map is not perfectly

symmetrical, this is because of inherent misalignment imperfections Hale, M. R. (1967) and R. P., Ravi, R. U., & Anu, J. (2011).

The same procedure above was repeated for a hemispherical five-hole probe in a hydraulic pipeline. The experiment was carried out under the same condition and flow domain, and the calibration map generated by the data measured in the pipeline flow is shown in figure 7.2.

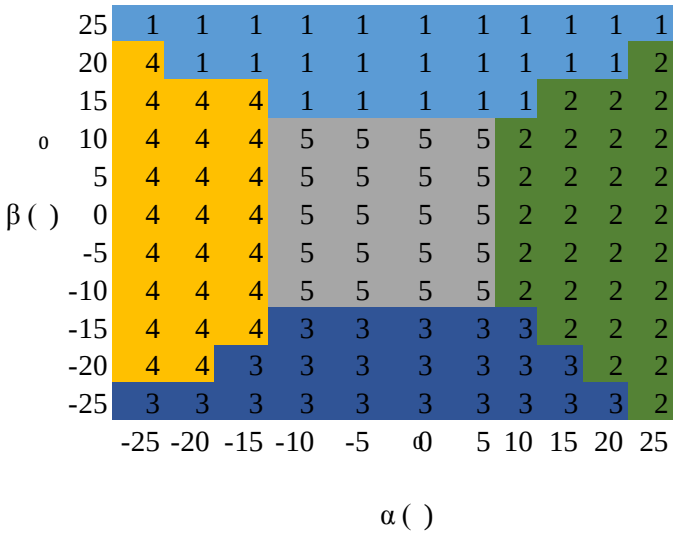

Figure 7.2. Experimental sector map for hemispherical five-hole pressure probe for hydraulic pipeline calibration

Figure 7.2 depicts the calibration map generated by the data measured by the hemispherical five-hole pressure probe in a hydraulic pipeline flow. The y-axis of the calibration sector map represents the yaw, while the x-axis represents the pitch. Similar to figure 7.1, the areas marked by the number one (sector 1) are the grids covered by the top hole of the probe. The area marked by the number 3 (sector 3) are the grids covered by the bottom hole. Furthermore, the areas marked by number four (sector 4) are the grids covered by the left hole. Similarly, the fields marked by number two (sector 2) are the grids covered by the right hole. Also, the centre area covered by the number five are the grids covered by the centre hole (sector 5) of the probe.

It can be seen that the top hole (sector 1) registers the highest pressure from $\alpha = -25^{o}$ to 25^{o} and $\beta = 15^{o}$ to 25^{o}, however, at higher pitch angles (beyond $\pm 15^{o}$), the yaw angle range becomes narrower. Similarly, the bottom hole (sector 3) registers the highest pressure from $\alpha = -25^{o}$ to 20^{o} and $\beta = -15^{o}$ to -25^{o} but at higher pitch angles (beyond $\pm 15^{o}$), the yaw angle range becomes narrower. Furthermore, the right holes (sectors 2) register maximum pressure from $\alpha = 10^{o}$ to 25^{o}

and $\alpha = -15^{o}$ to -25^{o} for the left hole (sector 4) respectively, where the yaw angle ranges from $\beta = -25^{o}$ to 20^{o} for the right hole (sector 2) and $\beta = -20^{o}$ to 20^{o} for the left hole (sector 4). Also, it can be seen that the centre hole (sector 5) registers maximum pressure from pitch angle $\alpha = -10^{o}$ to 10^{o} and at yaw angles, it registers the highest pressure from $\beta = -10^{o}$ to 10^{o}. Although the calibration map generated by the data measured from the pipeline flow using the conical probe shows that the holes are evenly distributed, it can be noticed that the hemispherical five-hole sector map is not perfectly symmetrical, this is because of inherent misalignment imperfections.

Based on data reduction techniques, and using a sixth order polynomial curve fitting method, the calibration coefficients for all the sectors of both the probes have been calculated. These calibration coefficients are summarised in appendixes 7.1a to 7.1d and appendix, where appendixes 7.1a and 7.1b summarise the calibration coefficients for sectors 1 and 5 of the conical five-hole pressure probe, while appendixes 7.1c and 7.1d present the calibration coefficients in sectors 1 and 5 of the hemispherical five-hole pressure probe. In comparison, with appendixes 7.1a to 7.1d and appendix 7.1c to 7.1d, it can be noticed that the calibration coefficients, for both the probes, in hydraulic pipeline flows are slightly different in predicting calibration parameters.

To validate the accuracy of the calibration coefficients of the conical and hemispherical five-hole pressure probes, the coefficients of determination, for all the sectors of the probes, and for the different calibration parameters, have been computed (see section 3.9). These coefficients have been summarised in tables 7.1 and 7.2 for the conical and hemispherical head probes respectively.

Table 7.1. Experimental coefficients of determination for conical five-hole pressure probe

Calibration parameters	Sector 1 (r^2)	Sector 2 (r^2)	Sector 3 (r^2)	Sector 4 (r^2)	Sector 5 (r^2)
Pitch angle (^{o})	0.9999	0.9987	1.0000	1.0000	1.0000
Yaw angle (^{o})	0.9999	0.7768	1.0000	1.0000	1.0000
Total pressure (Pa)	0.9999	0.9996	1.0000	1.0000	0.9999
Static pressure (Pa)	0.9999	0.9996	1.0000	1.0000	0.9999

It can be seen in table 7.1 that all sectors except sector 2 have a perfect correlation with the measured pressure data. For sector 2, the correlation is quite accurate, except for the yaw angle. In the present study of the conical five-hole probe in hydraulic pipeline flows, a correlation of more than 90% has been considered adequate for correlating the measured and the calculated coefficients, any correlation that is below 90% is not acceptable for this study. The same process and procedure have been repeated for the hemispherical five-hole probe, and the result is shown in table 7.2.

Table 7.2. Experimental coefficients of determination for hemispherical five-hole pressure probe

Calibration parameters	Sector 1 (r^2)	Sector 2 (r^2)	Sector 3 (r^2)	Sector 4 (r^2)	Sector 5 (r^2)
Pitch angle (°)	0.9999	0.1265	1.0000	1.0000	1.0000
Yaw angle (°)	0.9999	0.2978	1.0000	1.0000	1.0000
Total pressure (Pa)	1.0000	0.9999	1.0000	1.0000	0.9999
Static pressure (Pa)	1.0000	0.9999	1.0000	1.0000	0.9999

Table 7.2 shows that there is a perfect correlation with measured pressure data for fall sectors except for sector 2, for sector 2, the correlation is rather precise, except pitch and yaw angles. In the current study on a hemispherical five-hole probe in hydraulic pipeline flows, a correlation of more than 90% in the flow of hydraulic pipelines is considered sufficient to correlate the measured and calculated coefficients, any correlation below 90% is not acceptable in this study.

Like chapter 5 and 6, it is expected that the measurements based on these correlations will not yield accurate results for actual flow measurements. Hence, additional high accuracy data is needed that can be used alongside the measured data, to develop correlations that have better validity to compensate for sector 2 in table 7.1 and 7.2. It has been achieved in the presented study by incorporating data obtained using CFD based numerical simulations. Before moving on to the CFD numerical calibration of the probes, the validation of the conventional calibration equations obtained here for both the probes needs to be carried out, and this is depicted in figure 7.3 and 7.4 respectively.

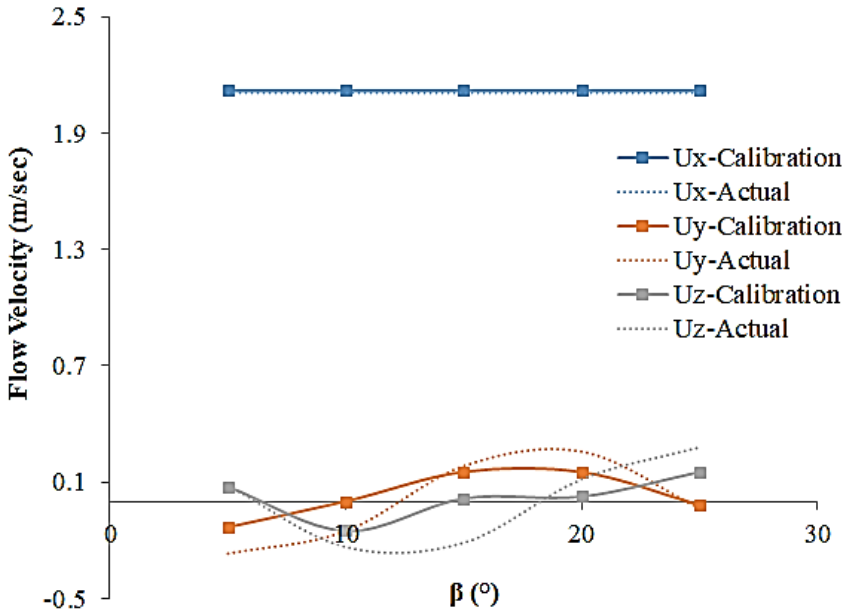

Figure 7.3. Validation of the experimental calibration dataset for a conical five-hole pressure probe

Figure 7.3 demonstrates the validity of the experimental dataset and the calibration equation of the conical five-hole probe in internal flow information. Flow information measured and calculated using calibration dataset is compared with known. The figure indicates that the axial velocity measured using the conical probe maintained a 100% accuracy concerning flow angles. Similarly, it can be noticed that there are variation in the radial and azimuthal velocities in the ±0.2m/sec and ±0.5m/sec. The same process is also applied using the hemispherical five-hole probe in the same flow under the same flow condition, and the result is depicted in figure 7.4.

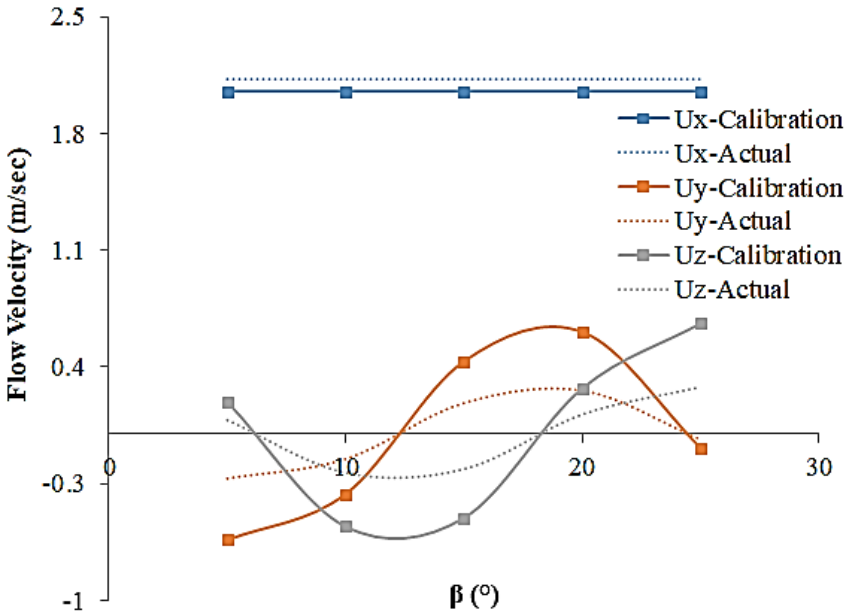

Figure 7.4. Validation of the experimental calibration dataset for a hemispherical five-hole pressure probe

Figure 7.4 shows the accuracy level of the experimental dataset and the calibration equation for the conical five-hole probe in the measurement of internal flow information. Flow information measured and calculated using the calibration data of the hemispherical probe is compared with known flow field. It can be seen that the axial velocity measured and calculated using probe has a variation of 0.1m/sec about the flow angles compared to the actual flow field information. Furthermore, it is also seen that the radial and azimuthal velocity changes are about ± 0.5m/sec and ± 0.3m/sec.

The validations of both probes have been carried out against a known flow field, i.e. U = 2.12m/sec and $\alpha = -25^{o}$, at various flow angles (yaw angle). Figures 7.3 and 7.4 depict the validation graph of the conventional calibration for the conical and hemispherical five-hole pressure probes

respectively. It can be seen in figure 7.3 that although the axial velocity component measured through the use of calibration equation is entirely accurate, however, there are significant differences between the actual and calibrated radial and azimuthal velocity respectively. In the case of the hemispherical probe in figure 7.4, there are noticeable differences in the axial velocity of the calibrated and actual flow field as well. Similarly, it is the same with the radial and azimuthal velocities respectively. Therefore, this shows that the conventional method of calibrating five-hole probes in measuring pipeline flow properties is not very accurate, as it ought to be.

7.2.1 Experimental Measurements Error Analysis

This section briefly discusses the error analysis for the conical and hemispherical five-hoe pressure probe measurements. Throughout this section, the notation σ is used to represent uncertainty and S_E is used to describe standard errors in measurement of the arbitrary flows. In each experiment, the probe is used to measure total and static pressures and velocity. The uncertainty in the measurements of a variable depends on the uncertainty in the measurements of the five individual pressures $\overline{P_{1-5}}$. The uncertainty in an arbitrary measured variable is expressed as shown in equation (7.1).

$$\delta_\theta = \sqrt{\frac{1}{n}\sum_{i=1}^{5}(\theta_{i,calculated} - \theta_{actual})^2} \qquad (7.1)$$

The uncertainty in the conical and hemispherical probe's measurements are calculated using the equation stated above. The absolute dimensional and non-dimensional uncertainties errors in the pitch and yaw angles, total and static pressures and velocities, and are summarised in table 7.3 and 7.4 respectively.

Table 7.3. Uncertainties and standard errors in measurement for a conical five-hole pressure probe

Statistical parameters	Pitch angle (°)	Yaw angle (°)	Total pressure (Pa)	Static pressure (Pa)	U (m/sec)	U_x (m/sec)	U_y (m/sec)	U_z (m/sec)
Standard error	0.0607	0.2266	0.1106	0.1150	0.1800	0.0131	0.1365	0.0045

Table 7. 3 shows the uncertainty errors of the conical probe in hydraulic pipeline measurements. Table 7.3 shows an average error of about ±0.1436° for flow angles; similarly, the average error of total and static pressure is about 0.0042Pa. Furthermore, the average three-dimensional velocity

error is approximately 0.0689m/sec. Table 7.4 summarises uncertainty error analysis of the hemispherical five-hole pressure probe.

Table 7.4. Uncertainty errors in the measurement for a hemispherical five-hole pressure probe

Statistical parameters	Pitch angle (°)	Yaw angle (°)	Total pressure (Pa)	Static pressure (Pa)	U (m/sec)	U_x (m/sec)	U_y (m/sec)	U_z (m/sec)
Standard error	0.1863	0.0011	0.0054	0.0031	0.2510	0.0934	0.0120	0.1014

Table 7.4 shows the uncertainty errors of the hemispherical five-hole pressure probe in hydraulic pipeline measurements. It can be seen that there is an average uncertainty error of about ±0.0937° for flow angles; similarly, the average error of total and static pressure is about 0.0043Pa. Also, the average three-dimensional velocity uncertainty error is approximately 0.0698m/sec.

By comparing table 7.3 to 7.4, it can be seen that both probes perform reasonably the same in measuring flow pressure. For the measurement of flow angles, the hemispherical probe performs slightly better. It is the same for the three-dimensional velocity of flow. Conclusively. It can be said that both probes perform very well in measuring hydraulic pipeline flow parameters. However, using CFD, these errors can still be improved.

The next section explains the novel method of using CFD numerical method to simulate conical and hemispherical probes in hydraulic pipeline flow domain to create a new set of CFD based numerical datasets to create new calibration equations aimed at improving the experimental calibration coefficients shown in sector 2 of table 7.1 and table 7.2. Furthermore, the CFD numerical datasets also aimed at improving the flow measurements results shown in figure 7.3 and 7.4 respectively. The next section describes in details of the method and procedures in both qualitative and quantitative terms.

7.3 Numerical Simulation of the Five-hole Pressure Probe Heads

The flow field analysis approximately the conical and hemispherical five-hole pressure probes have been carried out first. The flow field analysis is shown in figures 7.5 and 7.6, for the conical and hemispherical probes respectively. For valid comparison purposes, the range (i.e. maximum and minimum values) of these variations has been kept the same. The flow parameters' variations shown in these figures correspond to the maximum expected average flow velocity of 2.12m/sec in

the pipeline flow, and at $\alpha = \beta = 0^0$. It can be seen that the presence of a conical head five-hole pressure probe disturbs the uniformity of the flow within the hydraulic pipeline.

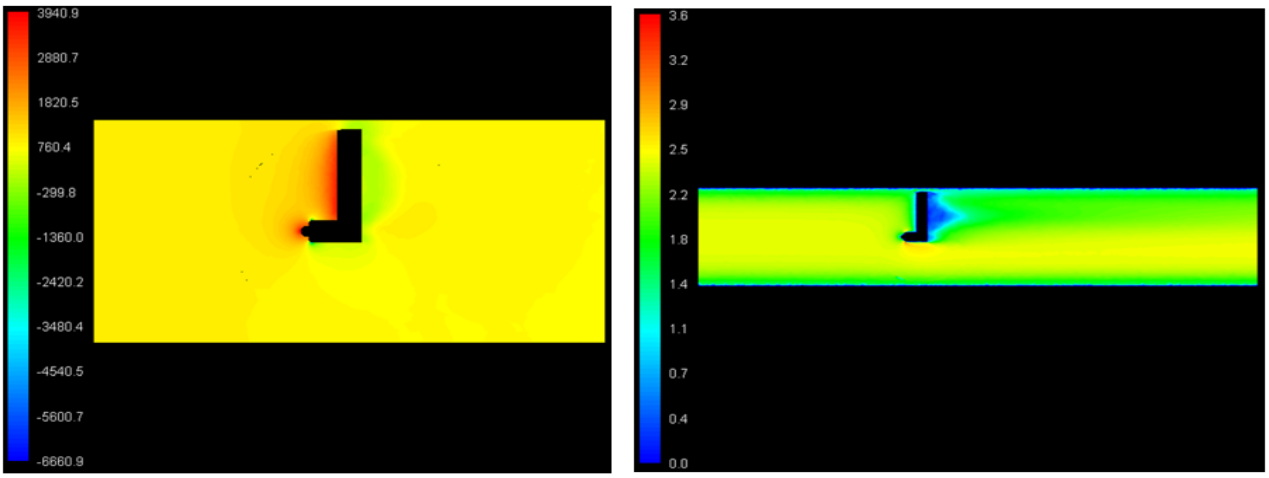

Figure 7.5. Variations in (a) flow field static gauge pressure and (b) flow field velocity magnitude in the vicinity of conical five-hole pressure probe at $\alpha=\beta=0^o$

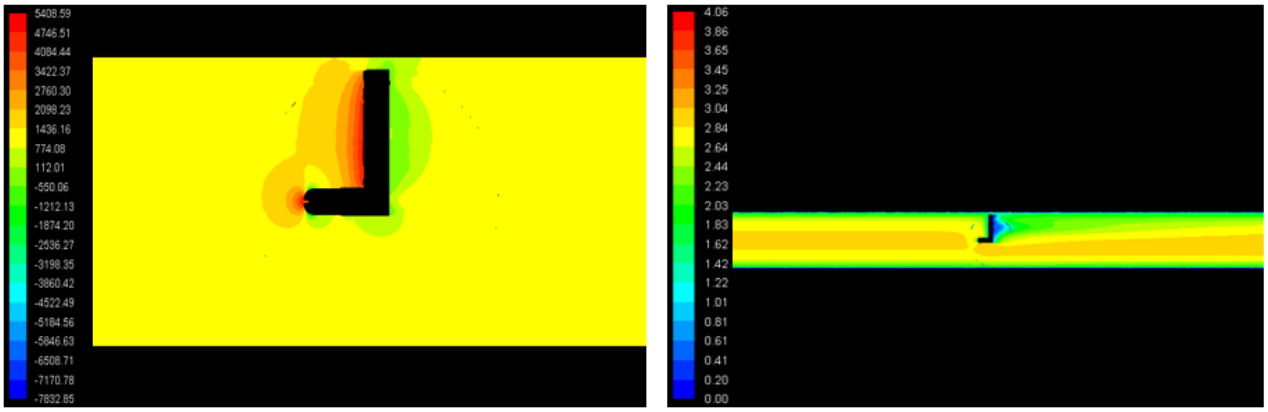

(a) Static gauge pressure (b) Flow velocity magnitude

Figure 7.6. Variations in (a) flow field static gauge pressure and (b) flow field velocity magnitude in the region of hemispherical five-hole pressure probe at $\alpha=\beta=0^o$

As the probe offers resistance to the flow, the static gauge pressure is higher on the front section of the probe, while it is low downstream. Comparing 7.5(a) to figure 5.5(a), the flow static gauge pressure variations in hydraulic pipeline flows are significantly higher for the conical five-hole probe. Furthermore, the situation is the same for the flow velocity magnitude variations depicted in figure 7.5(b). Similarly, in case of hemispherical head five-hole pressure probe described in figure 7.6 (a), it can be seen that the effect of the probe is felt to a much smaller distance downstream the hydraulic pipeline flows compare to figure 6.4(a) and (b). The reason for this behaviour is the higher density and dynamic viscosity of water. Malviya, V., Mishra, R., & Palmer, E., (2015). The

flow variation analysis has established that the numerically obtained pressure dataset can be used for calibration and be integrated with the experimental dataset to obtain strong calibration coefficients and calibration constants that can be used to measure complex three-dimensional flow information with accuracy beyond 95%.

7.3.1 Calibration of the Conical and Hemispherical Probes CFD Numerical Datasets

The coefficient of determination for the yaw angle in sector 2 in table 7.1 and the pitch and yaw angles in table 7.2, need to have a value of more than 0.9 (i.e. 90%) as discussed in the previous section that. For this purpose, CFD based numerical simulations have been carried out to improve the accuracy of the conventional calibration method (experimental) for both the probes. The CFD based numerical simulations have been carried out to develop conventional numerical calibrations for both probes. The pressure dataset on the five holes of the probes has been recorded respectively for processing.

The pressure dataset measured by the conical and hemispherical five-hole pressure probes has been recorded and stored in a safe file respectively. It has then been used to form the sector maps of the probes, depicted in figure 7.7 and figure 7.8 respectively. The CFD based numerically obtained calibration sector maps in the hydraulic pipeline flows cover a wider range of angles for the conical probe especially on the yaw angle plane as compared to the hemispherical probe. The calibration coefficients for sector 1 and sector 5 of the conical and hemispherical five-hole pressure probes have been summarised in appendix 7.2a to 7.2d. Comparison of these appendixes indicates that the calibration coefficients of both the probes in pipeline flows are slightly different in the percentage of 0.01%.

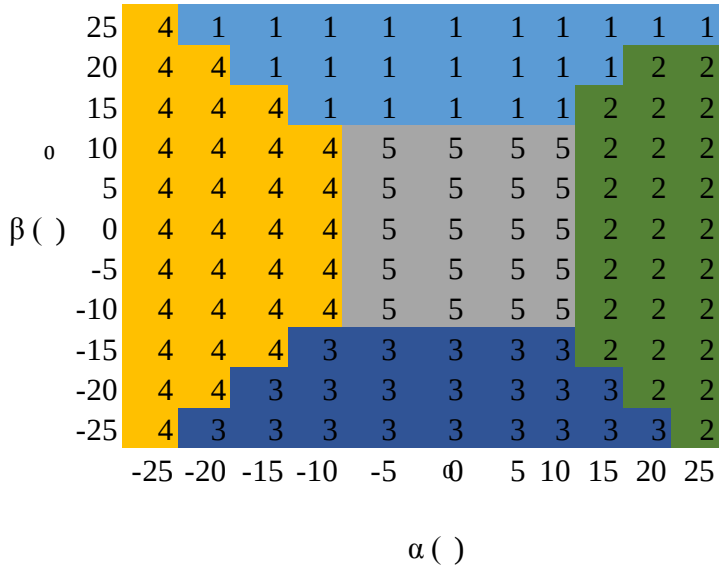

Figure 7.7. CFD based numerical sector map for a conical five-hole pressure probe for hydraulic pipeline calibration

Just like figure 7.1 and figure 7.2, figure 7.7 depicts the calibration map generated numerically by the data measured by the conical five-hole pressure probe in a hydraulic pipeline flow. The y-axis of the calibration sector map represents the yaw, while the x-axis represents the pitch. The areas marked by the number one (sector 1) are the grids covered by the top hole of the pressure probe and the area marked by the number 3 (sector 3) are the grids covered by the bottom hole. Also, the fields marked by number four (sector 4) are the grids covered by the left hole and the fields marked by the number two (sector 2) are the grids covered by the right hole of the probe. Furthermore, the area of the calibration map marked by number 5 the grid covered by the centre hole (sector 5) of the probe.

It can be seen that the top hole (sector 1) registers the highest pressure from $\alpha = -20^{o}$ to 25^{o} and $\beta = 15^{o}$ to 25^{o}, however, at higher pitch angles (beyond $\pm 15^{o}$), the yaw angle range becomes narrower. Similarly, the bottom hole (sector 3) registers the highest pressure from $\alpha = -25^{o}$ to 20^{o} and $\beta = -15^{o}$ to -25^{o} but at higher pitch angles (beyond $\pm 15^{o}$, the yaw angle range becomes narrower. Furthermore, the right holes (sectors 2) register maximum pressure from $\alpha = 15^{o}$ to 25^{o} and $\alpha = -10^{o}$ to -25^{o} for the left hole (sector 4) respectively, where the yaw angle ranges from $\beta = -25^{o}$ to 20^{o} for the right hole (sector 2) and $\beta = -25^{o}$ to 25^{o} for the left hole (sector 4). Also, it can be seen that the centre hole (sector 5) registers maximum pressure from pitch angle $\alpha = -10^{o}$ to 10^{o} and at yaw angles, it registers the highest pressure from $\beta = -10^{o}$ to 10^{o}. Although the calibration sector map generated by the datasets measured in the hydraulic pipeline flow using the

conical probe shows that the holes are evenly distributed, it can still be noticed that the calibration sector map is not perfectly symmetrical.

The same procedure as above was repeated for the hemispherical five-hole probe in a hydraulic pipeline using CFD numerical method to generate pressure datasets. Computational fluid dynamics based numerical setup was the same as the experimental setup, and under the same flow conditions using the same flow domain. The CFD based calibration sector map generated by the datasets measured in the hydraulic pipeline flow domain is depicted in figure 7.8.

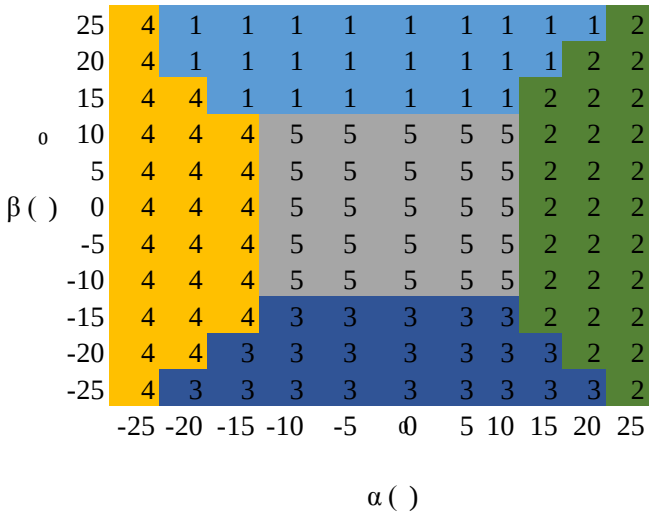

Figure 7.8. CFD based numerical sector map for a hemispherical five-hole pressure probe for hydraulic pipeline calibration

Figure 7.8 describes the calibration sector map generated numerically by the data measured by the hemispherical five-hole pressure probe in a hydraulic pipeline flow. The y-axis of the map represents the yaw, while the x-axis represents the pitch. The areas covered by the number one (sector 1) are the grids covered by the top hole during pressure measurements and the area represented by the number 3 (sector 3) are the grids covered by the bottom hole. Furthermore, the fields marked by number 4 (sector 4) are the grids covered by the left hole, and the same is true for regions characterised by number two (sector 2). Also, the centre area of the calibration map covered by the number 5 is the grid covered by the centre hole (sector 5) of the probe during calibration.

The calibration map demonstrates that the top hole of the probe registers the highest pressure from α = -20° to 20° and β = 15° to 25° , however, at higher pitch angles (beyond ±15°), the yaw angle range becomes narrower. Similarly, the bottom hole (sector 3) registers the highest pressure from α = -25° to 20° and β = -15° to -25° but at higher pitch angles (beyond ±15°), the yaw

angle range becomes narrower. Similarly, the right holes (sectors 2) register maximum pressure from $\alpha = 15^{o}$ to 25^{o} and $\alpha = -15^{o}$ to -25^{o} for the left hole (sector 4), while the yaw angle ranges from $\beta = -25^{o}$ to 20^{o} for the right hole (sector 2) and $\beta = -25^{o}$ to 25^{o} for the left hole (sector 4). Furthermore, the centre hole, also known as sector 5, registers maximum pressure from pitch angle $\alpha = -10^{o}$ to 10^{o} and at yaw angles, it records the highest pressure from $\beta = -10^{o}$ to 10^{o} within the calibration grid. Although the map shows that datasets are evenly distributed, the calibration map is not perfectly symmetrical in shape; this is due to inherent imperfections during setup. In this study, these inborn errors are negligible.

Based on the calibration coefficients for conical and hemispherical head five-hole pressure probes, the coefficients of determination have been computed for all the sectors of the probes, and for all the different calibration coefficients considered in the present study. It can be seen that all the coefficients of determination are => 90% in both table 7.5 for conical five-hole pressure probe and 7.6 for the hemispherical five-hole probe (see section 3.9). Hence, the coefficients related to the pitch angle, in the case of a conical head five-hole pressure probe, in sector 2, will be replaced by the coefficients obtained numerically. Similarly, the coefficients related to the pitch and yaw angles, in case of hemispherical head five-hole pressure probe, in sector 2, will be replaced by the coefficients obtained through the process of CFD based numerical calibration. It is expected that this will enhance the accuracy of measurements from both of these probes.

Table 7.5. CFD based numerical coefficients of determination for a conical head five-hole pressure probe

Calibration parameters	Sector 1 (r^2)	Sector 2 (r^2)	Sector 3 (r^2)	Sector 4 (r^2)	Sector 5 (r^2)
Pitch angle (^{o})	0.9999	0.9999	1.0000	1.0000	1.0000
Yaw angle (^{o})	1.0000	0.9999	1.0000	1.0000	1.0000
Total pressure (Pa)	0.9999	0.9999	1.0000	1.0000	0.9999
Static pressure (Pa)	0.9999	0.9999	1.0000	1.0000	0.9999

Table 7.6. CFD based numerical coefficients of determination for a hemispherical head five-hole pressure probe

Calibration parameters	Sector 1 (r^2)	Sector 2 (r^2)	Sector 3 (r^2)	Sector 4 (r^2)	Sector 5 (r^2)
Pitch angle (^{o})	1.0000	0.9999	1.0000	1.0000	1.0000
Yaw angle (^{o})	1.0000	0.9999	1.0000	1.0000	1.0000
Total pressure (Pa)	1.0000	0.9999	1.0000	1.0000	0.9911
Static pressure (Pa)	1.0000	0.9999	1.0000	1.0000	0.9911

Table 7.5 and 7.6 for both conical and hemispherical probes have proved to give accurate results regarding returning the calibration coefficients of determinations for the pitch and yaw angles, true local static and a total pressure of the hydraulic pipeline flow. The results shown in these tables have demonstrated that the calibration method developed in this section is unaffected by velocity variations and pipe vibrations or wall proximity effect. Therefore, CFD data can satisfactorily be integrated with experimental data to develop a strong integration and extension calibration methods that can further increase measurements accuracies that can be used for optimum operations.

Before establishing the CFD based integration calibration method, the CFD calibration dataset and equations generated in the calibration method have been used to measure flow information to validate the calibration equations against the actual comparison. The results are depicted in figure 7.9 and 9.10 for both the conical probe and a hemispherical probe. The validations have been carried out against known flow fields.

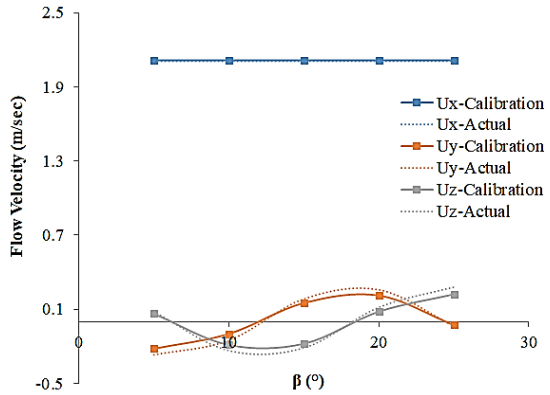

Figure 7.9. Validation of the CFD based numerical calibration dataset for conical five-hole pressure probe

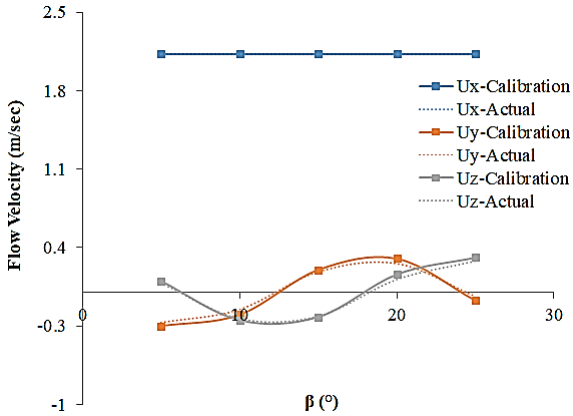

Figure 7.10. Validation of the CFD based numerical calibration dataset for hemispherical five-hole pressure probe

The validation of the CFD based numerical calibration equations obtained here for both the probes needs to be carried out. The validations have been carried out against a known flow field, i.e. U = 2.12m/sec and $\alpha = -25^{o}$, at various yaw angles. Figures 7.9 and 6.10 depict the validation of the conventional calibration for the conical head and hemispherical head five-hole pressure probes respectively. In comparisons, it can be seen that using the CFD based numerical calibration dataset to compute the flow information, the velocity components in x, y, and y directions, using the conical five-hole pressure probes, are 100%, accurate for the case of x component velocity. However, y and z components velocities are 1.5% and 1.7% lower on average. Similarly, using the hemispherical probe, it is about 100% accurate for x velocity components. However, y and z velocity components, it records approximately 1.4% and 1.2% compared to actual flow measurements. Furthermore, it can be seen in both figures that all the components of the pipeline flow velocity are matching accurately with the actual velocity components. Therefore, the reason for the differences, have now decreased significantly, resulting in much more accurate measurements.

7.3.2 Numerical Measurements Error Analysis

Applying the same formula described in section 7.2.1 for the CFD based numerical measurements, the uncertainty error analysis has been performed, and the results are summarised in table 7.7 and 7.8 for both conical and hemispherical five-hole probe. Table 7.7 and 7.8 validate figure 7.9 and 7.10 and further establish and confirm the accuracy of the measurements.

Table 7.7. Uncertainty errors in the measurements for a conical five–hole pressure probe

Statistical parameters	Pitch angle (^{o})	Yaw angle (^{o})	Total pressure (Pa)	Static pressure (Pa)	U (m/sec)	U_x (m/sec)	U_y (m/sec)	U_z (m/sec)
Standard error	0.0045	0.0531	0.0202	0.0194	0.0051	0.0068	0.0032	0.0033

Figure 7.7 shows the uncertainty error analysis for the conical five-hole pressure probe. It can be seen here that the average error in flow angle has been reduced to $\pm 0.0288^{o}$. The average flow total and static pressure are now approximately 0.0198Pa. Also, the uncertainty error in the three-dimensional velocity is about 0.1133m/sec. In comparing table 7.7 to 7.3, it can be seen that the accuracy of the conical probe has greatly improved for all measured flow parameters. The same analysis is carried for the hemispherical probe, and the results are summarised in table 7.8.

Table 7.8. Uncertainty errors in the measurements for a hemispherical five-hole pressure probe

Statistical parameters	Pitch angle (°)	Yaw angle (°)	Total pressure (Pa)	Static pressure (Pa)	U (m/sec)	U_x (m/sec)	U_y (m/sec)	U_z (m/sec)
Standard error	0.0028	0.1307	0.0028	0.0027	0.0010	0.0536	0.0643	0.0360

Figure 7.8 shows the uncertainty error analysis performed for the hemispherical five-hole pressure probe. It can be seen that the uncertainty error for flow angles has dropped to about ±0.0667°. It can be seen that the error has further decreased to approximately 0.0027Pa looking at the flow total and static pressure. Also, the accuracy of the three-dimensional flow velocity has greatly increased as the CFD based calibration has decreased the error to approximately 0.0513m/sec. In comparing table 7.8 to 7.4, it can be seen that the introduction of the CFD based calibration actively improves the accuracy of the hemispherical five-hole pressure probe. Overall, it can be seen that both probe five-hole pressure probes have performed well in predicting flow parameters of hydraulic pipeline flow. The effect of and influence of CFD based calibrations have once again been observed in these tables. The next section in this chapter discusses the results obtained from the CFD based integration calibration.

7.4 An Integrated Calibration Method for Five-hole Pressure Probes

The experimental calibration of the conical and hemispherical head five-hole pressure probe in pipeline flow resulted in a coefficient of determination of 77% for yaw angle in sector 2, and 12% and 29% pitch and yaw angles in sector 2 for the hemispherical head pressure probe, which is below the threshold of accuracy set in the present study. The numerical coefficient of determination for the same is however perfect (i.e. 100%) for both the probes. It means that the yaw angle measurements using the numerical calibration method are far more accurate than the experimental calibration measurements of the same conical head pressure probe. Similarly, the numerical coefficients of determination are far more accurate than the pitch and yaw angles measurements for the hemispherical head pressure probe. Hence, the numerical calibration method has been integrated with the experimental calibration to develop a novel, more accurate calibration method for both conical and hemispherical head five-hole pressure probes (see section 3.9). The processes of an integration calibration method for the hydraulic pipeline calibration is summarised in figure 7.11.

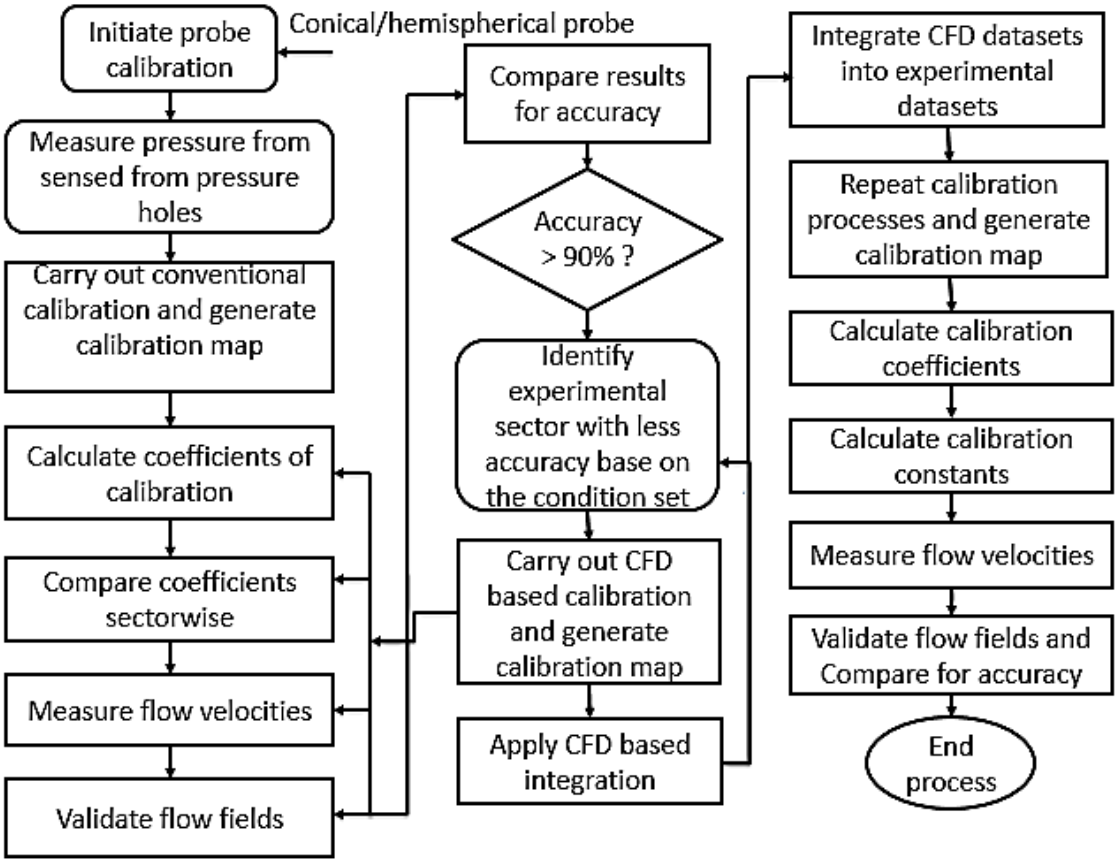

Figure 7.11. A flowchart summarising the novel CFD based integration calibration method in hydraulic pipeline flow

After the replacement of the less accurate experimental calibration coefficients for yaw angle with the more accurate numerical coefficients for the conical head pressure probe, the sector map of the integrated calibration method has been developed, as shown in figure 7.12. Similarly, using the same method, the sector map integrated calibration for the hemispherical head pressure probe has been developed as shown in figure 7.13. Based on the calibration sector maps generated for both the probes, the hemispherical five-hole probe shows a more symmetrical calibration sector map and covers a broader range of angle in sector four compared to the integrated calibration sector map of the conical five-hole pressure probe.

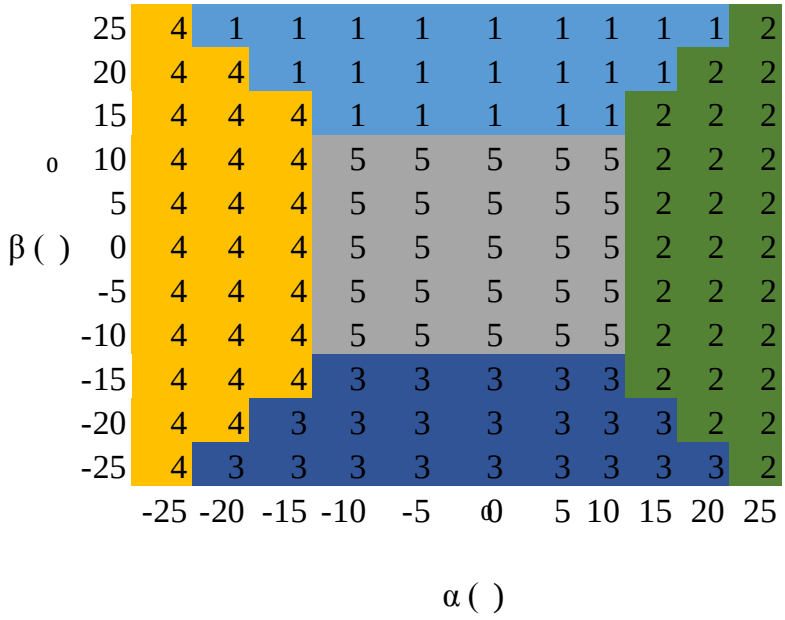

Figure 7.12. CFD based integrated sector map of a conical five-hole pressure probe for hydraulic pipeline calibration

Figure 7.12 depicts the calibration map generated using CFD based integrated datasets generated through the process of integrating CFD numerically simulated dataset into an experimental dataset of the conical five-hole pressure probe in a hydraulic pipeline flow. Just as the ones described above, the y-axis of the map represents the yaw plane, while the x-axis represents the pitch plane. The grid marked by the number 1 (sector 1) are the grids covered by the top hole of the probe during calibration. Similarly, the area marked by the number 3 (sector 3) represent the grids covered by the bottom hole. Furthermore, the fields marked by number 4 (sector 4) are the grids covered by the left hole, and the same is true for areas marked hole number two (sector 2). Also, the centre area of the calibration map marked by the number hole (sector 5) is the grid covered by the probe during pressure acquisitions.

The calibration sector map demonstrates that the top hole (hole 1) of the probe, also known as sector 1 in the calibration setup registers the highest pressure from $\alpha = -20^{o}$ to 20^{o} and $\beta = 15^{o}$ to 25^{o}, however, at higher pitch angles (beyond $\pm 15^{o}$), the yaw angle range become smaller. Similarly, the bottom hole (sector 3) registers the highest pressure from $\alpha = -20^{o}$ to 20^{o} and $\beta = -15^{o}$ to -25^{o} but at higher pitch angles beyond $\pm 15^{o}$, the yaw angle range becomes narrower. Furthermore, the right holes (sectors 2) of the probe register maximum pressure from $\alpha = 15^{o}$ to 25^{o} and $\alpha = -10^{o}$ to -25^{o} for the left hole (sector 4), and the yaw angle registers pressure on the yaw play from $\beta = -25^{o}$ to 25^{o} for the right hole (sector 2) and $\beta = -25^{o}$ to 25^{o} for the left hole

(sector 4). Similarly, the centre hole, also known as sector 5, registers maximum pressure from pitch angle $\alpha = -10^{o}$ to 10^{o} and at yaw angles, it records the highest pressure from $\beta = -10^{o}$ to 10^{o} within the calibration sector map. Although the calibration sector map shows that pressure datasets are distributed within the grid point evenly, it is not accurately symmetrically distributed due to inherent human errors which can be considered minor in this study.

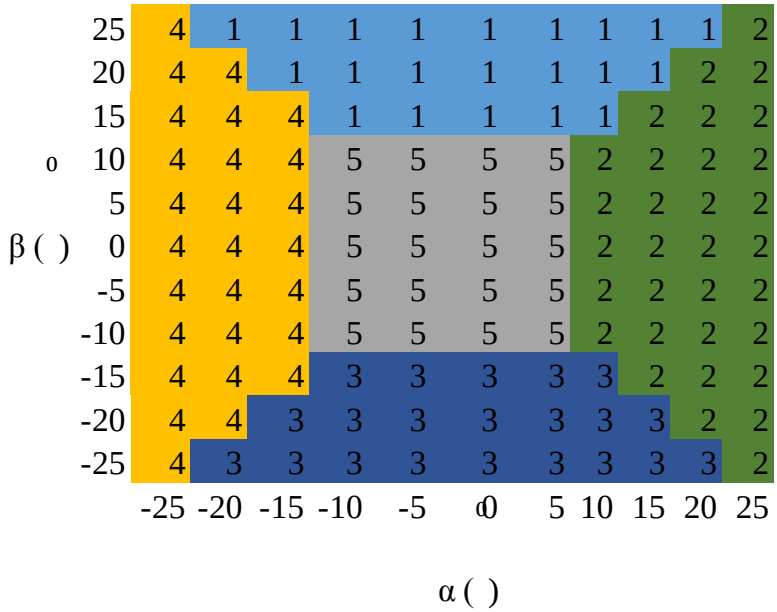

Figure 7.13. CFD based integrated sector map of a hemispherical five-hole pressure probe for hydraulic pipeline calibration

Figure 7.13 depicts the calibration map generated using CFD based integrated data generated through the process of integrating CFD numerically dataset into an experimental dataset of the hemispherical five-hole pressure probe measured in a hydraulic pipeline flow. As described above, the y-axis represents the yaw angle plane, while the x-axis represents the pitch angle plane. The number ones are the grids covered by the top hole (sector 1) of the probe, while the area with number 3 is the grids covered by the bottom hole (sector 3). Furthermore, number 4 is the areas covered by the left hole (sector 4). Similarly, the fields are represented by the number 2 is the grid covered by the right hole (sector 2) of the probe. Also, the field in the calibration map marked by the number 5 is the grid covered by the centre hole (sector 5) of the probe.

The calibration sector map demonstrates that the top hole (hole 1) of the probe, also known as sector 1 in the calibration setup registers the highest pressure from $\alpha = -20^{o}$ to 20^{o} and $\beta = 15^{o}$ to 25^{o}, however, at higher pitch angles (beyond $\pm 15^{o}$), the yaw angle range narrows. Similarly, the

bottom hole (sector 3) registers maximum pressure values from $\alpha = -20^{o}$ to 20^{o} and $\beta = -15^{o}$ to -25^{o}, however, at higher pitch angles beyond $\pm 15^{o}$, the yaw angle range narrows. Similarly, the right hole (sectors 2) of the probe registers maximum pressure on the pitch plane from $\alpha = 10^{o}$ to 25^{o} and $\alpha = -10^{o}$ to -25^{o} for the left hole (sector 4) while on the yaw plane it registers maximum pressure from $\beta = -25^{o}$ to 25^{o} and $\beta = -25^{o}$ to 25^{o} respectively. It can further be seen that the centre hole (sector 5) registers maximum pressure values from pitch angle $\alpha = -10^{o}$ to 10^{o} and at yaw angles plane, it registers the highest pressure from $\beta = -10^{o}$ to 10^{o}. Even though the calibration map appears to be symmetrical, which also demonstrate the accuracy of the integrated datasets it is not perfectly distributed because of inherent manual errors which can be negligible.

The calibration coefficients corresponding to sectors 1 and 5 of the conical five-hole pressure probe are summarised in appendixes 7.3a and 7.3b. The calibration coefficients corresponding to sector 1 and 5 of the hemispherical five-hole pressure probe have been summarised in 7.3c and 7.3d. Again, in comparison with the conical five-hole pressure probe in the same pipeline flow, the calibration coefficients of the hemispherical five-hole pressure probe, for the corresponding sector/s, are significantly different.

The coefficients of determination of the CFD based integrated calibration method for the conical and hemispherical pressure probes have been presented in table 7.9 and 7.10 respectively. It can be seen that the yaw angle coefficient of calibration, in sector 2, is now 0.9999 as highlighted, hence, improving the accuracy of measurements using a conical head five-hole pressure probe. Similarly, it can be seen that the coefficients of determination for pitch and yaw angle in sector 2 for table 7.10 are now 0.9999 each highlighted, thereby improving the accuracy of calibration and measurements using a hemispherical five-hole pressure probe (see explanation in section 3.9 and figure 7.11).

Table 7.9. CFD based integrated coefficients of determination for a conical five-hole pressure probe

Calibration parameters	Sector 1 (r^2)	Sector 2 (r^2)	Sector 3 (r^2)	Sector 4 (r^2)	Sector 5 (r^2)
Pitch angle (^{o})	0.9999	0.9987	1.0000	1.0000	1.0000
Yaw angle (^{o})	0.9999	0.9999	1.0000	1.0000	1.0000
Total pressure (Pa)	0.9999	0.9999	1.0000	1.0000	0.9999
Static pressure (Pa)	0.9999	0.9999	1.0000	1.0000	0.9999

Table 7.10. CFD based integrated coefficients of determination for hemispherical five-hole pressure probe

Calibration parameters	Sector 1 (r^2)	Sector 2 (r^2)	Sector 3 (r^2)	Sector 4 (r^2)	Sector 5 (r^2)
Pitch angle (°)	0.9999	0.9999	1.0000	1.0000	1.0000
Yaw angle (°)	0.9999	0.9999	1.0000	1.0000	1.0000
Total pressure (Pa)	1.0000	0.9999	1.0000	1.0000	0.9911
Static pressure (Pa)	1.0000	0.9999	1.0000	1.0000	0.9911

The validity of the integrated calibration of a conical and hemispherical five-hole pressure probe is presented in figure 7.14 and 7.15. It can be seen that the flow velocity components measured in the pipeline using the integrated calibration equations, for both five-hole pressure probes, are matching perfectly with the actual velocity components measured for a known flow field. Hence, the integrated calibration method of a five-hole pressure probe has proven to be more accurate than the conventional calibration method for predicting pipeline flow properties.

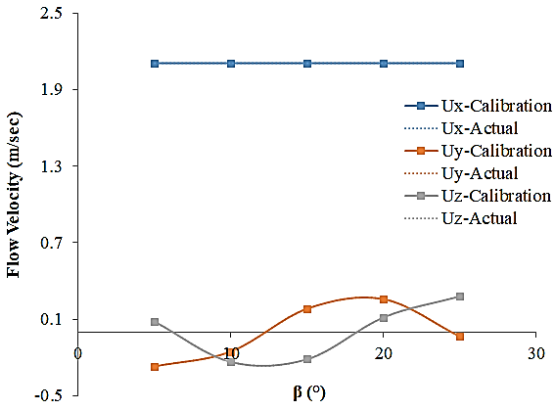

Figure 7.14. Validation of the CFD based integrated calibration dataset for conical five-hole pressure probe

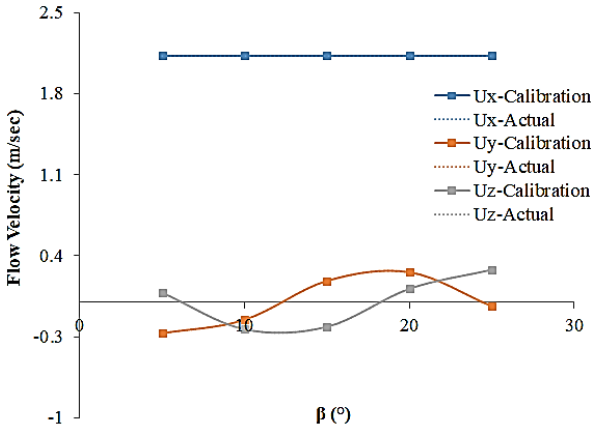

Figure 7.15. Validation of the CFD based integrated calibration dataset for hemispherical five-hole pressure probe

The validations for figure 7.14 and 7.15 have been carried out for the CFD based integrated calibration method against a known flow field, i.e. U = 2.12m/sec and $\alpha = -25^{o}$, at various yaw angles. It can be that although the axial velocity of the flow measured through the use of integrated calibration equation for both probes is perfect. Similarly, the radial velocity measured the use of integrated calibration equation for both probes is very accurate; the same is the case for the azimuthal velocity. Hence, this shows that the CFD based integrated method of calibrating five-hole pressure probes in measuring pipeline flow properties is very accurate and can produce 100% measurement accuracy.

7.4.1 Integrated Measurements Error Analysis

To further validate the results shown in figure 7.14 and 7.15, a comprehensive error analysis has been performed using the principle and equation described in section 7.2.1. This analysis ascertains the authenticity of the conical and hemispherical five-hole pressure probes. The results of this analysis are summaries in table 7.11 and 7.12 respectively.

Table 7.11. Uncertainties and standard errors in measurement for a conical five-hole pressure probe

Statistical parameters	Pitch angle (^{o})	Yaw angle (^{o})	Total pressure (Pa)	Static pressure (Pa)	U (m/sec)	U_x (m/sec)	U_y (m/sec)	U_z (m/sec)
Standard error	0.0045	0.0331	0.0202	0.0194	0.0051	0.0068	0.0032	0.0033

Table 7.12 Uncertainties and standard errors in measurement for a hemispherical five-hole pressure probe

Statistical parameters	Pitch angle (^{o})	Yaw angle (^{o})	Total pressure (Pa)	Static pressure (Pa)	U (m/sec)	U_x (m/sec)	U_y (m/sec)	U_z (m/sec)
Standard error	0.0028	0.1307	0.0028	0.0027	0.0010	0.0.0536	0.0643	0.360

As demonstrated in table 7.11 and 7.12, it can be seen that having integrated the CFD calibration data into experiment data, maximum measurement accuracy can be achieved. This table has shown the level accuracy that a CFD based calibration can have on the calibration of five-hole pressure probes. With these level of accuracy, efficient design and optimum operation of pipeline fluid systems are possible. These and many more knowledge gaps are what this study intends to bridge.

The next section discusses the extension of an angle range of conical and hemispherical five-hole calibration the results.

7.5 Extended Calibration Method for Five-hole Pressure Probes

As discussed earlier, the range of the CFD based integrated calibration methods developed here have limitations that restrict the applicability of the five-hole pressure probes to only ±25° in both pitch and yaw planes. Hence, CFD based numerical simulation datasets have been generated for α = -30° to -45° and from 30° to 45° , and β = -30° to -45° and from 30° to 45° . The calibration data for α = ±25° and β = ±25° is considered the same as in the CFD bases integrated calibration method (see section 3.9). Figure 7.16 shows a representation of interactions of a five-hole pressure and hydraulic pipeline flow fields at high flow angle.

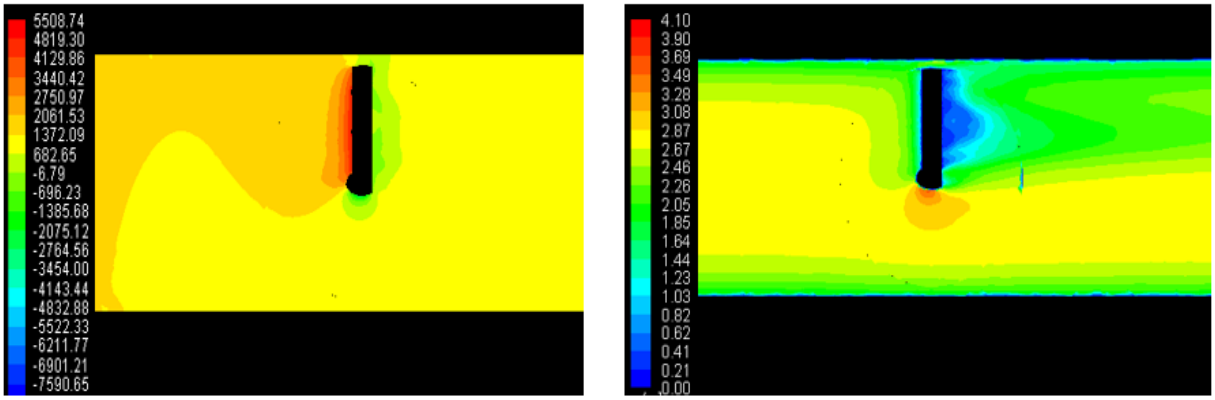

(a) Flow static gauge pressure (a) Flow velocity magnitude

Figure 7.16. Variation in (a) flow field static gauge pressure and (b) flow field velocity magnitude of five-hole pressure probe at high angle α=β=45°

The analysis carried out is to ascertain the interference caused by the probe at high flow angle. It is done by comparing the distribution of flow static gauge pressure upstream and downstream of the probe for probe placed at $\alpha=\beta=45^0$. As can be seen from figure 7.16, the static gauge pressure begins to rise early upstream. The static pressure in the flow field around the probe is a direct indication of how the probe influences the flow field. The transverse components of velocity in the x and y directions give reasonable evidence of the disruption of the flow field caused by the probe. It clearly shows that the longitudinal x-component dominate the influence of the probe decreases as these components fall to near zero values and the magnitude of velocity Malviya, V., Mishra, R., &

Palmer, E., (2007). Figure 7.17 is a summary of the activities of the CFD based extension of calibration range processes.

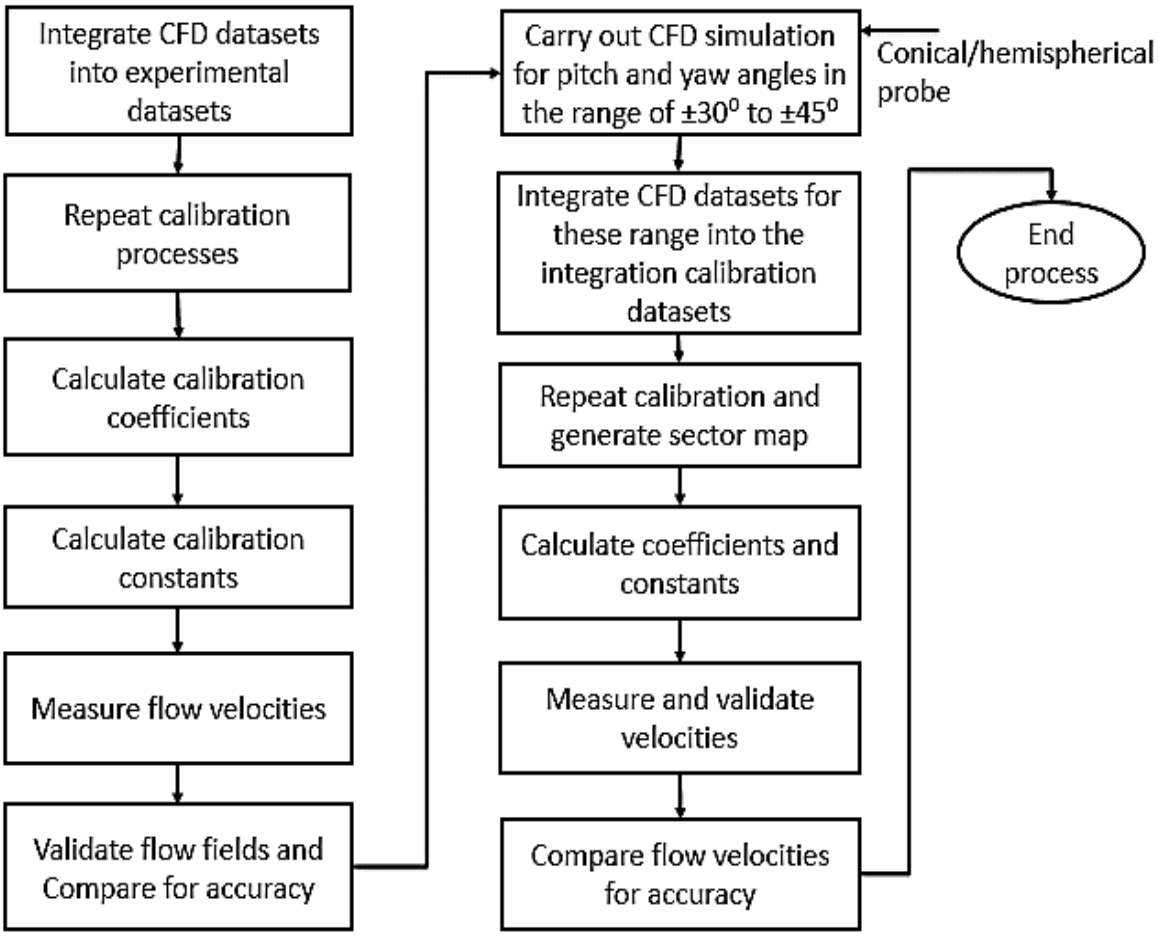

Figure 7.17. A flowchart summarising the novel CFD based extension of calibration angle range method in hydraulic pipeline flow

The extended calibration sector maps for the conical and hemispherical five-hole pressure probes are depicted in figure 7.18 and 7.19. The calibration sector dataset within the box in each figure of the extended calibration sector map is the same as in the CFD based integrated calibration methods for the two probes. In comparison, the conical head five-hole pressure probe's extended calibration sector map in figure 7.18 and the hemispherical head five-hole pressure probe's extended calibration sector map shown in figure 7.19, it can be seen that both these calibration sector maps are identical, confirming the qualitative similarities between the two probes. This further indicates that any qualitative analysis carried out, without the quantitative analysis, of the five-hole pressure probes is

not enough to analyse the calibration processes in detail Parameswanran, V., Jategaonkar, R., & Press, M. (2002) and Akshoy, R. P., Ravi, R. U., & Anu, J. (2011).

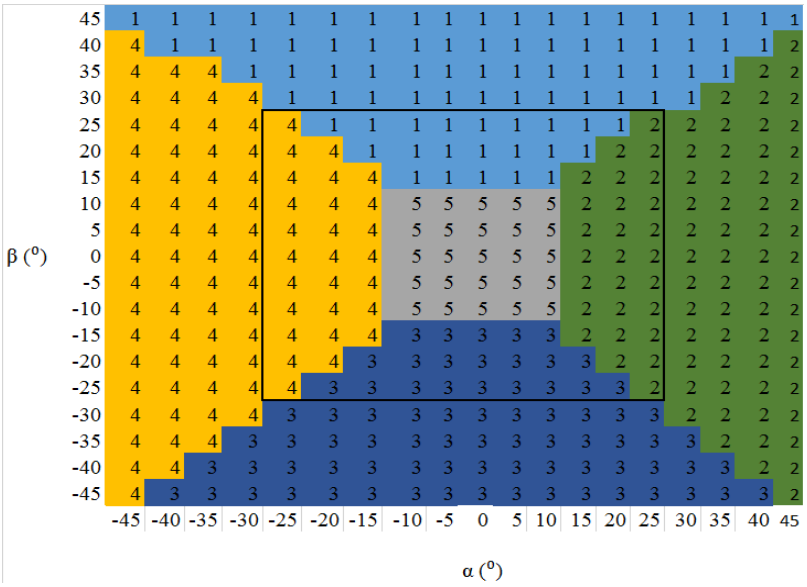

Figure 7.18. CFD based extended sector map of a conical head five-hole pressure probe generated for hydraulic pipeline calibration

Figure 7.18 depicts the calibration map generated using CFD numerically extended dataset of the calibration map shown in figure 7.12. The y-axis of the calibration map represents the yaw plane, while the x-axis represents the pitch plane. The calibration map is generated according to the pressure each hole sense in a particular pitch and yaw plane. The areas in the calibration sector map covered by the number 1 are the grids covered by the top hole (sector 1) as the probe face an oncoming flow in the hydraulic pipeline, while the areas represented by 3 are the grids covered by the bottom hole (sector 3). Furthermore, the areas covered by the number 4 are the area of the grid covered by the left hole (sector 4), and the areas are represented by the number 2 is the grid covered the right hole (sector 2) of the probe. Additionally, the centre area of the calibration map covered by the number 5 is the grid covered by the centre hole (sector 5) of the probe.

As depicted in figure 7.18, the top hole (sector 1) of the conical probe registers the highest pressure from $\alpha = -45^{o}$ to 45^{o} on the pitch plane and $\beta = 15^{o}$ to 45^{o} on the yaw plane, however, at higher pitch angles (beyond $\pm 15^{o}$, the yaw angle range becomes narrower. Similarly, the bottom hole (sector 3) of the maximum probe pressure from $\alpha = -40^{o}$ to 40^{o} on the pitch plane and $\beta = -15^{o}$ to -45^{o} on the yaw plane, however, at higher pitch angles (beyond $\pm 15^{o}$ the yaw angle range begins to narrow down). Furthermore, the right holes (sectors 2) of the probe register maximum pressure

from α = 15° to 45° on the pitch plane and β = -45° to 40° on the yaw plane, while the left hole (sector 4) of the probe registers maximum pressure from α = -15° to -45° on the pitch plane and β = -45° to 40° on the yaw plane. Lastly, the centre hole (sector 5) of the probe registers maximum pressure from α = -10° to 10° on the pitch plane and β of -10° to 10° on the yaw plane. A closer look at figure 7.18 shows that the accuracy of the CFD integrated datasets and the CFD numerically extension of the integrated datasets is visible on the symmetrical nature of the calibration sector map. The extended calibration map for the hemispherical probe has been generated as shown in figure 7.19 using the same procedure and principles.

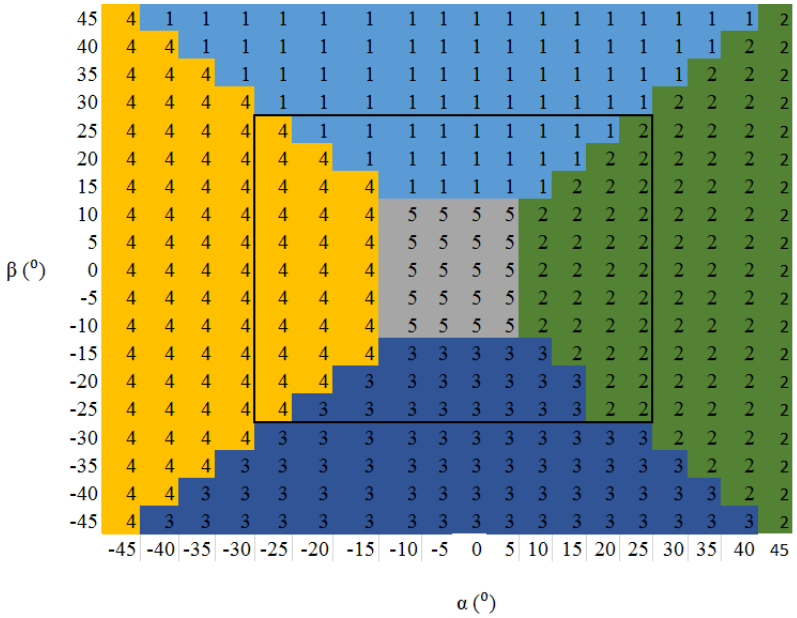

Figure 7.19. CFD based extended calibration sector map of a hemispherical five-hole pressure probe generated for hydraulic pipeline calibration

Figure 7.19 depicts the calibration sector map generated using CFD numerically extended data of the calibration map in figure 7.13. The y-axis of the calibration sector map represents the yaw plane, while the x-axis represents the pitch plane. One (1) in the calibration sector map represent the grids covered by the top hole (sector 1), while 3 represent the grids covered by the bottom hole (sector 3).

Furthermore, the areas 4 in the map resent the grids covered by the left hole (sector 4), and 2 represent the grids covered by the right hole (sector 2) of the probe. Furthermore, the centre area of the calibration map covered with the number 5 is the area covered by the centre hole (sector 5) of the probe during calibration Kim, S. H., & Kang, Y. J. (2009).

The top hole (sector 1) of the conical probe registers the highest pressure from $\alpha = -40^{o}$ to 40^{o} on the pitch plane and $\beta = 15^{o}$ to 45^{o} on the yaw plane, however, at higher pitch angles (beyond $\pm 15^{o}$, the yaw angle range becomes narrower. Similarly, the bottom hole (sector 3) of the maximum probe pressure from $\alpha = -40^{o}$ to 40^{o} on the pitch plane and $\beta = -15^{o}$ to -45^{o} on the yaw plane, however, at higher pitch angles (beyond $\pm 15^{o}$ the yaw angle range begins to narrow down). Furthermore, the right holes (sectors 2) of the probe register maximum pressure from $\alpha = 10^{o}$ to 45^{o} on the pitch plane and $\beta = -45^{o}$ to 45^{o} on the yaw plane, while the left hole (sector 4) of the probe registers maximum pressure from $\alpha = -15^{o}$ to -45^{o} on the pitch plane and $\beta = -45^{o}$ to 45^{o} on the yaw plane. Also, the centre hole (sector 5) of the probe registers maximum pressure from $\alpha = -10^{o}$ to 5^{o} on the pitch plane and β of -10^{o} to 15^{o} on the yaw plane. The accuracy of the CFD numerically extended calibration map is shown in the symmetrical nature of the calibration map and how evenly pressure measurements are distributed within the calibration grid.

Based on the sixth order polynomial curve fitting method, the calibration coefficients, corresponding to the different sectors of the conical and hemispherical five-hole pressure probe have been computed. The calibration coefficients for sectors one and five have been presented in appendix 7.4a and 7.4b. In comparison, with both tables for a conical five-hole pressure probe, it is clear that the calibration coefficients of the hemispherical five-hole pressure probe are significantly different in both these sectors, and for all the different calibration parameters considered in the present study.

Table 7.13 and 7.14 summarises the coefficients of determination for all the five sectors of the hemispherical five-hole pressure probe, for the extended range calibration dataset. It can be seen that the coefficients of determination for all the different parameters, and in all the five sectors, are => 90% (see explanation in section 3.9). Hence, the extension in the calibration range of the conical and hemispherical five-hole pressure probes have been reasonably accurate.

Table 7.13. CFD based Extension of range coefficients of determination for a conical five-hole pressure probe

Calibration parameters	Sector 1 (r^2)	Sector 2 (r^2)	Sector 3 (r^2)	Sector 4 (r^2)	Sector 5 (r^2)
Pitch angle (^{o})	0.9999	0.9999	1.0000	0.9999	1.0000
Yaw angle (^{o})	0.9999	0.9999	1.0000	0.9999	1.0000
Total pressure (Pa)	0.9999	0.9994	1.0000	0.9999	1.0000
Static pressure (Pa)	0.9999	0.9994	1.0000	0.9999	1.0000

Table 7.14. CFD based Extension of coefficients of determination for a hemispherical five-hole pressure probe

Calibration parameters	Sector 1 (r^2)	Sector 2 (r^2)	Sector 3 (r^2)	Sector 4 (r^2)	Sector 5 (r^2)
Pitch angle (°)	0.9556	1.0000	1.0000	0.9999	1.0000
Yaw angle (°)	0.9947	0.9999	1.0000	0.9999	1.0000
Total pressure (Pa)	1.0000	0.9999	1.0000	0.9999	1.0000
Static pressure (Pa)	1.0000	0.9999	1.0000	0.9999	1.0000

Figure 7.20 and 7.21 depicts the validity of the extended calibration data for the conical and hemispherical five-hole pressure probes against a known flow field, having an average flow velocity of 2.12m/sec and α = -45° . It can be seen that the extended calibration dataset is capable of predicting pipeline flow properties such as the three components of the flow velocity with reasonable accuracy using both probes. The extended calibration methods developed here are not just accurate but are also applicable to a broader range of measurements within internal flows, which is the highlight of these methods.

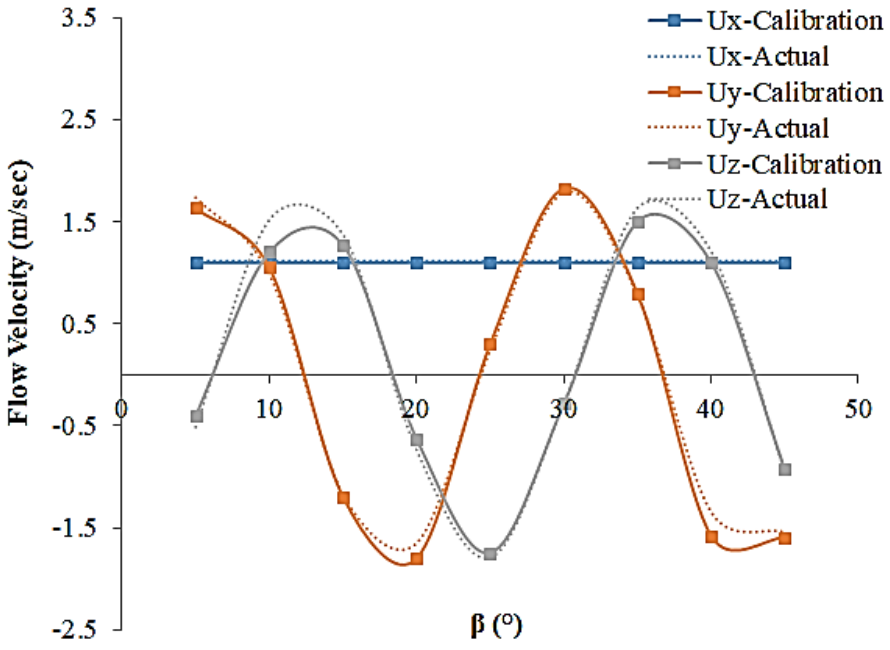

Figure 7.20. Validation of the CFD based extended calibration dataset for a conical five-hole pressure probe

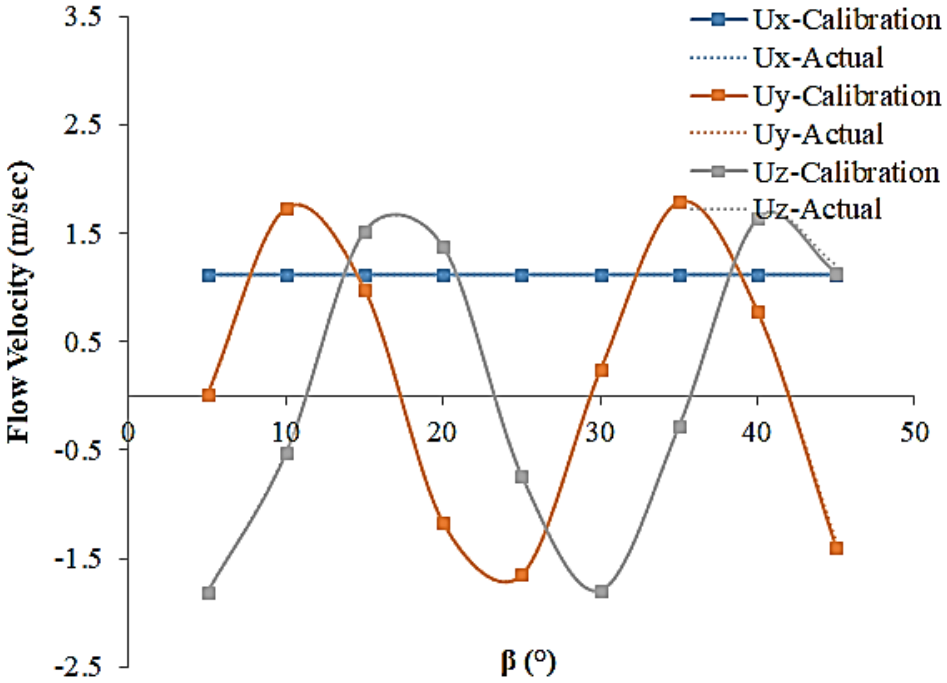

Figure 7.21. Validation of the CFD based extended calibration dataset for a hemispherical five-hole pressure probe

The validations for the CFD based extended calibration method have been carried out in a hydraulic pipeline flow against a known flow field, i.e. U = 2.12m/sec and α = -45° , at different yaw angles. Figures 7.20 and 7.21 depict the validation of CFD based extension calibration for the conical and hemispherical five-hole pressure probes respectively. It can be seen that in figure 7.20, although the axial velocity measured by using the calibration equation for a conical probe is entirely accurate with a variation of ± 0.2m/sec, however, there is a noticeable difference in the azimuthal speed between the actual and calibrated velocity in the flow angles of 15° and 36° respectively. Furthermore, in the case of the hemispherical probe shown in Figure 7.21, it can be seen very visibility that there is a perfect correlation in the axial speed of the calibrated and actual flow field.

Similarly, the same is the case with radial and azimuthal velocity respectively. Therefore, this analysis shows that the CFD-based extension method for calibrating five-hole probes in measuring pipeline flow properties is exact, with the hemispherical probe giving more accurate results than the conical five-hole probe.

7. 5.1 Extension Measurements Error Analysis

Using equation 7.1 and the principle of uncertainty error analysis described in section 7.2.1, qualitative error analysis of the conical and hemispherical five-hole pressure probe has been carried out for the extension of range calibration measurements. The investigation was carried out to flow angles, total and static pressures, and velocities. The research is carried out to further establish the authenticity of the probes as measurement instruments to validate figure 7.20 and 7.21. Table 7.15 and 7.16 shows the summary of the error analysis for each flow parameter measured by the conical and hemispherical five-hole pressure probe respectively.

Table 7.15. Uncertainties and standard errors in measurement for a conical five-hole pressure probe

Statistical parameters	Pitch angle (°)	Yaw angle (°)	Total pressure (Pa)	Static pressure (Pa)	U (m/sec)	U_x (m/sec)	U_y (m/sec)	U_z (m/sec)
Standard error	0.1043	0.0348	0.0691	0.0499	0.0001	0.1164	0.5865	0.5464

As shown in table 7.15, the probe has shown average flow angle error of ±0.0695°. It also records the average pressure error of about 0.0595Pa. Similarly, the three-dimensional velocity error is estimated to be approximately 0.4164m/sec. Table 7.15 have established the authenticity and accuracy of the CFD based probe angle range extension of calibration.

Table 7.16 Uncertainties and standard errors in measurement for a hemispherical five-hole pressure probe

Statistical parameters	Pitch angle (°)	Yaw angle (°)	Total pressure (Pa)	Static pressure (Pa)	U (m/sec)	U_x (m/sec)	U_y (m/sec)	U_z (m/sec)
Standard error	0.0003	0.0038	0.0001	0.0049	0.0007	0.0009	0.0065	0.0048

Table 7.16 shows the uncertainty error analysis of the hemispherical probe. It can be seen that the probe has an estimated angle error of approximately ±0.0021° . Similarly, the flow uncertainty error in the region of about 0.0025Pa and 0.0041m/sec for velocities. The accuracy reported in table 7.16 can be seen reflected in figure 7.21.

The validity of the conical and hemispherical five-hole probes has been demonstrated, and it can be concluded that even though both probes perform very well in the measurement of the hydraulic pipeline flow field, the hemispherical probe has better accuracy compared to the conical probe.

7.6 Summary

This work mainly deals with the fabrication and hence the novel calibration of a five-hole conical and hemispherical five-hole pressure probe in the hydraulic pipelines. The novel calibration method of a five-hole probe introduced in this study, as explained in this chapter, is a CFD-based numerical calibration, CFD-based integration calibration method, and a CFD based extension method of the calibration method. These calibrations are carried out in an internal flow in a hydraulic pipeline test sections within the University of Huddersfield fluid laboratory. This study analysed the pressure data sensed by the probe numerically through the use of computational fluid dynamics and experimentally. Furthermore, it analyses the probes coefficients of calibration, coefficients of determination and flow measurements analyses. From this analysis, the following comprehensive summary of the contents, general discussions and the results presented in this chapter is as follows:

1. The results resented in this chapter are derived from the methodology and experimental setup previously discussed in chapter 3 and 4.
2. The results presented in this chapter are in correlation to their relevance to the overall aims and objectives of this study.
3. The qualitative comparison of the conventional calibration process between hemispherical and conical five-hole pressure probes has indicated that both these probes perform similarly in pipeline flow.
4. However, significant differences in the quantitative analyses have been noticed, which suggests that the conventional calibration of conical and hemispherical five-hole pressure probes predict pipeline flow information accurately.
5. The flow associated with the hemispherical five-hole pressure probe has minimal differences in comparison with the flow field of the conical five-hole pressure probes.
6. An integrated calibration method for conical and hemispherical five-hole pressure probes has been developed, based on the calibration dataset from well-validated numerical simulations, at a range of operational parameters in the pipeline flow has been carried out.
7. The extended calibration method for conical and the hemispherical five-hole pressure probes greatly enhances the usefulness and applicability of such probes for accurate flow velocity immurements in pipeline flows.

8. The extended calibration methods for conical and hemispherical pressure probes have been tested in internal and external flows to carry out flow measurements, and this, have shown measurable accuracies.
9. Detailed comparisons of the use of the extended calibration equations developed for conical and hemispherical heads pressure probes in internal and external flows have proven not just to be perfect but accurately predicts flow properties.
10. The calibration data and equations developed for conical and hemispherical pressure probes in the hydraulic pipeline flows are capable of measuring flow information for average free stream velocities of 1m/sec, 1.5m/sec, 2m/sec, and 2.12m/sec.

Detailed investigations on the effect of the flow regime and fluid properties on the calibration of a conical and hemispherical five-hole pressure probe have been carried out. The performance of the probes in hydraulic pipeline flow properties prediction have been established for the different calibration methods developed in this study and have proven to maintain accuracy in air and water flows both in wind tunnel and hydraulic pipelines. For calibrations and measurements of this type to be meaningful, the calibration data must be repeatable and independent of the measured quantities. Each probe was calibrated four times to demonstrate the repeatability of the dataset and to permit the averaging of the data to reduce the minimal scatter further.

The probes have been used to investigate the three-dimensional flow fields in the hydraulic pipeline. These results agreed well with the actual flow fields. For all measurements, only the experimental measurements using experimental calibration data and equations have shown little variations in the calculated velocity magnitude and vector. All CFD based calibrations show strong correlations with actual flows filed. The performance of the novel CFD based calibrations methods in predicting flow information has substantiated the authenticity of this study. The CFD based integration calibration methods have also enabled understanding of the link between five-hole conical and hemispherical probe heads effect on flow regime and fluid flow properties on the calibration process.

A considerable advantage of the five-hole pressure-based probes is that they are robust and the only periodic calibration required is a static calibration of the pressure transducers. Although the results presented in this chapter is very accurate with a large angle of acceptance, care must be taken when choosing a suitable flow, flow rate (average free stream velocity) and type probe (shape) to be used.

Chapter 8 Comparisons of Calibration Sector Maps and Fluid properties for Wind Tunnel and Hydraulic Pipeline flows

The results of many datasets collected using conical and hemispherical five-hole pressure probes, at different calibration grid, and various flow velocities for air and water flows have been presented in this chapter. These datasets have been combined and parsed in several ways depending on the type of calibration and measurements investigation that has been carried, and results have been presented. Furthermore, comparisons of the performance analyses of the probes in generating calibration sector maps and predicting velocities in both air and water flows have been carried.

8.1 Introduction

The quantitative studies described in this chapter are structured in a way that each studied calibration method and measured information are analysed independently. The CFD novel calibration methods proposed in this study has been studied to analyse the performance of the probes in air and water flow respectively. A series of experiments have been undertaken to measure the local air and water flow velocities in the wind tunnel, and hydraulic pipeline flows using conical and hemispherical five-hole probes. Results have been presented and compared, which are extremely important for the overall benefit of this study as it demonstrates the overall performance accuracy of the calibration methods.

8.2. Performance of a Conical Five-hole pressure Probe in Wind tunnel and hydraulic Pipeline Flows

This section describes the performance comparisons of the calibration methods developed in this study for the conical five-hole pressure probe. It compares the calibration sector maps for each method in both air and water flows respectively. Furthermore, it compares the performance of the conical five-hole pressure probe in measuring air and water flow properties using each calibration method. Based on these analyses, conclusions have been drawn where necessary in order to establish where the probe performs better. In addition, for the sake of the comparison analyses, airflow represents wind tunnel flow and water flow represents hydraulic pipeline flow. These two terms are used interchangeably in this study, especially in this chapter.

8.2.1 Comparisons of Experimental Calibration Datasets

The conventional experimental calibration of the conical five-hole probe has been carried out in a wind tunnel (air) and hydraulic pipeline (water) flows. A performance comparison of the calibration sector maps generated by the conical five-hole pressure has been carried out. Figure 8.1 shows the comparison of the calibration sector map generated using experimental calibration datasets and figure 8.2 shows the comparison of flow information measured using experimental calibration coefficients calculated for each air and water flow respectively.

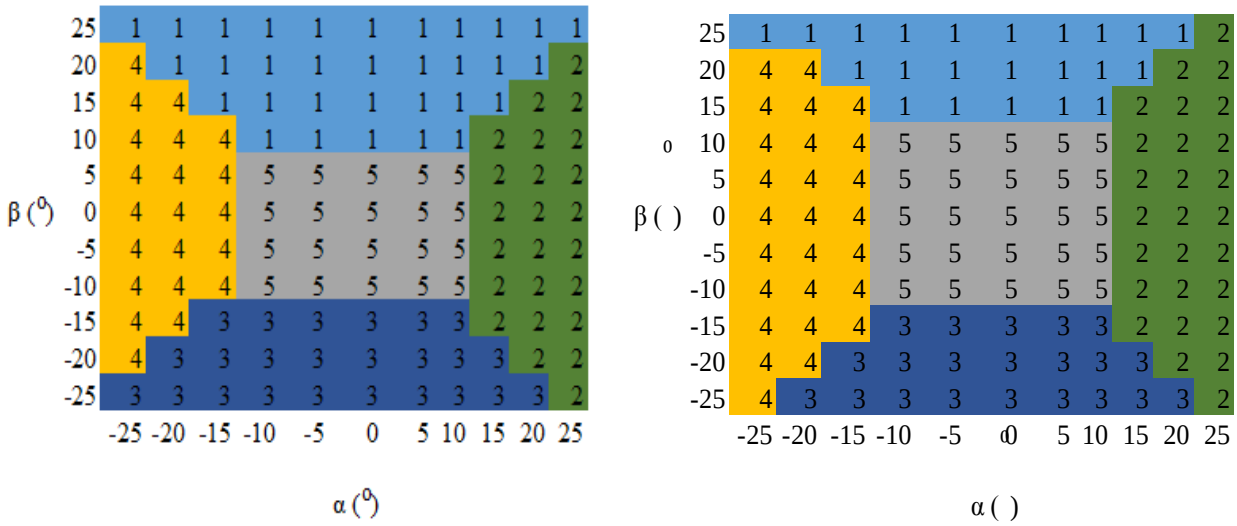

(a) Conical probe sector map for airflow (b) Conical probe sector map for water flow

Figure 8.1. Comparison of experimental calibration sector maps of conical five-hole pressure probe for air and water flow fields

In comparison, it can be seen that the calibration sector maps for airflow are slightly different from the calibration sector map of water flow. In the case of the airflow, the probe covers a wider range of pitch angle for sector 1 compared to water flow. On sector 3, the probe covers the same angle range for both the air and water flow. Similarly, for sector 2 and 4, the conical probe covers a wider range of pitch and yaw angles in water flow compared to airflow. To further, establish the performance of the conical probe in air and water flow, the datasets used to generate the calibration sector maps have been further analysed using curve-fit polynomial techniques to calculate the calibration coefficients, and the coefficients have used to compute flow information. Figure 8.2 shows the performance comparisons of air and water experimental datasets of the conical five-hole pressure probe.

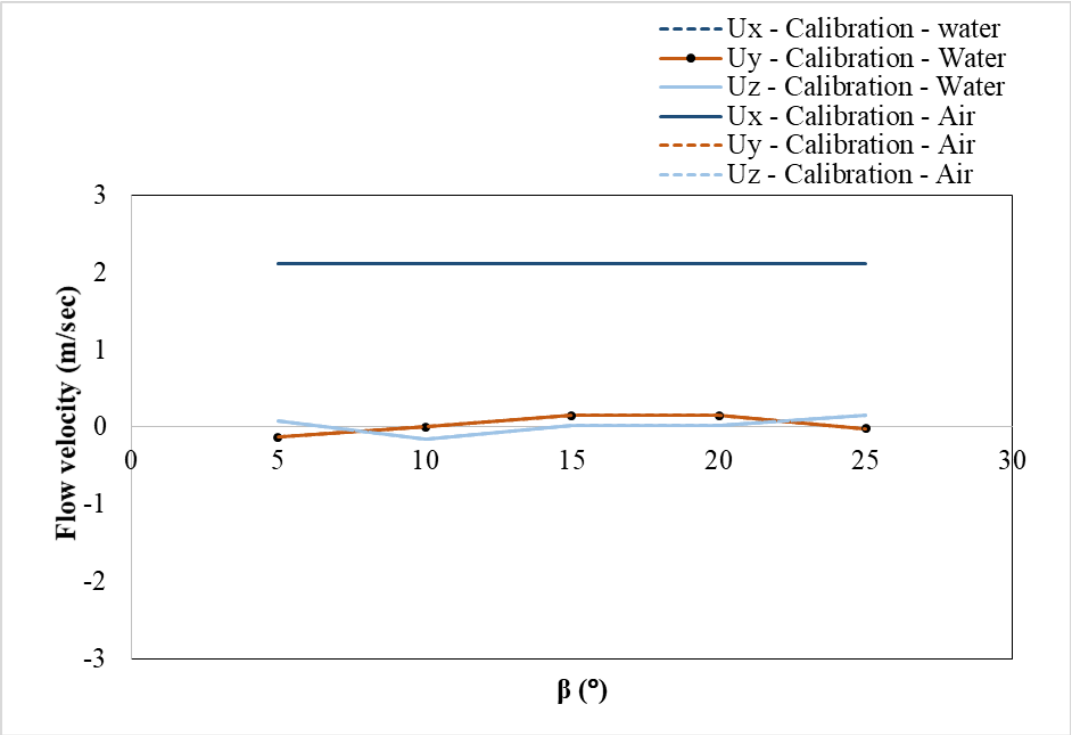

Figure 8.2. Comparisons of the experimental calibration dataset of the conical five-hole probe for air and water flow fields measurement

It can be seen that the x component of velocity, measured for the flow of water by the conical five-hole probe is perfectly correlating with almost 100% accuracy. Similarly, y and z components are of the airflow are also correlating perfectly with airflow y and z component velocities of the water flows. Therefore, figure 8.1 has demonstrated that the calibration dataset of the conical five-hole probe has predicted flow velocities with high accuracy in both air and water flows. Furthermore, it can be concluded that the conical five-hole pressure probe has a slight performance in airflow than in water flow.

8.2.2 Comparisons of CFD based numerical Calibration Datasets

A novel CFD based numerical calibration method has been developed in this study for air and flows. A performance comparison of the calibration method has been carried out in both flows. It involves a performance behaviour of the calibration sector maps generated by the conical five-hole pressure probe numerically. Furthermore, the performance of the probe in measuring air and water flow information has been carried out. Figure 8.3 compares the calibration sector maps for both flows, while figure 8.4 compares the flow information measured using CFD based numerical coefficients for air and water flow respectively.

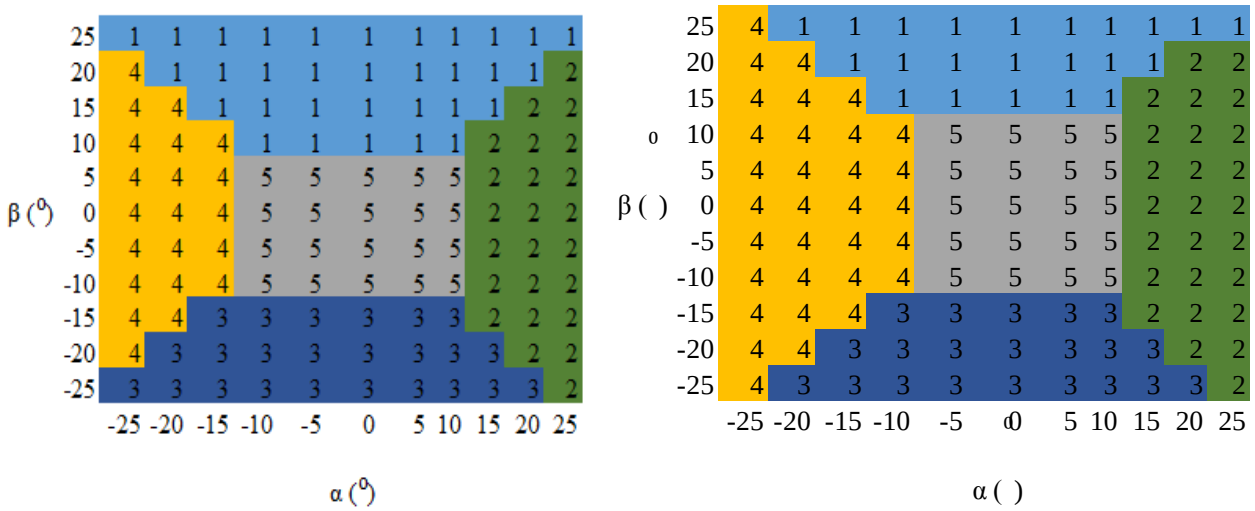

(a) Conical probe sector map for airflow (b) Conical probe sector map for water flow

Figure 8.3. Comparison of the CFD based numerical calibration sector maps of conical five-hole pressure probe for air and water flow fields

Figure 8.3 shows the comparison of the calibration sector of conical five-hole pressure probe for air and water flows. In comparison, it can be seen that the calibration sector for airflow cover a wider range of yaw angle for sector one compare to calibration sector map for water flow. Similarly, the calibration sector map for water flow covers a wider range of pitch angle compared to the calibration sector map of the airflow. Conclusively, it can be seen that the conical five-hole pressure probe produced a more symmetrical calibration map in airflow compared to water flow. The respective calibration coefficients corresponding to appendixes 5.2a and 7.2a have been used to compute the flow information for their corresponding flow as shown in figure 8.4 having produced a reasonably accurate calibration sector maps for both flow fields.

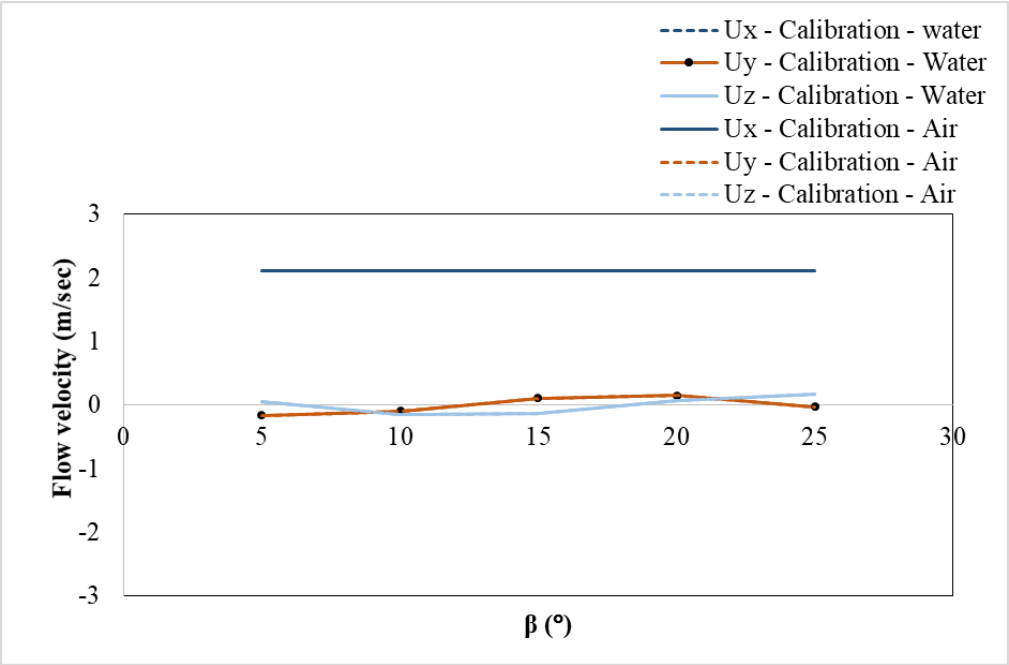

Figure 8.4. Comparisons of the CFD based numerical calibration dataset for a conical five-hole probe for air and water flow fields measurement

Figure 8.4 the performance analysis of the CFD based numerical calibration methods for a conical five-hole probe in both the air and water flows. It can be seen that the x component of velocity, measured for water flow by the conical five-hole probe, perfectly correlate the x component velocity of the airflow. Similarly, y and z components of the velocity for water flow are also perfectly correlating with the velocity of airflows. Therefore, Figure 8.4 shows that the CFD-based numerical calibration method of the conical five-hole probe have predicted the flow velocity with high accuracy for both air and water flow fields.

8.2.3 Comparisons of CFD based Integrated Calibration Datasets

For the methodological implementation of the CFD based novel integrated calibration method, refer to section 3.9. The novel method of CFD based integrated calibration is the same for air and water flow. The purpose of this section is to carry out a qualitative performance analysis of the conical five-hole pressure probe in air and water flow. The calibration sector maps produced by the conical five-hole pressure probe for air and water flows have been compared as shown in figure 8.5 to establish the analysis. Furthermore, the flow information measured by the same probe in both air and water flow has been compared as shown in figure 8.6.

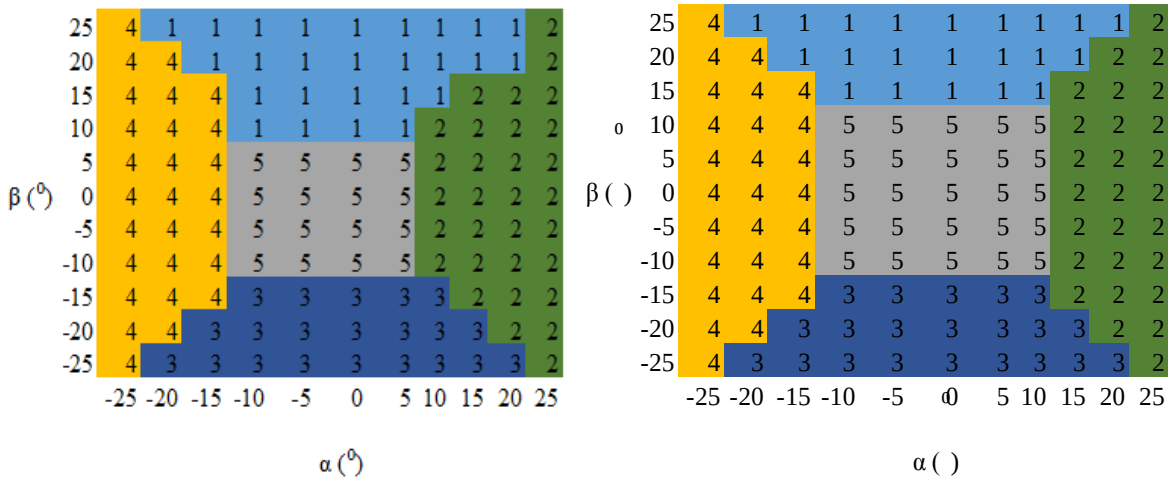

(a) Conical probe sector map for airflow (b) Conical probe sector map water flow

Figure 8.5. Comparison of the CFD based integrated calibration sector maps of conical five-hole pressure probe for air and water flow fields

Figure 8.4 shows the comparison of the novel CFD based integrated calibration sector maps of the conical five-hole pressure for air and water flows. In comparison, it can be seen that the novel integrated calibration sector map covers a wider range of pitch angle for sector 2 and 4 in both flows. Similarly, the probe covers a slight wider yaw angle range for sector 1 and 2 in airflow compared to water flow. Furthermore, it can be seen that the conical five-hole pressure probe produced a more perfectly symmetrical calibration sector map in water flow compared to the airflow for this calibration method. Conclusively, the CFD based novel integrated calibration method performs slightly better in water flow than in airflow regarding producing a calibration sector map. Calibration coefficients are corresponding to appendix 5.3a and 7.3a calculated using the respective datasets used in generating the calibration sector map shown above.

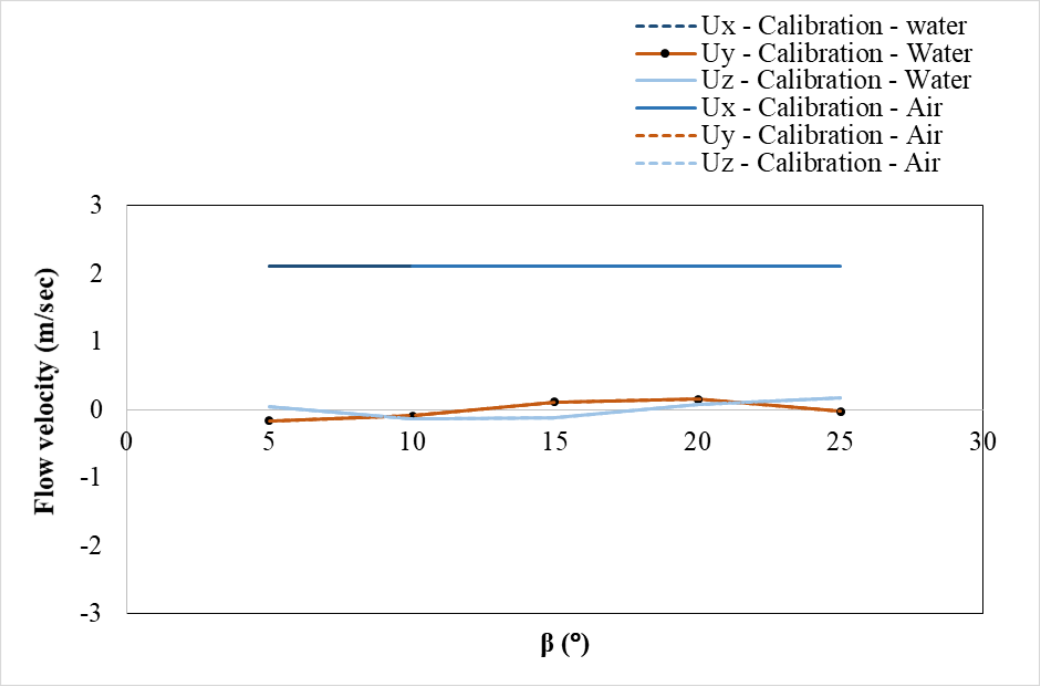

Figure 8.6. Comparison of CFD based integrated calibration dataset of the conical five-hole probe for air and water flow fields measurement

Figure 8.5 illustrates the validity of novel CFD-based integral calibration method for a conical five-hole probe in air and water flows measurements. It can be seen that the x component of the velocity, measured by the flow of water by the conical five-hole probe, perfectly matched the x component velocity of the airflow. Similarly, y and z components of the velocity for water flow are also perfectly correlating with the velocity of airflows. Therefore, Figure 8.5 has shown that CFD-based integration of the calibrated equations of a conical five-hole probe has predicted the flow velocity with high accuracy both air and water flow fields.

8.2.3 Comparisons of CFD based Extension of Range Calibration Datasets

For the methodological implementation and development of the novel CFD based extension of calibration range, refer to section 3.9. The calibration method and procedure is the same for both air and water flows. This analysis is carried out to establish the performance ability of the conical five-hole pressure probe in air and water flow respectively. For this purpose, a qualitative analysis of the calibration sector maps and velocities has been carried out for the conical five-hole pressure probe as shown in figure 8.7 and 8.8 respectively.

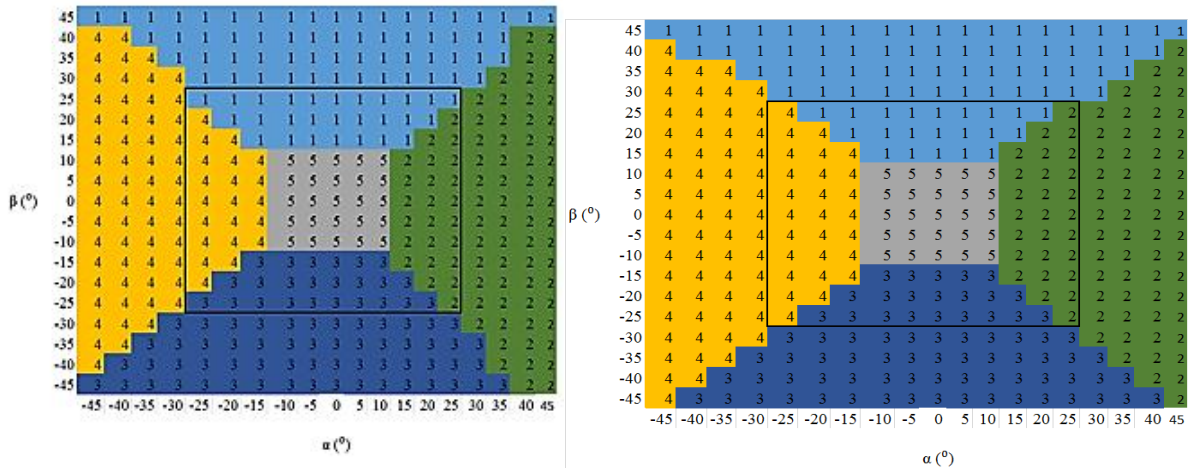

(a) Conical probe sector map for airflow (b) Conical probe sector map for water flow

Figure 8.7. Comparison of the CFD based extension of range calibration sector maps of the conical five-hole pressure probe for air and water flow fields

Figure 8.7 shows the comparison of the novel CFD based extension of range calibration sector map of the conical five-hole pressure probe for air and water flow respectively. It can be seen that the CFD based extension calibration sector map of the conical five-hole pressure probe is identical to both air and water flows, confirming the qualitative similarity of the probe. It can be seen that the pitch and yaw angle range are approximately equal in both flows. Again, looking at these calibration maps, it can be concluded that qualitative analysis is important to analyse the calibration processes of the CFD based extended calibration method. Based on the calibration maps generated for both flows, the calibration coefficients corresponding to appendix 5.4b and 7.4a have been calculated and used to compute their respective flow information as shown in figure 8.8.

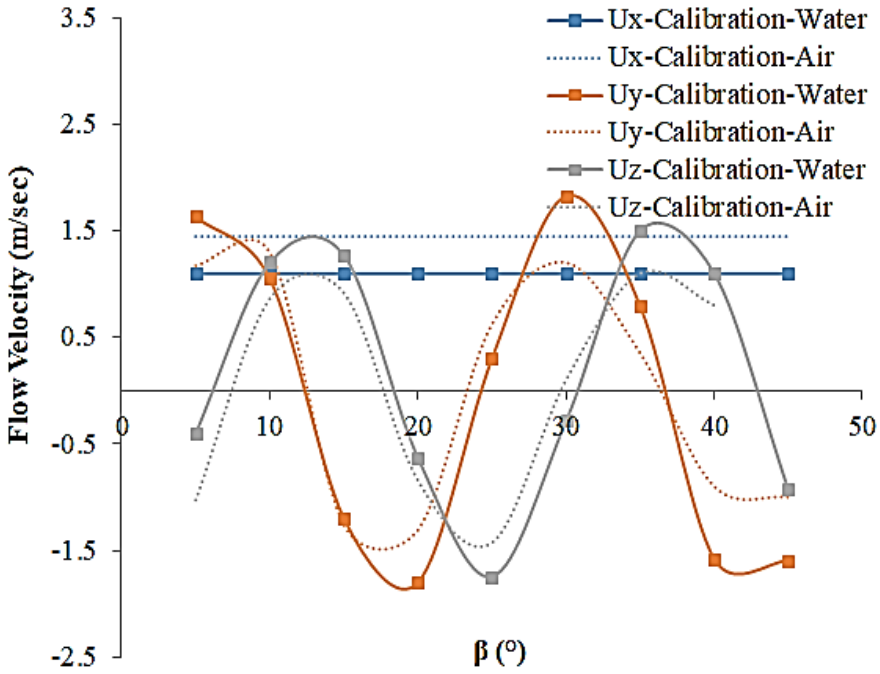

Figure 8.8. Comparison of the CFD based extension of range calibration dataset of the conical five-hole probe for air and water flow fields measurement

Figure 8.8 shows the performance comparison of the novel CFD based extension calibration of the conical five-hole pressure probe in air and water flow measurements. It can be seen that on average the x component of velocity, measured for water flow, is 11.5% higher than measured x component velocity for the airflow. Similarly, y and z components of the velocity of water flow are 65% and 70% lower than airflow. The performance of the conical probe in air and water flows have demonstrated that the novel CFD based extension method of calibration can significantly increase measurements accuracy of complex three-dimensional velocities as shown in figure 8.8.

8.3 Performance of a Hemispherical Five-hole Pressure Probe in Wind Tunnel and Hydraulic Pipeline Flows

This section describes the performance comparisons of the novel calibration methods developed for hemispherical five-hole pressure probe in both air and water flows. It compares the calibration sector maps and velocities. It also compares the results of both conical and hemispherical probe in both air and water flow fields.

8.3.1 Comparisons of Experimental Calibration Datasets

This procedure for the experimental calibration of the five-hole pressure probe in air and water flows is the same as section 8.2.1. See chapter 3, section 3.9 to see the procedure followed for the calibration method. A performance comparison of the hemispherical five-hole probe calibration sector maps in both air and water flows has been carried in this section as shown in figure 8.9. Using calibration datasets (coefficients) generated from the datasets that form the calibration sector maps, flow information has been computed using the hemispherical five-hole pressure probe for air and water flows as shown in figure 8.10.

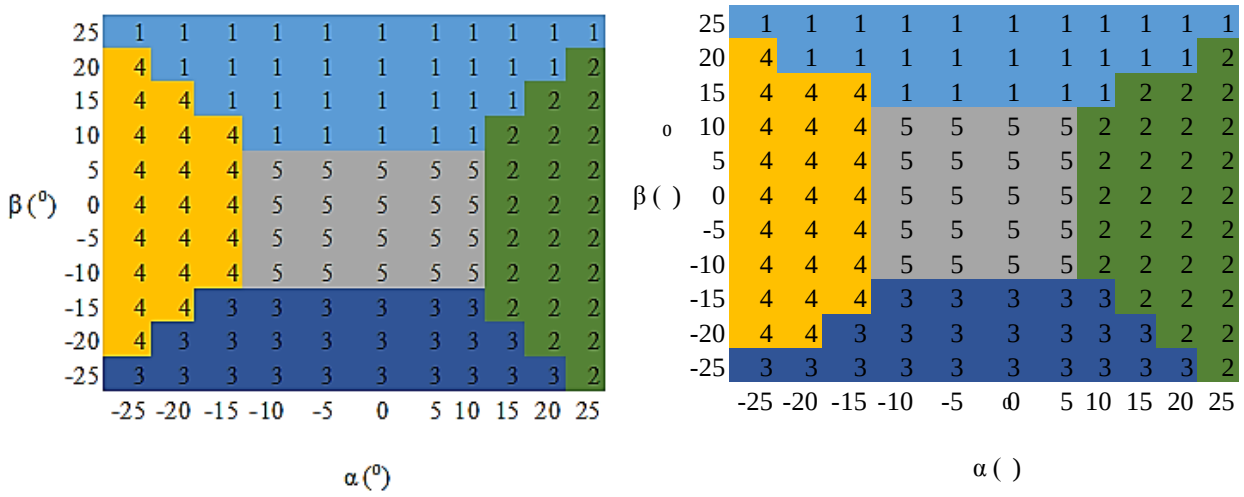

(a) Hemispherical probe sector map for airflow (b) Hemispherical probe sector map for water flow

Figure 8.9. Comparison of the experimental calibration sector maps of hemispherical five-hole pressure probe for air and water flow fields

Figure 8.9 shows the experimental calibration sector maps of the hemispherical five-hole pressure probe for air and water flows. In comparison, both sector maps, it can be seen that the probe covers a wider pitch angle range in airflow for sector 1 and the in water flow. Pitch-wise, the probe covers the same range for sector 2 and 4 in both flow fields. However, in water flow, the probe covers wider yaw angle range for sector two compared to airflow. Furthermore, regarding producing perfect symmetric maps, the probe performs fairly the same in both flows. In comparison to 8.1, it can be seen that the conical and hemispherical five-hole pressure probes perform fairly the same in producing calibration sector maps in both air and water flows. However, the only visible advantage for the hemispherical probe is that it covers a wider range of yaw angle for sector 2 in water flow compared to the conical probe. The calibration coefficients (a_0 to a_{27}) corresponding to appendixes 6.1a and 7.1c have been used to compute the respective flow information as shown in figure 8.10.

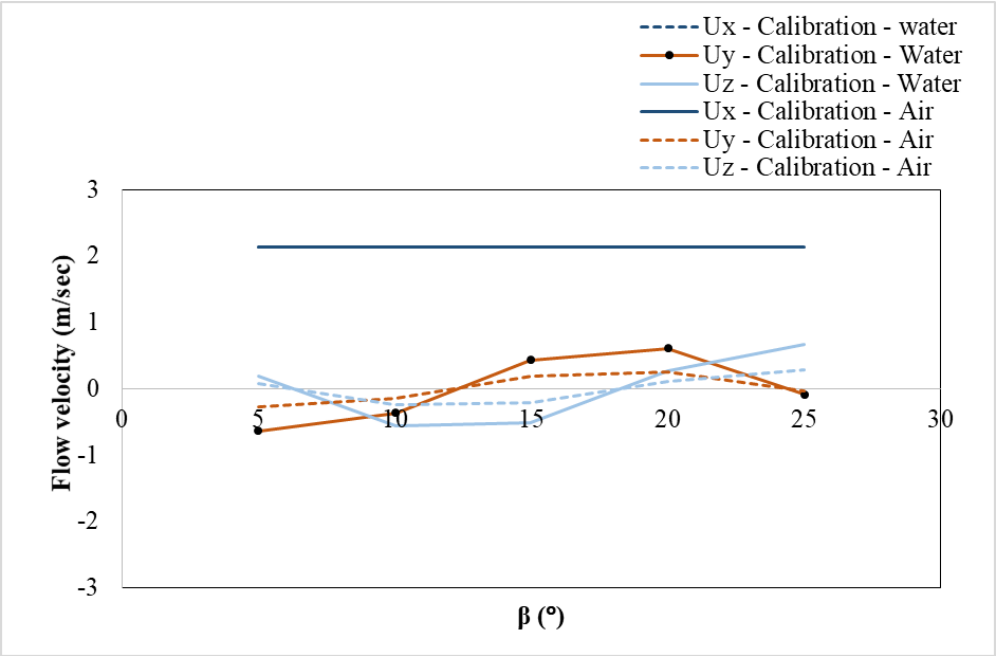

Figure 8.10. Comparison of experimental calibration dataset of the hemispherical five-hole probe for air and water flow fields measurement

Figure 8.10 shows information about air and water flow fields computed using the hemispherical probe quantities in air and water flows. It can be seen that the x component of velocity, measured for the flow of water by the conical five-hole probe, is perfectly matching with airflow. However, y components of velocity of water are higher by 50%, while the z component of the velocity of air is higher by 50%. Figure 8.10 has demonstrated that the calibration datasets of the hemispherical five-hole probe can predict flow information with reasonable accuracy in air and water flows. A detailed comparison of figure 8.10 and 8.2 suggest that using the experimental calibration methods, both conical and hemispherical five-hole probe measure three-dimensional complex flow properties with increased accuracy.

8.3.2 Comparisons of CFD based Numerical Calibration Datasets

The novel CFD based numerical calibration study developed for hemispherical five-hole pressure probe has been tested for air and water flows. The procedure is the same in this section as it is for sector 8.2.2. A performance comparison of the probe in both air and water flows has been carried out respectively. Here, the analysis of the calibration sector maps generated by the probe using the novel CFD based numerical calibration method for air and water flows have been carried out and compared as shown in figure 8.11. Similarly, a performance comparison of the developed novel calibration method has been used for the probe in predicting flow information for air and water

flows as shown in figure 8.12. Finally, a comparison has been made against the calibration and measurements results corresponding to conical five-hole pressure probe shown in figure 8.3 and 8.4.

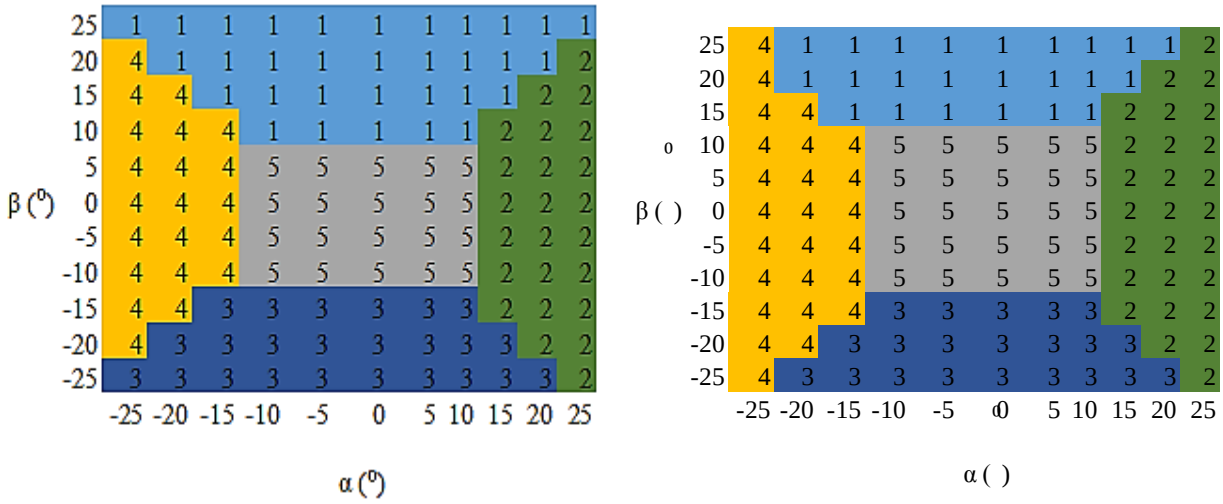

(a) Hemispherical probe sector map for airflow (b) Hemispherical probe sector map for water flow

Figure 8.11. Comparisons of the CFD based numerical calibration sector maps of the hemispherical five-hole pressure probe in air and water flow fields

Figure 8.11 shows the novel CFD based numerical calibration sector maps of the hemispherical five-hole pressure in air and water flows. It can be seen that for both sector maps, the probe covers wider-angle range in water flow for sector 2 and four compared to airflow. Similarly, the probe covers a wider range of pitch angle as shown by sector 5 in water flow than in airflow. Yaw angle wise, the probe covers a wider range in airflow in sector one than in water flow. Furthermore, it can be seen that the hemispherical five-hole pressure probe produced a perfect symmetrical calibration sector map in water flow calibration compared to airflow. However, it can generally be reported that the probe has performed very well in predicting CFD based numerical calibration maps for each flow as their symmetrical shape can be seen in all sectors. In comparison to figure 8.3, it can be seen that the hemispherical five-hole pressure probe produced a perfect symmetrical calibration sector maps in both flows than the conical five-hole pressure probe. The respective calibration coefficients (a_0 to a_{27}) corresponding to appendixes 6.2a (air) and 7.2c (water) has been used to compute flow information as shown in figure 8.12. These coefficients have been calculated using the respective calibration datasets that generate their respective calibration sector maps.

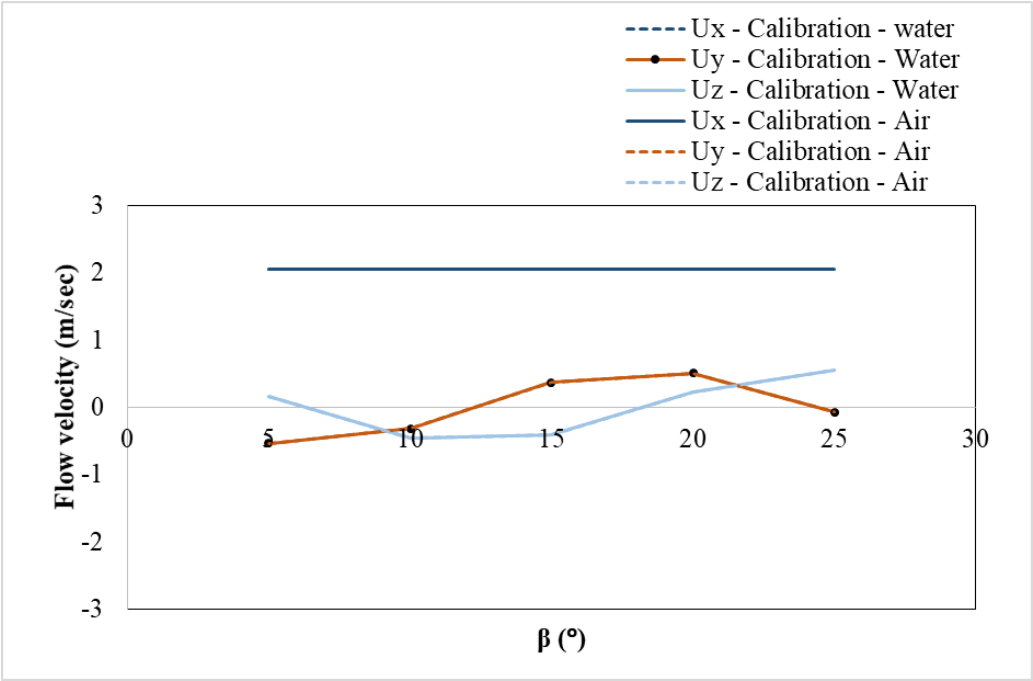

Figure 8.12. Comparison of CFD based numerical calibration dataset of the hemispherical five-hole probe in air and water flow fields measurement

Figure 8.12 shows the three-dimensional flow field measured using a five-hole pressure probe and its calibration coefficients. Detailed performance comparison in both flows suggests that using CFD base numerical calibration methods of the hemispherical five-hole pressure probe has a significant ability to increase the accuracy of the measurement of any complex three-dimensional flow field. All three component of velocities maintained perfect correlations in both air and water flow. It is a reflection of the accuracy of the calibration sector maps. A detailed comparison of figure 8.12 and figure 8.3 confirmed that CFD based numerical calibration could measure strong flow information with accuracy up to 95% in both air and water flow using either conical pressure probe or hemispherical pressure probe.

8.3.3 Comparisons of the CFD based integration Calibration datasets

The systematic approach of the novel CFD based integrated calibration method explained in section 3.9 is the same for hemispherical five-hole pressure probe. Therefore, the same procedures followed in section 8.2.3 are applied in this section. This section presents a performance analysis comparing the CFD based calibration method of a hemispherical five-hole pressure probe in both air and water flows. The calibration sector maps produced by the probe for both flows as shown in figure 8.13 have been compared. Furthermore, the flow information computed using the calibration datasets has

also been compared as shown in figure 8.14. Finally, comparisons are also made to figure 8.5 and 8.6.

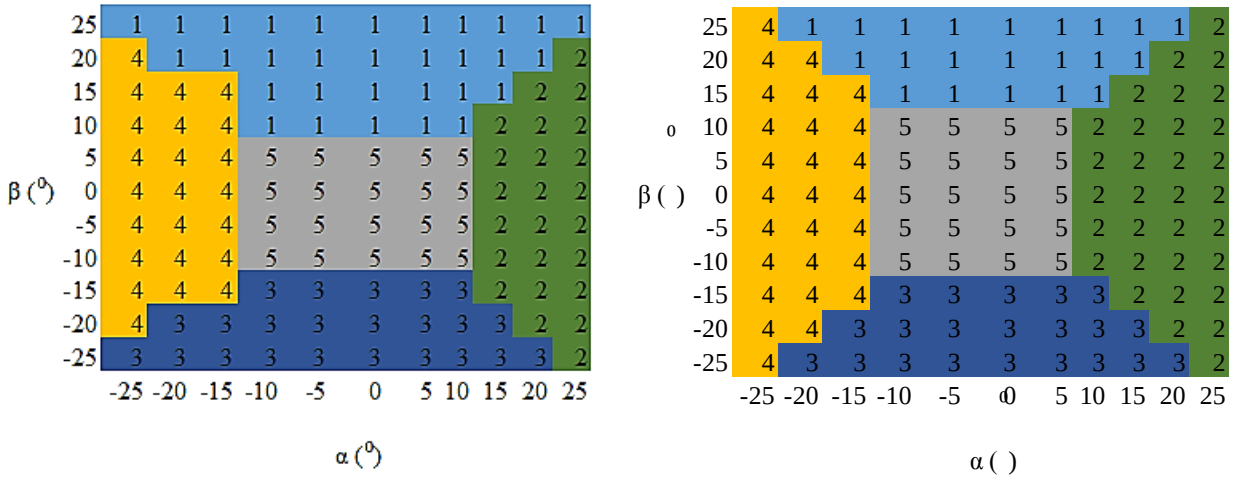

(a) Hemispherical probe sector map airflow (b) Hemispherical probe sector map for water flow

Figure 8.13. Comparisons of the CFD based integrated calibration sector maps of the hemispherical five-hole probe for air and water flow fields

Figure 8.13 shows the calibration sector maps of the hemispherical five-hole pressure probe in both air and water flows. It can be seen that the in sector map produced for water flow calibration, the probe covers a wider range of pitch angle in both sector 2 and four compared to airflow. Furthermore, sector two of the water flow slightly covers a wider range of yaw angle in sector two compared to airflow. A comparison of figure (a) and (b) suggests that the novel CFD based integrated calibration method produced a perfect calibration sector map in water flow than in airflow. In comparing, figure 8.13 and 8.5 suggest that the novel CFD based integrated calibration sector maps are symmetrical for both air and water flows. The flow information for both flow fields has been computed and compared as shown in figure 8.14 using the calibration coefficients (a_0 to a_{27}) corresponding to the appendix for airflow and appendix for water flow corresponding to appendix 6.3b and 7.3d.

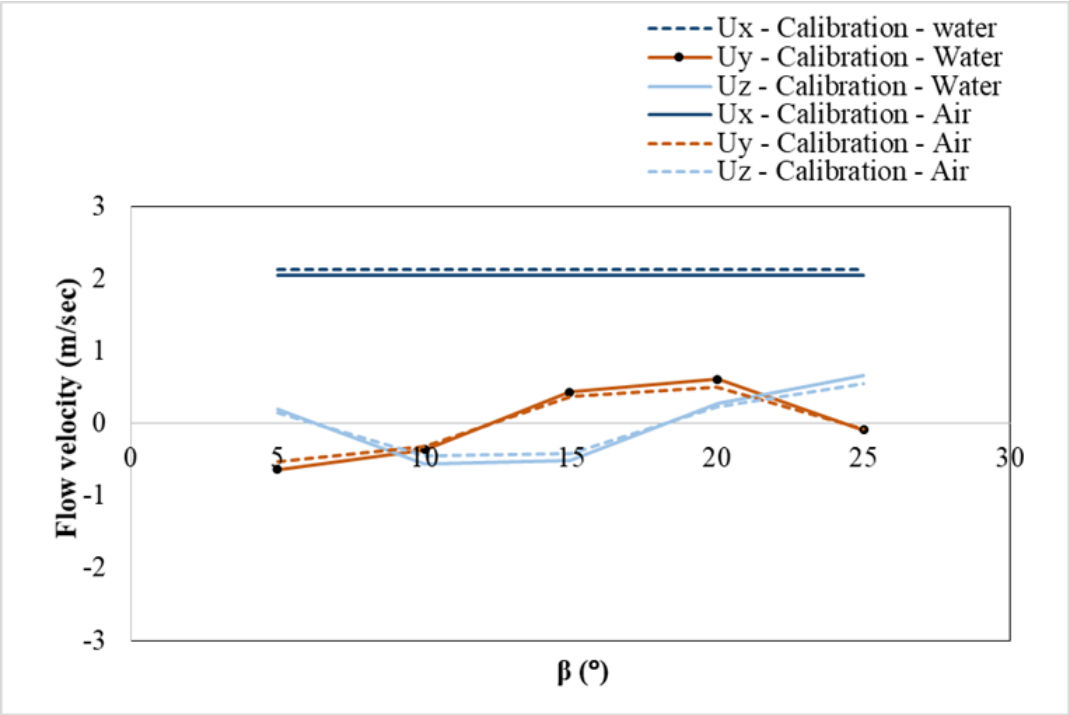

Figure 8.14. Comparison of the CFD based integrated calibration dataset of the hemispherical five-hole probe for air and water flow fields measurement

Figure 8.14 shows the flow information computed using the hemispherical five-hole pressure probe and the CFD based integrated calibration coefficients for air and water flow respectively. It can be seen that the x component of velocity, measured for the flow of water and airflows has a variation of about ±0.2m/sec. However, y-components of the velocity of water are higher by ±0.1m/sec, while the z component of the velocity of airflow is higher by 0.1m/sec. Therefore, figure 8.14 suggests that the CFD based integrated calibration datasets of the hemispherical five-hole pressure probe predicted flow velocities with high accuracy in both air and water flows. A detailed comparison of figure 8.14 and 8.6 suggests that the CFD based integrated calibration method works well for both air and water flows with maximum measurement accuracies.

8.3.4. Comparisons of the CFD based Extension of Calibration Range Datasets

The method followed in this section is the same method followed in section 8.2.3 (see section 3.9). Therefore, both air and water calibration and measurements followed the same procedures. The analysis presented in this section is to establish the performance accuracy of the hemispherical probe using the novel CFD based extension of the calibration range method in air and water flows. For this purpose, a qualitative performance analysis of the calibration sector maps for both air and

water flows as well as flow measurements have been carried for of comparison. The results of these analyses are shown in figure 8.15 and 8.16 respectively. Furthermore, these results have been compared to the results of the conical five-hole pressure probe shown in section 8.2.3.

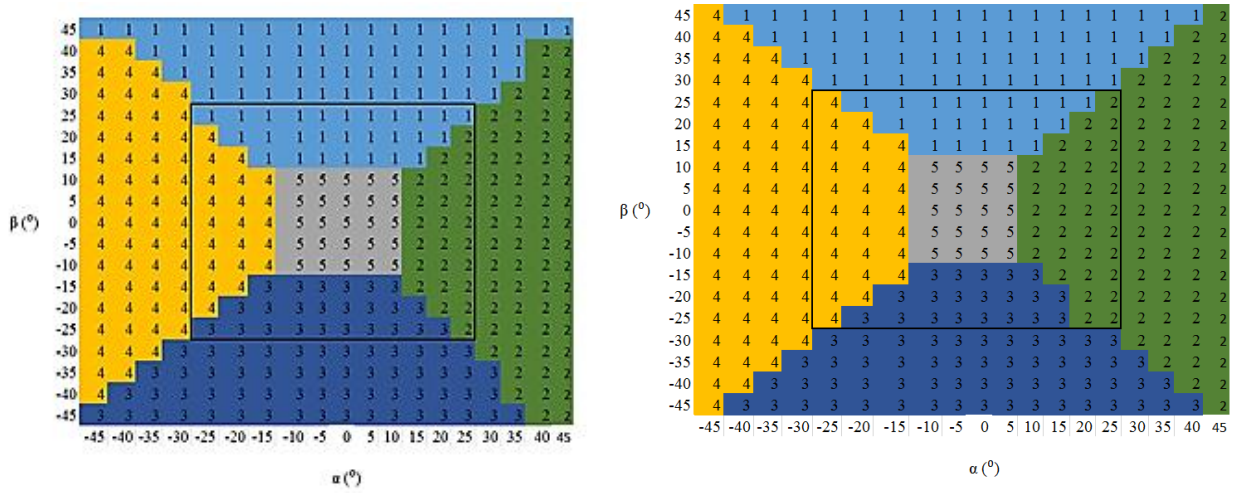

(a) Hemispherical probe sector map for airflow (b) Hemispherical probe sector map in water flow

Figure 8.15. Comparisons of the CFD based extension of calibration sector maps of the hemispherical five-hole probe in air and water flow fields

Figure 8.15 shows the comparison of the novel CFD based extension of range calibration sector maps of the hemispherical five-hole pressure probe for air and water flows. It can be seen in this figure that the novel CFD based extension of the calibration range method of the hemispherical probe has produced the same sector maps for both air and water flows. It has confirmed the qualitative similarity of the probe in both flows. Although both probes have produced the same sector maps, it can be noticed that the hemispherical probe produced a wider range of pitch angle for sector 2 and sector four compared to airflow.

Apart from this, both maps have maintained a perfect symmetric shape, and this is true for all calibration and measurements. Comparing figure 8.15 to 8.9, the accuracy of the novel CFD based calibration methods is evident in all calibration sector maps. Both conical and hemispherical five-hole pressure probe has performed very accurately in both air and water flows. Also, a closer look at both sector maps shows that the hemispherical probe covers a wider range of pitch angle for sector 2 and 4 for water flow compared to the conical pressure probe. It can be considered as the advantage the hemispherical pressure probe has in water flow over the conical probe. The calibration coefficients corresponding to appendix 6.4a (airflow) and 7.4c (water flow) have been used to compute the respective flow information as shown in figure 8.16.

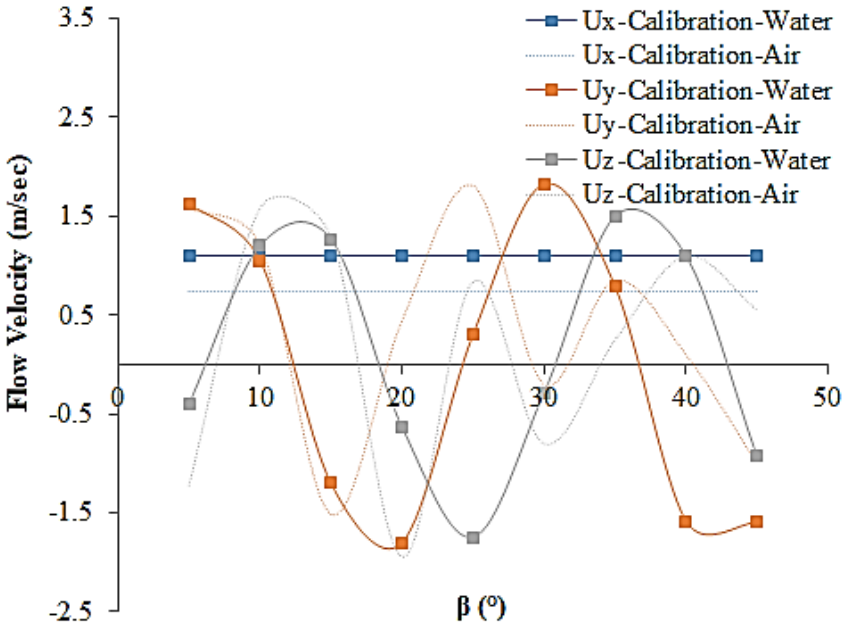

Figure 8.16. Comparison of the CFD based extension of calibration range dataset of the hemispherical head five-hole pressure probe for air and water flow fields measurement

It can be seen that on average the x component of velocity, measured for water flow, is 8.5% lower than measure airflow velocity. Similarly, y and z components of the velocity of water flow are 60% and 85% lower than airflow. Furthermore, figure 8.16 suggests that the extended calibration methods, the hemispherical probe measures flow properties with an increased accuracy significantly in the measurement of y and z components values for water flow. In comparison to figure 8.8, it can be seen that both the conical and hemispherical pressure probe using the novel extension calibration methods perform significantly accurate in the in both air and water flow fields.

8.6 Summary

In this chapter, the measurement of application of various novel calibration methods of the conical and hemispherical five-hole probe proposed in this study have been studied in wind tunnel and hydraulic pipeline flows. Results of each flow and probe have compared with one another, regarding calibration sector maps and velocity performances. Although the influence of both probes on velocity components are similar for most of the proposed calibration methods, the extent of disruption caused by each probe and perhaps the equation is significant. Particularly in airflow measurement, the conical probe appears to have higher accuracy than in water flows. Similarly, the hemispherical probe appears to have significant accuracy in water flow measurements compare to the conical five-hole pressure probe. The average velocity in airflow is 4.5% higher for the

hemispherical probe. It is supported by the generally higher values of y and z components of velocities for the conical five-hole probe in airflows.

Two different five-hole pressure probe (conical and hemispherical) has manufactured and calibrated at the University of Huddersfield Low-turbulence Wind Tunnel and Hydraulic Pipeline. The probes were each mounted carefully and traversed through a $\pm 25^{o}$ rang in each setup and using CFD to extend the angle range to $\pm 45^{o}$. The calibration datasets are in good agreement with repeatability as there are little variances between dataset and precision errors are relatively low for both air and water flows measurements. Each probe was calibrated at least three times for each wind tunnel and hydraulic pipeline respectively to verify repeatability of datasets. The calibration sector maps of each probe have been presented for both air and water flow using each of the novel calibration methods. Even though it has been reported that conical five-hole pressure probe performs fairly better in air flow than the hemispherical five-hole pressure, it can be seen that both probes perform fairly accurately in both flow fields.

Conclusively, from the results presented in this chapter, it has been established that both the conical and the hemispherical five-hole pressure probes showed remarkable calibration-predicted features with robust generalisation in wind tunnel and hydraulic pipeline flows respectively. Furthermore, both probes perform considerably well in predicting three-dimensional velocities of air and water flows with high accuracies for all the novel calibration methods developed in these investigations.

Chapter 9 Conclusions

From the results obtained in the previous chapters regarding the calibration of the conical head pressure probe, hemispherical pressure probe in wind tunnels and pipeline flows, definite conclusions have been drawn in this chapter. The major achievements and contributions to the existing knowledge-based are summarised and where necessary referenced back to the initial aims of this study. Finally, the works carried out in this study are evaluated, and requirements for future work in the area of flow measurement using multi-hole pressure probes are defined.

Calibration and measurement of fluid flows using multi-hole pressure probes have been in existence for many years. However, developing new techniques and methods for better measurement accuracy keep evolving and are gaining more and more importance globally due to an increase in demand for flow quality assurance and vessel designs. However, the majority of the research studies carried out in the area of five-hole pressure probe calibration is based on either experiment (both laboratories and on the field) or analytical studies which lack a detailed investigation into complex flow structure and behaviour within such probes. With the advent of powerful computing machines and sophisticated software to analyse flow fields, it has now become possible to computationally model, simulate, analyse, calibrate and establish interaction between the flow field and the probe in various flow systems.

In this study, two different shapes of multi-hole (conical and hemispherical five-hole) pressure probes suitable for three-dimensional measurement, the influence of the probe geometries on flow fields and calibration process and measurements performance have been investigated. Both pressure probes have been tested and calibrated while surface flow visualisation experiments have been conducted numerically using CFD based approach, to enhance the understanding of flow behaviour around the probes in different flow fields. Flow partners have been identified and correlated to calibration results. Furthermore, the suitability of sixth order polynomial regression for application to calibration datasets has been examined and assessed.

The tip geometry of the conical and hemispherical probes, leading edge and surface roughness prove to have a significant influence on the probe performance. Increased calibration angles slowed down flow separation and accelerated the transition, establishing a more stable and resistant to separation turbulent boundary layer, resulting in higher angular sensitivity, wider measurement range and better accuracy. The conical five-hole pressure probe configuration with $\pm 45^{o}$ chamfer angle is indicated as the best design regarding angular sensitivity. The design is the least deflected downwash effect of the flow effect, featuring reduced deflection of the maximum pressure values.

The Paul Akshoy algorithm of data analysis was successfully implemented for the interpolation of the novel CFD based calibration methods and their respective datasets, showing suitability, both in terms calibration and measurement accuracy. One of the essential features of the developed calibration methods is that measurement conditions and the nature of the measurands defined the functionalities of the novel CFD based calibration methods.

9.1 Major Achievements

This study investigated the use of CFD to develop novel calibration methods of conical and hemispherical five-hole pressure probes to improve calibration and flow measurements accuracies. The effect of the probe head is relatively well understood. Furthermore, the effect of flow regime and fluid properties on the calibration process have been understood. An essential aspect of the study presented in this thesis was the use of the CFD based calibration constants developed for conical and hemispherical pressure probe, which are capable of measuring flow properties. These measurements have been used to qualify the accuracy of internal and external flows. By the aims, the results of these experiments lead to the following observations.

- This study provides a detailed computational fluid dynamics (CFD), and experimental based novel calibration methodology for the measurement of wind tunnel flows using a conical head five-hole pressure probe. An experimental method embedded with numerical data for a conical five-hole pressure probe has been presented that resulted in coefficients of determinations for all measurement sectors within the flow field to be greater than 90%. The calibrations data interpolations have been carried out using a pressure normalisation method where the centre pressure hole is considered in defining the non-dimensional pressure coefficients. Furthermore, a sixth order polynomial regression method of data analysis was used for interpolation for accuracy purposes. Experimental and numerical calibration data have been integrated to generate a calibration map and calibration coefficients that have been used to calculate velocities to increase the accuracy of velocity measurements in wind tunnel flow using a conical five-hole pressure probe. The extension of the angular range of the conical five-hole pressure probe has been carried out numerically to cover a wider range of wind tunnel flow measurements. It has been carried out through the use of CFD. The set of pressure values generated for this purpose used and the calibration map and coefficients presented.

  Based on the experimental, numerical, integrated process and extension process calibration data, the behaviour of the conical five-hole probe in wind tunnel flows has been critically analysed both quantitatively and qualitatively. Qualitative analysis is carried out through the use of the calibration maps and the coefficient of determination of the conical head five-hole pressure probe in the wind tunnel flows while the quantitative analysis makes use of the normalised coefficients of calibration, uncertainty error analysis and the local flow velocities

for the analysis of velocity distribution within the wind tunnel cross-section. What these results have further demonstrated the appropriateness of the five-hole conical probe in wind tunnel flows for velocity measurements.

- This study provides a detailed computational fluid dynamic (CFD), and experimental based development of a novel calibration method and investigation of wind tunnel flows using a hemispherical head five-hole pressure probe. These include the effect of the shape on the probe performance and in this investigation, the effect of shape on the probe's performance as well as its accuracy in velocity measurement has been investigated. A CFD based integrated experimental and numerical calibration of a hemispherical five-hole pressure probe with coefficients of determinations for all sector greater than 90% have been presented. The calibrations data interpolations have been carried out using a pressure normalisation method where the pressure recorded by the centre hole is considered in defining the non-dimensional pressure coefficients. Effects of probe shape on sector map as well as non-dimensional coefficients have been enumerated. Experimental and numerical calibration process data have been integrated to generate a calibration map and calibration coefficients that have been used to calculate velocities to increase the accuracy of velocity measurement in the wind tunnel flow using a hemispherical five-hole pressure probe. The extension of the angular range of the hemispherical head five-hole pressure probe has been carried out numerically to cover wider range flow measurements. It has been carried out through the use of CFD. The set of pressure value generated for this purpose have been used, and the calibration map and coefficients presented. Effect of probe head shape on the calibration map has been quantified.
- Based on the experimental, numerical, integrated process and extension process calibration data, the behaviour of the hemispherical five-hole pressure probe in wind tunnel flows has been critically analysed both quantitatively and qualitatively. The qualitative analysis makes use of the flow field, the calibration map and the coefficient of determination of the five-hole pressure probe in the wind tunnel flows while the quantitative analysis makes use of the normalised coefficients of calibration, uncertainty error analysis and the local flow velocities for the analysis of velocity distribution within the wind tunnel cross-section. These results have further demonstrated the behaviour of the five-hole hemispherical probe in wind tunnel flows.

- Hydraulic pipeline flows are different to wind tunnel flows as the velocity may continuously vary along the pipe radius. In many applications, the hydraulic pipeline flow can be three-dimensional. The wind tunnel based calibration methodology may not work as required for the hydraulic pipeline. This study provides a detailed computational fluid dynamics (CFD) and experiments based development of a novel method of the calibration process for using a conical five-hole pressure probe. An experimental and a CFD based numerical calibration process of a conical five-hole pressure probe with coefficients of determinations for all sectors greater than 90% have been presented. The calibrations data interpolations have been carried out using sectoring scheme and a pressure normalisation method where the centre pressure hole is considered in defining the non-dimensional pressure coefficients. Sixth order polynomial regression analysis has been used for interpolation purposes. Experimental and numerical calibration data have been integrated to generate a set of calibration map, and calibration coefficients which then have been used to calculate hydraulic pipeline flow velocities to increase the accuracy of velocity measurement in hydraulic pipeline flow using a conical five-hole pressure probe. The extension of the angular range of the conical head five-hole pressure probe has been carried out numerically to cover a wider range of flow measurements. It has been carried out through the use of CFD.

  Based on the extensive experimental and CFD based numerical dataset, the behaviour of the conical five-hole pressure probe in hydraulic pipeline flows has been critically analysed. This involved determination of flow field around the five-hole pressure probe, the effect of flowing fluid on the probe performance as well as differences in sector map, calibration coefficients, and accuracy of measurement.
- As the hydraulic pipeline flows are significantly different from wind tunnel flow, different shapes of the probe may have different levels of accuracy. This study provides a detailed computational fluid dynamic (CFD) and experimental based evaluation of the effects of the probe shape on flowing fluid as well as velocity variations on calibration methodology. An experimental and CFD numerical calibration of a hemispherical five-hole pressure probe with coefficients of determinations for all sectors greater than 90% have been presented for hydraulic pipeline flows. The interpolations of the calibrations data have been carried out using a sectoring scheme, and a pressure normalisation method where the pressure recorded by the centre hole is considered in defining the non-dimensional pressure coefficients. Experimental and CFD based numerical calibration data have been integrated to generate a

set of calibration map and calibration coefficients that have been used to calculate velocities to increase the accuracy of velocity measurement in the hydraulic pipeline flow using a hemispherical pressure probe. The extension of the angular range of the hemispherical five-hole pressure probe has been carried out numerically to cover a wider range of flow measurements. This has been carried out through the use of CFD.

Based on the extensive novel experimental and numerical dataset, the behaviour of the hemispherical probe in hydraulic pipeline flow has been critically analysed. The analyses involved the determination of flow field around the hemispherical five-hole pressure probe, the effect of flowing fluid on the probe performance as well as differences in sector map, calibration coefficients, and accuracy of measurement. The effect of probe head on the accuracy of the measurement has also been quantified.

9.2 Thesis Conclusions

A comprehensive study has been carried out to support the existing literature regarding the calibration of multi-hole pressure probes in fluid flows and to provide novel additions to improve the current understanding of numerous calibration methods and using calibration data to compute flow velocities in wind tunnel, and hydraulic pipeline flows. The major conclusions from each facet of this study based on the objectives defined are summarised as follows:

- A novel calibration methodology has been developed that uses the experimental data to provide validation but then uses simulated data to increase the accuracy and resolution of the measurement system. This methodology has been implemented for conical five-hole probe working within wind tunnel flows. It can be concluded from the current investigations that the calibration methodology developed is reasonably accurate. The flow field information of a wind tunnel system investigated by the probes indicates that the probe design is adequate to enable measurement of accurate datasets as the effect of probe stem does not seem to affect the flow at the probe head. It has been seen that the velocity measurements with the improved method are more accurate and reliable. The developed method can be used with confidence for calibration of any type and shape pressure probes. The following section described the conclusions drawn from this study.
- Typically, the five-hole pressure probes can be used only within the flow range for which the calibrations have been carried out. There are obvious limitations in carrying out the experimental calibration for strongly three-dimensional flows. However, simulations can

provide significant data for this purpose. In this investigation, CFD based dataset has been used to extend the calibration range of the conical and hemispherical five-hole pressure probes respectively. It can be seen that the modified calibration method results in improved range and accuracy in the measurements of flow fields. With this, the probe can be used to measure flow information in complex three-dimensional flow fields. The extension of calibration range increases the usability of the probe in larger wind tunnel flows with large gradients and with higher free stream velocities.

- The novel calibration method and process developed in this investigation have very clearly provided two benefits. The first one is improved accuracy and resolution and the second is an extension in the operational range of the conical and hemispherical five-hole pressure probes in real-life application. There are systematic improvements in the accuracy with a fusion of simulated data with experimental data. There is a large increase in the range over which the calibrated conical and hemispherical five-hole pressure probes can be used now with enhanced accuracy.
- The head is the essential components of any multi-hole probe in the measurement system as it affects the flow field when the probe encounters an oncoming free stream. In this investigation, the calibration methods and processes developed has been used, and the effect of probe head on the flow field characteristics as well as calibration parameters has been quantified. It has been found that the modified calibration methodology works well for hemispherical five-hole pressure probe and the accuracy consistently improves with CFD integrated dataset. The effect of the probe shape can be seen in the pressure contours at the probe head, which is seen to be different from the conical five-hole probe. However, the effect of probe stem on the pressure field at the probe head is minimal.
- Validated CFD simulations have enabled the extension of the range of measurements that could be carried out through the five-hole probe with the hemispherical head. The effect of probe head on the calibration sector map and calibration coefficients has been enumerated. Furthermore, the effect of probe sensing head on accuracy and resolutions of measurements has been established. It has been seen that the use of a hemispherical probe has improved the accuracy and a higher level of correlation can be seen between the measured and predicted data.
- A comparative investigation has been carried out to obtain the effect of probe head on the accuracy of measurements through the three calibration processes presented in this study,

namely, experimental, integrated and integrated with the extension of the range has indicated that hemispherical five-hole probes are well suited for wind tunnel measurements. Both the accuracy and resolution of measurements has increased, and the usefulness of this probe for measuring unknown flow fields has increased.

- Unlike wind tunnel flows, hydraulic pipeline flows have continuously varying velocity flow fields. The suitability of a conical five-hole probe for hydraulic pipeline flows has been ascertained in this investigation. Experimental calibration resulted in a reasonable accuracy of measurements. Further data obtained from the numerical simulations have been integrated with the experimental data, and a CFD integrated calibration process has been developed to improve the accuracy of measurements, Furthermore, the results obtained for hydraulic pipeline flows have been compared with the results obtained for the wind tunnel flow to compare the performance of the probe in the two flow regimes. It can be observed that by integrating CFD numerical calibration dataset with experimental calibration data produced reasonable sector maps and coefficients that have better correlations for all flow parameters responsible that can be used for computing flow information. It is seen that the accuracy of measurement of the conical probe is better in the case of wind tunnel flow.
- The flows in hydraulic pipelines can be complex three-dimensional. It is necessary to calibrate the conical five-hole pressure probes over a wide range of flow conditions to measure such flows. In the present investigation, this has been achieved by carrying out an additional CFD based simulation to develop a sector map and obtain calibration coefficient over a wide range of hydraulic pipeline flow conditions. Comparison of extended range performance between the hydraulic pipeline flow and wind tunnel flow indicates that the probe performs equally well in the two flow regimes.
- From the investigation regarding the measurement of hydraulic pipeline flow velocities using the calibration dataset for the hydraulic pipeline flow, carried out in this study, it can be concluded that there is an increase in accuracy in measurement of velocity profile when used with the numerical calibration dataset. The accuracy of estimation of velocity profile measured by the conical five-hole probe in the hydraulic pipeline flow with simulated dataset has improved. Furthermore, the conical probe seems to work equally well in both the regimes of flow, i.e. wind tunnel flow and hydraulic pipeline flow.
- To establish the suitability of the hemispherical five-hole probe for flow field measurements within hydraulic pipeline flows, experimental and numerical calibrations have been carried

out. An integrated calibration methodology has also been developed that seems to improve the accuracy of prediction. The CFD based integrated methodology has been further improved so that the probe can be used for the measurement of complex three-dimensional flows. The flow field corresponding to such probes indicate that flow field at measurement location is undisturbed by the presence of the probe. It has also been seen that flow fields corresponding to two different shaped probes are different. It has also been seen that hemispherical head works equally well within the hydraulic pipeline flow as well as wind tunnel flow.

- The CFD based simulations have been used over a wide range of flow conditions to improve the suitability of both conical and hemispherical five-hole pressure probes for measurement of complex three-dimensional flow fields respectively. Also, the effect of the probes shape, as well as suitability of both the probes for wind tunnel and hydraulic pipeline flows, have been established. The flow fields corresponding to both the probes under different flow regimes have also been compared. It has been found that at the point of measurement the probes do not affect the flow field characteristics.
- From the investigation carried out in this study regarding the measurement of hydraulic pipeline flow velocities using the range of methods, it can be concluded that there is an increased accuracy in velocity profile measured when carried out with integrated calibration method. The accuracy of estimation in velocities measured by the hemispherical five-hole pressure probe in the hydraulic pipeline flow has been established. The effect of shape and flow regime on the accuracy of flow measurement has also been established.

3.3 Thesis Contributions

One of the most important contributions of the study in this thesis is the development of computational fluid dynamic (CFD) based calibration methods for any shape of multi-hole pressure probe and the validation of simulation methods to predict the flow measurements of standard five-hole pressure probe to an arbitrary laminar and turbulence flow fields. The first part of the CFD based simulation technique utilises the integration of CFD datasets into experimental datasets for standard conical and hemispherical five-hole pressure probes in the range of $\pm 25^{o}$, calibrate the datasets and used the calibration constants (coefficients) to predict flow angles and flow velocities. The integrated datasets were then extended using CFD to simulate the probe pitch and yaw to $\pm 45^{o}$ beyond $\pm 25^{o}$ to cover larger flow fields. These results were processed using data reduction

methods, sectoring and polynomial regression schemes to predict the measurement of the probe in larger flow fields. This method was used to predict the measurements of a conical pressure probe and hemispherical five-hole pressure probes in both wind tunnel and hydraulic pipeline flow fields. These results have been validated and compared to actual flow fields. The major contribution of the study with novelties is summarised in the following section.

- One of the major contributions of this study has been the improvements in the calibration methodology for the conical head five-hole probe through the combined use of experiments as well as CFD based simulations datasets. The integrated calibration methodology was further modified to include dataset corresponding to strongly three-dimensional flows. The available literature does not provide any information on such a calibration method for any conical five-hole pressure probe. Furthermore, the flow field disturbance effects caused by such probes have been analysed. The development of integrated calibration methodology is a novel contribution to the knowledge-based which can be used to estimate the velocity of a wind tunnel flows with reasonable accuracies.
- Another significant contribution of this study is the use of the calibration methodology for the hemispherical five-hole pressure probe and establish the effect of probe head on the accuracy of estimation of velocity fields, through the combined use of experiments as well as CFD simulations datasets. The integrated calibration methodology was again adapted to include datasets corresponding to complex three-dimensional flows. Still, the available literature does not provide any information on such a calibration method or probe head effect for any hemispherical five-hole pressure probe. Also, the flow field disturbance effects caused by such probes have been analysed and results presented. This development of CFD integrated calibration methodology is a novel contribution to the knowledge base, which can be used to estimate the velocity of a wind tunnel flow with reasonable accuracies using a hemispherical five-hole probe. Quantitative evaluation of the effect of hemispherical five-hole pressure probe head on calibration coefficients as well as the accuracy of measurements is a novel contribution to the study.
- Another major contribution of this study is the use of the advanced calibration methodology for a conical head five-hole probe for hydraulic pipeline flows through the use of experiments as well as CFD simulations. The integrated calibration methodology was further modified to include datasets corresponding to strongly three-dimensional flow. The

available literature does not provide any information on such a calibration method for a conical head pressure probe of any kind in any hydraulic pipeline flow. Furthermore, the flow field disturbance effects caused by such probes have been analysed. Also, the effect of flow regime on the accuracy of measurements has been quantified. The suitability of the conical five-hole pressure probe for the hydraulic pipeline as well as wind tunnel flow has been established.

- Another contribution of this study is a quantitative evaluation of probe head shape and flow regime on the accuracy of measurements using five hole probes with CFD based integrated calibration methodology. The available literature does not provide any information on such effects. It has been established both the probes can be used for velocity measurements with different flow regimes with good accuracy. This study has demonstrated for the first time that CFD based simulations can be gainfully used for calibration of any shape of multi-hole pressure probe with any amount of hole for flow measurements without compromising the reliability and accuracy of measurements. The overall comparisons of the simulations and experimental results have demonstrated that the CFD based calibration methods are capable of accurately predicting the response of the conical and hemispherical five-hole pressure probes in wind tunnel and hydraulic pipeline flow flows.

9.4 Recommendation for Future Work

The calibration and measurements of flows using multi-hole pressure probes in wind tunnels and hydraulic pipelines flows have been presented in the present study such that the gaps identified in the literature could be bridged. In light of the conclusions and contributions provided in the previous sections, there is a great potential for further research in this particular area associated with further performance and accuracy improvements in flow measurements. Throughout this study, many possible future topics of research have been identified. Recommendations for future study include:

- There are more advanced studies yet to be explored in conical and hemispherical five-hole pressure probes calibration and measurements. However, these type of probes is yet to be calibrated experimentally on two-phase air-water flow. To handle all the fluid flows, an experimental calibration of the five-hole pressure probe needs to be carried out on a single

air-water two-phase system. It can be integrated with CFD integrated calibration and further extend the angular range of the probe to increase measurement accuracies.

- Numerical studies on the five-hole pressure probe can be conducted for the calibration of the multi-hole pressure probe used in any two-phase flow to generate calibration data that can be used to estimate flow parameters. In such a condition, the pipe flow can have dispersed phase with a variety of volume fractions.
- It is recommended that a hemispherical head five-hole pressure probe is physically integrated with a conductivity probe to measure full flow information of air and water flow field to capture a full flow field of a two-phase air-water flow, The hemispherical five-hole probe should measure continuous (water) phase parameters such as velocities, pressure and angles while the conductivity probe should be used to measure dispersed (air) phase parameters such as velocities, void fraction and interfacial area concentration.
- CFD based numerical calibration study of conical and hemispherical five-hole probes can be carried to increase the resolution of calibration maps to help quantify the non-linear part located near the edges of the maps. It can easily be extended and easily adapted to other types of pressure probes with different shapes and numbering that can be calibrated at varying Reynolds number and pitch and yaw angles.
- Developing computational fluid dynamics (CFD) based integration and extension calibration methods for a conical and hemispherical five-hole pressure probe, calibration maps can be produced for ensemble averaging purposes. It will allow for an average of the calibration maps to be taken for analysis in producing strong calibration coefficients, and this will further increase accuracies of wind tunnel and hydraulic pipeline flow measurements.
- Direct interpolation and sixth order polynomial regression methods of data analysis can be applied to the computational fluid dynamics (CFD) based integration and extension of range calibrations, generate calibration maps and calibration coefficients for comparison purposes. The coefficients of both methods can be used to predict flow properties and then compare results to determine which method of data analysis perform better and in what fluid.
- A computational fluid dynamic (CFD) based integration and extension of range calibrations for conical and hemispherical five-hole pressure probe can be implemented using automatic calibration equipment such as motor control system to position the probe in its traverse angular planes automatically. It will eliminate manual errors in the calibration process thereby increasing the accuracy of wind tunnel and hydraulic pipeline flow measurements.

- A computational fluid dynamics (CFD) based integration and extension of range calibrations should be performed for the conical and hemispherical five-hole pressure probes, and then be integrated with particle image velocimetry (PIV) measurements to enhance measurement accuracy. Furthermore, this will aid the visualisation and understanding of flow interactions around the probe head and the effect of angle ranges in real life applications.

REFERENCES

1 Bryer, D.W., & Pankhurst, R.C. (1971). “Pressure-Probe Methods for Determining Wind Speed and Flow Direction", Her Majesty's Stationary Office, London. National Physical Library, pp.126.

2 Everett, K.N., Gerner A., & Durston, D.A. (1980). "Seven-Hole Cone Probe for High-Angle Flow Measurement Theory and Calibration", AIAA Journal, vol. 21, no. 7. pp. 992-998.

3 Huffman, G. D., Rabe, D. C., & Poti, N. D. (1980). "Flow direction Probes from a Theoretical and Experimental Point of View". Journal of Physics E: Scientific Instrumentation, vol.13, pp. 751.

4 Leland, B. J., Hall, J. L., Joensen, A.W., & Carroll, J. M. (1977). "Correction of S-Types Pitot-Static Tube Coefficients when Used for Isolation from Stationary Sources". Environmental Science and Technology, vol. 11, no. 7, pp.694-700.

5 Delhaye, D., Penagua G., & Fernandez J. M., (2011). "Enhanced performance of fast - response 3-Hole Wedge Probe for Transonic flows in Axial Turbine turbomachinery". Experiment in Fluids, volume 50, 1st edition, pp.163-177.

6 Pawel R., Kamila, G., Przenyslaw, M., Lucas, S., & Daniel, B. (2018) . "Use and Calibration Five-Hole Hemispherical Pressure Probes to Measure Airflow Velocity", Journal of KONES Power Train and Transport, vol. 25. no. 2 (2018), pp. 1231- 4005

7 Zilliac, G. G. (1989). "Calibration of Seven-Hole Probe for Use in High-Fluid Flows with Large Angularity". NASA Technical Memorandum 102200, December, vol. 14,issue 1-2, pp.104-120.

8 Kinser, R. E., & Rediniotis, O. K., (1998). “Development of a Near-Omnidirectional Velocity Measurement Pressure probe", AIAA Journal, vol. 36, no. 10, pp.1854-1860.

9 Koppel, P., Roduner, C., Kupferschmied, P. & Gyarmathy, G. (2000). “On the Development and Application of the Fast Response Aerodynamic Probe Systems in Turbomachines - Part 3: Comparison of average Methods applied to Centrifugal Compressor Measurements", Turbomachinery Journal, vol. 122, pp. 527-536.

10 Matsunaga, S., Ishibashi, H., & Nishi, M. (1980). "Measurement of Instantaneous Pressure and Velocity in Nonsteady Three-dimensional Water Flow by Means of a combined five-Hole Probe", Transaction of the ASME Journal of Fluid Engineering, vol. 102, pp.196-202.

11 Naughton, J. W, Cattafesta III, L. N, & Settles, G. S. (1992). "A Miniature, Fast-Response 5-Hole Probe for Supersonic Flow fields Measurements", AIAA-92-0266, 30th Aerospace Sciences Meeting and Exhibit, Reno, NV, January 6-9.

12 Rediniotis, O. K., & Pathak, M. M. (1999). “Simple Technology for Frequency Response Pressure Enhancement of Miniature Pressure Probes", AIAA Journal, vol. 37, pp.897-899.

13 Kupferschmied, P., Koppel, P., Roduner, C. & Gyarmathy, G. (2000). “On the Development and Application of the Fast Response Aerodynamic Probe Systems in Turbomachines - Part 1: The Measurement System," Journal of Turbomachinery, Vol. 122 pp.505-516.

14 Rediniotis, O. K, Johansen, E. S, Tsao, T., Seifert, A. & Pack, L.G. (1999). "MEMS-Based Probes for Velocity and Pressure Measurements in unsteady and turbulence Flow fields", AIAA-99-0521, 37 Aerospace Sciences Meeting and Exhibition, Reno, NV, 11-14. January.

15 Johansen, E. S., Rediniotis, O. K. & Jones, G. S. (2001). "The Compressible Calibration of Miniature Multihole Probes" Journal of Fluid Engineering, vol. 123, pp.128-137.

16 Kerrebrock, J. L., Thompkins, W. T. & Epstein, A. H. (1980). "A Miniature High-Frequency Sphere Probe", Proceedings of ASME Symposium on Measuring Methods in Rotating Components of Turbomachinery, pp.91-98.

17 Achenbach, E. (1971). “Influence of Surface Roughness on the Cross-Flow around a Circular Cylinder". Journal of Fluid Mechanics, vol. 46, pp. 321-335.

18 Shevchenko, A. M., & Shmakov, A. S. (2017). "Multihole Pressure Probes to Wind Tunnel Experiments and Air Data Systems". Khristianovich Institute of Theoretical and Applied Mechanics, SB RAS, 630090, Novosibirsk, Russia, 978-0-7354-1578-2.

19 Bonham, C., Thorpe, S., Erlund, M., & Stevenson, J. (2017)"Combination of Probes for Stagnation Pressure and Temperature Measurement in Gas Turbine Engines". Measurement Science and Technology, vol.29, issue 1, pp.1361-6501.

20 Sieverding, C. H., Arts, T., Denos, R., & Broukaert, J. F. (2000). "Measurement Techniques for Unsteady Flows in Turbomachines", Experiments in Fluids, vol. 28, pp. 285.-321.

21 Aschenbruck, J., Hauptmann, T., & Seume, J. R. (2015). "Influence of a Multihole Pressure Probe on the Flow Field in Axial-Turbines". Proceedings of 11th European Conference on Turbomachinery Fluid Dynamics & Thermodynamics, Madrid Spain, ETC2015-155.

22 Moffat, R. J. (1988). "Describing the Uncertainties in Experimental Result Uncertainty". Experimental Thermal and Fluid Science, vol. 1, no.1, pp.3-17.

23 Groth J., Johansson, A.V. (1988). "Turbulence Reduction by Screens". Journal of Fluid Mechanics, vol. 197, pp.139-155.

24 Laws, E. M., & Livesey, J. L. (1978). "Flow-Through Screens". Annual Review of Fluid Mechanics, Vol. 10, pp.247-246.

25 Lee, S.W., & Jun, S. B. (2005). "Reynolds Numbers Effects on the Non-Nulling calibration of a Cone Type Five-Hole Probe for Turbomachinery Applications". Journal of Mechanical Science and Technology, vol. 19, no. 8, pp.1632-1648.

26 Gallington, R. W. (1980). "Measurement of Very Large Flow Angles with Non-Nulling Seven-hole probes". Aeronautical Digest, spring/summer. USAFA-TR-80-17, pp. 60-88.

27 Gerner, A. A., Maurer, C.L., & Gallington, R.W. (1984). "Non-Nulling Seven-Hole Probes for high Angle Flow Measurement". Experiment in Fluids, vol 2, no. 2.

28 Zilliac, G. G. (1993). "Modelling, Calibration and Error Analysis of Seven-Hole Pressure Probe ". Experiment in Fluids, vol. 14, no. 2.

29 Pisdale, A. J., & Ahmed, N. A. (2004). "Development of Functional Relationships between port Pressures and Flow Properties for Calibration and application of Multihole Probes to Highly Three Dimensional Flows". Fluid Experimentation, vol. 36, pp.422-436.

30 Paul, C. (2013). "Design and Construction of a Velocity Probe Calibration Rig". Major Qualifying Project Worcester Polytechnic Institute, E-project-031113-224537.

31 Louis, N. (2012). "A Multihole Pressure Probe Accuracy Analysis" University of Florida, spring. International Journal of Innovative Research in Science, Engineering and Technology, vol. 5, issue 4.

32 Silva, M.C. G., Pereira, C.A.C., & Cruz, J.M.S. (2003). "On the Use of a Linear Interpolation Method in the Measurement Procedure of a Seven-Hole Pressure Probe." Experimental Thermal and Fluid Science, vol. 28, pp.1-8.

33 Sumner, D. (2002). "A Comparison of Data Reduction Methods for a Seven-Hole Probe". Journal of Fluids Engineering Technology ASME, Vol. 124, pp. 523-527.

34 Treaster, A. L., & Yocum, A. M. (1979). "The Calibration and Application of Five-Hole Probes, Instrumentation Society of American Trans". Vol. 18.3, pp. 23-34.

35 Sitaram N., & Treaster, A. L. (1985). "A Simplified Method of using a four-Hole Probe to Measure Three-dimensional Flow Fields." J. Fluid Engineering, vol. 107, pp.31.

36 Krause, L. N., & Dudzindki, T. J. (1969). "Flow Direction Measurement with fixed position probes in subsonic flows over a range of Reynolds numbers". NASA TMX-52576.

37 Akshoy, R. P., Ravi, R.U., & Anu, J. (2011). "A Novel Calibration Algorithm for Five-Hole Pressure Probes" International Journal of Engineering, Science and Technology, vol. 3, pp. 89-95.

38 Akima, H. (1970). "New interpolation Method of Interpolation and Smooth Curve Fitting Based on Local Procedures". Journal of the Association for Computing Machinery, vol. 17, no. 4.

39 Wenger, C. W., & Devenport, W. J. (1999). "Seven-Hole Pressure Probe Calibration Method Utilising Look-Up Error Tables". AIAA Journal, vol. 37, no. 6.

40 Rediniotis, O. K., & Vijayagopal, R. (1999). "Miniature Multihole Pressure Probes and their Neural Network Based Calibration". AIAA Journal, vol.37, no. 6, pp. 667-674.

41 Chue, S. H. (1975). "Pressure Probes for Fluid Measurement ". Progress in Aerospace Sciences, vol. 16, issue 2, pp. 147-223.

42 Armaly, B. F., Durst, F., Pereira, J. C. F., & Schonung, B. (1983). "Experimental and Theoretical investigation of Backward-Facing Step Flow". Journal of Fluid Mechanics, vol 127, pp.473-496.

43 Cantwell, B., & Coles, D.(1983). "An Experimental study of Entrainment and Transport in the Turbulent Near Wake of a Circular Cylinder". Journal of Fluid Mechanics. Vol. 136, pp.321-374.

44 Becker, H.A., & Brown, A.P.G. (1974). "Response of Pitot Tubes in Turbulent Streams". Journal of Fluid Mechanics, vol. 62, no.1, pp. 85-114.

45 Christiansen, T., & Bradshaw, P. (1981). "Effect of Turbulence of Pressure probes". Journal of Physics E: Scientific Instruments, vol. 14, pp. 992.

46] Kang, J. S., & Yang, S. S. (2010). "Fast Response Total Pressure Probe for Turbomachinery Application". Journal of Mechanical Science and Technology, Vol. 24, No. 2, pp. 569-574.

47 Fischer, A., Masden, HA, Bak, C., & Bertangnoli, F. (2009). "Pitot Tube Designed for High-Frequency Inflow Measurements on MW Wind Turbine Blades", EWEC 2009. Proceeding PO 299.

48 Ned, A., VanDeWeert, J., Goodman, S., & Carter S. (2011). "High Accuracy High-temperature Pressure Probes for Aerodynamic Testing". 49. AIAA Aerospace Sciences Meeting, pp. AIAA 2011-1201.

49 Crilly, J., & Fryer, P. (1993). "New directions in food science": the role of mathematics in models. Instrumentation, Mathematics and Applications, vol 5, pp. 265-282.

50 Pfau, A., Schlienger, J., & Kalfas, A., & Abhari, S. (2003). "Unsteady 3D Flow Measurement Using a Miniature Virtual Four Sensor Fast Response Aerodynamic Probe", ASME Turbo Expo 2003, Collected with the 2003 International Joint Generation Conference, vol.10, Issue GT2003, pp. 307-315.

51 Babinsky, U., Kuschel, H., Moore, D., & Welland, M. (1993). "The aerodynamic Design and use of a Multi-Sensor Pressure Probes for MEMS Applications". Cambridge University, Department of Engineering, Trumpington Street Cambridge, CB2 1PZ, UK

52 Woong, K., Nguyen, D., Saeng, H., Jae, S., Hee, S., & Yong, M. (2015). "Experimental and Numerical Investigations of the Factors Affecting the S-type Pitot Tube Coefficients". Flow Measurement and Instrumentation, vol. 44, pp.11-18.

53 Wecel, D., Chmielniak, T., & Kotowicz, J. (2008). "Experimental and numerical investigations of the averaging Pitot tube and analysis of installation effects on the flow coefficient". Institute of Power Engineering and Turbomachinery, the Silesian University of Technology in Gliwice, 44-100, Poland.

54 Gong, W., Zhang, H., & Liu, C. (2015). "Study on Multihole Pressure Probe System Based on LabView". Department of Fluid Machinery and Engineering, School of Energy and Power Engineering, Xi'an Jiaotong University, 710049, Shaanxi, China. Society for Experimental Mechanics, vol.39, pp. 42-54

55 Hooper, J., & Musgrove, A. (1997). "Reynolds Stress, Mean Velocity, and Dynamic Static Pressure Measurement by a Four-Hole Pressure Probe", C. S.I.R.O. Division of Minerals, Lucas Heights RE., PMB No. 5, Menai, New South Wales 2234, Australia. Experimental Thermal and Fluid Science, vol. 15, issue4, pp. 375-383.

56 Paul, A., Upadhyay, R., & Jain, A. (2011). "A novel calibration algorithm for five-hole pressure probe", Department of Applied Mechanics, Motilal Nehru National Institute of Technology, Allahabad, Department of Mechanical Engineering, Motilal Nehru National Institute of Technology, Allahabad, India. International Journal of Engineering, Science and Technology, vol.3, no.2, pp.89-95.

57 Árpád, V., & Márton, B. (2013). "Development of a multi-hole probe for atmospheric boundary layer measurements", Theodore von Kármán Wind Tunnel Laboratory, Department of Fluid Mechanics, Budapest University of Technology and Economics, Budapest, Hungary. Internal workshop on physical modelling of Flow and Dispersion Phenomena EnFlo Laboratory, University of Surrey, UK, 16^{th} – 17^{th}.

58 Susheela, V., & Michael, S. (2004). "Use of a Four-Hole Cobra Pressure Probe to Determine the Unsteady Wake Characteristics of Rotating Objects", University of Illinois-Urbana Champaign, Urbana, IL61820. 24th AIAA Aerodynamic Measurement Technology and Ground Testing Conference Portland, Oregon, 28, June –1, July, pp. AIAA-2004-2299.

59 Malviya, V., Mishra, R., & Palmer, E. (2010). "CFD Investigation on 3-Dimensional Interference of a Five-Hole Probe in an Automotive Wheel Arch", Department of Engineering and Technology, University of Huddersfield, Queensgate, Huddersfield HD1 3DH, UK. Advances in Mechanical Engineering, 2010.pp.1-19. ISSN 1687-8132.

60 Bryant, R., & Johnson, A. (2011). "Comparison of Gas Velocity Measurements and CFD Predictions in the Exhaust Duct of a Stationary Source", National Institute of Standards and Technology Gaithersburg, MD 20899. Continuous Emission Monitoring User Group Conference & Exhibit, June 8-2011, Chicago, IL

61 Kim, S. H., & Kang, Y. J. (2009). "Calibration of a Five-Hole Multi-Function Probe for Helicopter Air Data Sensors", Department of Mechanical and Aerospace Engineering, Gyeongsang National University, Jinju, Korea. International Journal of Aeronautical & Space Sciences, vol.10, no.2

62 Malviya, V., Mishra, R., Palmer, E., & Majumdar, B. (2007). "CFD Based Analysis of the Effect of Multi-Hole Pressure Probe Geometry on Flow Field Interference". Presented at 34th National Conference on Fluid Mechanics and Fluid Power. Birla Institute of Technology, India, pp.113-122.

63 Duquesne, P., IIiescu, M., Fraser, R. Deschenes, C., & Ciocan G. (2010). "Monitoring of Velocity and Pressure field within an Axial Turbine", 25th IAHR Symposium on Hydraulic Machinery and Systems, September 20-24, Timisoara, Romania, IO' Conference Series Earth and Environmental Science, pp.1-9.

64 Brennan, M., Fry, M., Narasimha, M., & Holtham, P. (2007). "Water Velocity inside a Hydrocyclone using and Aeroprobe and Comparison with CFD predictions", 16th Australian Fluid Dynamics Conference, Crown Plaza, Gold Coast, Australia, 2-7 Dec. 2007, pp.1-6.

65 Vijay,B., Pravin, S., Nilesh, P., & Pankaj, V. (2016). “Fabrication and Calibration method of Five Hole Pressure Probe”. International Journal of Innovative Research in Science, Engineering and Technology, vol. 5, issue 4

66 Shah, R., & Banerjee, J. (2012). “Isothermal Analysis of CAN Type Combustor Using Five-Hole Probe”. The Institute of Engineers, vol.93, issue 4, pp.313-324.

67 Ligrani, P., Singer, B., & Baun R. (2014). “Miniature Five-hole Pressure Probe for Measurement of Three Mean Velocity Components in Low-Speed Flows.” Journal of Physics. Scientific Instrument, vol.22, no, 10, pp.22-868.

68 Lien, S., & Ahmed, N. (2011). “An Examination of the suitability of Multi-Hole Pressure Probe Technique for Skin Friction Measurements in Turbulent Flows”. School of Mechanical & Manufacturing Engineering, UNSW Sydney NSW 2052, Australia. Flow Measurement Instrumentation, vol. 22, issue3, pp. 153-164.

69 Zilliac, G. G. (1993). “Modelling, Calibration, and Error Analysis of Seven-hole Pressure Probe”. National Aeronautics and Space Administration (NASA), Ames Research Centre, Moffett Field, California 94035, USA. Experimental in Fluids, vol. 14, issue 1-2, pp. 104-120.

70 Pisasale, A. J., & Ahmed, N. (2004). “Development of a Functional Relationship between Port Pressures and Flow Properties for the Calibration and Application of Multihole Pressure Probe to Highly Dimensional Flows”. School of Mechanical and Manufacturing Engineering, the University of New South Wales, 2052 Sydney, Australia. Experiments in Fluids, vol. 19(2), pp.138-141.

71 Christopher, C., Shinder, I., & Michael, R. (2013). “Effect of Turbulence on a Multihole Pitot Tube Calibration”. Sensor Science Division National Institute of Standards and Technology (NIST), 100 Bureau Dr Gaithersburg, MD 20899, USA. Flow Measurement and Instrumentation, vol.33 (2013), issue 4, pp. 106-109.

72 Hsin-Hung, L., Iosif, I.S., John, D.W., & Michael R.M. (2014). “Application of ANFIS Method to the Non-nulling Calibration of Multi-hole Pitot Tube”, Center for Measurement Standards, Industrial Technology Research Institute, Taiwan R.O.C. National Institute of Standards and Technology, U.S.A. Procedia Engineering, vol. 79(2014), pp.125-132.

73 Jason, T., & Cengiz, C. (2014). "Sub-Miniature Five-Hole Probe Calibration using a Time Efficient Pitch and Yaw Mechanism and Accuracy Improvements", Turbomachinery Aero-heat Transfer laboratory, Department of Aerospace Engineering, The Pennsylvania State University, University Park, Pennsylvania 16802. Turbine Technical Conference and Exposition, vol.3, issue 11, pp.349-359.

74 Aschenbruck, J., Hauptman, T., & Seume, J.R. (2015). "Influence of a Multi-hole Pressure Probe on the Flow Field in Axial –Turbines", Institute of Turbomachinery and Fluid Dynamics (TFD), Leibniz Universitaet Hannover, Hannover, Germany. Proceedings of the 11th Europeans Turbomachinery and Thermodynamic, ETC11, March 23-27, Madrid Spain.

75 Remigiusz, J., Jaroslaw, M., & Jacek, P. (2017). "Probe Positioning for the Exhaust Emissions Measurements", TRANSCOM 2017: International Scientific Conference on Sustainable, Modern and safe transport Poznan University of technology, Piotrowo Street 3, Poznan 60-965, Poland. Procedia Engineering, vol. 129(2017), pp.381-386.

76 Elisabeth, S.S., Ewoud, J.J.S., Bart, R., Christopher, D.W., & Qiping, C. (2017). "Incremental Nonlinear Dynamic Inversion and Multi-hole Pressure Probes for Disturbance Rejection Control of Fixed-Wing Micro Air Vehicles", Delft University of Technology, 2629 HS Delft, the Netherlands. International Micro Air Vehicle Conference and Flight Competition 2017, Toulouse, France, pp.111-120

77 Pantelidis, K., & Hall, C.A. (2017). "Reynolds Number Effects on the Aerodynamics of Compact Axial Compressors", Whittle Laboratory, University of Cambridge, 1 JJ Thompson Avenue, Cambridge, CB3 0DY, UK. Proceedings of the 12th European Conference on Turbomachinery Fluid Dynamics & Thermodynamics ETC12, April 3-7, 2017 Stockholm, Sweden. pp. ETC2017-227.

78 Reinaldo, A., Gomes, Julia, K., & Reinhard, N. (2018). "Development and Implementation of a Technique for fast Five-Hole probe measurements downstream of a Linear Cascade. Institute of Jet propulsion, University der Bundeswehr Munchen, 85577 Neubiberg, Germany. Proceeding of the European Turbomachinery, vol.134, issue 5, pp. ETC2017-290.

79 Marcel, B., & Reinhard, N. (2018). "Development of an Additive Manufactured Miniaturised Wedge Probe Optimised for 2D Transonic Wake Flow measurements", Institute of Jet Propulsion, Bundeswehr University Munich, Neubiberg, Germany. XXIV Biannual Symposium on Measuring Techniques in Turbomachinery Transonic and Supersonic Flow in Cascades and Turbomachines MTT2418B21, August 29-32, 2018, Prague, Czech Republic.

80 Marcel, B., Martin, B., & Reinhard, N. (2018). " On the Challenges of Five-hole Probe Measurements at High Subsonic Mach numbers in the wake of Transonic Turbine Cascades", Bundeswehr University Munich, Werner-Heisenberg-Weg 39, Neubiberg, 85577, Germany.

81 Eny, Y.J., Zeng, Z., & Gordon, L. (2018). "Seven-Hole Probe calibration in a Low-Speed Wind Tunnel". Department of Aerospace Engineering, Embry-Riddle Aeronautical University, Daytona Beach, Florida, U.S.A. Embry-Riddle Aeronautical University, vol.17(2018), pp. 1-3.

82 Lien, S., & Ahmed, N. (2011). "An Examination of the suitability of Multi-Hole Pressure Probe Technique for Skin Friction Measurements in Turbulent Flows". School of Mechanical & Manufacturing Engineering, UNSW Sydney NSW 2052, Australia. Flow Measurement and Instrumentation, vol.22, issue 3, pp.153-164.

83 Wysocki, M., & Drobniak, S. (2001). "Comparative analysis of correction method for total head probes in large velocity-gradient flows". Institute of Thermal Machinery, Technical University of Czestochowa, Al. Armii Krajowej 21, 42-200 Czestochowa, Poland. Journal of Wind Engineering and Industrial Aerodynamics, vol.89, issue 1, pp. 31-43.

84 Rex, K. (1998). "Air velocity and Flow Measurement Using a Pitot Tube". King Industries Inc., 500 Lehman Avenue, Bowling Green, OH 43402, USA. ISA Transactions, vol.37, issue 4, pp.257-263.

85 Seshadri, V., Gandhi, B., Singh, S., & Ratnesh, K. (2001). "Analysis Effect of Body shape on Annubar Factor Using Computational Fluid Dynamics (CFD)". Department of Applied Mechanics, India Institute of Technology, Hauz Khas, New Delhi 110016, India. Measurement, vol.35, pp.25-32.

86 Freescale Semiconductor Technical Datasheet, "MPXV7002 Integrated Silicon Pressure Sensor On-Chip Signal Conditioned, Temperature Compensated and Calibrated". Freescale Semiconductor, vol.3, issue 01(2015), pp. MPXV7002. Retrieved from http://www.farnell.com/datasheet/1

87 Vijay, R., & Rediotis, O.,K. (2004). "Calibration and Data Reduction Algorithms for Non-conventional Multihole Probes". Texas A&M University, College Station, Texas 77843-3141 USA. AIAA Journal, vol.43, no.5, pp.941-952.

88 Samantha, S., Alex, T., & David, M. (2014), "The calibration and use of n-hole velocity probes". University of Surrey, Guildford, Surrey, UK GU2 7XH. American Institute of Aeronautics and Astronautics, vol. 43, no.5, pp.941-952.

89 Simon, W. (1990). "Measurement of Fluctuating Flows Using Multi-Hole Probes", Mechanical and Manufacturing Engineering", RMIT University, Bundoora East Campus 264 Plenty Road, Mill Park 3083, Australia. Flow Measurement and Instrumentation, vol. 26, pp. 102-110

90 Fluent Inc., "FLUENT 6.3 User's Guide," 2006. Ansys, Inc. Retrieved from http://www.shacnet.ca/software/fluent/html/ug/main_pre.htm.

91 Jason, T., & Cengiz, C. (2011). " Sub-Miniature Five-Hole Probe Calibration using a Time Efficient Pitch and Yaw Mechanism and Accuracy Improvements", Proceeding of ASME Turbo Expo Turbine Technical Conference, June 6-10,2011, Vancouver, Canada. Turbine Technical Conference and Exposition, Page No. GT2011-46391, vol.3, pp. 349-359.

92 Naveenji, A., Malavarayan, S., & Kaushik, M. (2010). "CFD Analysis on Discharge Coefficient during Non-Newtonian Flows through Orifice Meter", Department of Chemical Engineering, Sri Venkateswara College of Engineering. Chennai, 60210, India. International Journal of Engineering Science and Technology, vol.2 (7), issue 2010,pp.3151-3164.

93 R´egert, T., & Lajos, T. (2007). "Description of the flow field in the wheelhouses of cars," International Journal of Heat and Fluid Flow, vol. 28, no. 4, pp.616–629.

94 Rauch, R., & Batira, D. (1991). "Spatial Adoption Procedures on Unstructured Meshes for Accurate Unsteady Aerodynamic Flow Computations". Technical Report, American Institute of Aeronautics and Astronautics, vol.91, pp:1106.

95 Versteeg , H. K., & Malalasekera, W. (1995). "An Introduction to Computational Fluid Dynamics": The Finite Volume Method, Prentice Hall, Upper Saddle River, NJ, USA.

96 Rauch, R., & Batira, D. (1991). "Spatial Adoption Procedures on Unstructured Meshes for Accurate Unsteady Aerodynamic Flow Computations". Technical Report, American Institute of Aeronautics and Astronautics, vol.91, pp.1106.

97 Shih, T., Liou, W., Shabbir. A., Yang, Z., & Zhu, J. (1995). "A new k-ε eddy viscosity model for high Reynolds number turbulent flows," Computers & Fluids, vol. 24, no. 3, pp. 227–238.

98 Barth, T. J., & Jespersen, D. (1989). "The Design and Application of Upwind Schemes on Unstructured Meshes". 27th Technical Report, Aerospace Sciences Meeting, Nevada, USA.

99 Ventikatakrishnan, V. (1993). "On the Accuracy of Limiters and Convergence to Steady State Solutions", Technical Report, American Institute of Aeronautics and Astronautics.

100 Munson, B. R., Young, D. F., & Okiishi, T. H. (2002). "Fundamentals of Fluid Mechanics", John Willey & Sons Inc., 7th Edition., USA. pp.1-716.

101 Shih, T H., Liou, W.W., Shabbir, A., Yang, Z., & Zhu, J. (1995). "A new k-ε eddy viscosity model for high Reynolds number turbulent flows," Computers & Fluids, vol. 24, no. 3, pp. 227–238, 1995.

102 Bendell, E. (2005). "Investigation of a Coupled CFD and Thermal Modelling Methodology for Prediction of Vehicle Underbody Temperatures", 7Th Vehicle Thermal Management Systems Conference, SAE Paper issue. 200501-2044.

103 Anderson, J.D. (1995). "Computational Fluid Dynamics", Basics with Applications, International Editions McGraw-Hill, ISBN 0-07-113210-4.

104 Taylor, J.R. (1997). "An Introduction to Error Analysis The Study of Uncertainties in Physical measurements", University Science Books, Sausalito, CA, pp. 75, chap.3.

105 Nowack, C.F.R. (1970). “Improved Calibration Method for a Five-hole Spherical Pitot Probe”, Journal of Physics E: Scientific Instruments, vol. 1, pp. 21-26.

106 Dominy, R.G., & Hodson, H.P. (1993). “An Investigation of Factors Influencing the Calibration of Five-hole Probes for Three-Dimensional Flow Measurements”, Journal of Turbomachinery, vol. 115, pp.513-519.

107 Doebelin, E. O. (1990). “Measurement System: Application and design”, McGraw-Hill, New York, Fourth Edition. ISBN: 978-0070173385.

108 Lamb, H. (1932). “Hydrodynamics”, Dover Publications, New York, ISBN: 978-0486602561.

109 Hale, M.R. (1967). “The Analysis and Calibration of the Five-hole Sphere Piot”, Tech. Rep. ASME Publication 67-WA/FE-24, Amer. Society of Mechanical. Engineering, New York.

110 Parameswanran, V., Jategaonkar, R., & Press, M. (2002). “ Calibration of Five-hole Probe for Flow Angles from Dynamic and Tower Fly-by Maneuvers”, In AIAA atmospheric flight Mechanic Conference and Exhibit, Monterey, CA, 5-8, AIAA: Navigation, Control and Co-located Conferences.

APPENDIXES

Appendix 5.1a. Gauge pressure values measured from five-hole pressure probe using pressure transducers.

Pitch Angle	Yaw Angle	Top Hole Pressure	Bottom Hole Pressure	Centre Hole Pressure	Right Hole Pressure	Left Hole Pressure	Total Pressure	Static Pressure
(º)	(º)	(Pa)	(Pa)	(Pa)	(Pa)	(Pa)	(Pa)	(Pa)
-25	-25	102.8373	245.1614	171.9402	132.2610	3.4288	1045.5900	910.3200
-25	-20	119.5400	245.5600	194.1600	157.5400	23.9200	1045.5900	910.3200
-25	-15	140.3500	244.2800	214.5300	180.9100	51.3500	1045.5900	910.3200
-25	-10	154.3100	235.9900	229.4300	198.1700	83.1400	1045.5900	910.3200
-25	-5	150.2000	209.1400	216.7000	194.9400	104.8100	1045.5900	910.3200
-25	0	148.5700	197.8200	212.9700	194.2100	121.1900	1045.5900	910.3200
-25	5	148.9900	185.6700	220.9400	206.7100	145.4400	1045.5900	910.3200
-25	10	157.7600	184.3400	239.9000	215.4000	164.4800	1045.5900	910.3200
-25	15	157.8400	169.6900	241.1300	215.6800	180.7300	1045.5900	910.3200
-25	20	154.1000	139.2200	236.3400	208.3100	197.0400	1045.5900	910.3200
-25	25	141.9800	111.1200	226.5700	197.8200	202.5800	1045.5900	910.3200
-20	-25	117.5300	248.0700	175.6200	120.1100	0.3500	1045.5900	910.3200
-20	-20	134.5200	247.5400	195.6900	143.5600	21.1600	1045.5900	910.3200
-20	-15	155.6300	246.6100	215.8800	163.5500	46.7700	1045.5900	910.3200
-20	-10	165.5500	238.2500	229.3000	185.3700	76.5700	1045.5900	910.3200
-20	-5	166.3500	219.2800	226.7000	191.6000	103.8000	1045.5900	910.3200
-20	0	152.0500	200.2700	220.2100	201.2700	125.5700	1045.5900	910.3200
-20	5	160.2200	187.3500	224.0400	200.2700	144.9100	1045.5900	910.3200
-20	10	173.1200	185.3200	238.2200	200.3200	162.4000	1045.5900	910.3200
-20	15	169.6600	172.4900	242.1100	205.4100	178.5000	1045.5900	910.3200
-20	20	171.2100	145.6900	242.0800	200.4500	199.2700	1045.5900	910.3200
-20	25	160.1200	118.3300	232.0100	189.3200	204.0800	1045.5900	910.3200
-15	-25	125.8200	247.6700	174.1400	108.4900	4.9400	1045.5900	910.3200
-15	-20	146.2900	247.8700	196.9700	132.1600	17.7300	1045.5900	910.3200
-15	-15	166.0300	245.1600	215.8500	152.8800	43.2300	1045.5900	910.3200
-15	-10	177.1800	237.9500	226.9000	172.1200	72.8200	1045.5900	910.3200
-15	-5	171.3400	223.5200	226.7700	186.8400	99.4200	1045.5900	910.3200
-15	5	166.2800	192.6800	233.4100	200.3700	149.1400	1045.5900	910.3200
-15	10	183.1400	186.6400	236.6700	190.5500	157.8900	1045.5900	910.3200
-15	15	187.2500	165.1500	242.9800	191.2800	182.6100	1045.5900	910.3200
-15	20	181.6800	144.8100	242.6600	191.4300	197.8400	1045.5900	910.3200
-15	25	174.9700	119.9400	235.9400	181.9100	205.4800	1045.5900	910.3200
-10	10	200.0200	177.3500	241.1500	175.0700	168.0100	1045.5900	910.3200
-10	15	200.4700	160.7700	240.1300	173.1400	179.7300	1045.5900	910.3200
-10	20	203.6500	138.9500	239.9300	167.2600	191.9100	1045.5900	910.3200
-10	-20	162.2200	243.2800	193.6800	108.8600	9.3200	1045.5900	910.3200
-10	-15	174.2900	241.1300	208.6100	128.0800	32.3400	1045.5900	910.3200
-10	-10	191.3800	238.3500	224.5000	146.8900	61.4400	1045.5900	910.3200
-10	-5	197.8200	231.8100	231.3800	156.2600	85.2200	1045.5900	910.3200
-10	0	202.4000	219.2300	239.8800	172.1400	119.8600	1045.5900	910.3200
-10	5	201.2200	195.8600	242.2100	175.8000	149.2400	1045.5900	910.3200
-10	-25	143.4800	242.7600	172.1400	84.3700	13.5300	1045.5900	910.3200

-10	25	195.1600	109.9200	234.9900	170.1100	202.5000	1045.5900	910.3200
-5	-25	144.2900	242.7300	169.4900	78.2000	16.3600	1045.5900	910.3200

Appendix 5.1b. Experimental calibration coefficients ($a_{0\ to}\ a_{27}$) for sector 1

Pitch angle coefficient	Yaw angle coefficient	Total pressure coefficient	Static pressure coefficient
-4.9322	-18.9930	-7.5835	-7.3226
65.2185	20.7689	8.3898	6.9786
-23.3214	-30.5074	2.4379	2.0476
0.0000	0.0000	0.0000	0.0000
29.0580	97.5613	-11.7853	-9.8864
94.8548	137.4428	-3.0261	-2.5137
0.0000	0.0000	0.0000	0.0000
-14.1907	-75.4931	19.3231	16.1224
-47.4083	22.2455	-14.6520	-12.1348
18.7877	20.4133	-27.8504	-23.7219
0.0000	0.0000	0.0000	0.0000
-161.9513	-488.3112	19.8767	16.1224
0.0000	0.0000	0.0000	0.0000
0.0000	0.0000	0.0000	0.0000
-40.4793	-54.0961	-35.6432	-30.2659
0.0000	0.0000	0.0000	0.0000
0.0000	0.0000	0.0000	0.0000
0.0000	0.0000	0.0000	0.0000
0.0000	0.0000	0.0000	0.0000
0.0000	0.0000	0.0000	0.0000
-18.3558	-20.4835	-14.8600	-12.5612
-0.6768	-0.6812	0.0715	0.0602
2.1137	5.2226	-0.1622	-0.1465
15.9775	8.2990	-2.4217	-2.0634
0.0000	0.0000	0.0000	0.0000
0.0000	0.0000	0.0000	0.0000
-48.9200	-20.4277	5.7541	4.9224
0.0000	0.0000	0.0000	0.0000

Appendix 5.1c. Experimental calibration coefficients ($a_{0\ to}\ a_{27}$) for sector 5

Pitch angle coefficient	Yaw angle coefficient	Total pressure coefficient	Static pressure coefficient
-3.3114	-4.0710	-8.1141	-7.7812
0.0000	0.0000	0.0000	0.0000
-21.4470	11.1666	-4.4785	-3.4645
-207.8382	214.3627	-50.8124	-42.1695
158.2277	-158.1382	41.1405	34.1868
0.0000	0.0000	0.0000	0.0000
539.4110	-543.6032	52.7346	42.8298
0.0000	0.0000	0.0000	0.0000
337.5707	-257.2132	20.3891	17.3333
-373.2897	388.2213	-84.8505	-72.0493
1264.9230	-142.3718	500.3982	414.4606
2287.4702	-269.9627	643.1513	533.77784
1102.5171	-127.1228	223.2809	186.2136
-0.9441	1.1700	-0.0939	-0.0883
-304.9344	371.6725	-140.0933	-115.9557
-226.7599	74.2356	58.6516	47.7935
-1.5122	2.3046	-0.8841	-0.7350
-1843.8783	3700.9515	-880.7902	-726.8005
-5359.7686	8918.9666	-1670.6072	-1379.9864
-3044.85	5122.3233	-833.4383	-686.2399
144.1576	71.6888	40.1887	35.0827
-1578.7588	2039.7775	-366.1144	-305.9258
-5469.2583	6922.9333	-1192.2255	-995.7011
0.6431	-2.6823	0.2290	0.1390
1957.6684	-247.9324	4046.9839	3378.0595
2666.1799	-3284.11	5631.8096	4698.0288
1285.4922	-157.1091	2870.1871	2392.2786
1821.2599	-221.4363	452.9903	377.2455

Appendix 5.2a. Numerical calibration coefficients ($a_{0\ to}\ a_{27}$) for sector 1

Pitch angle coefficient	Yaw angle coefficient	Total pressure coefficient	Static pressure coefficient
-64.8745	195.4715	-3.8188	-4.8593
382.3869	-1922.1591	-20.8236	-9.9617
40.1970	74.7603	0.5452	0.3474
-997.6360	7948.6096	65.1537	26.3515
-5.4245	41.5583	1.6365	1.2413
-306.3639	-767.0654	-4.1010	-2.4587
885.6747	2735.5496	11.1282	5.9829
10.6181	-253.18	-17.4726	-13.8767
944.1811	-17283.6735	7.1497	60.0458
10.2196	1.1005	0.5942	0.4964
19.2625	584.0620	47.2324	37.8076
-1243.0627	-4696.3199	-11.2812	-4.0729
-45.3245	-15.0565	-3.1570	-2.6313
45.4543	20741.1418	-214.3486	-235.42
3.1869	2.2343	-0.2124	-0.1686
-668.0710	-12838.4274	256.9133	244.4021
876.1348	3779.8282	1.3394	-2.8765
-11.9588	-655.2832	-50.5522	-40.4390
54.9468	61.4376	5.3429	4.3983
-13.3533	-1.8175	0.1851	0.1141
1.5011	-1.5342	0.0239	0.0264
322.0481	3113.1928	-86.4724	-78.3227
-260.8106	-1146.0639	2.7431	3.3508
-3.8509	319.9125	14.2346	11.1201
-14.6087	-48.8208	-2.8993	-2.3357
8.3150	-6.1891	0.8909	0.7778
-2.4790	1.7509	-0.0358	-0.0408
0.2717	0.2298	-0.0368	-0.0300

Appendix 5.2b. Numerical calibration coefficients ($a_{0\ to}\ a_{27}$) for sector 5

Pitch angle coefficient	Yaw angle coefficient	Total pressure coefficient	Static pressure coefficient
3.7825	4.9020	-4.7663	-4.8444
-9.1411	0.4469	0.1915	0.1601
11.3889	-9.2385	0.1732	-0.2678
-0.2096	-0.4359	-0.2970	-0.1112
23.0369	-2.7590	0.0291	0.2289
-0.5363	-1.5226	0.2755	0.0180
3.4612	0.3292	0.0416	-0.0745
0.0189	0.1174	-0.0942	0.0832
-0.9300	-0.6029	0.0960	-0.4438
-42.9791	2.1938	-0.7776	0.1628
5.8321	-0.9548	0.2293	0.0252
0.0562	-0.2892	0.0327	-0.7298
0.8667	4.7528	-0.8894	-0.2573
0.5662	0.9657	-0.3157	-0.9689
-88.4986	10.4524	-1.7130	-0.0437
0.6496	0.2426	-0.0502	0.0000
-0.2551	-0.0685	-0.0000	-0.0723
0.7192	0.3071	-0.0869	-0.0745
-5.5278	0.2130	-0.0749	-0.0359
1.3702	-0.2950	0.0653	0.0459
24.6453	-1.1266	0.4496	0.2569
-0.3634	-0.3451	0.1098	0.0906
0.0645	0.0589	0.0069	0.0057
0.3794	0.0526	-0.0194	-0.0175
0.0000	0.0000	0.0000	0.0000
-10.3206	1.3535	-0.2470	-0.1527
-1.7432	-2.3395	0.4692	0.3913
49.5354	-5.8109	0.9610	0.5451

Appendix 5.3a. Integrated calibration coefficients ($a_{0\ to}\ a_{27}$) for sector 1

Pitch angle coefficient	Yaw angle coefficient	Total pressure coefficient	Static pressure coefficient
-64.8745	195.4715	-3.8188	-4.8593
382.3869	-1922.1591	-20.8236	-9.9617
40.1970	74.7603	0.5452	0.3474
-997.6360	7948.6096	65.1537	26.3515
-5.4245	41.5583	1.6365	1.2413
-306.3639	-767.0654	-4.1010	-2.4587
885.6747	2735.5496	11.1282	5.9829
10.6181	-253.18	-17.4726	-13.8767
944.1811	-17283.6735	7.1497	60.0458
10.2196	1.1005	0.5942	0.4964
19.2625	584.0620	47.2324	37.8076
-1243.0627	-4696.3199	-11.2812	-4.0729
-45.3245	-15.0565	-3.1570	-2.6313
45.4543	20741.1418	-214.3486	-235.42
3.1869	2.2343	-0.2124	-0.1686
-668.0710	-12838.4274	256.9133	244.4021
876.1348	3779.8282	1.3394	-2.8765
-11.9588	-655.2832	-50.5522	-40.4390
54.9468	61.4376	5.3429	4.3983
-13.3533	-1.8175	0.1851	0.1141
1.5011	-1.5342	0.0239	0.0264
322.0481	3113.1928	-86.4724	-78.3227
-260.8106	-1146.0639	2.7431	3.3508
-3.8509	319.9125	14.2346	11.1201
-14.6087	-48.8208	-2.8993	-2.3357
8.3150	-6.1891	0.8909	0.7778
-2.4790	1.7509	-0.0358	-0.0408
0.2717	0.2298	-0.0368	-0.0300

Appendix 5.3b. Integrated calibration coefficients ($a_{0\ to}\ a_{27}$) for sector 5

Pitch angle coefficient	Yaw angle coefficient	Total pressure coefficient	Static pressure coefficient
3.7825	4.9020	-4.7663	-4.8444
-9.1411	0.4469	0.1915	0.1601
11.3889	-9.2385	0.1732	-0.2678
-0.2096	-0.4359	-0.2970	-0.1112
23.0369	-2.7590	0.0291	0.2289
-0.5363	-1.5226	0.2755	0.0180
3.4612	0.3292	0.0416	-0.0745
0.0189	0.1174	-0.0942	0.0832
-0.9300	-0.6029	0.0960	-0.4438
-42.9791	2.1938	-0.7776	0.1628
5.8321	-0.9548	0.2293	0.0252
0.0562	-0.2892	0.0327	-0.7298
0.8667	4.7528	-0.8894	-0.2573
0.5662	0.9657	-0.3157	-0.9689
-88.4986	10.4524	-1.7130	-0.0437
0.6496	0.2426	-0.0502	0.0000
-0.2551	-0.0685	-0.0000	-0.0723
0.7192	0.3071	-0.0869	-0.0745
-5.5278	0.2130	-0.0749	-0.0359
1.3702	-0.2950	0.0653	0.0459
24.6453	-1.1266	0.4496	0.2569
-0.3634	-0.3451	0.1098	0.0906
0.0645	0.0589	0.0069	0.0057
0.3794	0.0526	-0.0194	-0.0175
0.0000	0.0000	0.0000	0.0000
-10.3206	1.3535	-0.2470	-0.1527
-1.7432	-2.3395	0.4692	0.3913
49.5354	-5.8109	0.9610	0.5451

Appendix 5.4a. Extended calibration coefficients ($a_{0\ to}\ a_{27}$) for sector 1

Pitch angle coefficient	Yaw angle coefficient	Total pressure coefficient	Static pressure coefficient
-0.6805	141.0404	-0.1229	-0.1168
-143.0239	-3.1987	7.3891	6.1765
242.5116	-3921.1306	-13.2669	-11.0379
1192.1488	10291.2015	-123.2999	-108.3674
-7765.4141	-3223.7164	116.3813	77.3953
2818.5485	-192.6454	337.0395	316.1397
-7815.3130	56.4842	1082.0568	705.7838
183.9378	5897.4769	-9.4944	-7.9433
-659.3440	20555.6527	37.5346	31.3795
-3259.2285	-5027.4034	378.8932	334.7587
40939.9586	0.0000	-593.1848	-391.4752
-1867.5562	-56.9631	-1524.4184	-1448.0917
0.0000	0.0000	0.0000	0.0000
450.5298	-5813.0031	-26.1673	-21.9192
0.0000	99999.7617	0.0000	0.0000
2846.6422	0.0000	-384.9451	-342.0977
47590.4263	1973.1975	2716.3591	2619.6237
0.0000	0.0000	0.0000	0.0000
-805.9680	28429.4431	130.6135	116.7814
0.0000	0.0000	0.0000	0.0000
56322.4895	28429.44	-736.8717	-472.6653
-5655.6201	-9840.4941	-2384.1765	-2341.1850
32950.1381	48259.0561	1030.6801	1034.3802
0.0000	0.0000	0.0000	0.0000
-3338.2041	-1818.0141	323.3768	182.9009
-7433.4858	-9392.8961	-175.5716	-180.9297
30017.7538	16314.6630	-234.3793	-116.9532
-7716.2457	-4331.3385	41.1215	12.7918

Appendix 5.4b. Extended calibration coefficients ($a_{0\ to}\ a_{27}$) for sector 5

Pitch angle coefficient	Yaw angle coefficient	Total pressure coefficient	Static pressure coefficient
3.1030	4.8848	-4.7696	-4.8440
-13.4670	0.5382	0.2194	0.2040
10.8452	-9.5078	-0.2688	-0.2751
13.1926	-0.5383	-0.3217	-0.3519
4.8737	-0.0539	-0.4854	-0.4429
-3.6873	-0.2760	0.0196	0.0276
0.0024	0.0000	-0.0000	-0.0005
3.1047	-0.3325	-0.2380	-0.2134
14.4535	-0.7731	0.0433	-0.0296
-39.3114	3.0918	0.8889	0.9271
2.7099	-0.5436	0.0785	0.0486
1.9965	0.1151	-0.0732	-0.0727
13.1848	0.2872	0.0223	-0.0444
-24.7382	1.1830	-0.2485	-0.0767
-24.3005	0.8894	0.3583	0.4167
-8.0706	0.3106	-0.0254	0.0134
2.1104	0.0253	-0.0587	-0.0593
3.6912	0.0692	0.0259	0.0085
-7.3941	0.5062	0.2561	0.2499
-3.9541	0.2262	0.1703	0.1604
22.7923	-1.5196	-0.5338	-0.5534
8.7988	-0.4279	0.0836	0.0262
-1.6483	-0.0479	0.0357	0.0383
-2.8750	0.1475	-0.0551	-0.0261
2.4668	0.1626	-0.0016	-0.0125
-3.4582	0.4345	0.1421	0.1335
-8.6228	-0.1707	0.0394	0.0738
14.7749	-0.5845	-0.2367	-0.2676

Appendix 6.1a. Experimental calibration coefficients ($a_{0\ to}\ a_{27}$) for sector 1

Pitch angle coefficient	Yaw angle coefficient	Total pressure coefficient	Static pressure coefficient
1.2778	-0.2290	-0.9152	-0.7157
-9.4489	-10.262637	6.4259	5.2263
36.4549	39.7041	-20.0673	-16.4880
0.0000	0.0000	0.0000	0.0000
-34.1679	80.3351	7.4407	5.1161
-733.70	-967.4723	379.4386	311.8645
944.99	1373.3204	-375.0753	-308.6270
0.0000	0.0000	0.0000	0.0000
0.0000	0.0000	0.0000	0.0000
114.8945	67.1357	-77.5792	-63.5385
1.4009	-6.8560	-2.8456	-2.1843
0.0000	0.0000	0.0000	0.0000
0.0000	0.0000	0.0000	0.0000
0.0000	0.0000	0.0000	0.0000
-261.6864	-3686.9664	1014.0117	834.3717
-930.0508	-970.4386	424.2657	343.2508
-42.5983	-50.7129	20.9058	17.1466
699.9311	567.5993	-316.4291	-255.0809
0.0000	0.0000	0.0000	0.0000
-69.0471	-27.4360	43.4610	35.2810
0.0000	0.0000	0.0000	0.0000
2893.5576	3408.0921	-1481.0457	-1214.5109
-3226.7	-3560.2796	1681.0244	1376.9317
322.5191	410.1992	-140.3563	-113.7610
4230.6457	5337.96	-1864.1419	-1535.2071
962.5901	1001.2246	-507.5884	-415.0363
-327.6897	-3738.5250	1628.9420	1342.2981
727.3144	730.5256	-438.0875	-362.1121

Appendix 6.1b. Experimental calibration coefficients ($a_{0\ to}\ a_{27}$) for sector 5

Pitch angle coefficient	Yaw angle coefficient	Total pressure coefficient	Static pressure coefficient
-1.5497	6.5428	-0.8152	-1.4405
-334.8319	345.9814	3164.0861	2636.0832
0.0000	0.0100	0.0500	0.0200
476.2627	-473.0266	-4502.4569	-3751.0646
1998.5868	-2033.8318	-18935.2159	-15776.2116
0.0110	0.0100	0.0500	0.0100
0.0100	0.0100	0.0300	0.0100
0.0000	0.0100	0.0100	0.0400
0.0000	0.0100	0.0300	0.0100
132.2628	-127.4346	-1247.1887	-1039.0010
0.0100	0.0100	0.0100	0.0500
0.0100	0.0100	0.0100	0.0300
0.0200	0.0100	0.0100	0.0700
0.0200	0.0100	0.0200	0.0100
-843.8669	859.8445	8000.1563	6665.4966
-138.6593	138.7964	1311.2299	1092.4423
0.0200	0.0100	0.0200	0.0100
0.0200	0.0100	0.0500	0.0300
0.0200	0.0100	0.0300	0.0500
0.0200	0.0100	0.0100	0.0100
-76.1743	74.2449	719.3182	599.2670
48.6096	-50.6799	-461.9151	-384.8704
0.0300	0.0000	0.0300	0.0400
0.0100	0.0000	0.0100	00200
-359.9711	362.7024	3404.2039	2836.2108
0.0000	0.0000	0.0000	0.0100
-51.4445	53.3728	488.8438	407.3041
0.0300	0.0100	0.0100	0.0100

Appendix 6.2a. Numerical calibration coefficients ($a_{0\ to}\ a_{27}$) for sector 1

Pitch angle coefficient	Yaw angle coefficient	Total pressure coefficient	Static pressure coefficient
0.0061	-0.0029	0.0003	0.0003
0.0489	-2.2969	-0.0090	-0.0072
1.0968	0.2222	-0.4556	-0.3695
3.0539	1.4085	0.1889	0.1319
-350.0129	-16.6162	37.8122	29.6396
1119.8029	613.3345	1106.9260	918.9136
26289.1916	5201.2006	-3899.8577	-3205.1112
-0.0114	0.0065	0.0152	0.0042
-0.4957	-0.0313	0.2354	0.1911
-1.8344	-1.1439	-0.0153	0.0103
147.3266	16.9011	-14.2868	-11.2964
-896.6617	-533.4066	-862.3853	-716.3294
-2011.1091	-5879.7893	3791.9357	3145.2073
-0.0421	0.0200	-0.0474	-0.0314
-1479.2841	1011.4911	-289.9257	-256.3500
0.1554	0.0621	0.0077	0.0001
-125.2846	-62.7535	-73.9891	-61.1759
52.6813	-5.2452	-7.0291	-5.4729
0.0165	-0.0877	-0.0451	-0.0277
4594.6916	1108.2361	-783.6580	-647.6208
-24.8351	0.2148	2.7028	2.0950
259.3893	135.5677	201.2495	167.0818
-63.4074	-40.1257	-48.1461	-39.9932
1.7306	-0.0285	-0.0863	-0.0673
-1263.2466	-560.0217	307.1739	256.7693
3.5463	-3.0976	2.6069	2.1672
93.7052	89.4253	-34.4289	-29.1796
-16.7657	1.0323	-4.1931	-4.3133

Appendix 6.2b. Numerical calibration coefficients ($a_{0\ to}\ a_{27}$) for sector 5

Pitch angle coefficient	Yaw angle coefficient	Total pressure coefficient	Static pressure coefficient
3.0426	5.2573	-3.3539	-3.6574
-9.5112	-0.2241	-1.0931	-0.9143
0.4486	-6.7325	0.3226	0.2722
-17.5380	-2.5616	-7.0025	-5.8680
-0.2283	-0.1346	0.0827	0.0628
-1.2149	0.2666	-0.6858	-0.5725
-4.8387	0.5575	-3.1582	-2.6362
0.0000	0.0000	0.0000	0.0000
-8.0134	-2.2277	-3.1230	-2.6239
-0.0951	-0.2618	-0.0396	-0.0332
1.1009	0.0110	0.1788	0.1489
0.1261	-0.1018	-0.0957	-0.0798
0.2819	-0.0752	0.0295	0.0246
15.4018	1.9586	6.2635	5.2401
0.0189	0.0538	-0.0378	-0.0319
13.4828	2.9491	5.4750	4.5917
5.1604	-0.8169	3.1729	2.6484
0.8879	0.0025	0.2468	0.2066
0.5177	-0.0100	0.1364	0.1138
0.0756	-0.0000	0.0109	0.0091
0.0045	0.0187	0.0031	0.0026
2.8802	0.8742	1.1671	0.9810
2.1213	-0.3242	1.3247	1.1157
0.1654	0.0032	0.0667	0.0559
0.2074	-0.0111	0.0686	0.0573
0.0559	-0.0015	0.0164	0.0137
-0.0063	0.0115	0.0012	0.0010
-0.0030	-0.0064	0.0030	0.0025

Appendix 6.3a. Integrated calibration coefficients ($a_{0\ to}\ a_{27}$) for sector 1

Pitch angle coefficient	Yaw angle coefficient	Total pressure coefficient	Static pressure coefficient
0.0061	-0.0029	0.0003	0.0003
0.0489	-2.2969	-0.0090	-0.0072
1.0968	0.2222	-0.4556	-0.3695
3.0539	1.4085	0.1889	0.1319
-350.0129	-16.6162	37.8122	29.6396
1119.8029	613.3345	1106.9260	918.9136
26289.1916	5201.2006	-3899.8577	-3205.1112
-0.0114	0.0065	0.0152	0.0042
-0.4957	-0.0313	0.2354	0.1911
-1.8344	-1.1439	-0.0153	0.0103
147.3266	16.9011	-14.2868	-11.2964
-896.6617	-533.4066	-862.3853	-716.3294
-2011.1091	-5879.7893	3791.9357	3145.2073
-0.0421	0.0200	-0.0474	-0.0314
-1479.2841	1011.4911	-289.9257	-256.3500
0.1554	0.0621	0.0077	0.0001
-125.2846	-62.7535	-73.9891	-61.1759
52.6813	-5.2452	-7.0291	-5.4729
0.0165	-0.0877	-0.0451	-0.0277
4594.6916	1108.2361	-783.6580	-647.6208
-24.8351	0.2148	2.7028	2.0950
259.3893	135.5677	201.2495	167.0818
-63.4074	-40.1257	-48.1461	-39.9932
1.7306	-0.0285	-0.0863	-0.0673
-1263.2466	-560.0217	307.1739	256.7693
3.5463	-3.0976	2.6069	2.1672
93.7052	89.4253	-34.4289	-29.1796
-16.7657	1.0323	-4.1931	-4.3133

Appendix 6.3b. Integrated calibration coefficients ($a_{0\ to}\ a_{27}$) for sector 5

Pitch angle coefficient	Yaw angle coefficient	Total pressure coefficient	Static pressure coefficient
3.0426	5.2573	-3.3539	-3.6574
-9.5112	-0.2241	-1.0931	-0.9143
0.4486	-6.7325	0.3226	0.2722
-17.5380	-2.5616	-7.0025	-5.8680
-0.2283	-0.1346	0.0827	0.0628
-1.2149	0.2666	-0.6858	-0.5725
-4.8387	0.5575	-3.1582	-2.6362
0.0000	0.0000	0.0000	0.0000
-8.0134	-2.2277	-3.1230	-2.6239
-0.0951	-0.2618	-0.0396	-0.0332
1.1009	0.0110	0.1788	0.1489
0.1261	-0.1018	-0.0957	-0.0798
0.2819	-0.0752	0.0295	0.0246
15.4018	1.9586	6.2635	5.2401
0.0189	0.0538	-0.0378	-0.0319
13.4828	2.9491	5.4750	4.5917
5.1604	-0.8169	3.1729	2.6484
0.8879	0.0025	0.2468	0.2066
0.5177	-0.0100	0.1364	0.1138
0.0756	-0.0000	0.0109	0.0091
0.0045	0.0187	0.0031	0.0026
2.8802	0.8742	1.1671	0.9810
2.1213	-0.3242	1.3247	1.1157
0.1654	0.0032	0.0667	0.0559
0.2074	-0.0111	0.0686	0.0573
0.0559	-0.0015	0.0164	0.0137
-0.0063	0.0115	0.0012	0.0010
-0.0030	-0.0064	0.0030	0.0025

Appendix 6.4a. Extended calibration coefficients ($a_{0\ to}\ a_{27}$) for sector 1

Pitch angle coefficient	Yaw angle coefficient	Total pressure coefficient	Static pressure coefficient
0.0173	-0.0374	0.0045	0.0040
-0.0527	0.0100	-0.0028	-0.0028
-0.3126	-0.1404	0.0427	0.0386
0.7888	19.1819	0.2302	0.2078
0.0000	0.0000	0.0000	0.0000
6.1599	-27.2986	-0.7987	-0.8961
1.7913	45.0809	13.2873	11.5482
0.0000	0.0000	0.0000	0.0000
0.0141	-0.0052	-0.0021	-0.0018
-0.5862	-6.8664	-0.0990	-0.0884
3.8193	4.4109	-2.7589	-2.4334
-5.9777	-74.2892	-0.5361	-0.2470
195.7677	-69.9170	-91.0103	-79.5559
-0.1375	0.3306	-0.0539	-0.0476
0.0000	0.0000	0.0000	0.0000
0.4684	0.2744	0.0001	0.0000
0.0000	0.0000	0.0000	0.0000
2.2814	-2.2923	0.1481	0.1415
-0.1387	0.1386	0.0300	0.0261
-241.3999	31.5751	83.8750	73.4511
0.6142	0.1379	-0.0601	-0.0535
0.6440	15.9839	0.6988	0.5455
-1.0437	-7.2541	-0.0479	-0.0294
0.0917	-0.4967	0.1154	0.0956
35.8253	-7.4372	-21.4176	-18.7965
0.3666	-5.5809	-0.0696	-0.0596
-30.0543	4.1307	11.8118	9.9924
-12.8470	4.5892	-6.1507	-5.9786

Appendix 6.4b. Extended calibration coefficients ($a_{0\ to}\ a_{27}$) for sector 5

Pitch angle coefficient	Yaw angle coefficient	Total pressure coefficient	Static pressure coefficient
0.2313	5.4656	-3.2962	-3.6104
-4.6472	-0.6075	-1.1547	-0.9640
-0.1698	-6.5589	0.1175	0.0988
15.0804	-4.9108	-7.7905	-6.5121
0.1334	-0.1606	0.0739	0.0556
0.3719	-0.1430	-0.2122	-0.1790
2.1713	-1.3647	-0.8721	-0.7373
-0.3268	-0.0075	0.0617	0.0511
8.0184	-3.0718	-4.0483	-3.3868
0.0031	-0.2737	-0.0338	-0.0283
-0.6992	0.1336	0.2328	0.1932
-0.0084	-0.1656	0.0350	0.0286
0.0011	-0.0531	0.0331	0.0275
-12.9198	4.0817	6.8031	5.6794
-0.0070	0.0563	-0.0382	-0.0322
-13.1093	4.5712	6.6251	5.5380
-2.3585	1.1184	0.9399	0.7934
-0.4394	0.1244	0.2333	0.1950
-0.1413	0.0757	0.0722	0.0603
0.0155	0.0089	0.0032	0.0027
0.0024	0.0186	0.0036	0.0030
-3.1736	1.1738	1.5495	1.2964
-0.9765	0.4844	0.3852	0.3252
-0.0948	0.0312	0.0569	0.0478
-0.0764	0.0366	0.0282	0.0237
0.0169	0.0053	0.0105	0.0088
-0.058	0.0121	0.0003	0.0003
-0.0011	-0.0066	0.0030	0.0025

Appendix 7.1a. Experimental calibration coefficients ($a_{0\ to}\ a_{27}$) for sector 1 of a conical five-hole pressure probe

Pitch angle coefficient	Yaw angle coefficient	Total pressure coefficient	Static pressure coefficient
-0.3380	3.1246	0.8453	0.81189
0.1167	3.0622	-0.1193	-0.1148
-84.4852	973.0944	168.4539	161.7415
1861.9735	-4134.7591	-2924.9116	-2809.4528
-2330.6821	32388.1042	3530.9165	3389.3744
1298.9612	-2149.0677	-2035.0035	-1954.6251
-379.7530	-4925.6246	563.5677	541.7742
-0.0446	-1.1889	0.0279	0.0269
133.3603	-1424.6050	-262.6612	-252.2008
-1175.4321	2949.1717	1848.5116	1775.5747
6849.0094	-93994.5955	-10499.0633	-10078.3028
-4309.8827	8316.2923	6760.3732	6493.4219
6267.7510	-65338.9890	-9395.6976	-9021.1713
-49.9069	498.0730	95.2045	91.4138
-18743.8675	253048.0645	28254.3221	27123.6040
360.0360	-1003.0120	-566.1358	-543.8098
0.0000	0.0000	0.0000	0.0000
-7408.5750	99198.8417	11418.9288	10961.4688
-42.5491	125.0068	66.7114	64.0823
24091.8108	-34595.4071	-36377.4163	-34919.9017
3451.5689	-44865.2263	-5297.0484	-5084.9060
0.0000	0.0000	0.0000	0.0000
0.0000	0.0000	0.0000	0.0000
-571.9903	7284.6678	864.0169	829.4118
-15502.0940	223833.5947	23321.6801	22386.9555
0.0000	0.0000	0.0000	0.0000
4848.5861	-6912.0796	-7232.2858	-6942.3890
-595.1020	8222.0598	823.9928	789.9533

Appendix 7.1b. Experimental calibration coefficients ($a_{0\ to}\ a_{27}$) for sector 5 of a conical five-hole pressure probe

Pitch angle coefficient	Yaw angle coefficient	Total pressure coefficient	Static pressure coefficient
3.3842	4.9498	-32.0000	-31.7200
-9.0880	-0.0557	0.4018	0.3874
-0.3847	-8.4204	0.5807	0.5585
-0.2975	1.0277	0.1455	0.1345
-0.0783	0.4216	-1.9885	-1.9112
0.0441	0.0579	-0.1389	-0.1331
0.0375	0.1777	0.1607	0.1538
0.8935	0.1824	-0.3283	-0.3154
0.1952	0.2551	1.9501	1.8716
0.3229	-1.1172	-2.4350	-2.3400
-0.1380	0.4360	0.1189	0.1144
-0.0168	-0.3008	-0.3767	-0.3632
0.0753	0.2447	0.4271	0.4108
0.1074	-2.2735	-3.5399	-3.3991
0.1528	-0.9648	-1.0296	-0.9896
0.0636	-0.1935	-0.7815	-0.7502
0.0088	-0.07436	-0.1207	-0.1158
-0.0471	0.0796	0.2300	0.2207
-0.0230	0.0256	-0.0673	-0.0647
-0.2086	-0.0827	0.1145	0.1101
-0.0929	0.8566	1.3610	1.3079
0.0000	0.7881	1.1524	1.1066
-0.0291	0.1310	0.1959	0.1886
0.0004	-0.4067	-0.4582	-0.4401
0.0188	-0.0810	-0.1620	-0.1557
-0.0073	0.0464	0.0616	0.0592
-0.0738	-0.0881	-0.0622	-0.0599
-0.0430	0.4604	0.6436	0.6185

Appendix 7.1c. Experimental calibration coefficients ($a_{0\ to}\ a_{27}$) for sector 1 of a hemispherical five-hole pressure probe

Pitch angle coefficient	Yaw angle coefficient	Total pressure coefficient	Static pressure coefficient
0.6722	-0.9652	-1.8779	-1.8029
2.5976	-6.6169	-8.0497	-7.7295
62.0903	-80.6542	-179.5853	-172.4257
-777.8081	1432.7296	2025.0259	1944.0619
2192.2081	-5198.6434	-2791.2926	-2676.7352
3295.5215	-4121.8252	-9533.3879	-9153.2093
-2195.0235	32345.5725	60375.1186	57964.9814
0.8649	-1.0602	-2.2729	-2.1820
-25.4585	34.7661	72.2475	69.3661
715.1229	-1262.6121	-1845.2641	-1771.4663
-4730.6413	8946.3907	8762.8869	8409.0598
0.0000	0.0000	0.0000	0.0000
0.0000	0.0000	0.0000	0.0000
-2.6007	3.7537	7.2474	6.9579
61882.9735	-87525.95	-177394.1645	-170319.3176
-188.5337	327.4557	485.2518	465.8443
-3439.8903	3531.7232	10135.1806	9731.0772
2791.3238	-4764.6645	-5753.9753	-5522.4945
5.4440	-10.6793	-12.9225	-12.4048
-6571.5750	87043.8647	179413.5548	172260.0817
-561.1591	903.4932	1219.6894	1170.6995
2034.4702	-1973.4626	-6070.6726	-5828.6635
-415.3478	396.3191	1253.0497	1203.1026
28.4308	-43.8338	-65.7566	-63.1212
22993.3928	-32703.2655	-68093.2108	-65378.8228
28.7009	-37.8585	-85.6294	-82.2154
-3424.4304	4881.6174	10261.8104	9852.8223
114.5295	-179.7177	-425.2040	-409.2518

Appendix 7.1d. Experimental calibration coefficients ($a_{0\ to}\ a_{27}$) for sector 5 of a hemispherical five-hole pressure probe

Pitch angle coefficient	Yaw angle coefficient	Total pressure coefficient	Static pressure coefficient
2.6403	7.6061	-27.3323	-27.2329
-10.5204	-7.5931	3.5873	3.4456
0.1465	-6.7212	-0.3452	-0.3315
-12.0998	-23.6396	11.6283	11.1680
-0.6480	-1.4355	2.4773	2.3787
-0.1683	-0.8162	0.1758	0.1690
0.1078	-0.0629	-0.2629	-0.2525
0.0596	0.4032	-0.5633	-0.5410
6.5005	15.7714	-7.2564	-6.9697
-0.2532	-0.1258	0.3588	0.3446
0.8083	1.6947	-1.6115	-1.5483
-0.1226	0.1788	0.2670	0.2563
0.0000	0.0000	0.0000	0.0000
16.5523	30.7673	-13.6871	-13.1469
0.4324	0.8053	-1.1828	-1.1265
-1.8938	-5.2963	2.6873	2.5810
-0.1290	-0.2419	0.4310	0.4139
-0.1346	-0.3698	-0.2047	-0.1967
0.1301	0.2834	-0.3427	-0.3292
0.0159	0.0212	0.3732	0.3585
0.0562	-0.1074	0.0055	0.0053
-5.2035	-9.1260	3.7873	3.6378
0.2202	0.3601	-0.3122	-0.2998
-0.2869	-0.4832	0.6886	0.6615
-0.0619	-0.2965	-0.0639	-0.0614
-0.1776	-0.4344	0.1282	0.1232
0.0369	0.2107	0.0443	0.0425
-0.0778	-0.0947	0.1126	0.1082

Appendix 7.2a. Numerical calibration coefficients ($a_{0\ to}\ a_{27}$) for sector 1 of a conical five-hole pressure probe

Pitch angle coefficient	Yaw angle coefficient	Total pressure coefficient	Static pressure coefficient
-1.0347	3.1371	1.8226	1.7509
-11.8954	38.2875	12.3865	11.8911
-199.4874	453.9264	188.7806	181.1570
571.1247	-1673.0651	-367.0083	-351.9420
362.2789	-2207.2344	-347.6641	-333.7517
1929.5868	320.2634	-1496.4072	-1434.9165
-2642.6982	6552.8922	2044.2376	1961.1437
6.3572	-21.0291	-7.0122	-6.7323
267.1997	-587.1180	-285.1734	-273.7107
-1017.3965	2944.5669	613.8730	588.5533
1281.2287	267.7909	-852.4330	-817.1323
-8212.2565	4974.5147	6209.7402	5954.8754
3228.3872	-7817.9552	-2647.5899	-2540.4029
-86.8597	179.8924	97.9434	94.0272
0.0000	0.0000	0.0000	0.0000
612.3627	-1745.3991	-352.3513	-337.7604
12348.5209	-12227.0144	-9157.0023	-8781.2810
-3125.6030	4234.3451	2543.9215	2440.4562
-123.7195	349.9134	69.9082	67.0771
0.0000	0.0000	0.0000	0.0000
1984.4797	-3303.0599	-1717.4949	-1648.0008
-8560.8691	10339.9791	6245.4441	5989.1601
2778.9629	-3726.0008	-1998.9769	-1916.9285
-380.1754	681.7378	331.6367	318.2346
-1629.1153	3637.9914	1448.8219	1390.5808
-338.7563	470.4195	240.4900	230.6162
1050.0557	-2342.9403	-921.9839	-884.9402
-193.7869	404.8488	122.3941	116.4663

Appendix 7.2b. Numerical calibration coefficients ($a_{0\ to}\ a_{27}$) for sector 5 of a conical five-hole pressure probe

Pitch angle coefficient	Yaw angle coefficient	Total pressure coefficient	Static pressure coefficient
3.3103	4.9922	-32.0587	-31.7755
-9.5179	-0.0742	0.3723	0.3590
3.7994	-8.1292	-0.0977	-0.0944
1.7654	0.5654	0.5828	0.5531
1.2740	0.5759	-1.7556	-1.6903
0.1551	-0.2610	-0.6315	-0.6073
0.6329	0.2869	0.1708	0.1635
1.8053	0.2715	1.9632	1.8839
0.0000	0.0000	0.0000	0.0000
-15.3651	-2.3854	0.0476	0.0485
0.4679	0.5109	0.0847	0.0861
-0.3929	0.0450	-0.3358	-0.322
-0.1265	0.6649	2.0986	2.0179
-3.6751	-1.5713	-4.1671	-3.9990
-5.4090	-1.8459	-1.4064	-1.3513
-0.6849	-0.1781	-0.8079	-0.7753
-0.1930	-0.0799	-0.1448	-0.1389
0.4531	0.1196	0.2434	0.2335
-0.7573	-0.0539	0.0465	0.0447
0.1518	-0.0240	-0.0977	-0.0938
8.6365	1.5579	-0.0171	-0.0180
1.3088	0.5641	1.3472	1.2929
0.2003	-0.0036	0.1835	0.1763
-1.0151	-0.3475	-0.4811	-0.4616
-0.0806	0.0429	-0.0858	-0.0823
0.5034	-0.0264	0.0000	0.0002
0.2241	-0.3635	-1.0036	-0.9652
3.0200	0.9627	0.8122	0.7805

Appendix 7.2c. Numerical calibration coefficients ($a_{0\ to}\ a_{27}$) for sector 1 of a hemispherical five-hole pressure probe

Pitch angle coefficient	Yaw angle coefficient	Total pressure coefficient	Static pressure coefficient
0.0031	-0.0014	0.0034	0.0033
0.0363	0.0194	-0.0392	-0.0377
-1.4139	0.9235	0.5128	0.4959
-37.5492	4.2919	-46.4708	-44.6335
-20.8874	6.3195	-33.7871	-32.4675
0.0000	0.0000	0.0000	0.0000
0.1346	-0.0010	-0.0006	-0.0006
0.0097	-0.0027	0.0051	0.0049
-0.4428	0.3491	0.0935	0.0904
-31.7361	4.5810	-36.6872	-35.2351
-136.6379	-1.9490	-150.9503	-144.9705
0.0000	0.0000	0.0000	0.0000
0.0000	0.0000	0.0000	0.0000
-0.0126	0.0264	0.0056	0.0150
0.0000	0.0000	0.0000	0.0000
-7.1932	0.8921	-7.4605	-7.1646
0.0000	0.0000	0.0000	0.0000
-91.0349	-7.7406	-103.8509	-99.7372
-0.2655	0.1112	-0.2567	-0.24666
0.0000	0.0000	0.0000	0.0000
-18.1284	-2.4790	-20.9952	-20.1659
6.5828	21.3577	0.2636	0.2466
3.0807	-1.3646	-0.3552	-0.3442
-0.7030	-0.1673	-0.8643	-0.8289
-53.4679	1.1140	3.8454	3.7301
0.1250	5.1511	-0.0847	-0.0814
0.6769	0.4279	37.7151	36.2346
-14.8189	5.0586	37.3653	36.8705

Appendix 7.2d. Numerical calibration coefficients ($a_{0\ to}\ a_{27}$) for sector 5 of a hemispherical five-hole pressure probe

Pitch angle coefficient	Yaw angle coefficient	Total pressure coefficient	Static pressure coefficient
1.4104	5.0649	-25.8749	-25.8329
-7.0462	0.1077	0.1608	0.1544
-0.0840	-6.6969	0.0578	0.0557
-0.0902	0.2079	0.6233	0.5975
-0.0922	0.1341	0.5219	0.5002
0.0000	0.0000	0.0000	0.0000
-0.1307	0.3576	-0.1636	-0.1572
-0.1401	0.2250	0.1249	0.1201
-0.1584	-0.0393	0.0209	0.0201
0.0359	-0.1792	-0.0178	-0.0172
0.0156	0.0395	-0.1202	-0.1157
0.0673	-0.1594	0.0361	0.0347
0.0179	-0.0262	0.1173	0.1127
0.0421	-0.1938	-0.1534	-0.1475
0.0463	-0.0552	-0.1003	-0.0965
0.0000	0.0000	0.0000	0.0000
0.0239	-0.0935	-0.0166	-0.0160
0.0290	-0.0762	-0.0573	-0.0551
-0.0070	0.0077	-0.0003	-0.0003
0.0049	-0.0172	0.0017	0.0016
-0.0064	0.0065	0.0084	0.0181
-0.0083	0.0369	0.0127	0.0122
0.0000	0.0000	0.0000	0.0000
0.0016	-0.0313	-0.0125	-0.0120
-0.009	-0.0006	-0.0394	-0.0379
-0.0069	0.0075	0.0068	0.0066
-0.0016	0.0039	-0.0046	-0.0044
-0.0059	0.0077	0.0077	0.0074

Appendix 7.3a. Integrated calibration coefficients ($a_{0\ to}\ a_{27}$) for sector 1 of a conical head five-hole pressure probe

Pitch angle coefficient	Yaw angle coefficient	Total pressure coefficient	Static pressure coefficient
-1.0347	3.1371	1.8226	1.7509
-11.8954	38.2875	12.3865	11.8911
-199.4874	453.9264	188.7806	181.1570
571.1247	-1673.0651	-367.0083	-351.9420
362.2789	-2207.2344	-347.6641	-333.7517
1929.5868	320.2634	-1496.4072	-1434.9165
-2642.6982	6552.8922	2044.2376	1961.1437
6.3572	-21.0291	-7.0122	-6.7323
267.1997	-587.1180	-285.1734	-273.7107
-1017.3965	2944.5669	613.8730	588.5533
1281.2287	267.7909	-852.4330	-817.1323
-8212.2565	4974.5147	6209.7402	5954.8754
3228.3872	-7817.9552	-2647.5899	-2540.4029
-86.8597	179.8924	97.9434	94.0272
0.0000	0.0000	0.0000	0.0000
612.3627	-1745.3991	-352.3513	-337.7604
12348.5209	-12227.0144	-9157.0023	-8781.2810
-3125.6030	4234.3451	2543.9215	2440.4562
-123.7195	349.9134	69.9082	67.0771
0.0000	0.0000	0.0000	0.0000
1984.4797	-3303.0599	-1717.4949	-1648.0008
-8560.8691	10339.9791	6245.4441	5989.1601
2778.9629	-3726.0008	-1998.9769	-1916.9285
-380.1754	681.7378	331.6367	318.2346
-1629.1153	3637.9914	1448.8219	1390.5808
-338.7563	470.4195	240.4900	230.6162
1050.0557	-2342.9403	-921.9839	-884.9402
-193.7869	404.8488	122.3941	116.4663

Appendix 7.3b. Integrated calibration coefficients ($a_{0\ to}\ a_{27}$) for sector 5 of a conical head five-hole pressure probe

Pitch angle coefficient	Yaw angle coefficient	Total pressure coefficient	Static pressure coefficient
3.3103	4.9922	-32.0587	-31.7755
-9.5179	-0.0742	0.3723	0.3590
3.7994	-8.1292	-0.0977	-0.0944
1.7654	0.5654	0.5828	0.5531
1.2740	0.5759	-1.7556	-1.6903
0.1551	-0.2610	-0.6315	-0.6073
0.6329	0.2869	0.1708	0.1635
1.8053	0.2715	1.9632	1.8839
0.0000	0.0000	0.0000	0.0000
-15.3651	-2.3854	0.0476	0.0485
0.4679	0.5109	0.0847	0.0861
-0.3929	0.0450	-0.3358	-0.322
-0.1265	0.6649	2.0986	2.0179
-3.6751	-1.5713	-4.1671	-3.9990
-5.4090	-1.8459	-1.4064	-1.3513
-0.6849	-0.1781	-0.8079	-0.7753
-0.1930	-0.0799	-0.1448	-0.1389
0.4531	0.1196	0.2434	0.2335
-0.7573	-0.0539	0.0465	0.0447
0.1518	-0.0240	-0.0977	-0.0938
8.6365	1.5579	-0.0171	-0.0180
1.3088	0.5641	1.3472	1.2929
0.2003	-0.0036	0.1835	0.1763
-1.0151	-0.3475	-0.4811	-0.4616
-0.0806	0.0429	-0.0858	-0.0823
0.5034	-0.0264	0.0000	0.0002
0.2241	-0.3635	-1.0036	-0.9652
3.0200	0.9627	0.8122	0.7805

Appendix 7.3c. Integrated calibration coefficients ($a_{0\ to}\ a_{27}$) for sector 1 of a hemispherical head five-hole pressure probe

Pitch angle coefficient	Yaw angle coefficient	Total pressure coefficient	Static pressure coefficient
0.0031	-0.0014	0.0034	0.0033
0.0363	0.0194	-0.0392	-0.0377
-1.4139	0.9235	0.5128	0.4959
-37.5492	4.2919	-46.4708	-44.6335
-20.8874	6.3195	-33.7871	-32.4675
0.0000	0.0000	0.0000	0.0000
0.1346	-0.0010	-0.0006	-0.0006
0.0097	-0.0027	0.0051	0.0049
-0.4428	0.3491	0.0935	0.0904
-31.7361	4.5810	-36.6872	-35.2351
-136.6379	-1.9490	-150.9503	-144.9705
0.0000	0.0000	0.0000	0.0000
0.0000	0.0000	0.0000	0.0000
-0.0126	0.0264	0.0056	0.0150
0.0000	0.0000	0.0000	0.0000
-7.1932	0.8921	-7.4605	-7.1646
0.0000	0.0000	0.0000	0.0000
-91.0349	-7.7406	-103.8509	-99.7372
-0.2655	0.1112	-0.2567	-0.24666
0.0000	0.0000	0.0000	0.0000
-18.1284	-2.4790	-20.9952	-20.1659
6.5828	21.3577	0.2636	0.2466
3.0807	-1.3646	-0.3552	-0.3442
-0.7030	-0.1673	-0.8643	-0.8289
-53.4679	1.1140	3.8454	3.7301
0.1250	5.1511	-0.0847	-0.0814
0.6769	0.4279	37.7151	36.2346
-14.8189	5.0586	37.3653	36.8705

Appendix 7.3d. Integrated calibration coefficients ($a_{0\ to}\ a_{27}$) for sector 5 of a hemispherical head five-hole pressure probe

Pitch angle coefficient	Yaw angle coefficient	Total pressure coefficient	Static pressure coefficient
1.4104	5.0649	-25.8749	-25.8329
-7.0462	0.1077	0.1608	0.1544
-0.0840	-6.6969	0.0578	0.0557
-0.0902	0.2079	0.6233	0.5975
-0.0922	0.1341	0.5219	0.5002
0.0000	0.0000	0.0000	0.0000
-0.1307	0.3576	-0.1636	-0.1572
-0.1401	0.2250	0.1249	0.1201
-0.1584	-0.0393	0.0209	0.0201
0.0359	-0.1792	-0.0178	-0.0172
0.0156	0.0395	-0.1202	-0.1157
0.0673	-0.1594	0.0361	0.0347
0.0179	-0.0262	0.1173	0.1127
0.0421	-0.1938	-0.1534	-0.1475
0.0463	-0.0552	-0.1003	-0.0965
0.0000	0.0000	0.0000	0.0000
0.0239	-0.0935	-0.0166	-0.0160
0.0290	-0.0762	-0.0573	-0.0551
-0.0070	0.0077	-0.0003	-0.0003
0.0049	-0.0172	0.0017	0.0016
-0.0064	0.0065	0.0084	0.0181
-0.0083	0.0369	0.0127	0.0122
0.0000	0.0000	0.0000	0.0000
0.0016	-0.0313	-0.0125	-0.0120
-0.009	-0.0006	-0.0394	-0.0379
-0.0069	0.0075	0.0068	0.0066
-0.0016	0.0039	-0.0046	-0.0044
-0.0059	0.0077	0.0077	0.0074

Appendix 7.4a. Extended calibration coefficients ($a_{0\ to}\ a_{27}$) for sector 1 of a conical five-hole pressure probe

Pitch angle coefficient	Yaw angle coefficient	Total pressure coefficient	Static pressure coefficient
-2.1198	27.1498	2.3640	2.2874
-0.7885	170.7880	-1.2368	-1.1440
-16.9376	-344.6261	-5.8746	-5.7400
-32.8103	-376.9082	24.7924	23.3411
-85.6977	762.3447	36.1277	35.4032
-623.2089	-641.3491	148.8420	144.2499
1178.0292	787.7666	-295.3090	-285.6218
0.5223	-228.3067	1.9136	1.7854
94.1280	503.8205	-7.7360	-7.3764
126.9527	150.2986	-73.6527	-69.3789
626.8878	-783.8183	-216.5752	-210.376
3789.2792	5012.3592	-995.7951	-961.9883
-7541.2176	-7796.4876	1907.4250	1841.8824
-89.2254	-197.3125	9.1192	8.7634
19324.1737	23243.9563	-4881.4175	-4708.5633
-157.6714	947.0269	65.8025	61.8564
-9097.0492	-1212.8275	2545.4585	2454.1797
-1719.7622	-1624.1219	536.3797	518.5070
64.5426	-624.1490	-17.1166	-15.9746
-2482.0532	-3160.2034	6237.68	6012.1753
1903.2317	2692.2431	-534.5886	-515.6800
10769.9076	13120.3337	-3129.9311	-3013.7931
-6286.0960	-6662.7429	1864.4946	1793.6831
-690.1222	-1030.1565	172.9755	166.7038
16916.8087	21619.9713	-4183.5132	-4029.7921
1446.1467	1319.2393	-432.9845	-416.2636
-5626.2322	-6945.5841	1420.2018	1367.1501
680.4787	773.0714	-214.0385	-206.8394

Appendix 7.4b. Extended calibration coefficients ($a_{0\ to}\ a_{27}$) for sector 5 of a conical five-hole pressure probe

Pitch angle coefficient	Yaw angle coefficient	Total pressure coefficient	Static pressure coefficient
-17.2851	-58.4674	-79.1262	-77.0269
-355.0829	1093.7119	-1147.9102	-1103.2463
-5.0221	718.8280	340.7020	327.4493
-1804.6215	10218.0031	-6338.1021	-6090.9250
1259.1780	-6249.0438	4536.6458	4359.7783
2464.3151	-7058.0117	9138.9466	8783.4057
10801.5575	-6981.4504	46234.1379	44432.1612
5299.8930	-3127.9174	19473.2630	18713.9999
-2896.8684	1143.0731	-7851.2089	-7545.0977
1539.4912	-3380.6762	2070.4631	1990.3163
0.0000	0.0000	0.0000	0.0000
11041.0706	-9838.5456	53212.5648	51137.0083
4646.3792	-8982.8029	6734.5746	6473.5670
0.0000	0.0000	0.0000	0.0000
-2642.7229	7307.7472	-7960.0985	-7649.9826
2963.2544	1550.5121	2870.4090	2759.2003
0.0000	0.0000	0.0000	0.0000
-1100.8165	71028.3109	-42320.7375	-40670.2982
0.0000	0.0000	0.0000	0.0000
-9809.1336	24932.3147	-23648.2602	-22728.0359
-474.1811	1121.8470	-322.2302	-309.9068
1444.0473	2953.9011	599.5402	576.6302
-1584.1042	19953.6995	-10211.1203	-9812.4824
-5405.2210	35946.7775	-21103.5116	-20280.4376
-5345.4287	12558.6983	-12584.3410	-12094.6667
-1019.1282	27614.2442	-25096.7058	-24119.8973
-163.9563	251.7662	1505.1143	1446.0720
661.2067	-2131.3235	2514.1291	2416.0832

Appendix 7.4c. Extended calibration coefficients ($a_{0\ to}\ a_{27}$) for sector 1 of a hemispherical five-hole pressure probe

Pitch angle coefficient	Yaw angle coefficient	Total pressure coefficient	Static pressure coefficient
0.0188	-0.1311	0.2923	0.2868
-6.2312	5.4523	-7.5734	-7.2666
-152.4061	50.9312	-126.3833	-121.6985
-3395.9922	-9940.1322	-12477.0734	-11991.2532
-1361.9065	-1458.3691	-2932.7634	-2812.6117
2685.1395	9407.9411	6695.8466	6437.4822
-1015.6585	21608.6423	83231.87	80212.0103
-3.6933	2.9277	-4.9721	-4.7758
-158.3431	65.9878	-116.6511	-112.3834
-5614.3360	-1610.5734	-20953.5923	-20137.2621
0.0000	0.0000	0.0000	0.0000
0.0000	0.0000	0.0000	0.0000
-1265.3282	20372.7467	100000.4232	96368.5727
-40.3878	21.4465	-26.8353	-25.8745
0.0000	0.0000	0.0000	0.0000
-3062.3306	-8773.2523	-11714.7012	-11258.1525
0.0000	0.0000	0.0000	0.0000
3405.7915	28613.4511	6061.1223	5813.22
-549.7411	-1573.2923	-2178.0813	-2093.1887
0.0000	0.0000	0.0000	0.0000
2806.2162	21399.6023	4709.2011	6829.1001
4442.1535	16279.5003	11743.6123	35309.5722
3625.8395	13562.3884	9815.3403	2097.2243
634.0196	4479.3053	1025.8211	50249.8368
-5650.4318	2534.7110	52147.2100	983.9745
785.0941	2992.3464	2182.2613	9435.2780
-3436.2554	30.1180	36642.6715	11289.2312
-7221.8560	-313.9042	7086.5123	4516.8010

Appendix 7.4d. Extended calibration coefficients ($a_{0\ to}\ a_{27}$) for sector 5 of a hemispherical five-hole pressure probe

Pitch angle coefficient	Yaw angle coefficient	Total pressure coefficient	Static pressure coefficient
0.0000	0.0000	-5.7311	-5.6510
-0.0000	0.0003	-7.5418	-7.4100
0.0000	-0.0002	-0.1598	-0.1850
0.0101	-0.0004	-1.4100	-1.1444
0.0000	0.0000	-0.3011	-0.1333
0.0635	0.0108	-2.0006	-2.001
-0.3977	-0.5515	-0.2108	-0.3300
-0.0111	0.0115	-0.0122	-0.2101
-0.0531	0.0331	-0.0008	-0.0000
0.0523	-0.1022	-0.0012	-0.0033
0.5733	-3.5100	-0.0102	-0.0104
-0.3311	-0.1282	-0.1101	-0.0022
2.1712	3.2311	-0.0111	-0.0011
-0.2623	2.1241	0.0111	0.0011
-3.2511	-14.0000	-0.1100	-0.0101
-2.3110	12.0136	0.0111	0.0116
13.7823	-82.7483	0.0000	0.0000
1.1779	-6.0043	-0.0104	-0.0007
-5.5545	59.0081	-0.0007	-0.0001
104.2111	-643.3565	-0.0123	-0.0003
-45.1513	226.5673	0.0000	0.0003
4.8000	-76.4645	0.0003	0.0005
-435.0034	2073.6423	0.0001	0.0001
-61.1139	821.6489	0.0002	0.0001
-46.1004	-289.2327	0.0001	0.0003
-344.5078	5932.4541	0.0024	0.0002
-1654.5000	7389.4343	0.0011	0.0003
-824.2613	17611.9110	0.0005	0.0003